UNIVERSITÉ DE STRASBOURG

ÉCOLE DOCTORALE DES SCIENCES DE LA VIE ET DE LA SANTÉ

[Laboratoire de Biophotonique et Pharmacologie – UMR 7213]

THÈSE

présentée par :

Ievgen SHULOV

soutenue le : **05 janvier 2016**

pour obtenir le grade de : **Docteur de l'université de Strasbourg**

Discipline/ Spécialité : Sciences du Vivant / Biophysique

Synthesis of fluorescent organic nanoparticles for biological applications

THÈSE dirigée par :

M. Klymchenko Andrey	Directeur de recherche CNRS, Université de Strasbourg
M. Pivovarenko Vasyl	Professeur, Université nationale Taras Chevtchenko de Kiev

RAPPORTEURS :

Mme. Fery-Forgues Suzanne	Directeur de recherche CNRS, Université Toulouse III
Mme. Gergely Csilla	Professeur, Université Montpellier II

EXAMINATEUR :

Mme. Bourel Line	Professeur, Université de Strasbourg

To those who inspire me

An indispensable hypothesis, even though still far from being a guarantee of success, is however the pursuit of a specific aim, whose lighted beacon, even by initial failures, is not betrayed.

— Max Planck

Nobel Lecture in Physics (2 Jun 1920)

Acknowledgements

First of all, I would like to thank my both supervisors: Dr. Andrey Klymchenko and Prof. Vasyl Pivovarenko.

I would like express my appreciation to my mentor, Dr. Andrey Klymchenko, for his encouragement, guidance and expert advising during this challenging and exciting project. By his inspiration and knowledge we started better understand the fundamental photophysical processes within fluorescent organic NPs.

Vasyl, thanks a lot for your support and input, especially as you mostly offered a different perspective on things about the project. French Embassy in Ukraine along with University of Strasbourg and Taras Shevchenko National University of Kiev are acknowledged for the financial support of this work.

I would also like to express my gratitude to the committee members for their willingness to participate in the examining of my PhD thesis: Prof. Csilla Gergely from University of Montpellier, Dr. Suzanne Fery-Forgues from University of Toulouse and Prof. Line Bourel from University of Strasbourg.

I would like to acknowledge the head of the Laboratory of Biophotonics and Pharmacology, Prof. Yves Mély and also my colleagues working in UMR 7213, with whom I had a pleasure to work together during my PhD studies. My special thanks to Jurga Valanciunaite for proofreading of the manuscript, Youri Arntz for his help with AFM measurements, Sule Oncul for accomplishing some cellular studies and Guy Duportail for his kind help and continuous support.

The fruitful collaboration and discussions with Mayeul Collot, Andreas Reisch, Kateryna Trofymchuk, Rémy Kreder, Redouane Bouchaala, Nicolas Humbert, Ludovic Richert and others resulted in improved experimental design and high quality results obtained in this work with the use of fluorescence techniques. I also thank to the group of Dr. Alain Wagner for spending time together and having fun, especially to the Sasha, Sergii, Sylvain and Igor.

These years in Strasbourg were a big adventure for me. And for this I am very grateful to my friends, whom I met here. There are some of them with whom I have spent good time inside the lab and outside as well: Marianna Sholokh, Iuliia Konko, Iuliia Karpenko, Nataliia Voievoda, Viktoria Postupalenko, Iryna Lysova, Marian Dryzhakov, Gosia Nowicka, Lesia Kovalenko, Vasyl Kilin, Leonid Andronov, Artem Osypenko and all the other people with whom I had a pleasure to be together.

The very last lines are dedicated to Olena, I simply enjoy every second we spend together. Thanks for your love and support. You mean the world to me.

Finally, I thank my mom for her love and support throughout all my studies. I felt your presence right beside me all the time, and it helped me to accomplish this thesis.

List of used abbreviations

BODIPY	boron-dipyrromethene fluorescent dye
Cy3	Cyanine 3
Cy5	Cyanine 5
DDSN	Dye-doped silica nanoparticles
DIPEA	N,N-Diisopropylethylamine
DLS	Dynamic Light Scattering
DMF	N,N-Dimethylformamide
DMSO	Dimethyl sulfoxide
FCS	Fluorescence Correlation Spectroscopy
FP	Fluorescent protein
FRET	Förster (or Fluorescence) resonance energy transfer
FWHM	Full width at half maximum
Φ	Quantum yield (efficiency)
HBr	Hydrobromic acid
HBTU	2-(1H-Benzotriazole-1-yl)-1,1,3,3-tetramethyluronium hexafluorophosphate
HPLC	High-performance liquid chromatography
mM	millimolar
NIR	Near infrared
NPs	Nanoparticles
PDI	Polydispersity index
PEG	Polyethylene glycol
QD	Quantum dot
RhB	rhodamine B
TEA	Triethylamine
TFA	Trifluoroacetic acid
THF	Tetrahydrofuran
τ	Fluorescence lifetime
λ_{abs}	Position of absorption maximum
λ_{ex}	Excitation wavelength
λ_{em}	Emission wavelength
UV	Ultraviolet
µM	Micromolar

Contents

1. BIBLIOGRAPHICAL OVERVIEW

1.1 Principles of fluorescence 1

1.1.1 Fluorescence resonance energy transfer (FRET) 4

1.1.2 Advantages of fluorescence 8

1.2 Fluorescent dyes and proteins 8

1.2.1 Small-molecule fluorophores 8

1.2.2 Fluorescent proteins 13

1.3 Fluorescence of dye ensembles 15

1.3.1 Exciplex and excimer formation 15

1.3.2 Aggregation-Caused Quenching (ACQ) 16

1.3.3 H- and J-aggregates 19

1.3.4 Aggregation-induced emission (AIE phenomenon) 20

1.4 Fluorescent nanoparticles 22

1.4.1 Quantum Dots (QDs) 22

1.4.2 Dye-doped silica nanoparticles 25

1.4.3 Carbon-based nanoparticles 28

1.4.4 Nanoparticles from organic dyes 31

1.4.5 Dye-doped polymer nanoparticles 33

1.4.6 Dye-doped lipid nanoparticles 37

1.4.7 Conjugated polymer nanoparticles (Pdots) 39

1.4.8 Fluorescent nanoparticles assembled from amphiphiles 40

1.5 Techniques for characterization of nanoparticles 49

1.5.1 Atomic force microscopy (AFM) 49

1.5.2 Transmission electron microscopy (TEM) 52

1.5.3 Dynamic light scattering (DLS) 55

1.5.4 Zeta potential 57

1.5.5 Fluorescence Correlation Spectroscopy (FCS) 59

References 62

Aim of the PhD thesis 69

2. RESULTS AND DISCUSSION 70

2.1 Highly lipophilic fluorescent dyes in nano-emulsions: towards bright non-leaking nano-droplets 71

2.2 Fluorinated counterion-enhanced emission of rhodamine aggregates: ultrabright nanoparticles for bioimaging and light-harvesting 74
2.3 Non-coordinating anions assemble cyanine amphiphiles into ultra-small fluorescent nanoparticles 79
2.4 Shell-cross-linked calixarene micelles with cyanine corona: protein-sized ultrabright fluorogenic nanoparticles 83
General conclusions & perspectives 87
3. MATERIALS AND METHODS 91
3.1 Synthetic procedures of fluorescent organic building blocks 92
3.1.1 Synthesis of lipophilic dyes for the encapsulation into lipid or polymer matrix 92
3.1.2 Synthesis of alkyl rhodamines for the NPs by nanoprecipitation approach 97
3.1.3 Synthesis of building blocks for counterion-assembled micelles. 102
3.1.4 Synthesis of building blocks for polymerized micelles. 111
3.2 Preparation of fluorescent nanoparticles 114
3.2.1 Preparation of lipid nanodroplets 114
3.2.2 Preparation of ion-associated NPs from rhodamine B alkyl esters 114
3.2.3 Counterion-promoted micellization as a synthesis of micellar NPs 114
3.2.4 Preparation of shell-cross-linked micelles 115
3.3 Physical measurements 116
3.3.1 Optical spectroscopy 116
3.3.2 Atomic force microscopy (AFM) measurements 117
3.3.3 Fluorescence correlation spectroscopy (FCS) and data analysis 117
3.3.4 Single-particle imaging 118
3.3.5 Cellular studies 118
3.3.6 Other software 119
Publication list of I. Shulov 121
Résumé de la thèse en Français 123

1. BIBLIOGRAPHICAL OVERVIEW

1.1 Principles of fluorescence

The process of fluorescence can be schematically represented by the Jabłoński diagram shown in Figure 1.1, a.[1] Firstly, molecule in a singlet electronic ground state (S_0) absorbs a photon of suitable energy (Figure 1.1, a (i)). This promotes an electron to higher energy orbitals, which relax quickly to the first singlet excited state (S_1). The decay of the excited state can take place with photon emission (*i.e.*, fluorescence) (Figure 1.1, a (iii)) or through a nonradiative (NR) process (Figure 1.1, a (iv)), including bond rotation or vibration, molecular collision, and photoinduced electron transfer (PET). If the fluorophore is excited to the second electronic singlet state (S_2), it rapidly falls down to the S_1 state due to internal conversion that corresponds to a non-radiative transition between two electronic states of the same spin multiplicity (Figure 1.1, a (ii)). From S_1, internal conversion to S_0 is also possible but is less efficient than conversion from S_2 to S_1, due to the much larger energy gap between S_1 and S_0. Therefore, internal conversion from S_1 to S_0 can compete with emission of photons (fluorescence). The emission rates of fluorescence are typically about 10^8-10^{10} s^{-1}. If the excited state undergoes intersystem crossing (ITC) to the triplet excited state (T_1) (Figure 1.1, a (v)), subsequent relaxation occurs by either photon emission, so-called phosphorescence (Figure 1.1, a (vi)), or by nonradiative (NR) decay (Figure 1.1, a (vii)). In this case, transitions to the ground state are forbidden and the emission rates are slow, about 10^6-10 s^{-1}. The probability of ITC increases by substitution with, or proximity to, atoms with high atomic number due to spin–orbit coupling—a phenomenon commonly termed the “heavy atom effect”. For example, the halogenated fluorescein derivative Rose Bengal possesses a low fluorescence quantum yield ($\Phi < 2\%$) and a high intersystem crossing rate to the triplet state[2], that makes it a potent singlet oxygen generator for a diverse range of applications.[3] Halogen substitutients also produce a significant batochromic shift of absorption and fluorescence emission wavelengths ($\lambda_{abs}/\lambda_{em}$ = 548/566 nm), thus denoting that substitutes, which are located in aromatic system, can significantly affect the emission properties of the dye rather than simply extending the conjugation of the aromatic system. Another important pathway for decay of the singlet excited state involves Fluorescence/Förster resonance energy transfer (FRET) to an acceptor molecule. FRET is highly dependent on the distance between the fluorescent species and can be used as a “spectroscopic ruler” to measure the proximity of labeled entities on a molecular level.

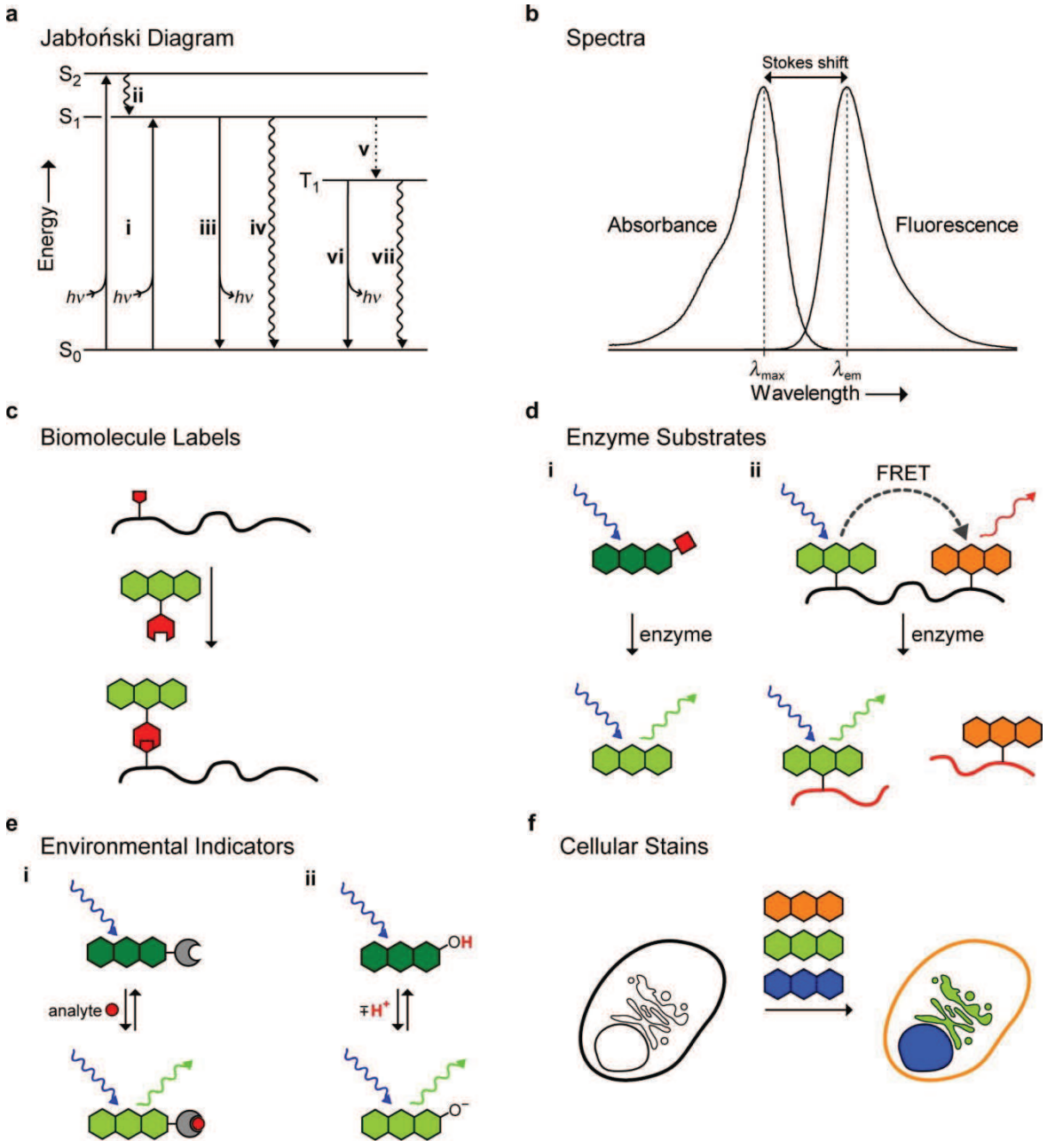

Figure 1.1 Photophysical concepts (a, b) and biological applications (c–f) of small-molecule fluorophores: a) Jabłoński diagram (i) absorption of a photon gives an excited state, (ii) internal conversion to S_1, (iii) fluorescence, (iv) nonradiative decay, (v) intersystem crossing to T_1, (vi) phosphorescence, (vii) nonradiative decay; b) generic absorption and emission spectra; c) site-specific labeling of a biomolecule by an orthogonal reaction between two functional groups (red).; d) enzyme substrates (i) enzyme-catalyzed removal of a blocking group (red) elicits a change in fluorescence, (ii) enzyme catalyzes the cleavage of a labeled biomolecule (red) and concomitant decrease in FRET e) environmental indicators (i) binding of an analyte (red) elicits a change in fluorescence, (ii) protonation of a fluorophore elicits a change in fluorescence; f) staining of subcellular domains by distinct fluorophores. Reprinted from ref.[4]

A generic absorption/emission spectrum is presented in Figure 1.1, b. The maximal absorption (λ_{abs}) is related to the energy between the S_0 and the higher energy levels. The absorption capability of a molecule at λ_{abs} is given by the extinction coefficient (ε), defined by the Bouguer–Lambert–Beer law ($A = \varepsilon \times c \times l$, where c = concentration of the solution of fluorophore, l = length of the light path). The maximal emission wavelength (λ_{em}) is longer (*i.e.*, lower in energy) than λ_{abs} due to energy losses by solvent relaxation (reorganization) or other processes, such as vibrational or rotational relaxation. The difference between λ_{abs} and λ_{em} is termed the "Stokes shift", by the name of George Stokes, who has first demonstrated it by rudimentary setup of a filter set.[5]

However, there is an exception from the $\lambda_{abs} < \lambda_{em}$ rule, that occurs under multiphoton excitation, when two or more photons are absorbed simultaneously to yield the singlet excited state.[6] This «anti-Stokes shift » behavior can be also observed in upconversion nanoparticles (UCNPs).

The average time between excitation and emission is known as fluorescence lifetime (τ), and is related to the relative rates of fluorescence and competing nonradiative processes, which give to this parameter essential role for time-resolved and fluorescence polarization measurements. Usually, organic fluorophores stay in the excited state about 10^{-8} to 10^{-9} s, but fluorescence lifetime (τ) can also vary from 0.1 to > 10 ns and is an important parameter for time-resolved measurements[7] and fluorescence polarization applications.[8] Another crucial property of a fluorophore is the quantum yield or quantum efficiency of fluorescence (Φ)—essentially the ratio of photons emitted to those absorbed. Quantum yield is also one of the key parameters for total brightness, which is defined as the product of the multiplication $\varepsilon \times \Phi$, where (ε) is extinction coefficient and (Φ) is quantum yield. This allows making reasonable comparison of photonic performance between different classes of molecular reporters (e.g., dyes and fluorescent proteins) under the same light intensity.[4]

Dyes with red-shifted spectra are preferred for bioimaging as their use avoids autofluorescence eliciting from the cells and allows deeper tissue imaging as longer excitation wavelengths can penetrate deeper.[9] Synthetic organic chemistry provides wavelength tunability for the organic dyes. One possible solution to get emission shifted more into a red region is to extend the conjugation system of chromophore. As an example, fusion of an additional phenyl ring to the fluorescein to form naphthofluorescein leads to a dramatic bathochromic shift with $\lambda_{abs}/\lambda_{em}$ = 708 nm/790 nm, ε = 56 000 M^{-1} cm^{-1}, but extremely low quantum yield of <1% due to the aggregation quenching by π-π stacking.[10] Fluorophores can be employed in many ways, including as labels for biomolecules (Figure 1.1, panel c), enzyme substrates (Figure 1.1, d), environmental indicators (Figure 1.1, e), and cellular stains (e.g. DAPI, Hoechst 33342, LysoTracker Green DND-26 etc.) (Figure 1.1, f). A variety of fluorogenic probes can be created by attachment of groups, that can be cleaved by light, enzymes, changes in chemical environment in order to create caged fluorescent dyes, that are able to produce

high fluorescence after cleavage from the blocking groups.[11] This, in particular, can serve for vast number applications in bioimaging. The usefulness of a particular fluorophore is defined by its specific chemical properties (*e.g.*, reactivity, lipophilicity, pK_a, stability), photophysical properties (*e.g.*, λ_{abs}, λ_{em}, ε, Φ, τ) and its cost (*i.e.* price) as well.

Fluorescent dyes, probes and tags are used in many ways for in-vitro diagnostics. Fluorescence is used to detect protein-protein interactions, in immunoassays and DNA hybridization, in molecular diagnostics and infectious diseases diagnostics. For these applications, fluorescence-tagged antibodies, proteins and oligonucleotides take a critical part of the diagnostic assays.

Elaboration of these core structures has resulted in numerous advanced probes for assaying biological systems. Nonetheless, the new challenges in biochemical and biological research will require even more sophisticated and tailored probes.

1.1.1 Fluorescence resonance energy transfer (FRET)

A nonradiative process whereby an excited state donor (D) (usually a fluorophore) transfers energy to a proximal ground state acceptor (A) through long-range dipole–dipole interactions[12,1] is so-called Fluorescence resonance energy transfer (FRET, Figure 1.2). The energy should be absorbed by acceptor at the emission wavelength(s) of the donor, with further emission of energy by acceptor. Acceptor can also proceed to the dark state without any emission of energy itself (*i.e.,* dark quenching).

The efficiency of energy transfer relies on three main factors, such as spectral overlap between the emission spectra of the donor and absorption spectra of the acceptor, the relative orientation of the transition dipoles, and, most importantly, the distance between the donor and acceptor molecules.[13,14] The distances from 2 up to 10 nm allows FRET to occur, which are comparable to the dimensions of biological macromolecules. This fact makes FRET a very powerful technique to study biomolecular interactions.

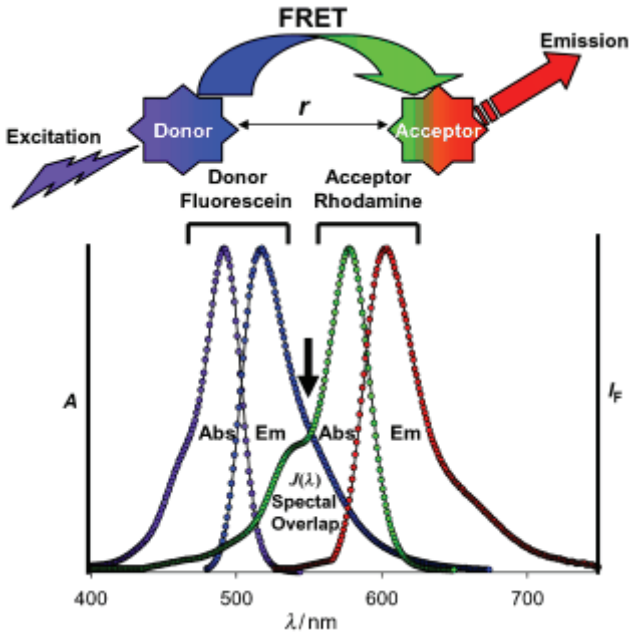

Figure 1.2 Schematic representation of the FRET process: Upon excitation, the excited-state donor molecule transfers energy nonradiatively to a proximal acceptor molecule located at distance r from the donor. The acceptor releases the energy either through fluorescence or nonradiative channels. The spectra show the absorption (Abs) and emission (Em) profiles of one of the most commonly used FRET pairs (fluorescein as donor and rhodamine as acceptor).[15] Fluorescein can be efficiently excited at 480 nm and emits at around 520 nm. The spectral overlap between fluorescein emission and rhodamine absorption, as defined by $J(\lambda)$, is observed at 500–600 nm. The Förster distance R_0 for this pair is 5.5 nm. Thus, in an optimal configuration ($0.5R_0 < R < 1.5R_0$), excitation of fluorescein below 500 nm can result in a significant FRET emission of rhodamine above 600 nm. *A* = normalized absorption, I_F = normalized fluorescence. Adapted from the ref.[16]

The energy transfer rate $k_T(r)$ between a single D/A pair is dependent on the distance r between D and A and can be stated in terms of the Förster distance R_0, which is a distance between D and A at which 50 % of energy decay proceed through FRET mechanism and another part through other radiative or nonradiative processes. Förster distance R_0 can be calculated from the following equation, which considers energy transfer between a single linked D/A pair separated by a fixed distance r and originates from the early calculations by Förster[17, 18] :

$$R_0 = 9.78 \times 10^3 \, [\kappa^2 \eta^{-4} \Phi_D J(\lambda)]^{1/6} \quad \text{(in Angstroms)}$$

The D/A transition dipole orientation is described by the factor κ^2, which can vary in range from 0 (perpendicular) to 4 (collinear/parallel). There is no possibility to measure this factor experimentally,

except only few cases when crystal structure of the D/A molecules can be determined. Therefore, this creates some ambiguity in FRET calculations.[1, 19, 20] However, it was found from the mobility and statistical dynamics of the dye linker that the κ^2 value of approximately 2/3 in almost all biological applications. This approximation also sets a maximum error limit of 35% on any calculated distance (R_0).[1] A value of 1.4 is attributed for the refractive index for biomolecules in aqueous solution. Φ_D is the quantum yield of the donor in the absence of the acceptor and *J(λ)* is the overlap integral between the donor emission and the acceptor absorption, which stand for the degree of spectral overlap.

The efficiency of the FRET can be calculated from either steady-state or time-resolved measurements by the following equations:

$$E = 1 - \frac{F_{DA}}{F_D}$$

or

$$E = 1 - \frac{\tau_{DA}}{\tau_D}$$

where F is the relative donor fluorescence intensity in the absence (F_D) and presence (F_{DA}) of the acceptor, and τ is the fluorescent lifetime of the donor in the absence (τ_D) and presence (τ_{DA}) of the acceptor.

The FRET efficiency is extremely sensitive to the distance between the donor and acceptor (proportional to r^6), which makes it useful in versatile applications for bioanalysis, ranging from the assay of interactions of an antigen with an antibody in vitro to the real-time imaging of protein folding in vivo.[21, 22] The various compounds from different classes of materials can play the role as either FRET donor or FRET acceptor, such as organic «classical» dye fluorophores, dark quenchers, and polymers; inorganic materials such as metal chelates, and metal and semiconductor nanocrystals; fluorophores of biological origin such as fluorescent proteins and amino acids; and biological compounds that exhibit bioluminescence upon enzymatic catalysis. This creates large flexibility in experimental design, as well myriad FRET configurations and techniques, which are currently in use. However, there are several requirements imposed on properties for probes applied in FRET: (a) suitable excitation and emission wavelengths; (b) poor environment-sensitivity; (c) high extinction coefficients and (d) sufficient photostability (especially for the molecule of FRET acceptor, which plays the role of «antenna», while gathering the energy of photons from a large number of FRET donors).

Frequently, a non-fluorescent quencher molecule is used as acceptor in FRET measurements. In such a case, only the donor molecule emits, and its fluorescence decreases while donor and acceptor

molecules coming closer. The principal advantage of using such acceptors over their fluorescent counterparts is the elimination of background fluorescence originating from direct acceptor excitation or re-emission. Dabcyl (4-(4'-dimethylaminophenylazo)benzoic acid) and Dabsyl (4-dimethylaminoazobenzene-4'-sulfonyl) (Figure 1.3) are two of the most commonly used nonfluorescent acceptors, having absorption maxima centered at 485 and 466 nm, respectively. Other examples of commercial quencher families include the QSY, Black Hole (BHQ), (Figure 1.3), QXL, ATTO, BlackBerry, etc. They generally exhibit broad absorption spectra, which allow their application with a variety of fluorescent markers.

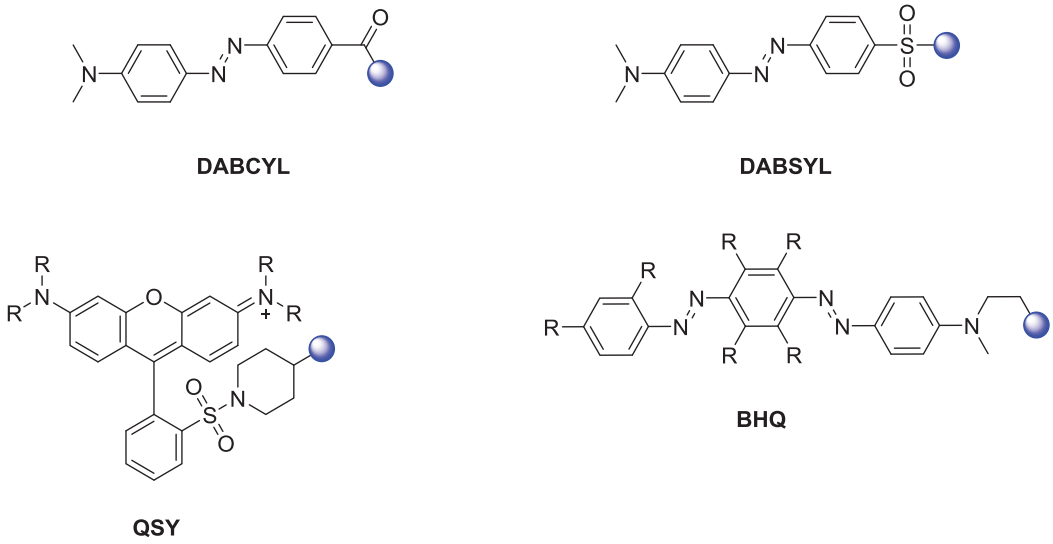

Figure 1.3 Commonly utilized fluorescence quenchers. Blue ball shows conjugation position.

The one key disadvantage is that intermolecular FRET assay requires attachment of both components, which is a challenging task to accomplish when a large set of compounds is tested. Moreover, such crucial properties of biomolecules as folding and/or activity could be strongly affected upon the labeling of the biomolecules by dyes that are bulkier than aminoacids or nucleotides, and which should be checked afterwards. Site-specific labeling of proteins with two synthetic fluorophores implies the use of multistep and a complicated synthesis.[23] For intracellular experiments, it could be replaced by fluorescent protein-tag technique[24], nevertheless interpretation of FRET results in the large protein complexes is not a trivial task.

Fluorophores with small Stokes shifts (e.g. Bodipy etc) tend to self-quench by energy transfer, so-called homo-FRET, therefore limiting the number of labels that can be tagged to a biomolecule.[25]

1.1.2 Advantages of fluorescence

The broad applications of fluorescence techniques in biological studies are related to its major advantages over other research techniques:

• **High sensitivity.** With a proper selection of experimental conditions as well as bright fluorescent marker, it is possible to investigate events on a single molecule level (*e.g,* activity of protein or enzyme of interest). While absorbance can be reliably measured at concentrations down to micromolar, fluorescence techniques can be applied at nano and picomolar concentrations and even femtomolar with up-to-date developments (*e.g.,* single-molecule microscopy).

• **Low time of response.** The monitoring of very rapid processes is possible with the use of fluorescence, since the response is limited only by the fluorescence lifetime within the range 10^{-8}–10^{-10} s.

• **Non-invasive character.** The fluorescence techniques possess nondestructive character. For example, biological sample remains almost intact during application of moderate laser power. Thus, adverse side effects in living cells and tissues are rather limited while using fluorescence techniques.

There is a large range of applications, where fluorescence techniques already have already been applied, as for instance: study of membrane structure and function (membrane probes); measurement of ion concentrations inside living cells (ion-sensors); imaging of cell compartments (tracers); binding of ligands to biomolecules, including *in vivo*; measurement of distances within macromolecules and biological assemblies upon their interactions (FRET assays). Thus, fluorescence provides a powerful tool for studying molecular interactions in analytical chemistry, biochemistry, cell biology, physiology, photochemistry, environmental science (*i.e.* ecology) etc.

1.2 Fluorescent dyes and proteins

1.2.1 Small-molecule fluorophores

Small-molecule organic fluorophores stay essential tools for studying processes in chemical biology, as they are ubiquitous as biomolecular labels, enzyme substrates, environmental indicators, and cellular stains.[26, 27, 28, 29, 1, 30, 31, 32] Various commercial suppliers (*e.g.,* Thermo Fisher, Sigma etc) provide numerous commercial fluorophores, therefore choosing an appropriate fluorophore to visualize a biochemical or biological process should not be a tough task. However, some applications require new fluorophores through *de novo* design and synthesis. Synthetic organic chemistry allows

intrinsic modulation of the core fluorophore structure as well as attachment of various suitable side moieties, such as reactive groups, substrate moieties, chelating components, and other chemical entities to a number of "core" of historically established fluorophores.[33] That gave rise to the ensemble of different families of probes. In general, these fluorophore families are characterized by excellent spectral characteristics, high chemical stabilities, and convenient organic syntheses. Fluorescent organic dyes typically have narrow but asymmetric absorption and emissions spectra. This means that they can only be excited in narrow spectral range and also have red tail in emission, which can be a drawback for some applications, such as FRET. As it was mentioned before, the brightness

(ε × Φ) is the key parameter for the comparison of molecular probes. Figure 1.4 displays a plot of brightness *versus* λ_{abs} for the major classes of biologically significant fluorescent dyes.

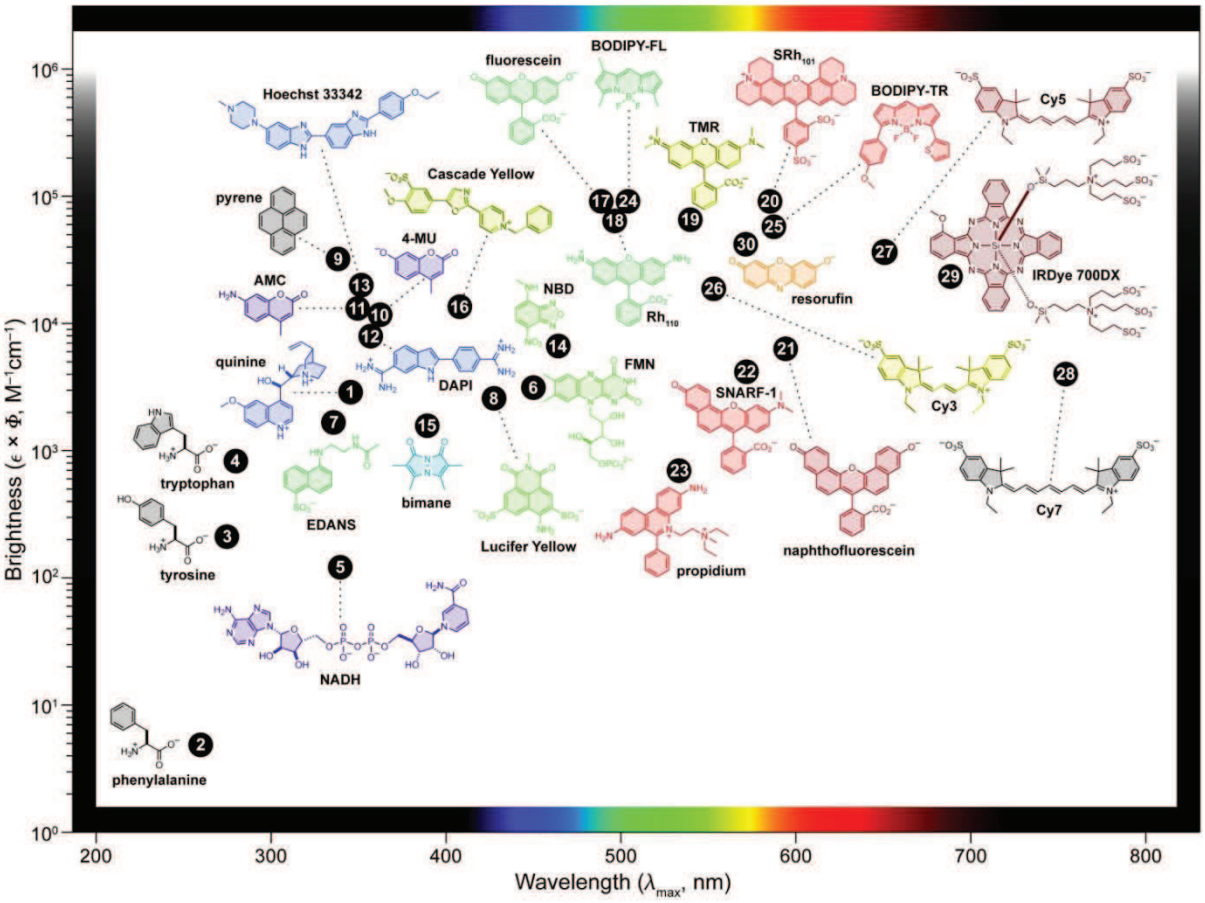

Figure 1.4 Plot of brightness (ε × Φ) *versus* the wavelength of maximum absorption (λ_{abs}) of the most biologically relevant fluorophores. The color of the structure indicates the wavelength of maximum emission (λ_{em}). For adequate clarity, only the chromophore system of some dye molecules is shown**.** Adapted from ref. [4]

As can be seen from Figure 1.4, the brightest dyes are Fluorescein (17), Rhodamine (19, 20) and BODIPY (25) as well as Cy5 (27) in the far-red region. Fluorescein (17) and rhodamine derivatives (19, 20) are the most well-known and probably the most utilized fluorescent markers. Fluorescein (17) was firstly synthesized by Baeyer in 1871[34] and remains one of the most popular dyes together with its improved analogue Alexa®488[35] – fluorescein bearing two sulfonate groups for better aqueous solubility and reduced tendency to aggregate. Rhodamine is an amino-containing analog of fluorescein, which carries a positive charge delocalized between two amino groups through a conjugated aromatic system. Rhodamines are much more photostable and less pH-sensitive than fluorescein. Rhodamine labels are often paired with fluorescein derivatives for FRET-based experiments because of efficient energy transfer between these xanthene compounds due to adequate Forster radius.[35] Tetramethylrhodamine as a most prominent example (TMR; 19) has longer excitation and emission wavelengths ($\lambda_{abs}/\lambda_{em}$ of 544/571 nm in methanol) (Figure 1.5) compared to fluorescein (17) or rhodamine 110 (Rh_{110}; 18), but a lower quantum yield (Φ = 0.68) in methanol.[36] This feature is probably due to decay of the excited state via rotation around the C-N bond.[37] This undesirable property can be circumvented by freezing the C-N bond via introduction of rigid julolidine ring systems. A particular example, such as sulforhodamine 101 (SRh_{101}; 20) shows higher quantum yield (Φ = 0.77) than do the unrestricted dyes (TMR ; 19) and exhibit longer excitation and emission wavelengths.[38] The amine-reactive sulfonyl chlorides julolidine-containing rhodamines are known as a Texas Red™ derivatives.[35] However, there are some limitations due to potential toxicity of rhodamines as they are cationic and non-biodegradable, which could limit their applications in vivo.

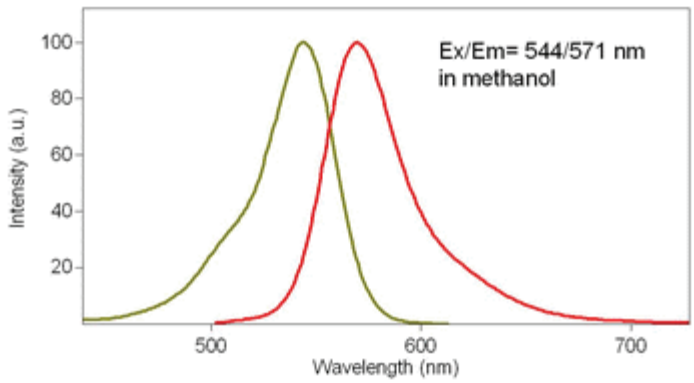

Figure 1.5 Representative absorption and emission spectra of Tetramethylrhodamine (6-TAMRA, 6-TRITC) in methanol.

Another common dye family is BODIPY derivatives, which were firstly introduced in 1968 by Treibs and Kreuzer.[39] They are strongly absorbing small molecules that emit a relatively narrow

fluorescence band with high quantum yields. BODIPY dyes are relatively insensitive to the polarity and pH of their environment and are reasonably stable under physiological conditions. Meantime, they have some disadvantages like poor water solubility and small Stokes shift[35, 40], which may result in *homo*-FRET process mentioned above. In a recent time, the chemistry and application of BODIPY dyes were increasingly developing [41, 42, 43, 44] with a particular attention on the BODIPY emitting in NIR region[45, 46, 47].

The term "cyanine dye"[48] stands for a dye system with a polymethine chain between two amino/imino groups, which can be illustrated by the simple representation (*i.e.,* $R_2N\text{-}(CH{=}CH)_n\text{-}CH{=}N^+R_2$). The study of this dye family probably has been performed most systematically in terms of molecular basis of color.[49] Most popular cyanine dyes contain heterocyclic rings that increase the stability and make the synthesis more convenient. This family of dyes is characterized by high extinction coefficients and red-shifted absorption maxima but moderate quantum yields as well as photostability. Perhaps the most well-established cyanine dyes in modern biology research are the CyDye fluorophores, which are based on a sulfoindocyanine structure.[50] Cy3 (26) possess spectral properties that are comparable to TMR - λ_{abs} = 554, λ_{em} = 568 nm, ε ~ 1.3 × 10^5 M^{-1} cm^{-1}, and Φ = 0.14 in water. Cy5 (27) exhibits longer wavelengths with λ_{abs} = 652 nm, λ_{em} = 672 nm, ε ~ 2.0×10^5 M^{-1} cm^{-1}, and Φ = 0.18 in water. Longer cyanine derivatives, such as Cy7 (28), exhibit a λ_{abs} / λ_{em} of 755/788 nm, although with a lower quantum yield (Φ = 0.02), which is a disadvantage.[51] The emission properties depend strongly on the length of the polymethine chain, therefore they can be wisely modulated for the specific application purpose. Further elaboration of the cyanine core moieties can provide an additional control over wavelength. For example, an introduction of a fused benzo ring in the dihydroindole moieties promotes a bathochromic shift of ~20–30 nm.[52] This structural modification is designated with a ".5" suffix (*e.g.,* Cy5.5).

Coumarin dyes represent one of the oldest dye class, which found a number of biological applications mainly due to their very small size and good water solubility.[53] However, their fluorescence properties, such as absorptivity in UV-region and low photostability are the clear drawbacks compared to all other dye families mentioned above.

Recently developed commercial dyes, such as Alexa™, ATTO™, DyLight™, HiLyte Fluors™, CF™ etc. are characterized by significantly improved spectroscopic properties, such as brightness and photostability.

A summary of common synthetic pathways of main small-molecule fluorophores is presented on Figure 1.6.

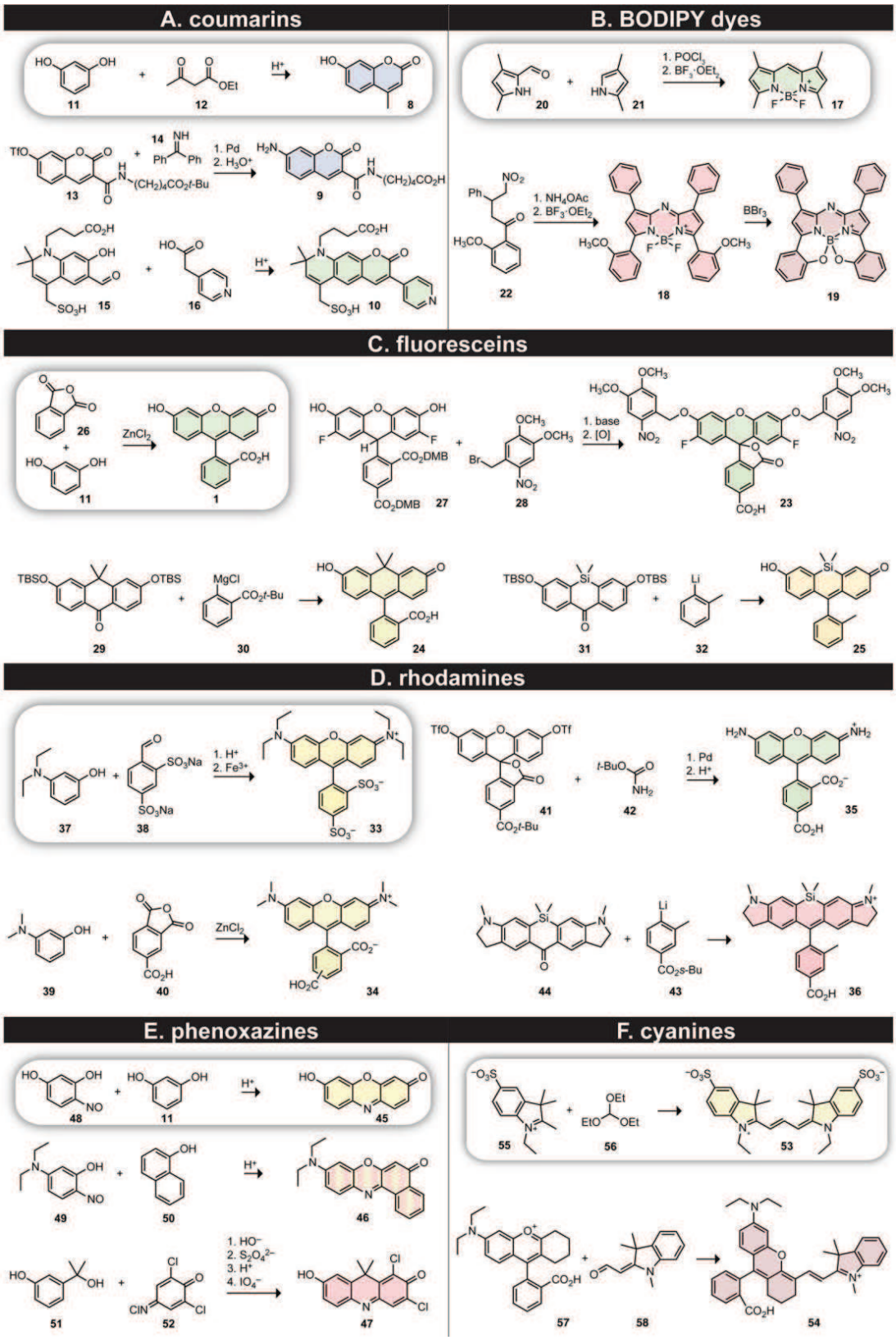

Figure 1.6 Common synthetic pathways to key small-molecule fluorophores: (A) coumarins, (B) BODIPY dyes, (C) fluoresceins, (D) rhodamines, (E) phenoxazines, and (F) cyanines. The classical route to each fluorophore is boxed. The color of a fluorophore structure indicates the wavelength of maximum emission (λ_{em}). Adapted from ref.[54]

1.2.2 Fluorescent proteins

The history of fluorescent proteins (FPs) begins in the 1960s from the discovery and isolation of green fluorescent protein (GFP) as naturally occurring in luminescent Pacific Northwest jellyfish.[55] Afterwards, in the early 1990s, the jellyfish GFP was cloned and expressed in model systems. Fluorescent proteins also have been found in Indo-Pacific reef corals, and these have also been cloned and expressed and are known as "GFP-like" proteins. Since the award of Nobel Prize in chemistry in 2008 to Asamu Shimomura (Japan), Martin Chalfie and Roger Tsien (United States) for their research, the green fluorescent proteins (GFPs) and their modifications were recognized by community of scientists as the important class of imaging agents.

The three-dimensional structure of GFP is an 11-stranded beta sheet (comprising 238 amino acids) wrapped in a pseudosymmetric cylinder (Figure 1.7). This structure is referred to as a beta-can with the imidazolinone fluorophore embedded inside. The unique feature of fluorescent protein is that it is self-sufficient to generate an intrinsic chromophore entirely composed from its own polypeptide sequence. It does not require any other specific proteins or cofactors to initiate post-translational modification leading to the mature chromophore. This property of being luminescent without any external cofactor or protein makes fluorescent proteins extremely utile to the life sciences. The field of fluorescent proteins (FPs) as fundamental tools of biological research was rapidly growing about 20 years ago. This development has led to the generation of various modification of wild type (wtGFP) that produced variants emitting in the blue (BFP), cyan (CFP) and yellow (YFP) regions [56, 57, 58] (Figure 1.7). In 1999, the scientists achieved to isolate the first FP with red emission from a non-bioluminescent reef coral, which was further introduced in cell biology research.[59]

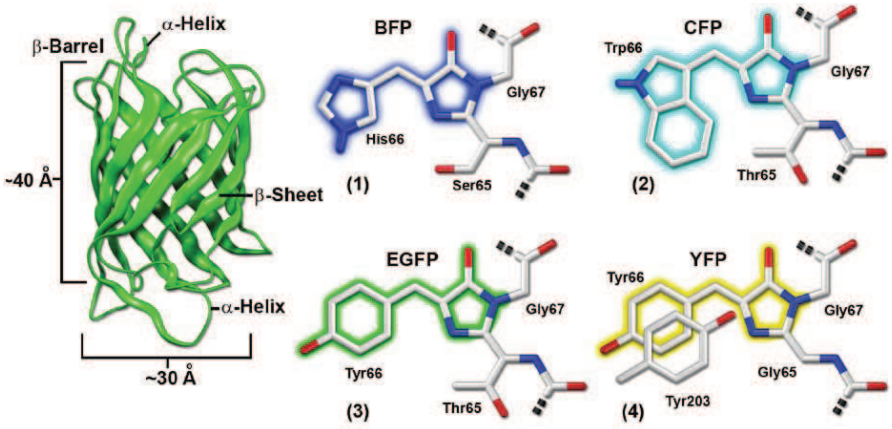

Figure 1.7. Model of GFP with dimensions (left) and fluorophore structures of different fluorescent proteins: (1) BFP – blue, (2) CFP- Cyan, (3) EGFP - enhanced green and (4) YFP - yellow. Adapted from ref.[60]

Despite the recent progress in FP technology, the enhanced version of wild-type GFP (EGFP), as well as the original cyan and yellow derivatives (ECFP and EYFP) are the most commonly used proteins for imaging applications. Although the major efforts are now focused on the development of proteins emitting in the orange-to-far-red spectral regions, recent BFP and CFP variants have emerged as probes for multi-color imaging of protein-protein interaction sensing by using two different FP simultaneously (on confocal or FLIM microscopy). Moreover, recently introduced photo-switchable fluorescent proteins suggest new applications particularly in high resolution fluorescence microscopy.[61, 62] Photoactivable FPs vary fluorescent states upon illumination by a specific light wavelength, and can change color when stimulated by a specific light wavelength. Changes in color and intensity can be either reversible or irreversible.

Since their first commercial introduction in 1994, FPs have entered into a range of fluorimetric methods, including flow cytometry, fluorescence microscopy, spectrofluorimetry, fluorimetric plate reading, fluorescence-activated cell sorting. Except use in research applications, GFPs were successfully applied in drug discovery as an embedded reporter of target behavior in cell-based drug screens. For this kind of application, GFP is fused with genetically encoded drug targets. The addition of the GFP coding nucleic acid sequence to the one of the target protein allows the expression of this protein with a GFP fluorescent tag. One of the most important advantages of this approach is the possibility to label almost any cell-expressible proteins and to track them in vivo.[60] Other important applications of FP include studying the fusion-protein localization, dynamics and function in live cells, monitoring intracellular enzyme activity as well as fluorescent imaging of small animals. Moreover, fluorescent proteins can be expressed in whole organisms and this makes them useful as non-invasive detection tools, such as detecting metastases in cancer.

The shortcomings of FPs are their low brightness and photostability compared to the best organic dyes (*e.g.,* Alexa™ or ATTO™ series of commercial rhodamines). Their relatively large size (about 3.5 nm) that modifies the folding and activity of a number of proteins, limits the use of FPs in some *in vitro* and *in vivo* applications. Moreover, the need to overexpress the tagged proteins may produce some artifacts related to the high concentration in comparison to the natural one. After all, the greatest advantage of FPs remains the facility of their use in molecular biology as they can be genetically encoded with the protein of interest and expressed inside transfected cells. FPs stay one of a key imaging technologies for life science research and particularly for studying Alzheimer's and cancer diseases.

1.3 Fluorescence of dye ensembles

1.3.1 Exciplex and excimer formation

Many polynuclear aromatic hydrocarbons, such as pyrene and perylene, can form charge-transfer complexes with amines. These excited-state complexes are known as exciplexes. The particular example is the charge-transfer complex formed between the excited state of anthracene and diethylaniline.[63] The structured emission at short wavelengths is referred to as mirror image of the absorption spectrum of anthracene. The unstructured emission at long wavelengths is referred to as a charge-transfer complex formed. Emission spectrum of anthracene in the presence of diethyl-aniline is shown on the Figure 1.8, which represents the one example of exciplex formation.

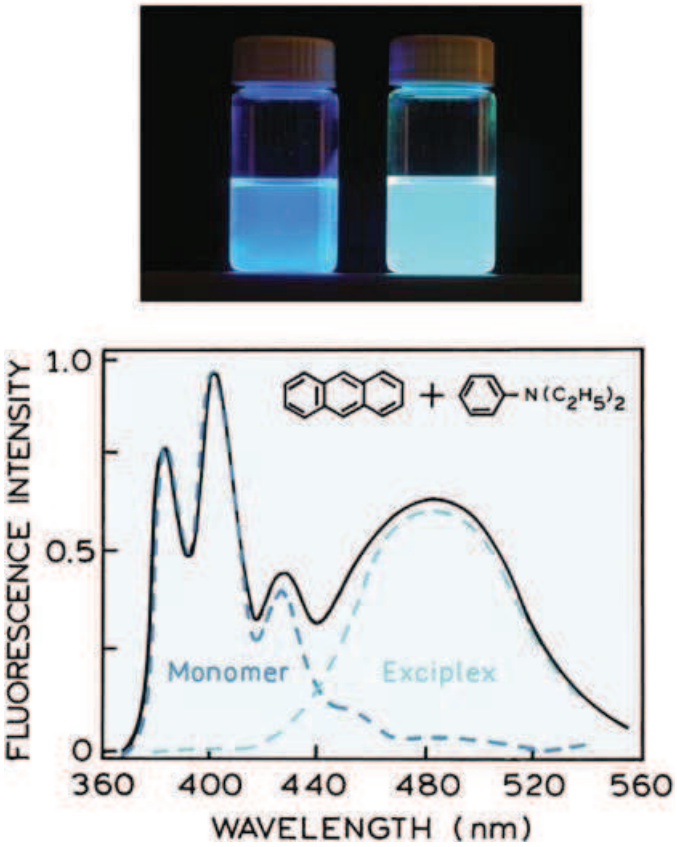

Figure 1.8 Emission spectrum of anthracene in toluene containing 0.2 M diethylaniline. The dashed lines show the separated emission spectra of anthracene or its exciplex with diethylaniline. Adapted from ref.[63]

Some fluorescent molecules in the excited state can also form fluorescent complexes with themselves. The one most common example is pyrene fluorophore. At low concentrations pyrene displays a highly structured emission, which follows the mirror symmetry rule (Figure 1.9). At high

concentrations the previously invisible UV emission of pyrene comes out in a visible range at 470 nm. This long-wavelength emission is attributed to excimer formation. Thus, an excited-state dimer is named shortly "excimer".

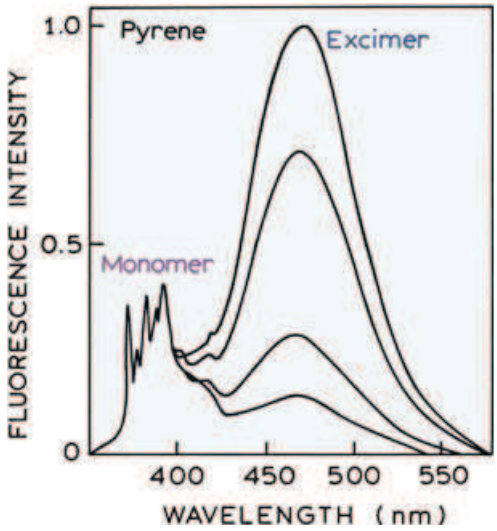

Figure 1.9 Emission spectra of pyrene and its excimer. The relative intensity of the excimer peak (470 nm) decreases as the total concentration of pyrene is decreased from 6 x 10^{-3} M (top) to 0.9 x 10^{-4} M (bottom). Adapted from ref.[64]

1.3.2 Aggregation-Caused Quenching (ACQ)

The most straightforward way to enhance fluorescence signals is to increase the concentration of fluorescent reporters available for detection. Alternatively, higher signal could be obtained by concentrating the dyes within a fluorescent nanoparticle (NP), however, at high concentrations fluorophores tend to self-quench at close-proximity.[65] This was frequently observed for antibodies substituted with multiple fluorophores at high labeling density. At high degrees of labelling (Figure 1.10), the extra fluorescence gained per added fluorophore typically decreases.[35] Thus, fluorescence quenching can be considered as a bimolecular process when the quantum yield is reduced, but the fluorescence emission spectrum remains without changes. Transient excited-state interactions (collisional quenching), the formation of non-fluorescent ground-state species, and electron transfer processes may be the origin of fluorescence quenching.

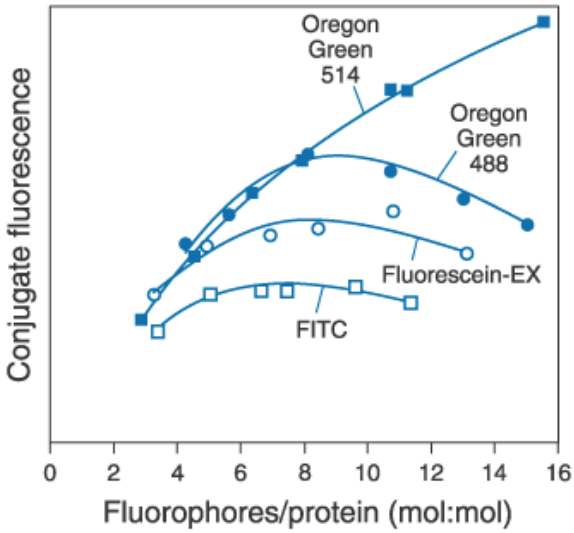

Figure 1.10 Comparison of relative fluorescence as a function of the number of fluorophores tagged to protein for goat anti–mouse IgG antibody conjugates prepared using Oregon Green 514 carboxylic acid succinimidyl ester (filled square), Oregon Green 488 carboxylic acid succinimidyl ester (filled circle), fluorescein-5-EX succinimidyl ester (open circle) and fluorescein isothiocyanate (FITC; open square). Conjugate fluorescence is determined by measuring the fluorescence quantum yield of the conjugated dye relative to that of the free dye and multiplying by the number of fluorophores attached to protein. Reproduced with a permission from the ref.[35]

Many organic chromophores show different spectroscopic properties in concentrated and diluted solutions. For example, fluorescence is often becoming lower or quenched while increasing the concentration of luminophores. This phenomenon is known as "concentration quenching''. It is commonly related to the formation of aggregates.[64] Thus, it was termed "aggregation-caused quenching" (ACQ). This effect of fluorescence quenching is well known for the fluorescein fluorophore. This effect is shown in Figure 1.11. The dilute solution (15 µM) of fluorescein in water is highly fluorescent. While increasing of the acetone content into water, the emission is weakened, due to poor solubility of fluorescein with acetone that increases the local fluorophore concentration and promotes the aggregation process of fluorescein molecules. When the fraction of acetone (f_a) reaches 60 vol%, the ACQ effect becomes clearly visible. With a further increase, the solvating power of the water/acetone mixture becomes low with an appearance of severe amount of nanoscopic non-emissive aggregates formed from many solute molecules and as a result the light emission of fluorescein gets completely quenched. The fluorescein molecule possesses a planar polycyclic aromatic structure, which enable its molecules to stack (pack) well in the non-fluorescent H-aggregates via strong π-π interactions between the solute molecules. The absence of light emission also is observed for the powder of fluorescein, thus displaying a clear ACQ effect in the solid state. This phenomenon is common for most aromatic hydrocarbons and their derivatives (*e.g.,* perylene,

xanthene, rhodamine etc).[64] Since organic luminescence is mainly dictated by electronic conjugation, many efforts have been devoted to increase the extent of pi-conjugation by addition of more aromatic rings into the structure in order to achieve more red-shifted emission and/or better two-photon absorption properties. However, within this modification ACQ effects become more severe. Excimer or exciplex formation can compete with an ACQ process at high concentration of fluorophore. This ACQ phenomenon has also been observed in inorganic semiconductor nanocrystals (quantum dots).[66, 67] In solid state, where concentration of fluorophore is maximal, ACQ effects play even more significant role. For example, it is a detrimental obstacle to the fabrication of efficient organic light-emitting diodes (OLEDs),[68] where thin solid films of luminophores are used.

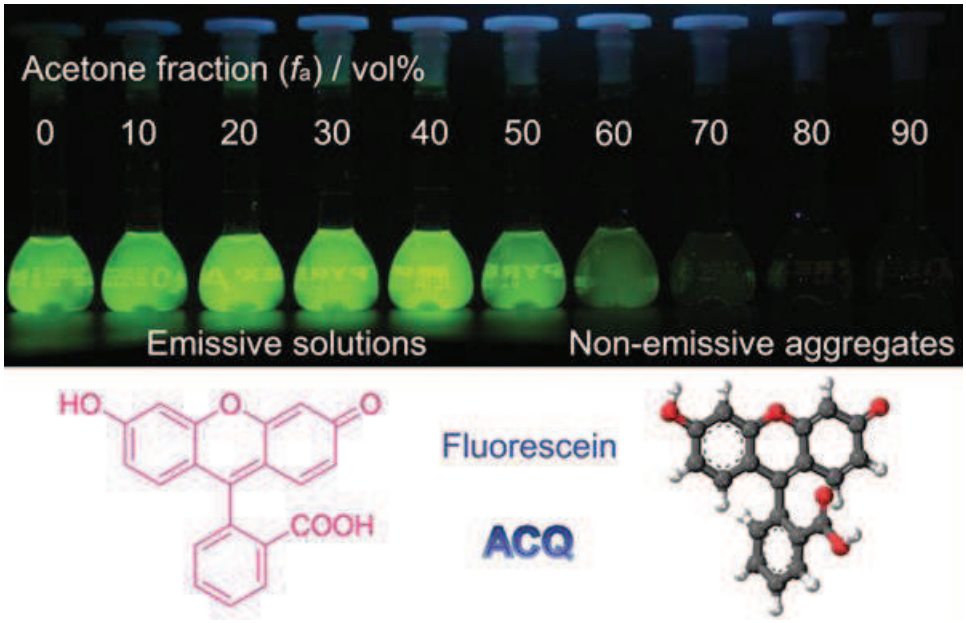

Figure 1.11 Photographs of fluorescent solutions/suspensions of fluorescein (15 μM) in water/acetone mixtures with different fractions of acetone (f_a). Adapted from ref.[69]

One more cause of fluorescence quenching frequently observed in the presence of a large assembly of dyes, which are located at a distance shorter than the Forster radius, is a *homo*-FRET process (i.e. FRET between the fluorophores of the same kind). In this case, the energy can freely migrate fast from one molecule to another and can end up at the non-emissive species.[70] These non-emissive species, so-called traps of energy, could be dimers or oligomers, which are quenched by photoinduced electron transfer (PET)[71] or exiplex mechanism.[72] Similar phenomenon has been reported for the J-aggregates of cyanine dyes, where a single molecule can act as a fluorescence quencher of around 1000 molecules within the J-aggregate structure.[73] This phenomenon is known as superquenching, and is also well known from fluorescent conjugated polymers.[74]

1.3.3 H- and J-aggregates

Fluorescence self-quenching phenomenon is usually due to formation of H-aggregates. As stated by the exciton theory[75] the excitonic state of the dyes aggregate splits into two levels through the interaction of their transition dipoles.[76] The dye molecules may aggregate in a parallel way (plane-to-plane stacking) to form a "sandwich-type" folded structure, so-called H-aggregate, which are characterized by a higher energy transition (i.e. blue shifted absorption) compared to the free (monomeric) dye molecule (Figure 1.12). As another option, the formation of the dyes in aggregated state may lead to a head-to-tail arrangement (end-to-end stacking), so-called J-aggregates, exhibiting lower transition energy (red shifted absorption) compared to the free dye (Figure 1.12). According to the exciton theory the fluorescence emission in H-aggregates is forbidden, while J-aggregates are emissive.[77] Moreover, the absorption of these J-aggregates is much sharper than for molecular species and characterized by larger absorption coefficient at the maximum. The classical historical examples are acridine orange and PIC chloride in water, which show characteristic blue shifted and sharp red shifted absorption bands, respectively, corresponding to their H- and J- aggregates. Among the most characterized classes of organic dyes that form H and J-aggregates are cyanines[48], porphyrins[78, 79] and perylene-bisimides[77, 80, 81]. Formation of H-aggregate (dye-stack) is typical for many fluorescent dyes with planar structure of π-conjugated aromatic system, so that the H-aggregation is a very common mechanism of fluorescence quenching at high dye concentrations.

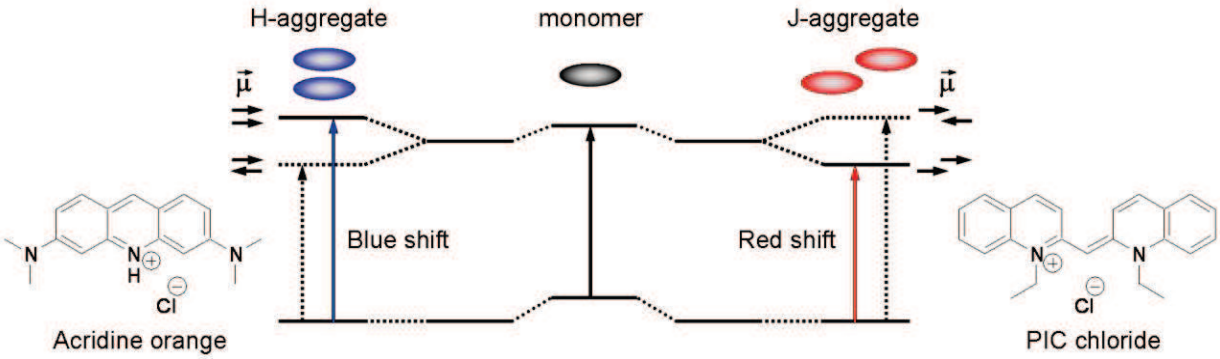

Figure 1.12 Simplified representation of energy diagram for the H- and J-aggregates with typical examples of the dyes participating in the formation. Adapted from the ref.[82]

1.3.4 Aggregation-induced emission (AIE phenomenon)

In 2001, a group of Chinese scientists studying silole derivatives described an interesting phenomenon, when individual molecules were non-emissive in dilute solutions but became highly fluorescent in concentrated solutions (aggregated state).[83, 84] As the emission was believed to be induced by aggregate formation, they termed this phenomenon ''aggregation-induced emission'' (AIE).[83]

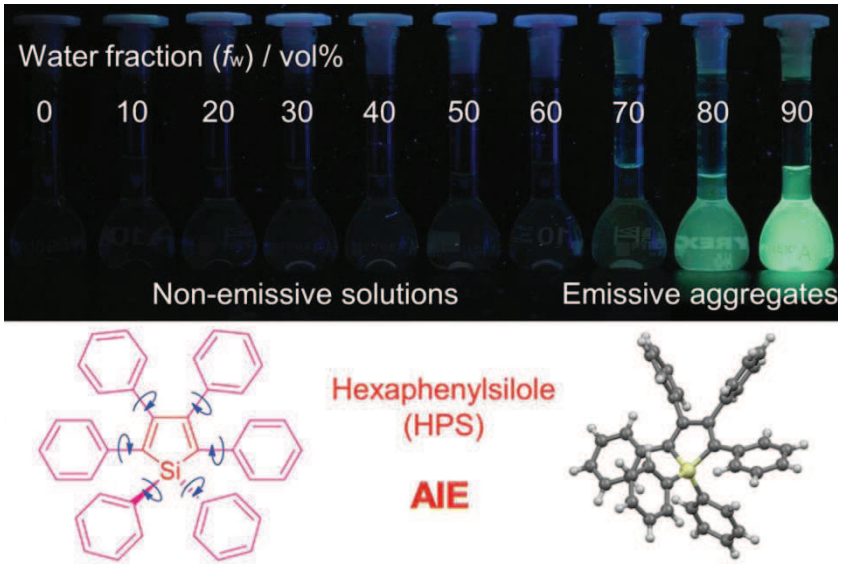

Figure 1.13 Photographs of fluorescent solutions (suspensions) of hexaphenylsilole (HPS; 20 μM) with different fractions of water (f_w) in THF/water mixtures. Adapted from ref.[69]

The pronounced AIE effect was found in a number of dyes with a propeller-shaped structure.[83, 84, 85] These dyes with AIE phenomenon are usually called as "AIEgens". The typical example of AIE is presented by hexaphenylsilole (HPS), which is not emissive when dissolved in THF, but becomes highly fluorescent with increase of water fraction (Figure 1.14).

An AIE process may be associated with such pathways as restriction of intramolecular rotation (RIR)[86] or intramolecular vibration (RIV), J-aggregate formation (JAF)[64], twisted intramolecular charge transfer (TICT)[87, 88, 89] and excited-state intramolecular proton transfer (ESIPT).[90, 91, 92, 93, 94, 95]

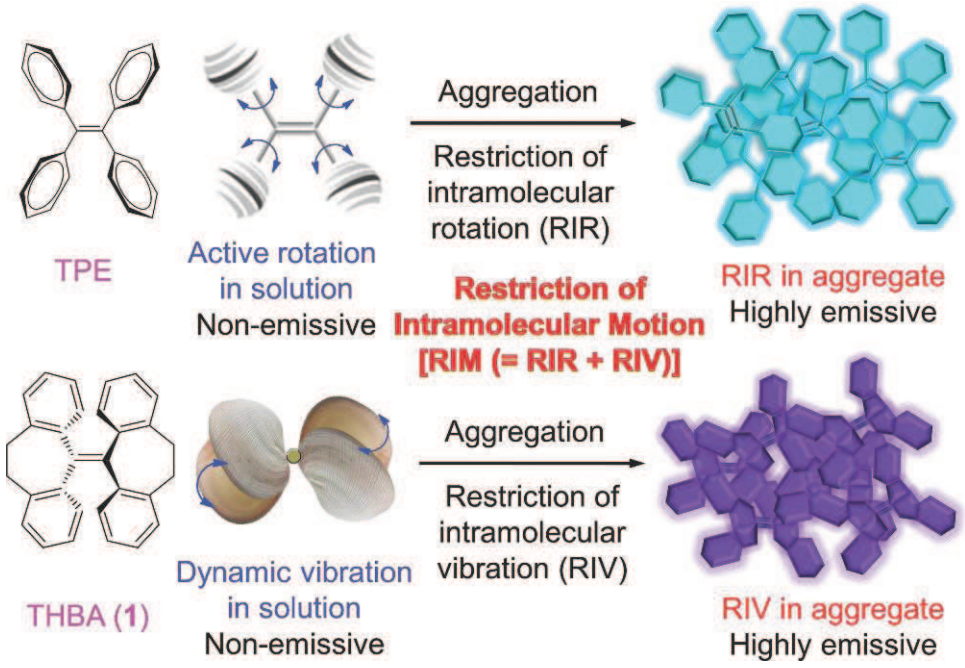

Figure 1.14 Illustration of emission activation process of AIEgens by intramolecular rotation (top) and vibration (bottom). Propeller-shaped luminogen of tetraphenylethene (TPE) is non-luminescent in a dilute solution but becomes emissive in the aggregated state, due to the restriction of intramolecular rotation (RIR) of its phenyl rotors against its ethylene stator in the aggregate state. Shell-like luminogen of 10,10',11,11'-tetrahydro-5,5'-bidibenzo[*a,d*][7]annulenylidene (THBA; 1) behaves similarly, due to the restriction of intramolecular vibration (RIV) of its bendable parts in the aggregate state. Adapted from ref.[69]

Two main mechanisms, which can explain the photophysical phenomenon of AIE, are RIR and RIV (Figure 1.14). The rotations and vibrations are participating in the molecular motions. In the hexaphenylsilole (HPS) AIEgen six phenyl substitutes are attached to a silole core. This phenyl rings can freely rotate against the silole stator on the single-bond axes[86] (Figure 1.13). Tetraphenylethene (TPE) has a structure similar to the HPS AIEgen, four phenyl rings are tethered to a central ethene bond through single bonds (Figure 1.14, top). These phenyl rings can freely rotate or twist against the ethene stator. It is strongly believed that active intramolecular rotations of individual molecules of TPE AIEgen in dilute solutions serve as a relaxation channel for the excited states to non-radiatively decay to the ground state. In the concentrated solutions or solid state (aggregated state), these intramolecular rotations are restricted due to physical constraint. This evidently blocks the radiationless relaxation channel and opens the radiative decay pathway. This proposed analysis assumes that RIR process in AIEgens is close to one happening in molecular rotor systems, in which change of fluorescence intensity is caused by the restriction of intramolecular rotational relaxation about the donor-acceptor bond of the fluorophores (*e.g.,* 9-(2,2-Dicyanovinyl)julolidine, 9-(2-

Carboxy-2-cyanovinyl)julolidine). Thus, AIE phenomenon of molecular rotor systems comes from RIR process. It has been discovered that HPS emits more efficiently in more viscous solvent, at lower temperature, and under higher pressure, which confirms that the RIR process is definitely involved in the AIE effect of HPS.[86, 96, 97]

There are some of AIE luminogens that cannot be explained by above mentioned RIR mechanism.[93] For instance, it is 10,10',11,11'-tetrahydro-5,5'-bidibenzo[a,d][7]annulenylidene (THBA), which does not carry any moiety that can rotate[98, 99] (Figure 1.14, bottom). But in this case, this molecule can be considered as two flexible parts, in each of which two phenyl rings are connected by bendable covalent bonds. These two parts adopt non-coplanar position, and the whole molecule stays in an anti–conformation. The phenyl rings of THBA are flexible and ready to dynamically bend or vibrate in the solution state through this bendable ethane connection. This allows the system to proceed relaxation for its excited state via non-radiative decay. Owing to the physical constraint involved in the aggregated state, the intramolecular vibrations become limited in space, resulting in the blockage of the radiationless pathway and the opening of the radiative decay channel, which renders THBA emissive in the aggregate state.

1.4 Fluorescent nanoparticles

1.4.1 Quantum Dots (QDs)

Quantum dots (QDs) are semiconductor nanocrystals with diameters in the range of 2-10 nanometers.[100] QDs display unique electronic properties, intermediate between those of bulk semiconductors and discrete molecules. The most apparent result of this is a tunable emission spectrum, wherein the frequency range of emitted light is inversely related to its size.[101] Thus, any emission color from UV to IR could be achieved by simply changing the size and/or composition of QDs.[102] Usually, the emission band of QDs is symmetric and narrow, while the absorption spectrum is broad, which enables their excitation by a wide range of wavelengths. Besides, multicolor QDs of different sizes can be excited by a single wavelength, which particularly facilitates the use of QDs in applications like multiplexed imaging and diagnostics. A typical example of the size-dependent emission color and spectra of absorption and emission of QDs is shown in Figure 1.15.

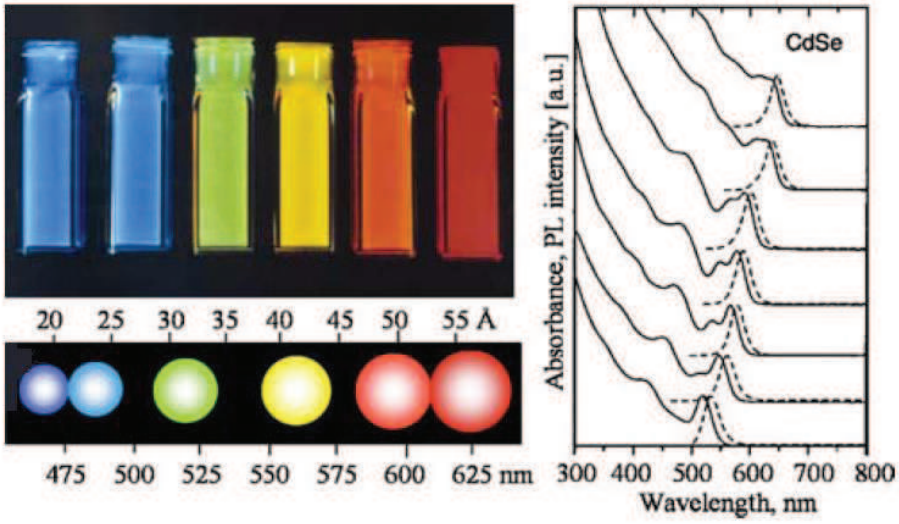

Figure 1.15 (a) Size-dependent emission color[103] and (b) schematic presentation of size, color, and emission wavelength of CdSe–ZnS QDs.[104] (c) Absorption (solid lines) and emission (dotted lines) spectra of CdSe QDs with various sizes. Adapted from ref.[105]

The core of QDs is typically composed of heavy metal atoms from elements of periodic groups II–VI (CdSe), or III–V (InP). The colloidal synthesis of QDs core such as CdSe, CdS, or CdTe, can be achieved by injecting liquid precursors of cadmium (dimethyl cadmium, $CdMe_2$) and selenium into hot (300°C) coordinating organic solvent composed of a mixture of trioctylphosphine (TOP) and trioctylphosphine oxide (TOPO).[106, 107] Adjusting the amount of precursors and crystal growth time generates QDs of specific sizes.[107] The fluorescence quantum yield of the nanocrystal core is relatively low (less than 10%).[106, 108] Usually, a shell of high band-gap semiconductor material, such as ZnS (Fig. 1.16), is epitaxially grown around the core to achieve the quantum yield of up to 80%.[107, 108] Further, several strategies are applied to make hydrophobic TOPO-capped QDs soluble in water for using them in biological medium.[109] The easiest approach is to exchange the hydrophobic surfactant molecules with bifunctional molecules, which bind to the ZnS shell – ligand exchange (Figure 1.16 (iii–v)). Most often, thiols (-SH) are used as anchoring groups on the ZnS surface and carboxyl (-COOH) groups are used as the hydrophilic ends. However, the long-term stability of the QDs depends on the bond between thiol- and ZnS, which is not strong enough. Another alternative approach involves coating the surface of QDs with amphiphilic polymers (Figure 1.16 (i, ii)).[110] Instead of exchanging the hydrophobic surfactant, QDs in this case are coated with a cross-linked amphiphilic polymer. The hydrophobic tails of the polymer intercalate with the surfactant molecules and the hydrophilic groups stick out to ensure water solubility of the particle. However, the final size of QDs after coating

is rather large. For CdSe/ZnS QDs, the diameter is between 19 and 25 nm[110], which could place restrictions on many biological applications.

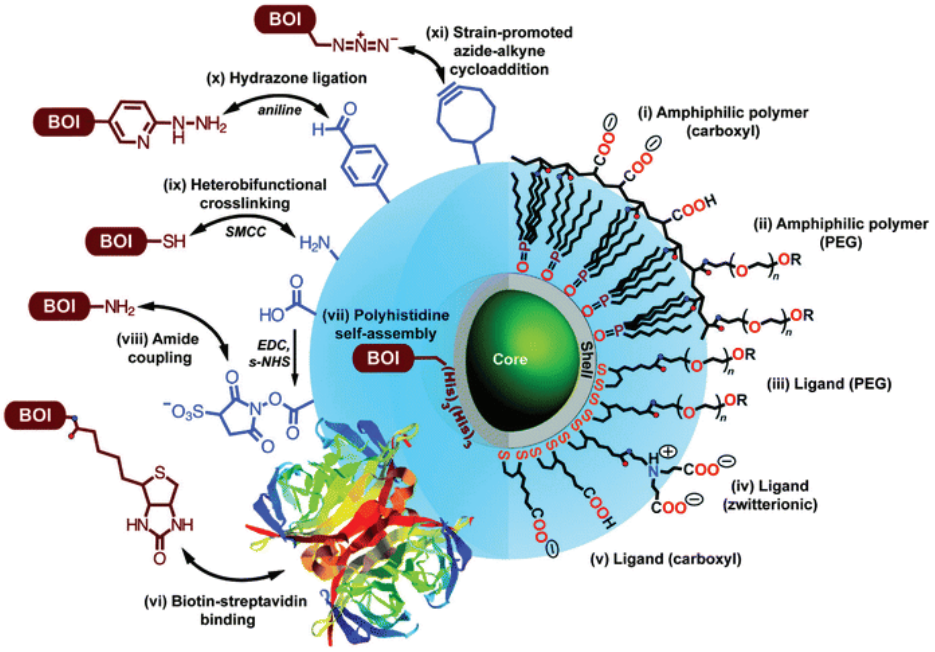

Figure 1.16 Examples of different bioconjugation strategies (left side, BOI = biomolecule of interest) and surface coating (right side) for QDs: (iii–v) cap exchange with hydrophilic ligands exploiting the thiol-affinity of the ZnS shell of the QD and (i, ii) encapsulation with amphiphilic polymers. Adapted from ref.[111]

Other approaches, such as QD surface silanization or coating the QDs with phospholipid micelles, dithiothreitol, organic dendron, and oligomeric ligands have also been reported.[112]

To make QDs more useful for biological applications, QDs can be conjugated to biological molecules, such as biotin, oligonucleotides, peptides and proteins, including avidin/streptavidin, albumin and antibodies[109, 113] (Figure 1.16 left). In these cases, the biological functions of these molecules have not been affected by linkage to QDs. Moreover, non-specific binding of QDs could also be avoided by manipulating QD coating and surface charge. For example, including PEG polymer into QDs coating prevents aggregation and nonspecific binding (Figure 1.16).

Besides size-tunable emission and high emission quantum yield, QDs possess a number of other unique properties compared to organic fluorophores. Firstly, QDs exhibit extreme brightness as a consequence from a much higher molar extinction coefficient (up to 50 times higher than single rhodamine dye). The second distinctive feature of QDs is their exceptional photostability due to inorganic composition. This extreme photostability makes QDs very attractive probes for imaging of

cells and tissues over long time periods. Thirdly, the long fluorescence lifetime of QDs (10-40 ns) is significantly longer than of typical organic dyes (few ns), which facilitates fluorescence imaging with reduced levels of background noise. Another important characteristic of QDs is their large two-photon cross-section that makes them very attractive for in vivo imaging and examination of thick specimens by using multiphoton excitation. Moreover, it has also been reported that QD fluorescence intensity increases upon excitation, an event so called photobrightening.[114] Although in most cases this property can be advantageous, it is problematic in fluorescence quantization studies. One photophysical feature of QDs that is usually considered as disadvantageous is referred to as blinking, i.e. when under illumination QDs randomly alternate between an emitting state and a non-emitting state. Since blinking limits the usage of QDs in single molecule detection applications, several strategies to prevent QDs blinking were already reported.[115-117]

The biological imaging applications for QDs include: recognition of biomolecules, in vivo targeted imaging, immunolabeling and cell tracking for cellular analysis; early detection of cancer biomarkers in serum or blood as in vitro diagnostics; multimodal or NIR deep tissue imaging as in vivo applicatons; the genomics and proteomics such as in situ hybridization.[109, 118] However, it should be noted that quantum dots are composed of toxic elements and they are not biodegradable, which is a considerable limitation especially for the biomedical applications.

1.4.2 Dye-doped silica nanoparticles

Among fluorescent nanomaterials dye-doped silica nanoparticles (DDSNs) are attractive candidates as bright fluorescent probes for bio- imaging and analysis in biology and medicine.

DDSN can be doped with a great number of fluorophores either organic or inorganic (tens of thousands of dye molecules). Consequently, a molar absorption coefficient of DDSNs of 10^6 L $mol^{-1}cm^{-1}$ can be achieved or even overcome this high value. The silica matrix, being an inert hydrophilic material, protects the entrapped fluorophores from photooxydation and external chemicals, thus providing good photo- and chemical stability and high value of fluorescence quantum yield.

There are two main methods for the synthesis of dye-doped silica particles. The first is the Stäber method, which consists of the hydrolysis of a silica alkoxide precursor (such as tetraethyl orthosilicate, TEOS) in an ethanol and aqueous ammonium hydroxide mixture (Figure. 1.17 (a)). Silicic acid is produced during hydrolysis and, when its concentration is above its solubility in ethanol, it nucleates homogeneously and forms silica particles of nanometer size. The method is comparatively simple and both organic and inorganic dyes can be incorporated using this method.[119] Nevertheless, because of the hydrolysis procedure, the DDSNs often have a relatively large size distribution. Some

modifications of the procedure have been introduced and optimized for the incorporation of more hydrophobic dyes inside the silica NPs. One is based on the combination of both hydrophobic and hydrophilic precursors in making the NPs, such as phenyltriethoxysilane (PTES, hydrophobic) and tetraethyl orthosilicate (TEOS, hydrophilic). Rhodamine 6G (R6G) has been successfully incorporated into silica NPs using this method.[120] The hydrophobic component keeps the organic dye in the silica matrix while the hydrophilic component allows the resulting NP to be dispersed in aqueous solutions. Another method for dye incorporation uses direct coupling of the organic dye to the silane reagent. Using this approach, van Blaaderen et al. have covalently linked fluorescein isothiocyanate (FITC) to 3-aminopropyltriethoxysilane, and successfully incorporated the dye into the silica matrix.[121]

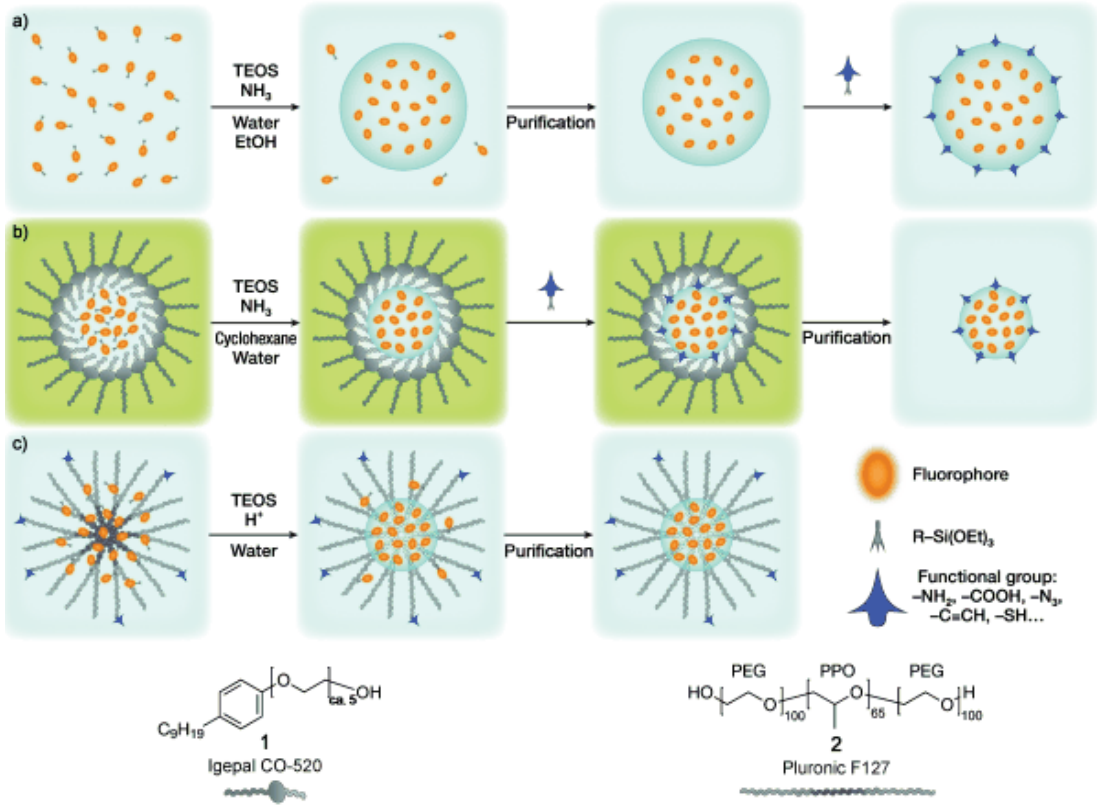

Figure 1.17 Strategies for the synthesis of silica nanoparticles: (a) Stöber–van Blaaderen method and (b) reverse microemulsion or (c) water-in-oil method synthesis of silica-core/PEG-shell NPs. Adapted from ref.[122]

The second main technique for DDSN synthesis is the reverse microemulsion method (Figure 1.17 (b)). It is based on the formation of a water-in-oil reverse microemulsion system. Three main components make up the main reaction mixture: water, surfactant, and oil (an organic solvent, which is present in a high proportion relative to water). The stabilized water nanodroplets formed in the oil solution act as small microreactors, where silane hydrolysis and the formation of NPs with dye

trapped inside take place.[123] The size of the NP is determined by the nature of surfactant, the hydrolysis reagent, and some other parameters, such as the reaction time, oil/water ratio, etc.[124] The NPs produced by this method usually show a high degree of uniformity and are well dispersed in water. A modification of the protocol has been reported that increases the amount of organic dye incorporated in the particle.[125]

Besides single-dye doping, multiple-dye incorporation into the silica matrix has been reported. For example, Wang et al. incorporated three different organic dyes, FITC, R6G, and 6-carboxyl-X-rhodamine (ROX) with overlapping emission and excitation spectra in order to achieve efficient fluorescent energy transfer.[126]

The group of Maitra developed an alternative synthesis method, based on the use of lipophylic organosilane derivatives, such as octyltriethoxysilane (OTES) or vinyltriethoxysilane (VTES), in direct micelle solution.[127] This method attracted a great attention and was profoundly developed afterwards by Prasad and coworkers. The nanoparticles produced, are ORMOSIL (organic modified silica), having size 20–30 nm range, with some degree of mesoporosity. Mancin and co-workers recently prepared different PEGylated DDSNs via similar strategy (with a diameter ranging 20, 50, 100 nm) with an alkoxysilane derivative of the cyanine dye IR775 inside the core.[128]

For the further functionalization of the DDSN surface with dyes, pH and chemosensors, PEG moieties, or bioactive molecules, such as oligonucleotides, peptides, proteins, antibodies, or DNA, proper functional groups should be introduced, such as those used in the most common coupling methods of bioconjugate chemistry (-NH2, -COOH, -SH) and through click-chemistry reactions (azide/alkyne). In this context, group of Prodi proposed a one-pot approach for the synthesis of functionalized core–shell DDSNs.[129] The method is based on the preparation of micelles of Pluronic F127 in water (Figure 1.17 (c)). This surfactant is a nonionic triblock copolymer terminating in primary hydroxy groups with a poly(ethylene glycol)– poly(propylene oxide)–poly(ethylene glycol) structure (PEGPPO- PEG; MW 12,600). TEOS and many kinds of dyes can be added to the Pluronic water solution, thereby leading to their inclusion inside the micelles. The condensation of TEOS in acidic conditions then encourages the formation of a silica core containing dozens of covalently linked or physically entrapped dyes, surrounded by an outer shell formed by the PEG part of the surfactant. In this case rhodamine B derivative was used, which bear reactive triethoxysilane group that can covalently link the dye to the silica matrix (Figure 1.18 (b)). The final material is a versatile multicompartment system characterized by high water solubility, excellent homogeneity of sizes (see Figure 1.18 (a)), stability, and brightness. Such silica-core/PEG-shell NPs also maintain their characteristics under simulated physiological conditions and in environments typical of most immunochemical protocols.

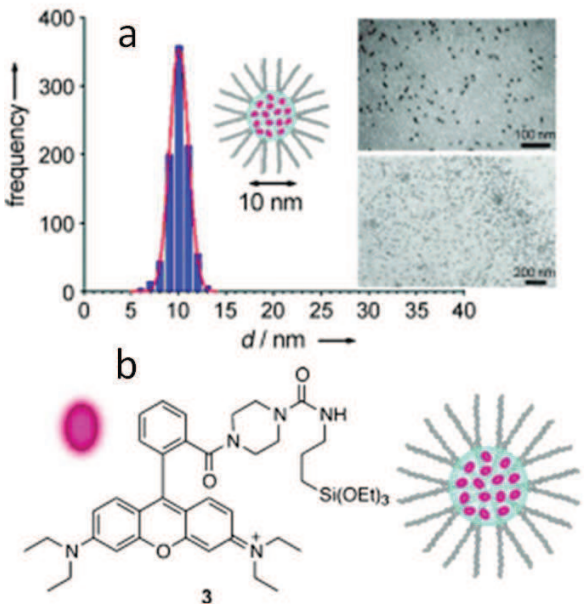

Figure 1.18 (a) Size distribution of silica-core/PEG-shell NPs from TEM images (inset) and (b) structure of dye, trialkoxy silane derivative of rhodamine B, used for covalent doping of silica NPs. Adapted from ref.[122]

Being extremely bright, highly photostable, biocompatible, non-toxic and easy-to-functionalize, the DDSNs are widely used as biosensors, in immunoassays, cellular imaging, multiplexed bioanalysis, nucleic acid analysis and etc.[120, 130, 131]

1.4.3 Carbon-based nanoparticles

Carbon-based NPs consisting of graphene quantum dots (GQDs) and carbon quantum dots (C-dots) are a new class of carbon nanomaterials with sizes below 10 nm. Compared to semiconductor QDs, C-dots are superior in terms of chemical inertness, smaller hydrodynamic size, low toxicity, and good biocompatibility, which makes them more suitable for bio-applications such as bioimaging, biosensor and biomolecule/drug delivery. However, the quantum yield of fluorescent C-dots produced by most popular synthetic methods is very low (~3 %).[132] Only few cases exist where a milligram-scale C-dots with quantum yields of 5 to 60% were reported after sophisticated high energy radiation-based synthesis.[133, 134] The excitation and emission spectra of C-dots are broad and usually extends from UV to far-red (650 nm), which exclude their application for the multi-color imaging/detection. C-dots can also be excited by multi-photon excitation.[135] The emission color of C-dots can be tuned to some extent by varying the conditions of their preparation. Recently, water-soluble ratiometric C-dots that emit in blue and green color with multiple sensing capabilities, such as temperature, metal ions and pH, have been reported.[134, 136] The examples of solid samples of C-dots with a respective excitation, absorption, and emission spectra are presented in Figure 1.19.

The C-QDs can be synthesized using both bottom-up and top-down approaches. The produced NPs can contain significant amount of oxygen fraction, which can reach up to 50%, and some nitrogen, if amino derivatives were used for the synthesis (e.g., amino acids).

The microwave induced thermal carbonization of carbon-containing synthetic precursors (e.g. glucose or other carbohydrates, citrate, polyethylene glycols) in a presence of a nitrogen-containing material such as EDTA or tryptophan remains the main method for the crude C-dots production. Furthermore, the microwave induced pyrolysis of glycerol with a presence of PEG analogue (i.e. 4,7,10-trioxa-1,13-tridecanediamine) can be applied for the synthesis of bright C-dots with passivated surface. The C-dots with multicolor fluorescence were obtained by the laser ablation of graphite followed by oxidation with nitric acid and functionalized thereafter with a diamine-terminated poly(ethylene glycol).[137] Hydrothermal oxidation of nanodiamonds can produce water dispersible C-dots.[138]

The preparation of C-dots may also involve the use of various organic materials and carbon-containing natural products. There are some recent reports, where C-dots have been successfully prepared and purified from the several commercial beverages (e.g. milk, beer, coffee) and even were made from urine[139], which were named “Pee-dots”.

Unlike other fluorescent NPs, the functionalization strategies are poorly developed for C-dots and usually bare C-dots are used for bioimaging and other applications. Moreover, their excitation maxima do not reach yet red-NIR regions.

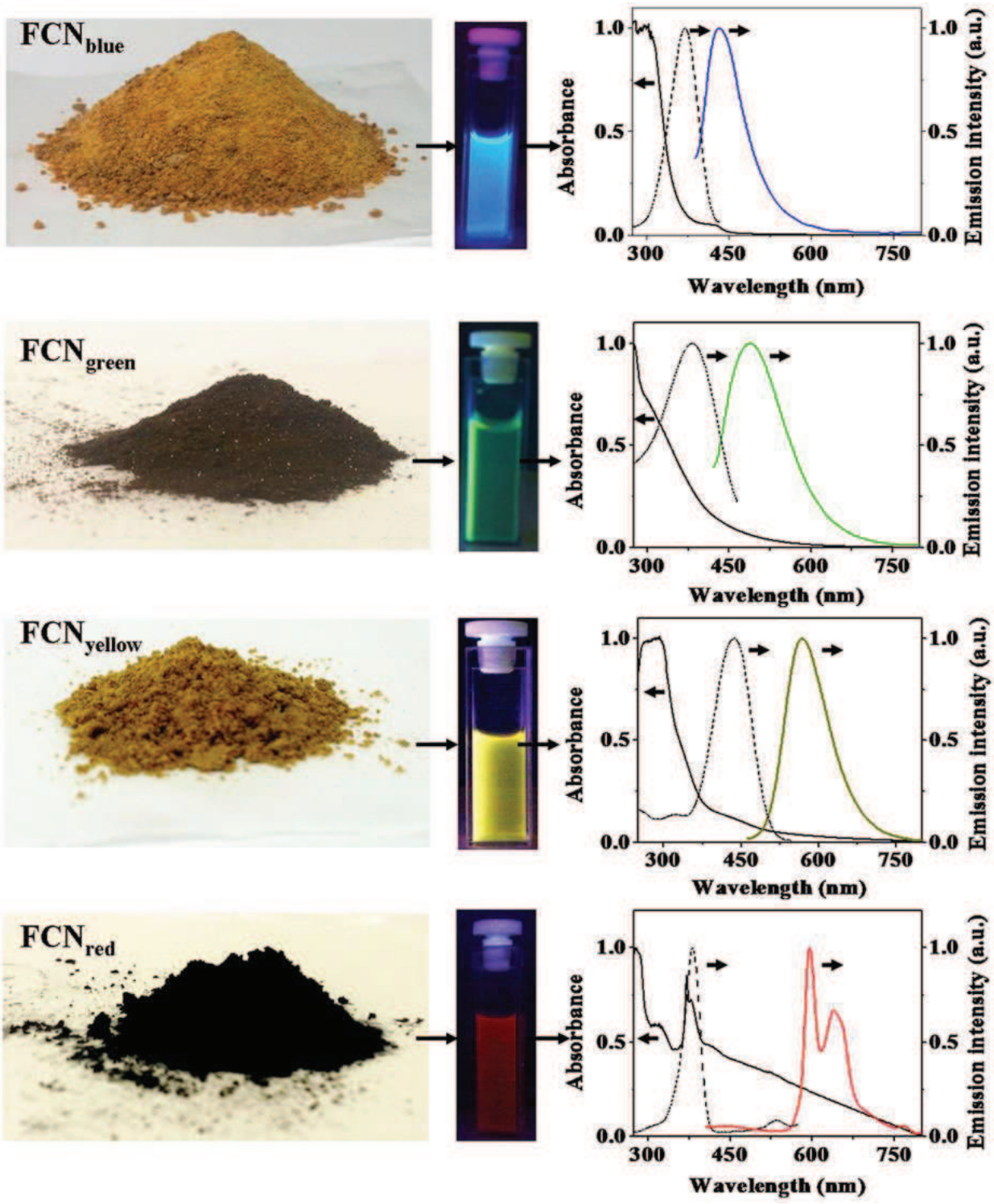

Figure 1.19 Photographs of solid samples of differently fluorescent C-dots and their solutions under appropriate excitations and their absorption (solid line), excitation (dotted line) and emission spectra (colored line). Emission spectra have been measured by exciting at 370 nm for FCN_{blue}, by exciting at 400 nm for FCN_{green}, by exciting at 425 nm for FCN_{yellow} and by exciting at 385 nm for FCN_{red}. All excitation spectra are recorded in respective emission maxima. Adapted from ref.[134]

1.4.4 Nanoparticles from organic dyes

A phenomenon of fluorescence enhancement similar to AIE phenomenon (see above) was observed in the solid state of cyano-stilbenes. Fluorescent organic NPs of 30-40 nm size prepared by self-assembly of cyano-stilbene derivatives were reported by Park et al, who mentioned the fact of "fluorescence enhancement by aggregation".[140] These molecules stay non-emissive in solution due to twisted conformation as a result of steric hinderance of cyano-group (Figure 1.20). The aggregated state induces the planar conformation of cyano-stilbene molecules, as a result of restoring of electronic conjugation system and making NPs emissive. Furthermore, the authors demonstrated assembly of the molecules within the NP in "J-aggregate"-type structure, as aggregation in "H-aggregate"-like structures of parallel stacked molecules is prevented by steric effect of cyano-group (Figure 1.20). Thus, we can conclude the fact, that strong fluorescence of NPs can be an outcome of the planarization of cyano-stilbene configuration within the "J-aggregate"-like structures.

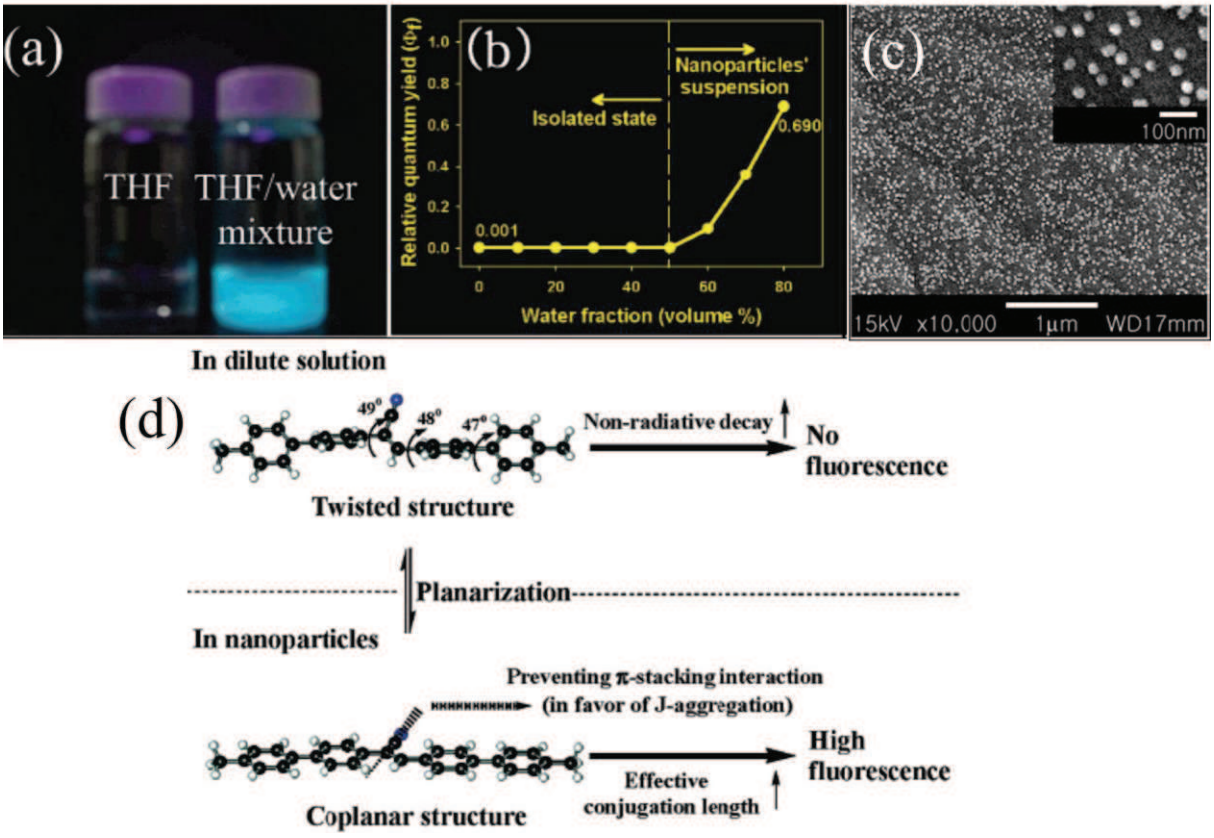

Figure 1.20 Fluorescent nanoparticles assembled from 1-cyano-trans-1,2-bis-(4'-methylbiphenyl)ethylene (CN-MBE). (a) The fluorescence of CN-MBE (20 mM) in THF (left) and THF/water mixture (80% volume fractions of water) (right) under the UV light (365 nm); (b) Relative quantum yields of CN-MBE depending on water fractions in THF; (c) SEM images of CN-MBE nanoparticles. Inset shows the magnified SEM image; (d) proposed mechanism of enhanced emission in CN-MBE nanoparticles. Adapted from ref.[140]

In 2003, the group of Fery-Forgues has reported a preparation of fluorescent organic microcrystals from fluorescent dye, 4-n-octylamino-7-nitrobenz-2-oxa-1,3-diazole (NBD-C8) (Figure 1.21 A) by reprecipitation method in aqueous media.[141] The study of crystallization kinetics was done using UV/vis absorption spectroscopy and the authors proposed the model of kinetics. The methods such as laser light scattering, fluorescence microscopy, and scanning electron microscopy (SEM) were applied in order to measure the particle size and to analyze the shape of the microcrystals. In the presence of PAMAM dendrimers of generation 2.5, 3.5, and 4.5 the rate of crystallization process has been dramatically increased. Thus, the preparation of crystals of smaller size and more uniform in terms of the size has been achieved. Moreover, introduction of PAMAM dendrimer drastically increased the colloidal stability of the particles and helped them not to agglomerate compared to those in pure water. The study showed that the dendrimers serve as templates and colloid stabilizers for the fluorescent microcrystals of NBD fluorophore. Thus, an addition of dendrimers or surfactants can modulate the size and shape of microcrystals, while affecting the arrangement pattern of NBD fluorophore within the dendrimer and thus affecting emission properties.

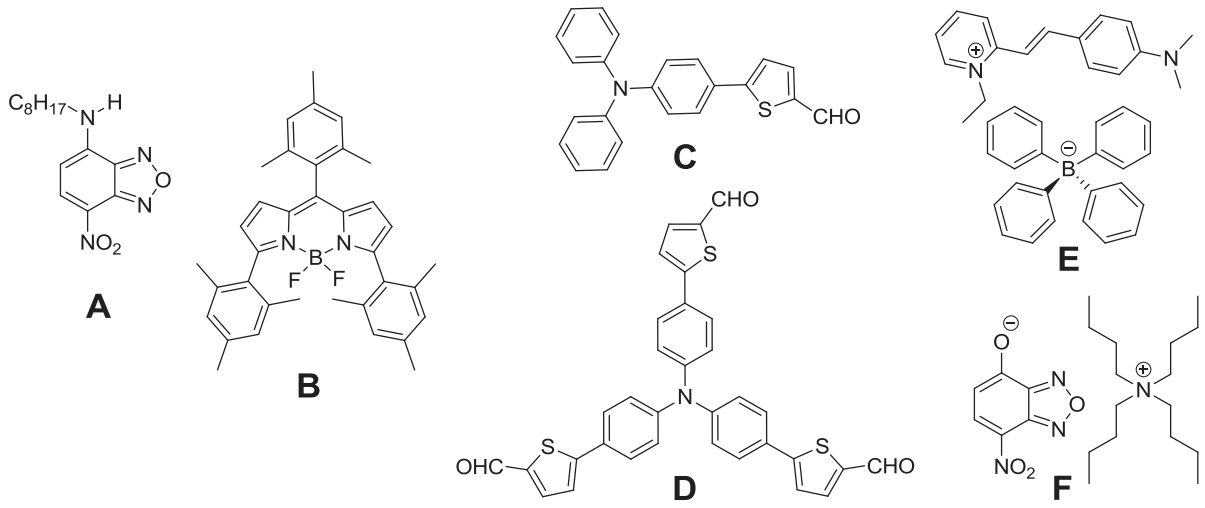

Figure 1.21 The representative structures of dyes recently presented in the form of fluorescent NPs.

In other studies, Pansu et al. have synthesized a trimesitylbodipy (TMB) derivative (Figure 1.21 B) bearing bulky moieties in order to prevent a stacking of fluorescent molecules into “H-aggregate” fashion.[142] The nano- and micro-crystal formation was observed as a result of their assembly. In trimesitylbodipy monocrystals the emission comes from excimer formed with a longer lifetime of 9.5 ns compared to that of the dye in monomeric state. Conversely, the BODIPY derivative, which does not possess bulky groups was found non-fluorescent in the aggregated state.

The suspension of NPs of size 30-40 nm from triphenylamine-based dipolar and octupolar fluorophores (Figure 1.21 C and D) was prepared by precipitation method in group of Blanchard-

Desce et al.[143] The quantum efficiency up to 15% has been reached for the dipolar derivative. The obtained NPs present the one- and two-photon brightness superior to semiconductor nanocrystals (QDs). The octupolar derivative within the NPs showed significantly red shifted emission compared to the one generated by NPs from dipolar dye, but in solution both displayed similar emission properties. Furthermore, it has been found, that octupolar derivative possesses the maximum two-photon absorption cross section of the NPs 55% larger than NPs formed from dipolar dye. The differences in chromophore molecular shape (rodlike versus three-branched) as well as charge distribution (dipolar versus octupolar), while affecting the packing mode within the NPs, lead in dramatically different experimental observations, such as spectroscopic properties and colloidal stability in pure water. The *in vivo* imaging of blood vessels (angiography) using obtained fluorescent NPs has also been investigated on Xenopus laevis tadpoles. Again, NPs from the two chromophores (dipolar and octupolar) displayed different behavior *in vivo*. It was noticed that NPs fabricated from the octupolar dye produce microagglomerates (2-5 µm scale) *in vivo*, which further proceeded to the lethal occlusion of the blood vessels and shut down of the system. The NPs of the dipolar dye did not display this drawback, which allowed imaging of blood vessels owing to their suitable size and brightness with absence of toxicity. The dissolved dye cannot be used for this purpose due to its permeability through the vessel walls and limited brightness as well.

In 2009, Yao et al. have reported the formation of NPs of 30-100 nm formed from an ion pair, which consisted of a cationic styryl dye and a bulky hydrophobic anion tetraphenylborate (Figure 1.21 E).[144] The significant red shift in the absorption spectra of the dye within NPs was attributed to internal twisting of the chromophore and the local polarity effect of the counter-anion as well. Besides that, a 20-fold enhancement in the emission intensity compared to the one of the dye monomer in water was observed and assigned to high rotational resistance of the dye together with polarity effect of the matrix that can partially suppress the non-radiative processes within the NPs. A similar phenomenon of fluorescence enhancement with use of counter-ions was applied for the fabrication of NPs from cyanine dyes[145] and a 4-hydroxy-7-nitrobenzoxadiazole (Figure 1.21 F).[146]

1.4.5 Dye-doped polymer nanoparticles

The dye-doped polymer NPs (DDPNs), in which molecular organic fluorophores are embedded in a non-fluorescent polymer, emerged as new type of brightly fluorescent biocompatible and biodegradable NPs. The different polymer matrices can serve as a host for the fluorescent dyes, such as polystyrene (PS), polymethylmethacrylate (PMMA), dextran, polylactic acid (PLA), polylactic-co-polyglycolic acid (PLGA). Remarkably, some of them (PLGA, PLA, etc) are biodegradable, which makes them attractive for in vivo bioimaging applications.

Synthesis of polymer NPs is most often realized starting either from preformed polymers that are assembled into NPs, or from the corresponding monomers that are polymerized in emulsions to yield NPs.[147-151] The integration of dyes with polymer NPs can be performed by encapsulation (internal labeling) or via post-modification with a reactive dye (external labeling). The internal labeling can be achieved via simultaneous precipitation of solvent mixture of polymer with a fluorescent dye. In this case, the water-insoluble dye diffuses into the polymer matrix due to phase separation, and it is entrapped when the solvent is removed from the particle through its transfer to an aqueous phase or evaporation.[152-154] In this case, the dyes may distribute randomly or in the form of clusters inside the polymer matrix. Both the nature of polymer matrix and the dye structure influence the efficient dye loading. For the encapsulation into hydrophobic polymer matrix the hydrophobic fluorescent dyes should be used in order to have better retention of the dye inside.

The group of Law used different carbocyanine fluorophores for the encorporation into a polymeric core to prepare bright fluorescent nanoparticles for multicolor imaging.[152, 153] The obtained NPs were relatively small (~60 nm) in diameter and had brightness much higher than commercial QDs. By encapsulating different cyanine dyes, the particle emission ranging from visible to near-IR was obtained. Through close proximity of encapsulated fluorophores inside the nanoparticle core, the sequential energy transfer was also achieved (Figure 1.22). By varying combinations, concentrations and ratios of encapsulated fluorophores that can work as an energy donors and acceptors, the optical properties of the particles can be finely tuned according to the particular application's needs. To achieve the specificity in targeting cancer cells, these NPs where functionalized with corresponding antibodies.

Encapsulation of hydrophobic fluorescent molecules into polymer matrix is relatively simple. On the other hand, at high concentrations, which are required to obtain high brightness, the fluorophores tend to self-aggregate, and this result in self-quenching affecting the total brightness, which becomes considerably reduced to the one calculated theoretically. For instance, in the system described above the particle brightness was maximal at 0.7 wt% of dye loading, while above these values NPs were less bright.[153]

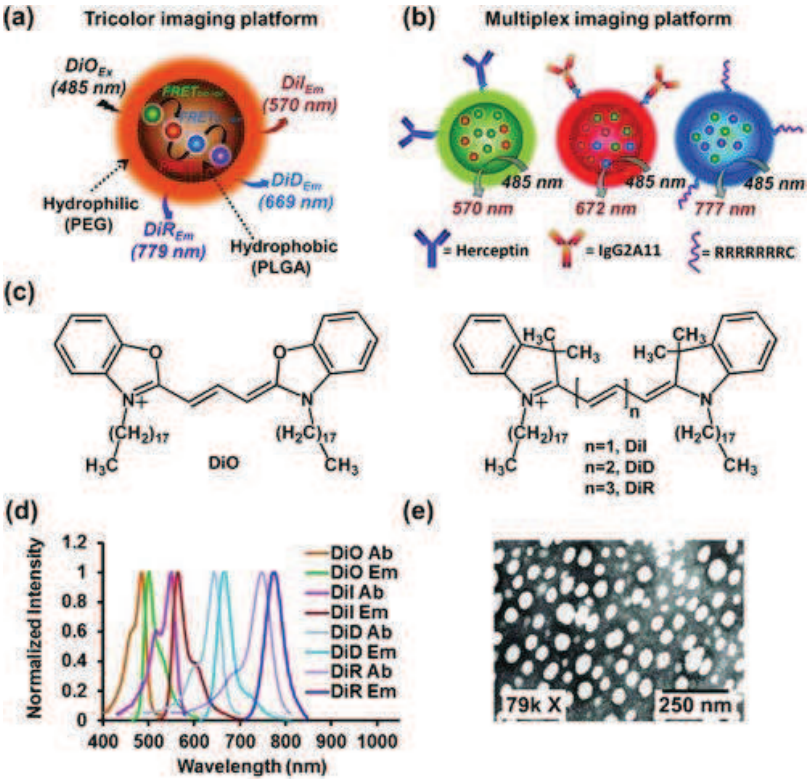

Figure 1.22 A schematic representation of particles designed for (a) multicolor and (b) multiplex imaging. (c) The chemical structures of DiO, DiI, DiD, and DiR. (d) A comparison of the normalized absorption and fluorescence emission spectra among the fluorophores in methanol. (e) A TEM image of Q7. The samples were negatively stained with 2% (w/v) uranyl acetate in deionized water. Adapted from ref.[152]

To solve the problem of the aggregation caused quenching in dye-doped NPs, our group followed two strategies. The first one was to use bulky side groups, as it was realized in the case of Lumogen Red, perylene diimide substituted with bulky groups in both imide and bay regions.[155] This dye showed weak aggregation for loadings from 0.02 to 5 wt% inside 40 nm polymer (PLGA) NPs, with the quantum yield varying only from 97 to 47 %. The high Lumogen Red dye loading and quantum yield enabled preparation of ultra-bright and highly photostable NPs which were ~10-fold brighter than QDs-585.

Moreover, our group also reported the preparation of ultra-bright fluorescent polymeric NPs containing hundreds of rhodamine fluorophores, where self-quenching is efficiently suppressed by introduction of a bulky hydrophobic fluorinated counterions[154], despite the high loading of polymer NPs. For the preparation of fluorescent dye-doped polymer nanoparticles, nanoprecipitation method of premixed solutions of biodegradable polymer PLGA (poly (D, L-lactide-co-glycolide)) with a corresponding fluorophore salt was employed. As the corresponding fluorophore salt, the cationic

fluorophore (octadecyl rhodamine B) with a bulky hydrophobic counterion (fluorinated tetraphenyl borate), was taken. In this case bulky fluorinated counterion serves as a spacer between the fluorophores that reduces dye self-quenching. The obtained nanoparticles of 40 nm diameter contained up to 500 fluorophores were 5 to 10 times brighter than the semiconductor QDs (Figure 1.23 A). Remarkably, they showed a phenomenon of light-induced alternation between fluorescent state and the dark state (Figure 1.23 B). Such blinking phenomenon had never been observed for nanoparticles loaded with a high number of fluorophores. The researchers demonstrated that this collective blinking ("flashing") behavior is due to an ultra-fast communication between all fluorophores induced by their special organization within the particle. The alternation between "on"(luminous) and "off" (dark) states (blinking) of this set of fluorophores was applied in super-resolution imaging, allowing distinguishing particles at distances of less than 100 nm (Figure 1.23 B). These NPs, being spontaneously endocytosed by living cells, show an excellent signal-to-noise ratio in cell microscopy (Figure 1.23 C), and an absence of toxicity. This concept based on fine tuning of the spatial organization of the fluorophores by counterion opened the way to a new class of organic nanomaterials for applications in cellular and biomedical imaging.

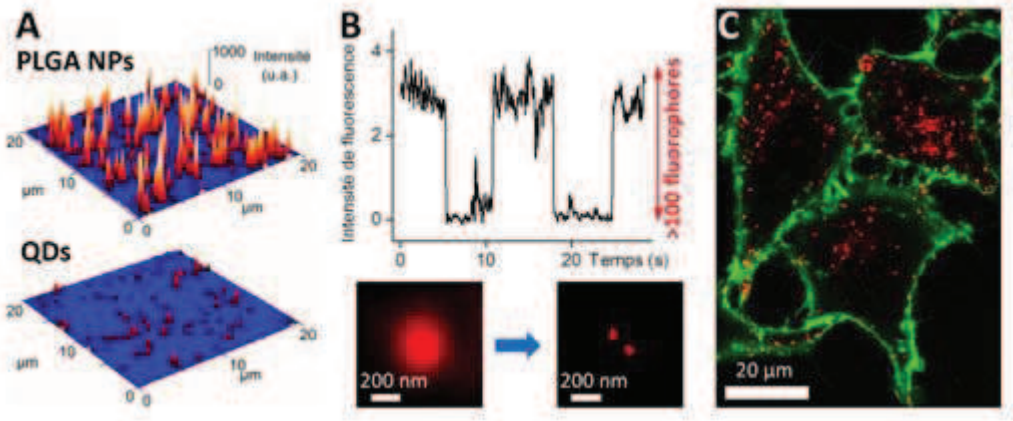

Figure 1.23 (A) Comparative fluorescence microscopy images of fluorescent polymer nanoparticles (on top) and quantum dots (QD605, bottom). (B) The results on fluorescence nanoparticles blinking (top) from "classic" fluorescence microscopy images (left) and super-resolved image (right). (C) Confocal image of nanoparticles (red) endocytosed into HeLa cells labeled with membrane probe WGA-Alexa488 (green). Adapted from ref.[154]

An alternative approach to prepare fluorescent polymer NPs is via polymerization of fluorescent monomer. Recently, Clavier et al using RAFT mini-emulsion polymerization of different BODIPY monomers obtained NPs of 60-90 nm size containing up to 5000 dyes per particle.[156] Despite the high dye loading (3 dyes per polymer chain of 15-20 kDa, ~8 wt% dye loading), fluorescence quantum

yield remained relatively high (35%). Theoretical calculation of brightness suggested that they are 200-2000 times brighter than usual quantum dots. In this case the dye was covalently attached to the obtained polymer matrix. The main advantage of this covalent linkage is that no dye leakage can proceed, though this procedure requires elimination of the unreacted fluorescent monomers. The other advantage of this approach is that it can use micro-emulsion polymerization technique, which is known to generate very small and highly monodisperse nanoparticles.[157, 158]

All the examples above were based on loading of the dyes inside the polymer NPs. Internal labeling can have several advantages: a) availability of functional groups of the NP surface for the further coupling reactions, b) dye molecules are more protected from the oxygen species inside the polymer matrix, which lead to the increase of their photostability, c) availability of large number of dyes (e.g. commercial) for the encapsulation, d) NPs may be heavily loaded in order to increase their brightness.

The second approach is based on the external labeling.[159] In this case, the blank polymer NPs are labeled with a reactive fluorescent derivative through peptide coupling, azide-alkyne cycloaddition ("click" reaction). The external labeling presents several advantages over the internal labeling: a) the use of environment-responsive dyes can act as sensors for certain application, b) no dye leakage, c) spectral properties of the dye molecules don't change significantly to those of free dye. However, in this case the dye is more exposed to oxygen and can be photobleached faster than when it is trapped inside. Moreover, the amount of dye that can be placed on the surface is lower than that encapsulated within the whole volume of the particle.

1.4.6 Dye-doped lipid nanoparticles

Lipid-based nanoparticles have been studied since many years for the delivery of lipophilic drugs. They are constructed with lipids such as mono-, di- or triglycerides, and/or amphiphilic lipids such as phospholipids, which present surfactant properties. Polymeric moieties can also be included in the structures: for instance hydrophilic poly(ethyleneglycol) moieties are often grafted on the external bilayer of lipid NPs to prevent their rapid *in vivo* reticuloendothelial system uptake and subsequent degradation. The greatest advantage of lipid NPs is their very low cytotoxicity.

According to architecture of lipids, dye-loaded lipid nanoparticles could be divided into lipid core nanoparticles (lipid NPs), lipoproteins (Figure 1.24 a and b, respectively), and self-assembled constructions (lipid micelles and liposomes (Figure 1.24 c and d, respectively).

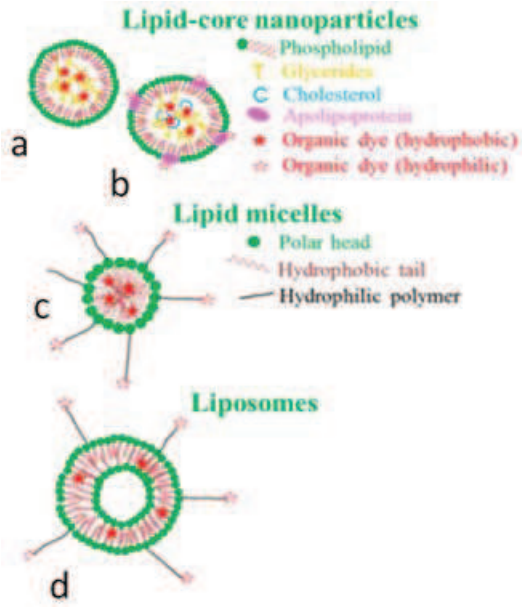

Figure. 1.24 Schematic structure of main dye-doped lipid NPs types: (a) lipid NPs, (b) lipoproteins, (c) lipid micelles, (d) liposomes. Adapted from ref.[160]

Recently, the highly bright, lipid-core dye loaded NPs ("Lipidots™") were produced by the group of Texier, who developed a technology for the encapsulation of lipophilic molecules, including NIR dyes, based on oil-in-water nanoemulsions processed by ultrasonication.[161] The main drawback of nanoemulsions - namely intrinsic poor colloidal stability - has been overcome by the use of a complex mixture of core lipids (mixture of long-chain mono-, di- and triglycerides) and surfactants (phospholipids and PEG-stearate), bringing entropy mixing stabilization to the physico-chemical system. Such lipid nanoparticles can be loaded with different lipophilic dyes, such as ICG, DiO, DiI, DiD, to obtain highly bright fluorescent nanoprobes. For example, they demonstrated that 10 times less DiD-loaded lipidots (2 pmol) could lead to the same image contrast than commercial QTracker™ QDs (20 pmol), while displaying decreased cytotoxicity on NIH-3T3 fibroblasts (IC50 < 30 nM for QDs, >70 nm for DiD-loaded lipidots).[162] As our group showed recently, encapsulation of cyanine dyes inside lipid NPs can be further improved by the use of hydrophobic counterions. The obtained 90 nm NPs could contain up to 8 wt% of cyanine dye, which were >100-fold brighter than corresponding QDs. These ultra-bright NPs enabled first single particle tracking in vivo on zebrafish.[163]

Another strategy is to use as fluorescent dye nanocarriers the natural lipoproteins present in the blood stream, especially high density lipoproteins (HDLs) and low density lipoprotein (LDLs).[164, 165] Lipoproteins (10 to 30 nm diameter) are formed of a glyceride and cholesterol core, coated by a phospholipid and apolipoprotein shell (Figure 1.24 (b)). HDLs and LDLs were modified by the inclusion of fluorescent phospholipids, or lipophilic fluorophores such as DiR or DiR-bis-oleate.[166, 167]

Phospholipid-PEG micelles were shown to improve ICG dye optical properties and prolong up to a few weeks its stability in aqueous buffer.[168, 169]. The PEG extremity can also be functionalized to design targeted nanomicelles directed against folate receptors and $\alpha_v\beta_3$ integrins.[168] However, in a similar way than polymer micelles, lipid micelles must be optimized to lower the cmc and avoids fast burst release of the fluorescent dye upon in vivo administration.

Liposomes labelled with the DY-676-C18 ester dye were used for NIR optical imaging of cultured macrophages and of inflammatory process like oedema in an in vivo mouse model.[170] ICG was included in different liposomal formulations (typical diameter from 70 to 150 nm) to image tumours [171, 172], arthritic tissues[171] or lymphatic vessels.[173] Porphysomes, nanovesicles formed from porphyrine-modified phospholipids self-assembled in bilayers, allowed imaging of the lymphatic system using photoacoustic tomography and fluorescence.[174]

1.4.7 Conjugated polymer nanoparticles (Pdots)

In the past few years, a great number of scientific reports were dedicated to the new class of highly fluorescent organic nanoparticles composed of conjugated polymers.[175, 176] Such NPs can be prepared practically from any conjugated polymer. They are water dispersible and show higher brightness and better photostability than molecular dyes. Their properties can be tuned easily for desired applications through the choice of conjugated polymers and surface modification. They are also very promising candidates for two-photon imaging.

To date, on the basis of the different backbone structures, conjugated polymers mainly fall into four basic types: poly(fluorene) (PF), poly(p-phenylenevinylene) (PPV), poly(p-phenyleneethynylene) (PPE), and poly(thiophene) (PT) (Figure 1.25). Most frequently, NPs from these polymers are prepared by nanoprecipitation, mini-emulsion and self-assembly methods (Figure 1.26).

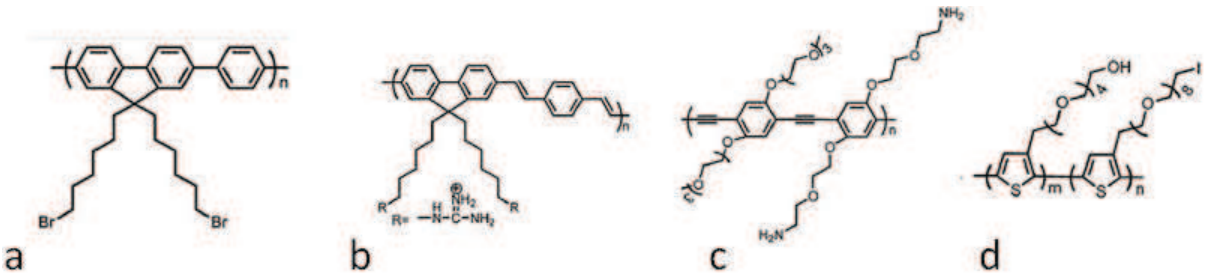

Figure 1.25 Types of conjugated polymers: poly(fluorene) and its derivatives, (a), poly(p-phenylenevinylene) ant its derivatives (b) poly(p-phenyleneethynylene) and its derivatives (c), and poly(thiophene) (d). Adapted from ref.[176]

The nanoreprecipitation method, is a modification of the reprecipitation method, where conjugated polymers dissolved in a ‘‘good’’ solvent for the polymer (e.g., THF) are rapidly added to an excess of ‘‘poor’’ solvent (e.g. water) under ultrasonic dispersion. The formation of NPs is attributed to the aggregation of polymers due to the significant change of solvent polarity. It was reported that the particle diameter is dependent on the starting concentration of the conjugated polymer in good organic solvents.[177] The higher is the starting concentration of conjugated polymer, the larger the diameter will be. In order to achieve a small particle size (15 nm), the group of Chiu used PFBT and PFBT/PF-DBT5 conjugated polymers in combination with amphiphilic polymer (poly(styrene-g-ethylene oxide) and poly(styrene-co-maleic anhydride.[178]

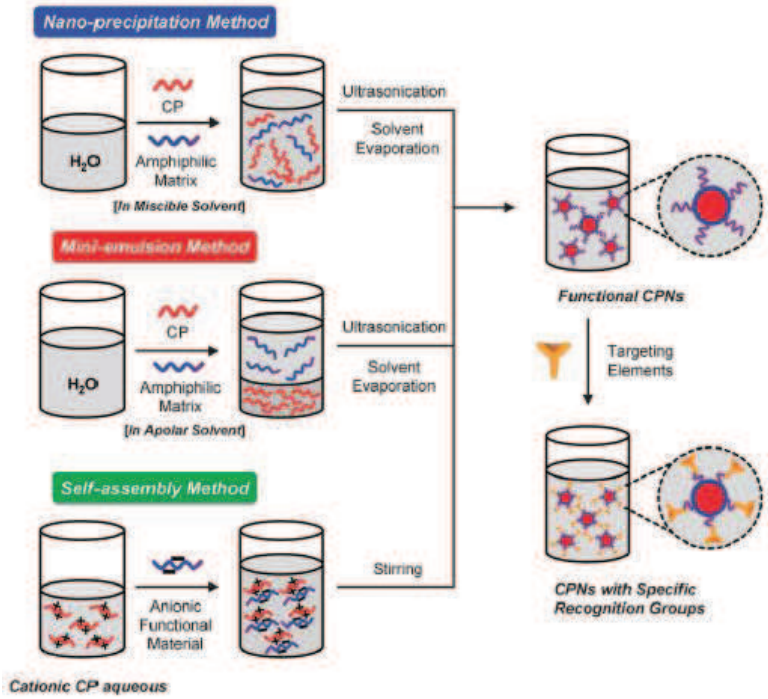

Figure 1.26 Preparation of conjugated polymer NPs by nanoprecipritation, miniemulsion and self-assembly methods. Adapted from ref.[176]

1.4.8 Fluorescent nanoparticles assembled from amphiphiles

Another type of fluorescent organic nanoparticles, which emerged only in the recent years, is mono-component nanoparticles composed of self-assembled amphiphilic fluorescent dyes. Besides biodegradability and biocompatibility, the key advantage of such NPs is enormous possibilities for their design using self-assembly. Bottom-up assembly from organic dyes appears as a powerful tool for obtaining NPs of controlled size and architecture. For example, amphiphilic molecules, comprising of hydrophobic and hydrophilic moieties, could self-assemble in aqueous solutions into highly organized aggregates with various morphologies such as spherical micelles (generally 5-10 nm),

wormlike micelles, spherical and hollow vesicles, planar bilayers, nanotubes, and others. From the fact the self-assembly takes place in water, the major driving forces of this process should be hydrophobic interactions, π-π stacking of aromatic fluorophore systems, electrostatic forces, while the hydrogen-bond infractions and van der Waals forces play minor role. The formation of these morphologies strongly depends on solvent parameters (polarity), molecular structure and shapes, as well as the ratio between the volumes of hydrophilic and hydrophobic parts. On the other hand, the stabilization of self-assembled superstructures through covalent linkage, for example, by polymerization, is usually applied in order to avoid the potential leakage of the constituent fluorescence materials, that can otherwise bias scientific results (e.g. by producing unpleasant background in live-cell imaging experiments). By covalent stabilization, the aggregate dimension and shape can be captured, and overall aggregate strength can be therefore increased.

However, though the self-assembling of amphiphilic fluorescent dyes appears a rather simple method for NPs production and it was already realized for some organic dyes, the successful examples of such NPs are limited to only a few reports.[179-181] The main difficulty of this method is a self-quenching of dyes inside NP that is frequently related to: 1) the formation of either non-fluorescent H-aggregate like structures or J-aggregates, exhibiting lower transition energy (red shifted absorption) compared to the free dye or 2) homo-transfer of energy, resulting in the energy trap. Therefore, a special design of dye amphiphiles is needed to obtain fluorescent micellar NPs.

1.4.8.1 Perylene bisimides

Probably the most remarkable class of dyes for the development of fluorescent self-assembled nanostructures is perylene bisimides (PBI). The profound knowledge on PBI nanostructures could be obtained from the works of groups of German scientists, particularly, groups of Frank Würthner [80, 182], Heinz Langhals[183, 184, 185] and Klaus Mullen[186]. A bare core of PBI tends to form non-fluorescent H-aggregates in the solution or solid state due to strong π-π interaction between the large aromatic systems. Therefore, many efforts were devoted to direct the dye assembly towards J-aggregates. This was done by introducing bulky substituents in the “bay area” (1,6,7,12-positions) of the perylene core. The group of Würthner reported an elegant approach of a molecular design of nanostructure architectures using substituted dumbbell-like PBIs of which the counterparts were methodically changed in order to understand the nature of PBI self-assembly (Figure 1.27).[180]

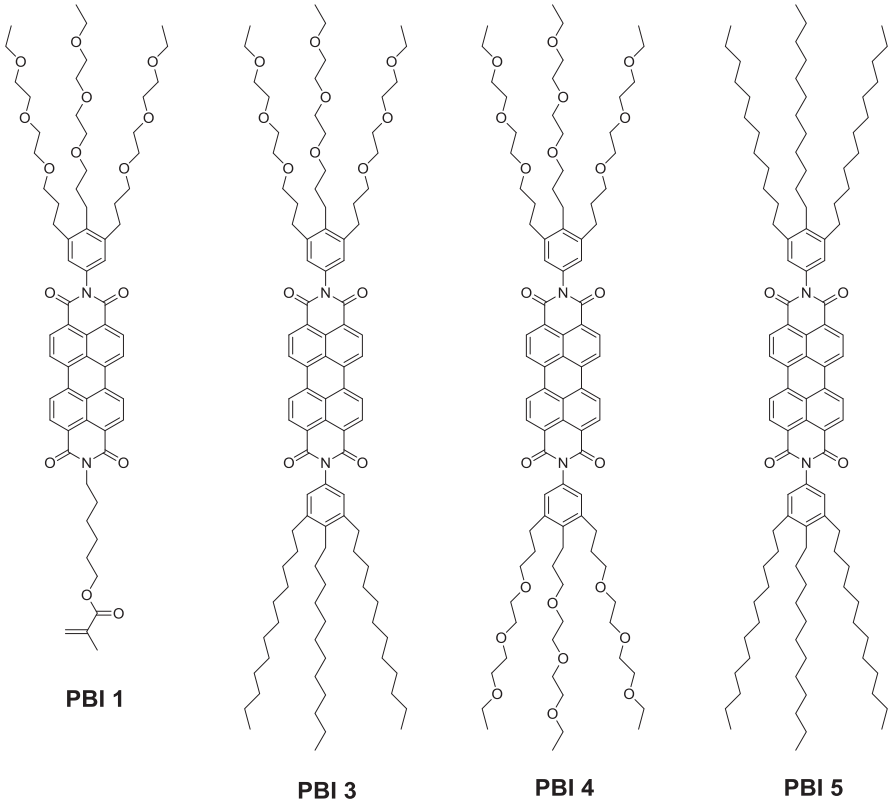

Figure 1.27 Structures of dumbbell-like perylene molecules.

The symmetrical dumbbell-like PBI 4 and PBI 5 molecules with two moities on both sides (apolar for PBI 4 and polar (PEGs) for PBI 5) form columnar stacks in organic media (Figure 1.28 bottom). The amphiphilic wedge-type PBI 1 form a micellar NPs with a narrow size distribution (4–6 nm in a diameter) in aqueous environment (Figure 1.28 top) with a strongly red shifted emission compared to the monomeric PBIs, probably due to excimer formation (Figure 1.29). The authors did not report the quantum yield of this supramolecular system with the excimer formation, but according to Figure 1.29 it is expected to be lower than for the monomers. Furthermore, the photopolymerization of functional acrylate moieties of these micellar structures of PBI 1 was done in order to achieve NPs stable in biologic environment. It should be noted, that after photopolymerization the size, shape and photophysical properties of these NPs remained unchanged.[180]

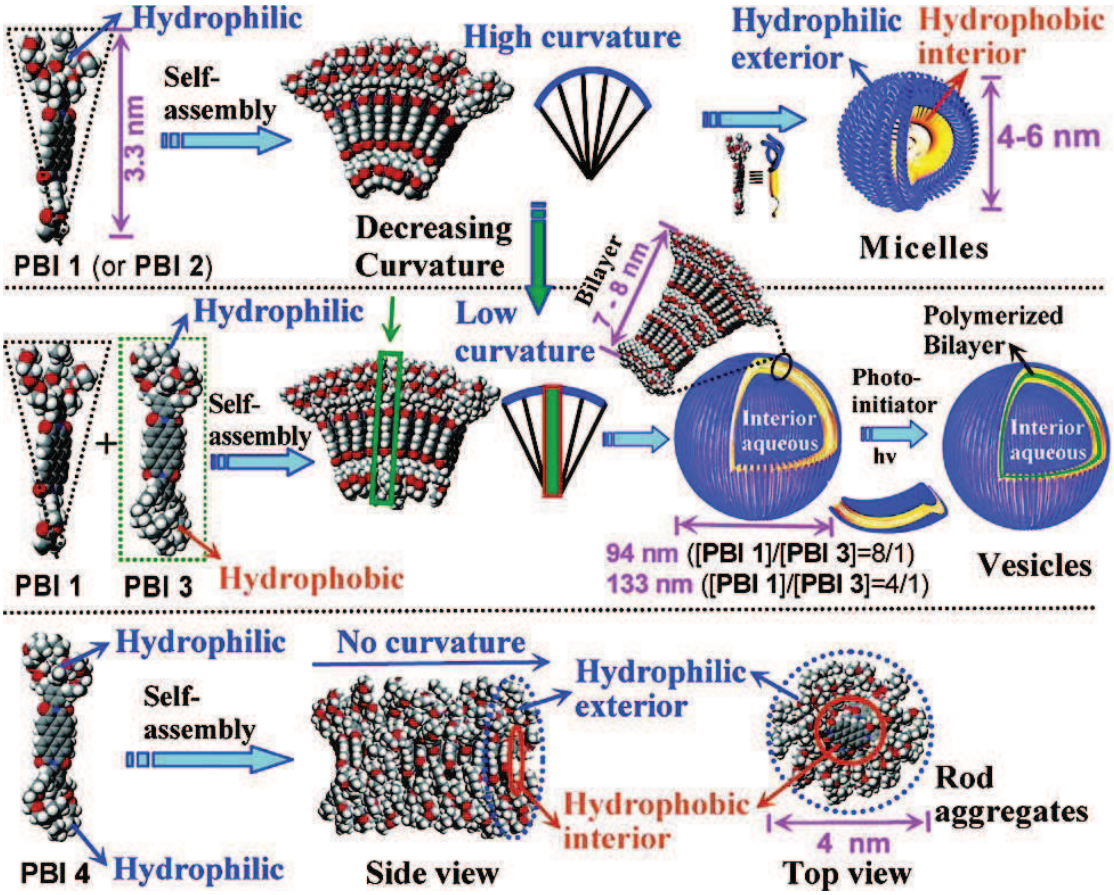

Figure 1.28 Schematic Illustration for the formation of micelles from wedge-shaped PBI 1 (top) and bilayer vesicles from the co-self-assembly of PBI 1 and dumbbell-shaped PBI 3 (middle), and rod aggregates from dumbbell-shaped PBI 4 (bottom). Adapted from ref.[180]

Interestingly, when dumbbell-like amphiphilic PBI 3 were introduced in a wedge-type amphiphilic PBI 1 within a 1:8 molar ratio with a subsequent co-aggregation, vesicular-type nanostructures with a bilayer membrane were formed (Figure 1.28 middle). In this case, the diameter of the vesicules was around 100 nm with a 7-8 nm membrane thickness. This feature of tuning surface curvature by a variation of an oligomer ratio opens the possibility to finely tune the size of these fluorescent NPs according to the researcher's needs.

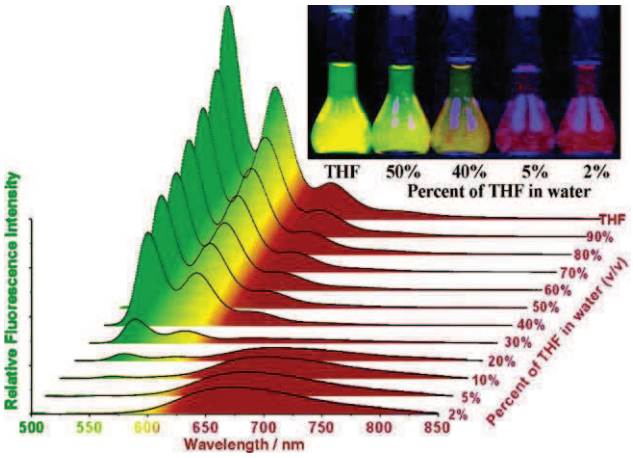

Figure 1.29 Fluorescence spectra of PBI **1** in THF and THF-containing water, λ_{ex} = 490 nm, [PBI **1**] = 2 µM. The inset shows a photograph of PBI 1 in THF and THF-containing water under UV-light irradiation. Adapted from ref.[180]

To demonstrate the potential for using these perylene bisimide NPs for pH sensing, Zhang et al. encapsulated a pH-sensitive bispyrene derivative, which worked as energy donor for the perylene bisimide shell.[187] From the spectral overlap modulation between the donors and acceptors while changing pH, the donor-loaded polymerized vesicles showed pH-dependent FRET, providing essential information about pH of their aqueous environment with exceptionally high sensitivity. Furthermore, the color changes of these loaded perylene vesicles covered the whole visible light spectrum, in a particular case at pH 9.0 producing white fluorescence.

1.4.8.2 Fluorene derivatives

The group of Schenning reported the preparation of a set of π-conjugated amphiphilic fluorene oligomers that self-assembled in water into fluorescent particles.[188, 189] The fluorene oligomers consist of two fluorene units connected by an aromatic linker unit with different electron-accepting capacity (Figure 1.30 (a)), resulting in their emission spectra varying from blue (1), to green (2), yellow (3) and red (4), thus covering the entire visible range. Self-assembly in water was observed after injection of concentrated THF stock solutions into water (typically between 100- and 1000-fold excess by volume). The spectral characteristics of samples prepared in this way changed compared to solutions in good solvents and suggested the formation of aggregates (vide infra), albeit with a low internal helical order. Remarkably, fluorescence quantum yields up to 70% were reported in aqueous solution. The fluorescence microscopy showed spherical objects with a size distribution between ca. 0.4-2 µm. Other than by variation of the chemical structures, it was demonstrated that the emission colours of such NPs could also be tuned by partial energy transfer.[190]

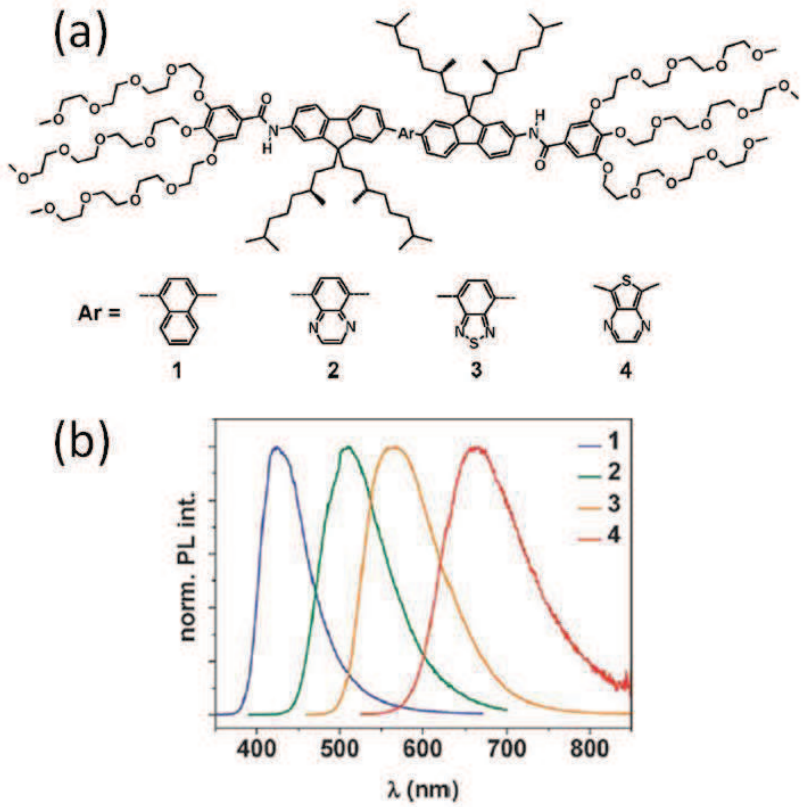

Figure 1.30 (a) Chemical structures of the fluorene oligomers 1-4 and (b) their normalized photoluminescence spectra in aqueous solution (μM). Adapted from ref.[190]

Similar to the mentioned above, stable NPs formed from oligofluorene derivatives with a size of 16 nm in diameter bearing azide groups for the further functionalization were reported by the group of Bard.[191] Two benzothiadiazole units, sterically hindered with triphenylamine groups, were bridged by a fluorene unit, which was substituted by two alkyl linkers bearing an azide moiety (Figure 1.31). Well dispersed, spherical NPs in aqueous solution were prepared by a reprecipitation method. While only the optoelectronical properties were explored until now, these azide bearing oligofluorenes may be useful for further functionalization with bioactive ligands and hence be explored in the domains of diagnostics and imaging.

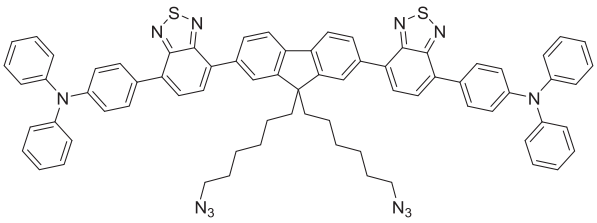

Figure 1.31 Chemical structure of an oligofluorene derivative bearing azide functionalities which enable further functionalization. Adapted from ref.[191]

Despite the success in the development of amphiphilic π-conjugated fluorescent NPs, their applications for biological imaging are still limited mainly due to the difficulty of their surface modification. To address this issue, Shenning et al. have successfully applied the strategy of pre- and post-functionalization of fluorene oligomers to achieve the active targeting ability of NPs.[179] Different fluorene oligomers (Figure 1.32 (a)) were on the one hand prefunctionalized with ligands for biological targeting, such as mannose, and on the other hand with azides to allow postfunctionalization of preformed nanoparticles via the copper-catalyzed azidealkyne cycloaddition (CuAAC) reaction. (Figure 1.32 (b)). The functional groups were introduced synthetically at the periphery of the PEG chains comprising the hydrophilic part of π-conjugated fluorene oligomer to guarantee the good exposure of these groups at the nanoparticle surface. Multitargeting of NPs was demonstrated through functionalization of the same nanoparticle with different ligands, which were recognized by their corresponding protein partners. It was proved that the self-assemblies obtained from these functionalized oligomers had the same structural rheology and photonic properties as a non-modified π-conjugated oligomers reported before. Efficient binding of mannose functionality to E. coli bacteria's FimH receptor and lectin concanavalin A (ConA), was successfully verified. Additional validation was performed by extraction of biotin-modified NPs using the magnetic streptavidin coated beads. These findings all together showed the wise method for fabrication of multivalent nanoparticles bearing two different functionalities efficiently exposed on the surface, which possess dual targeting ability comparable for both ligands.

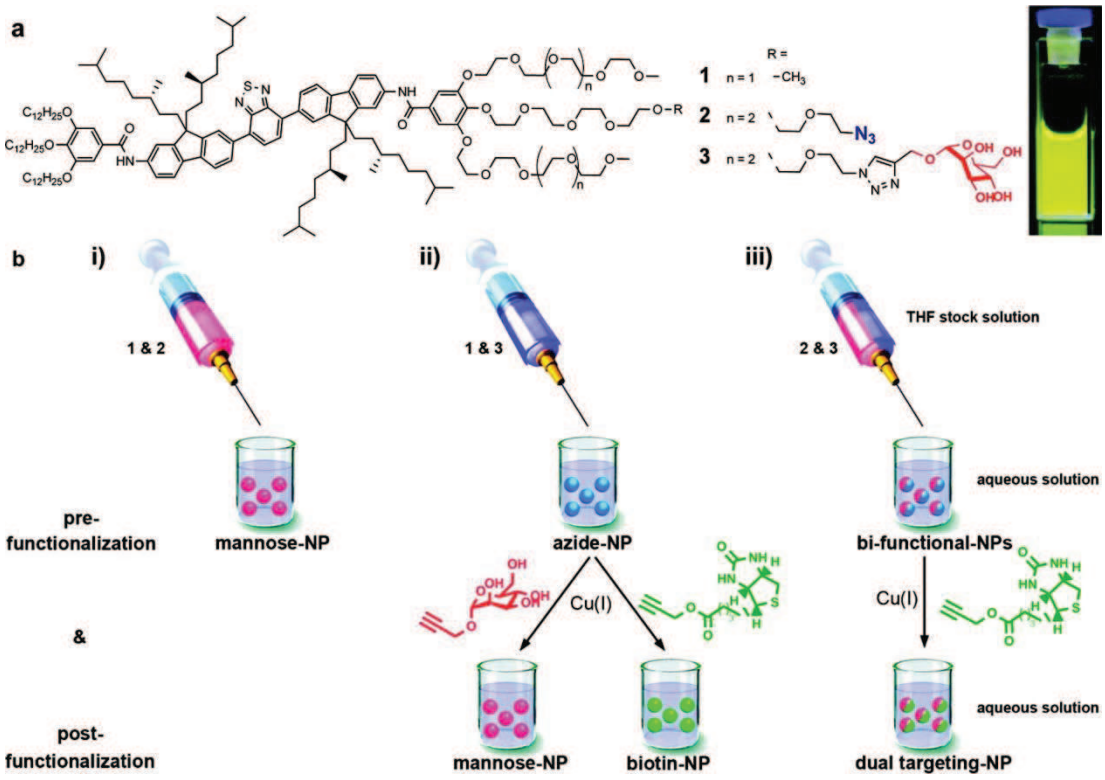

Figure 1.32 (a) Chemical structures of amphiphiles 1, 2, 3 and a photograph of a 0.3 µM nanoparticle solution under UV light (360 nm). (b) (i) Method of fabrication of nanoparticles prefunctionalized with mannose using mixtures of 1 and 2. (ii) Method of fabrication of nanoparticles prefunctionalized with azides using mixtures of 1 and 3 and subsequent postfunctionalization via copper catalyzed azide–alkyne cycloaddition with alkyne derivatives of either mannose or biotin. (iii) Method of fabrication of bifunctional nanoparticles containing azides and mannose using mixtures of 2 and 3 and subsequent postfunctionalization via copper catalyzed azide–alkyne cycloaddition with alkyne derived biotin yielding dual targeting mannose and biotin labeled nanoparticles. Adapted from ref.[179]

1.4.8.3 BODIPY derivatives

Boron-dipyrromethene (BODIPY) dyes have been widely used for bioimaging and sensing due to their intense fluorescence, narrow emitting band, and high stability under physiological conditions. In general, due to facile stacking of the electron-rich dipyrromethene core, the apolar BODIPY dyes form H- or J-aggregates, which are either non- or weakly fluorescent. Only recently, BODIPY-based amphiphiles have been designed forming strongly fluorescent NPs.[181, 192] These NPs display distinct optical properties from that of monomeric dyes, e.g. red-shifted near-infrared absorbance and fluorescence, which could be beneficial for their applications.

The group of Ziessel obtained the stable spherical NPs (~1.5 nm in diameter) self-assembled from amphiphilic BODIPY dye with an ammonium cation at the tip of central core and multiple alkyl chains at the outer periphery (Figure 1.33).[181] Self-assembling occurred after the addition of water (from 0 to 65%, v/v) to a THF solution of modified dye resulted in bathochromic shift of its absorption and fluorescence maxima to NIR indicating formation of J-aggregates. The authors suggested that NPs are formed via the accretion of a small number (four to five) of dye molecules in which the alkyl chains are shrunk at the center of the NPs and the polar head-groups are at the periphery of the object and solvated by water molecules. They also demonstrated that such NPs (hosts) can be easily intercalated with other BODIPY guest molecules that act as efficient energy donors with the FRET efficiency close to 100%.[181] The reversibility of the accretion and recovery of the entrapped guest dye was demonstrated by raising the concentration of THF in aqueous dispersion of NPs intercalated with guest dye.

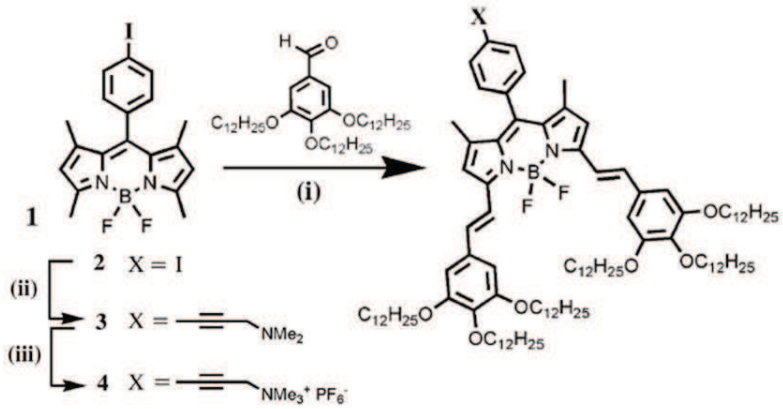

Figure 1.33 Outline of the synthesis protocols used to prepare key intermediates leading to the isolation of the amphiphilic BODIPY dye 4, forming fluorescent NPs. (i) Toluene, piperidine, *p*TsOH (tr), 140 °C, 53%; (ii) dimethylaminopropyne, [Pd-$(PPh_3)_2Cl_2$] (6 mol%), CuI (10 mol%), benzene, TEA, 50 °C, 82%; (iii) CH_3I, THF, room temperature, 3 h, 75%, followed by anion exchange with KPF_6 in a mixture of THF/water. Adapted from ref.[181]

Similarly, Fan et al. also reported the co-self-assembly of two structurally comparable BODIPY amphiphiles with distinct emission color in DMSO/water solution (Figure 1.34).[192] The fluorescence of both dyes was fully quenched inside vesicular NPs, but recovered after disassembly driven by solvent variation or cell uptake.

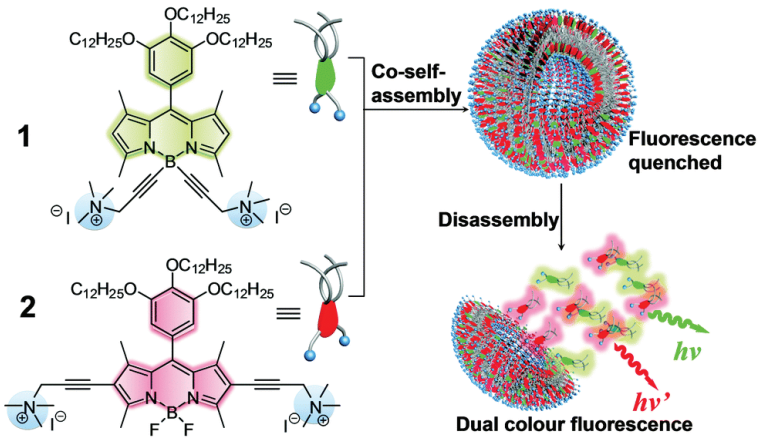

Figure 1.34 Schematic illustration of the formation of fluorescence quenched nanovesicular co-aggregates of 1 and 2 and the dequenching of fluorescence of both dyes upon disassembly driven by cell uptake or solvent variation. Adapted from ref.[192]

1.5 Techniques for characterization of nanoparticles

1.5.1 Atomic force microscopy (AFM)

Atomic force microscopy (AFM) is a Scanning Probe Microscopy (SPM) microscopy based on an indirect formation of image by using a specific interaction between a sharp tip and sample surface. First SPM was developed to overcome the diffraction limitation observed with optical microscopy (resolution limited to 200 nm) by using the tunnel current effect, established between an atomic terminated sharp tip and sample surface. This first type of SPM was not adapted for biological and aqueous environment applications and required a conductive sample surface. AFM overcame these limitations by using near field forces interaction between the probe and sample. AFM was developed in 1986 by Binning et al.

AFM microscopy technique includes a variety of scanning modes and applied for nanoscale characterization of different material properties such as electrical, magnetic and mechanical properties. AFM allows acquiring high-resolution images of the sample surface up to atomic resolution in vacuum. It is performed by scanning a small probe with a sharp tip back and forth in a controlled raster manner across a sample to measure the surface topography. To acquire an image, the AFM raster scans sample over a small area, measuring the local interactions simultaneously. The image is reconstructed by the successive scans of the surface by the probe and provides a topographical image.

There are three main modes of operation in AFM microscopy, first is the contact mode where a constant force is applied on the sample and regulated regarding the topography of the sample. This

mode is possible in vacuum, gas phase and liquid phase. A second mode is based on pure non-contact mode with an actuated cantilever at his resonance frequency. This mode is working only in vacuum environment. An intermediate mode mixing non-contact and contact is tapping mode. This mode is based on an intermittent contact of the sample with the probe in resonant mode to lower the interaction time and force applied (especially lateral forces) on the sample. The main disadvantage of operating in contact mode is a potential damage or distortion of some soft biological samples. Tapping mode minimizes this problem with only brief intermittent contacts while measurement. Additional information also is provided in this mode, such as sample surface stiffness change in the phase image, acquired simultaneously, with the height image.

Today AFM is a well-established technique for characterization of soft and biological material at the level of nanometer in liquid conditions.[193] The representative structure of the probe is given on the Figure 1.35, which appears as a 3-6 µm tall pyramid with 5-40 nm end radius. While the lateral resolution of AFM is low (~30 nm) due to the tip convolution, the vertical resolution can reach up to 0.1 nm.

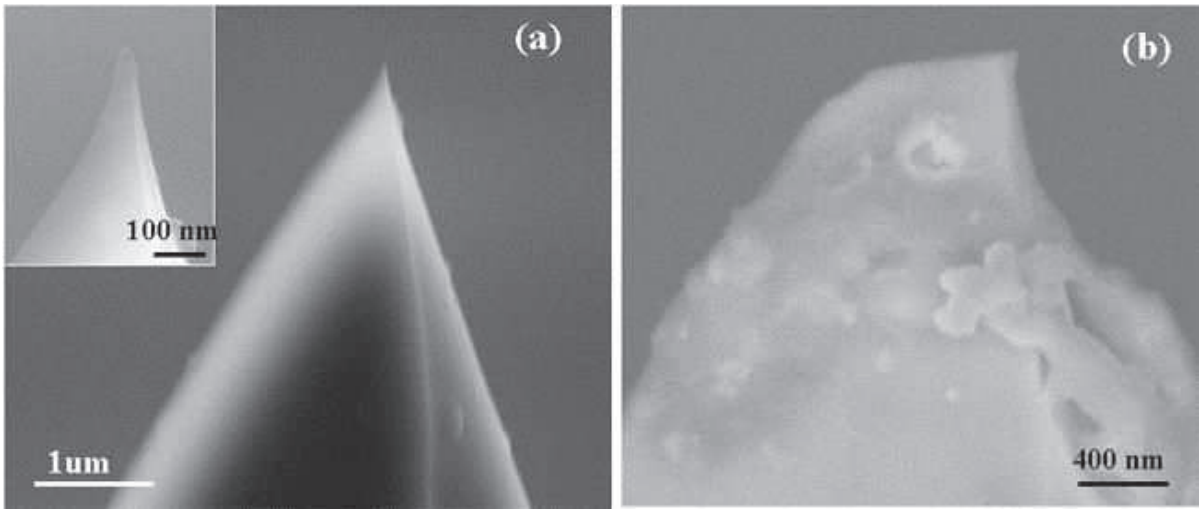

Figure 1.35 (a) A new AFM tip; inset: The end of the new tip. (b) A used AFM tip.

In case of tapping mode, the image formation is obtained indirectly by applying a constant damping of the free amplitude of cantilever at resonance frequency, corresponding to a constant distance between sample and probe. To reach this information the cantilever deflection has to be monitored. This deflection is obtained using an optical detection system composed of a laser reflected on the back of cantilever and redirected to a four quadrant diode. The photodetector indicate the position of the laser spot on the detector by measuring the change of signal intensity between the photodetector segments (Figure 1.36).

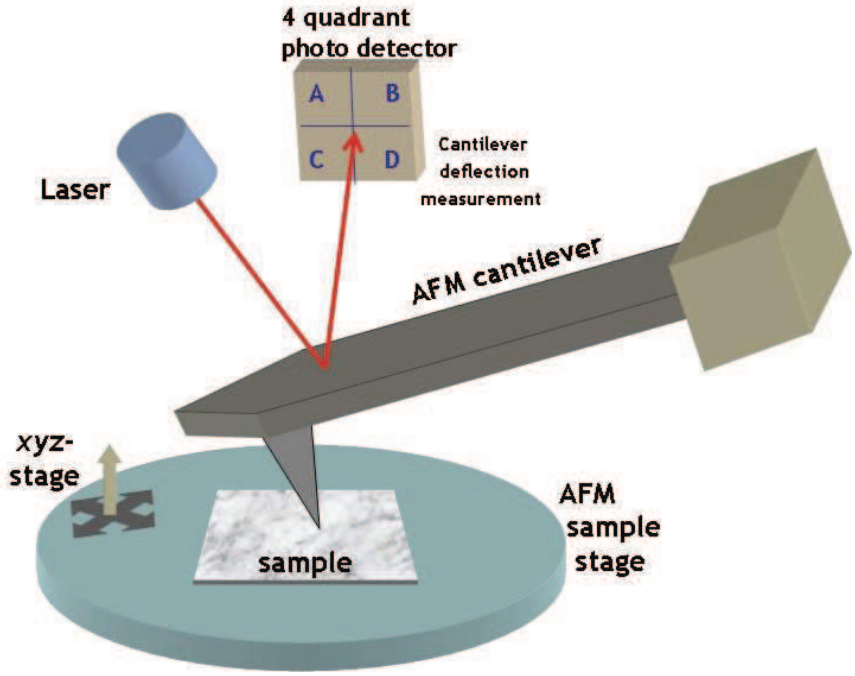

Figure 1.36 AFM operation combined with a use of an optical lever.

The sample is supported by a 3 axes piezoelectric crystal scanner: two directions devoted to sample scanning (X,Y) and the Z position for regulation of sample height. The damping of the free amplitude of cantilever is regulated by an electronic feedback loop driving the Z direction scanner to maintain the distance between the sample and tip constant. This loop includes two corrections: one proportional for high speed correction and an integrative part for a complete the correction.

AFM have several considerable advantages over the other techniques. As AFM microscope does not contain optical lens and beam irradiation, thus it is not suffered from a limitations such as a low space resolution due to a diffraction limit and an aberration, staining of the sample is not required and as well ensuring a space for guiding the beam (*e.g.,* as vacuum drawing). The main competitive technologies of the AFM are an optical microscope (confocal) and electronic microscopes (TEM, SEM). The difference between transmission electron microscope (TEM) and AFM is that, TEM provides only 2D (two-dimensional) projection or image of a sample, but AFM can provide information about 3D (three-dimensional) surface profile. Furthermore, AFM does not require any special treatments for its samples (such as metal/carbon coatings, treatment with uranyl acetate solution for staining in TEM) that can potentially irreversibly promote changes in the sample surface or size and also charge artifacts does not appear significantly in the final AFM image. Most AFM can operate well at ambient conditions in aqueous media, unlike the TEM microscopes, that require high vacuum line and/or frozen samples, which is important for studying of biological samples. This is very useful to study organic NPs assembled in aqueous conditions, because drying may change the mode

of their assembly or produce aggregation of the sample. AFM can be also combined with a use of fluorescence microscopy, a method so-called fluo-AFM allowing further expanding applicability of this technique. Primarily, this combined AFM-optical mode found its applications in biological sciences, as well in material research (*e.g.,* photovoltaics). This latter technique is particularly interesting to characterize fluorescent NPs because it can provide correlative information about their size as well as fluorescence characteristics.

A disadvantage of AFM is its speed compared with the scanning electron microscope (SEM). The one image by AFM requires several minutes, unlike the SEM, which capable to scan at near real time. This often leads to a thermal drift observed in the image, which makes AFM less suitable for the topographical distance measurements. Whereas SEM microscope can perform the imaging of area with a size of square millimeters and depth of field of millimeters, the AFM can image the area only about 150×150 micrometers with a maximum height of 10-20 micrometers. However, it has been recently improved by introduction of parallel mode with a use of multiple tips.

The image artifacts come often during AFM measurements. They could be caused by poor operating environment, operation mode such as not avoiding the collision with a sample (*e.g.,* particle movement induced by a force applied by a tip) unsuitable too-coarse tip, or even by the sample by itself, if it have unreasonably rough surface, causing actual wearing of the tip. Due to the instrumental limitations, the tip cannot correctly measure the steep walls or overhangs. For this purpose special type tips and cantilevers were designed and employed to modulate the probe sideways as well as up and down. However, such mode provides a lower lateral resolution and other additional artifacts.

Substantial instrumentation improvements, its combination with other techniques as well as more profound understanding of AFM technique have led to its broad application in many fields such as engineering, materials science and biology. As shown in results part (see below), AFM was systematically used to characterize newly obtained organic NPs.

1.5.2 Transmission electron microscopy (TEM)

Transmission electron microscopy (TEM) is a microscopy technique that images the transmission of a beam of electrons through a sample. It was introduced for the first time by Max Knoll and Ernst Ruska, who built the first TEM microscope in 1931. The scheme outlining the main components of a basic TEM system is shown in the Figure 1.37. While passing through a sample the beam of electrons interacts with an ultra-thin specimen. The resulted deviations in the amplitude and phase provide the contrast for the image, which is than magnified and focused onto an imaging device, such as a

CCD camera, fluorescent screen, or a layer of photographic film. The contrast depends as a function of the specimen thickness, which beam pass through and the material of the sample as well (*i.e.,* heavier atoms have a smaller electron mean free path of electrons as they scatter more than lighter atoms).

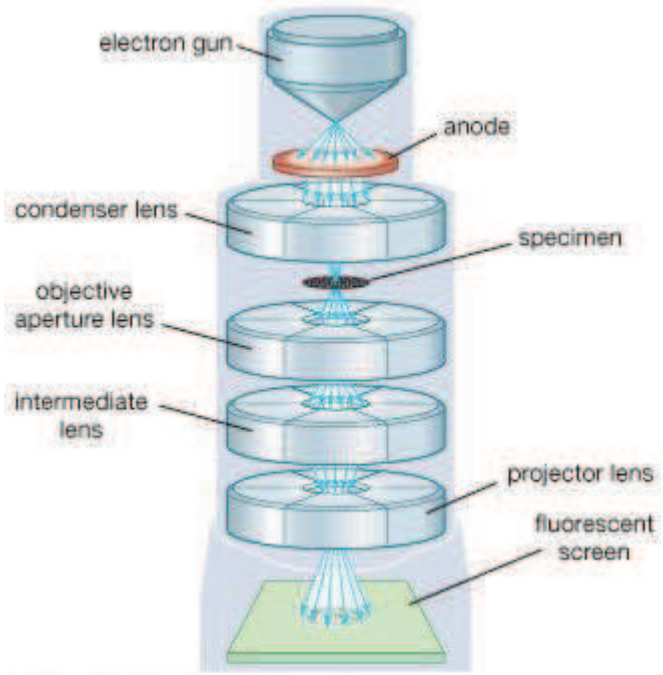

Figure 1.37 Scheme of TEM microscope. The upper part consist of an electron gun, which produces the electron beam, and the condenser system, which focuses the beam onto the object; the image-producing system, which consist of the objective lens, movable specimen stage, and intermediate and projector lenses, which focus the electrons passing through the specimen to form a real, highly magnified image; the image-recording system, which converts the electron image into some form perceptible to the human eye. A fluorescent screen for viewing and focusing the image and a digital camera for permanent records are the parts in the image-recording system. Adapted from Encyclopedia Britannica.

Higher resolution of TEM over the light-based imaging techniques arises from illumination with the high speed electrons, which wavelengths (de Broglie) are much smaller than the wavelength of light. Thus, using TEM instrument, it is possible to examine fine details, even a single column of atoms can be observed. However, at higher magnifications an expert analysis is required as complex wave interactions can modulate the intensity of the image. The image quality using TEM rely on the contrast of the sample relative to the background. Typically, the preparation of the sample is performed by drying nanoparticles on a copper grid coated with a thin layer of carbon. TEM imaging of the materials, which have electron density significantly higher than amorphous carbon, can be

done without relative difficulties providing a good contrast (*i.e.,* signal-to-background) for the final image. The examples of such materials include most metals (e.g., silver, gold, copper, aluminum), most oxides (e.g., silica, aluminum oxide, titanium oxide), and other particles such as polymer nanoparticles, carbon nanotubes, semiconductor nanoparticles (*i.e.,* quantum dots), and magnetic nanoparticles.

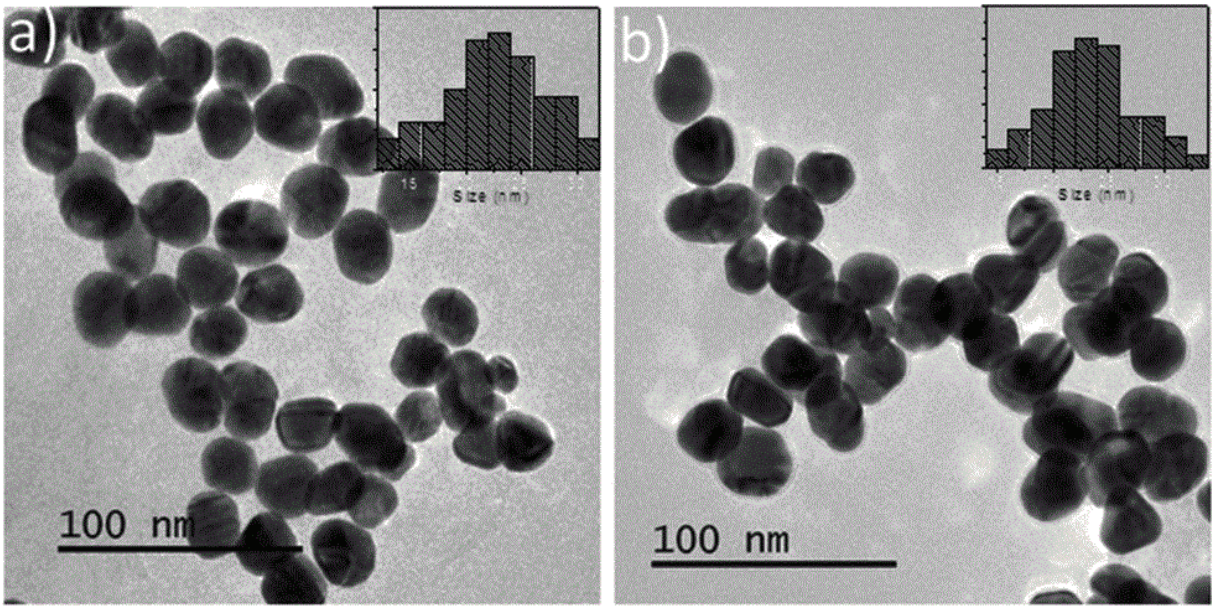

Figure 1.38 TEM images of (a) 60 mg L^{-1} AuNP suspension in MilliQ® water and (b) 750 µg L^{-1} AuNP suspension in standard sea water (SW) media. Insets in TEM images correspond to particle size distributions. Adapted from ref.[194]

TEM imaging remains one of the most suitable method to directly determine the particle size, morphology of nanoparticles, grain size and size distribution (Figure 1.38). The method accuracy lies typically within 3% of the actual value of the size. TEM imaging is one of major method of analysis in physical and biological sciences. It is found wide applications in the fields of cancer research, virology, pollution science, materials science (*e.g.,* semiconductor research). However, there are several limitations of the TEM technique. The some of them are time-consuming sample preparation to produce the sample thin enough to be electron transparent, therefore TEM have limited, rather low throughput of samples. The sample structure can be affected while the preparation process. The field of view is relatively small, raising the possibility of observing artifacts, such as analyzed region may not be characteristic for the whole sample. There is also a possibility of a potential damage of a sample by a beam of electrons, wich can be a particular case for biological samples. The recent advances in the field of TEM developments were in aberration corrector design, which enabled reduction of spherical aberrations.[195] Thus, resolution below 0.5 Ångströms (50 pm)[196] at

magnifications above 50 million times has been reached. This improved resolution enabled the possibility for the imaging of lighter atoms with less efficiency for electron scattering (*e.g.,* lithium atoms in lithium batteries).[197, 198] High-resolution TEM became indispensable tool for research including nanotechnology, heterogeneous catalysis and the development of semiconductor devices for electronics and photonics owing to its ability to determine the position of atoms within materials.[199]

1.5.3 Dynamic light scattering (DLS)

Dynamic Light Scattering (also referred to as Photon Correlation Spectroscopy or Quasi-Elastic Light Scattering) is a technique for measuring the size of particles (typically in the submicron region). It can also be employed to probe the behavior of complex fluids such as concentrated solutions of polymer. DLS actually measures the Brownian motion of the dispersed particles and relates it to their size. The bigger size particle has, the slower the Brownian motion will be. Smaller particles can be "kicked" further by the bombarding solvent molecules and therefore move more rapidly. An accurate value of temperature is also required for DLS, because of dependence of viscosity on the temperature. The term referred as translational diffusion coefficient (D) defines the velocity of the Brownian motion. It should be noted that measured value of the size refers to the hydrodynamic diameter, as it is calculated from the diffusion rate. Such factors as surface structure, concentration and type of ions in the medium also affect the measured value of size.

The size of the particle is calculated by Stokes-Einstein equation:

$$d(H) = \frac{kT}{3\pi\eta D}$$

where: $d(H)$= hydrodynamic diameter; D= translational diffusion coefficient; k= Boltzmann's constant; T= absolute temperature; η= viscosity.

The ions present in the medium as well as the total ionic concentration can influence the particle diffusion speed by changing the thickness of the electric double layer also referred as Debye length (K^{-1}). Thus a low conductivity medium will result in an extended double layer of ions around the particle, reducing the diffusion speed with a larger hydrodynamic diameter observed. The higher conductivity media will work in an opposite way, resulting suppressed electrical double layer with a smaller apparent hydrodynamic diameter.

The Rayleigh scattering theory tells that intensity of scattered light is directly proportional to the diameter in degree of 6 ($I \sim d^6$, where I = intensity of light scattered, d – particle diameter). The d^6

term shows us that a 100 nm particle will scatter one million times more light as 10 nm particle. It means that for the complex mixtures of nanoparticles, the smaller NPs would be hard to detect in the presence of the larger ones, as the larger particles swamp the scattered light from the smaller ones and low down their contribution to the total scattered light collected.

In DLS the diffusion speed of the particles due to Brownian motion is measured. This is done by measuring the rate at which the intensity of the scattered light fluctuates when detected using a suitable optical arrangement. The DLS setup consists of a monochromatic light source, usually a laser, which is oriented through a polarizer into a sample. The scattered light then passes through a second polarizer where it is collected by a photomultiplier and the resulting image is projected onto autocorrelator. This is known as a speckle pattern (Figure 1.39).

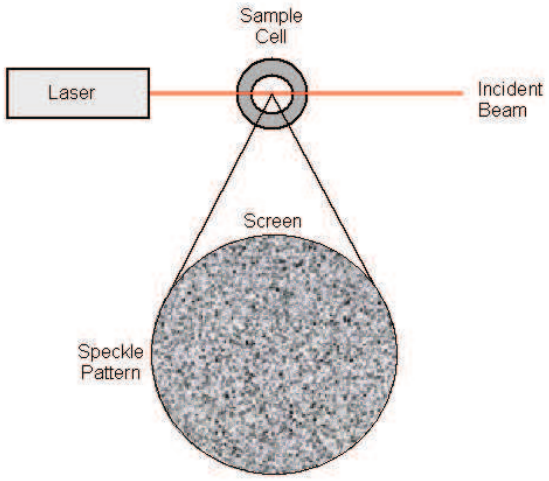

Figure 1.39 Schematic representation of a speckle pattern.

All of the particles in the solution are being hit with the light and all of these particles diffract the light in all directions. The scattered light can arrive in the same phase and therefore interfere constructively (light regions) or with a phase additions which are mutually destructive and cancel each other out (dark regions). This process is repeated at short time intervals and the resulting set of speckle patterns are analyzed by an autocorrelator that compares the intensity of light at each spot over time. The size of the particles depends on the rate at which these intensity fluctuations occur.

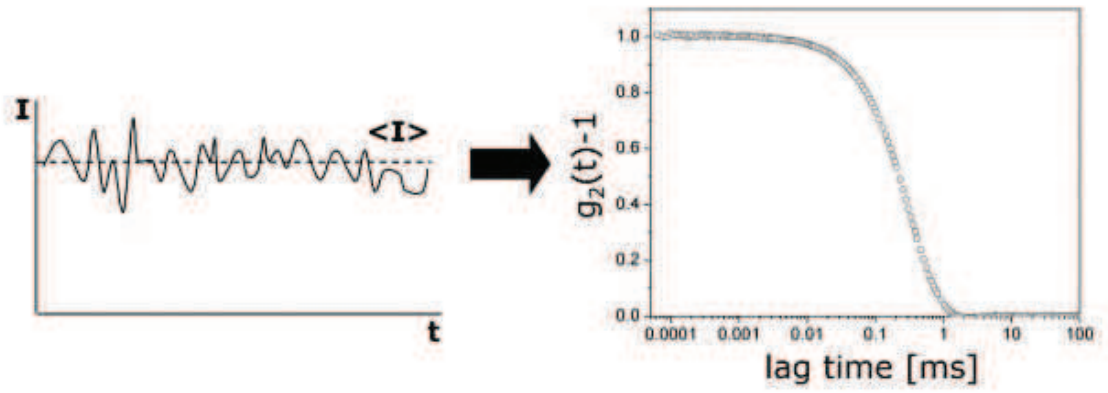

Figure 1.40 A DLS autocorrelation function. The time delay at which the function decreases corresponds to the nanoparticle diffusion rate, which is inversely proportional to the size. Larger particles show the correlation of the signal with a long time to decay, smaller particles move more rapidly so correlation decreases more quickly.

Brief look on the correlogram from a measurement can give a plenty of information about the sample parameters (Figure 1.40). The time at which the correlation starts to significantly decay indicates the mean size of the sample. The scope of the correlogram is a function of a sample polydispersity. The steeper the line, the more monodisperse the sample is. On the contrary, the more extended the decay becomes, the sample polydispersity is greater.

All particle-sizing techniques are oriented on a measure of ideal spherical particles, therefore any deviations to the non-spherical particles will cause inherent problem in describing their size. The hydrodynamic diameter of a non-spherical particle is estimated as a diameter of an ideal spherical particle with the same translational diffusion velocity. For the rod-like particles small changes in the length will strongly affect the diffusion speed, then the hydrodynamic size will change, whereas changes in the rod's diameter will not produce noticeable effect on apparent value of hydrodynamic size and will be hard to detect.

1.5.4 Zeta potential

Zeta potential is a potential that exists between the particle surface and dispersing liquid which varies according to the distance from the particle surface. Zeta potential also can be referred as the electrokinetic potential, is a measure of the "effective" electric charge on the nanoparticle surface, and quantifies the charge stability of colloidal nanoparticles. In situation when a nanoparticle possesses a net surface charge, the charge is "screened" by an increased concentration of ions of opposite charge close to the nanoparticle surface. Combined layer of surface charge and oppositely charged ions is called an electrical double layer. The liquid layer surrounding the particle exists as two

parts; an inner region (Stern layer) where the ions are strongly bound and an outer (diffuse) region where they are less firmly associated. Within the diffuse layer there is a notional boundary inside which the ions and particles form a stable entity. When a particle moves (e.g. due to gravity), ions within the boundary move it. Those ions beyond the boundary stay with the bulk dispersant. The potential at this boundary (surface of hydrodynamic shear) is the zeta potential (Figure 1.41).

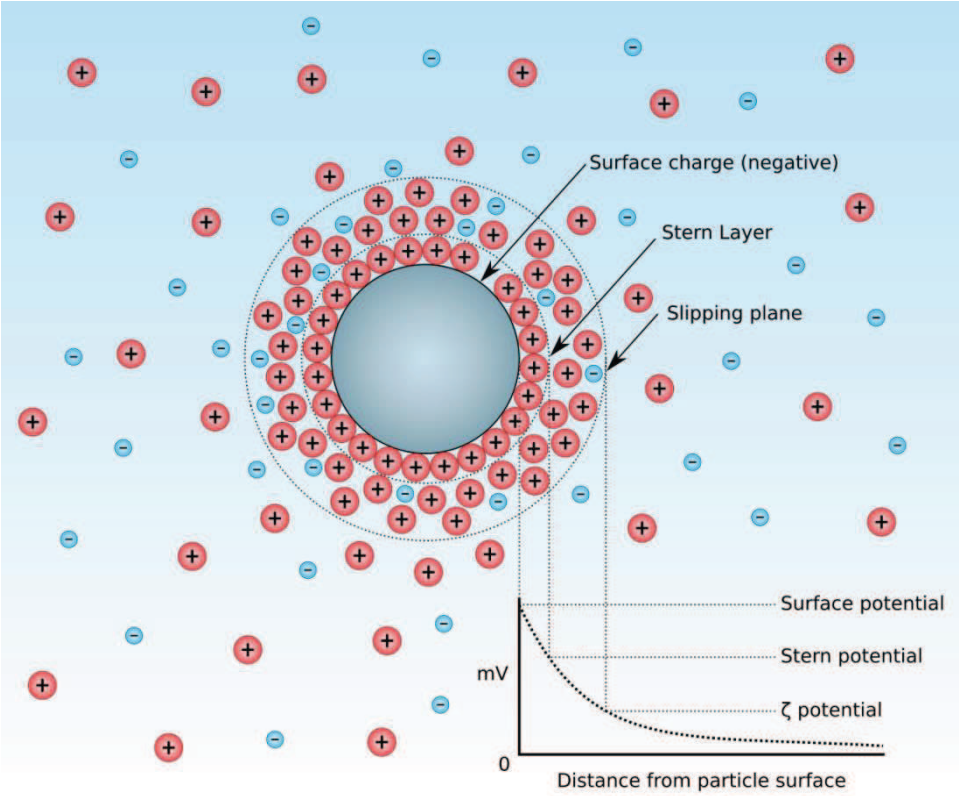

Figure 1.41 Schematic diagram showing the concentration of ions and potential difference as a function of distance from the charged surface of a particle suspended in a dispersion medium.

The value of zeta potential tells us about particle stability in the solution state, since higher magnitude potentials show increased electrostatic repulsion and consequently increased colloidal stability.

- in range of 0-5 mV: Particles tend to agglomerate or aggregate
- in range of 5-20 mV: Particles are minimally stable
- in range of 20-40 mV: Particles are moderately stable
- above 40 mV: Particles are highly stable

It is important to note the fact that solution pH value strongly affects the magnitude of the charge on the nanoparticle surface. The specific pH at which nanoparticle surface charge is reduced to zero referred to as the isoelectric point.

The measure of zeta potential is performed using a DLS instrument by placement of a solution to a cell that contains two gold electrodes. After the voltage is applied, the particles start to move towards the electrode possessing the opposite charge; their velocity is measured and expressed in unit field strength as their mobility. The measure of particle velocity as a function of voltage implies the use of Doppler technique (Laser Doppler Velocimeter), in which particle movements through the laser beam are detected by fluctuation of scattered light at a frequency proportional to the speed of the particles. The obtained data of the particle speed at multiple voltages is used to calculate the value of zeta potential.

1.5.5 Fluorescence Correlation Spectroscopy (FCS)

The fluorescence correlation spectroscopy (FCS) technique was introduced for the first time in the early 1970s and now became one of the widely utilized tools for biophysical studies as well as for characterization of nanoparticles. It is a powerful method of high-resolution spatial and temporal analysis of extremely low concentrated fluorescent biomolecules or nanoparticles.

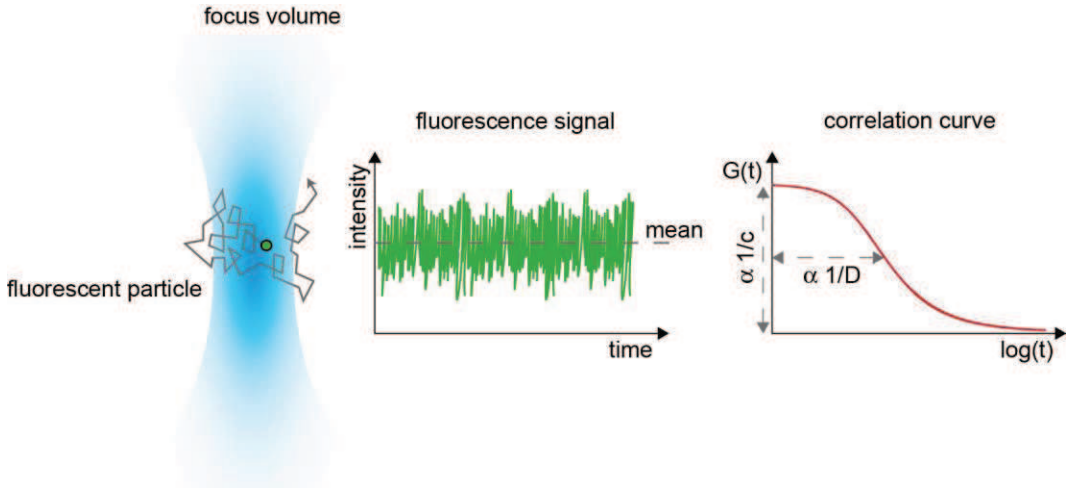

Figure 1.42 Fluorescent molecules/nanoparticles diffusing into and out of a diffraction-limited focus volume result in a fluctuating fluorescence signal according to the variations in the particle number. These fluctuations can be analyzed via calculating the auto-correlation curve, where G(t) is the temporal autocorrelation function. The diffusion coefficient (D) is inversely proportional to the width of the correlation function curve and the concentration inversely proportional to the amplitude (α).

Contrary to other fluorescence techniques, the parameter of primary interest of FCS is not the emission intensity by itself, but temporal intensity fluctuations occurring in a small volume of observation (Figure 1.42), similarly to those recorded by DLS. The amplitude and speed of the fluctuations are used to calculate the correlation function. This function gives precise information about height of the curve that is inversely proportional to the average number of fluorophores being observed and the position of the curve on the time axis which indicates the fluorophore's diffusion coefficient, which is inversely proportional to the size of the molecule/nanoparticle.

In 1990 Rigler and coworkers have made the final breakthrough for the FCS method. The single-molecule detection limit was reached by combining the FCS technique with a confocal setup, thus increasing the signal-to-noise ratio significantly. Confocal optics ensured a small detection volume (~1 femtoliter) required for FCS. With a laser beam, which is tightly focused and inserting a pinhole into the image plane, maximum lateral and axial resolution were achieved.

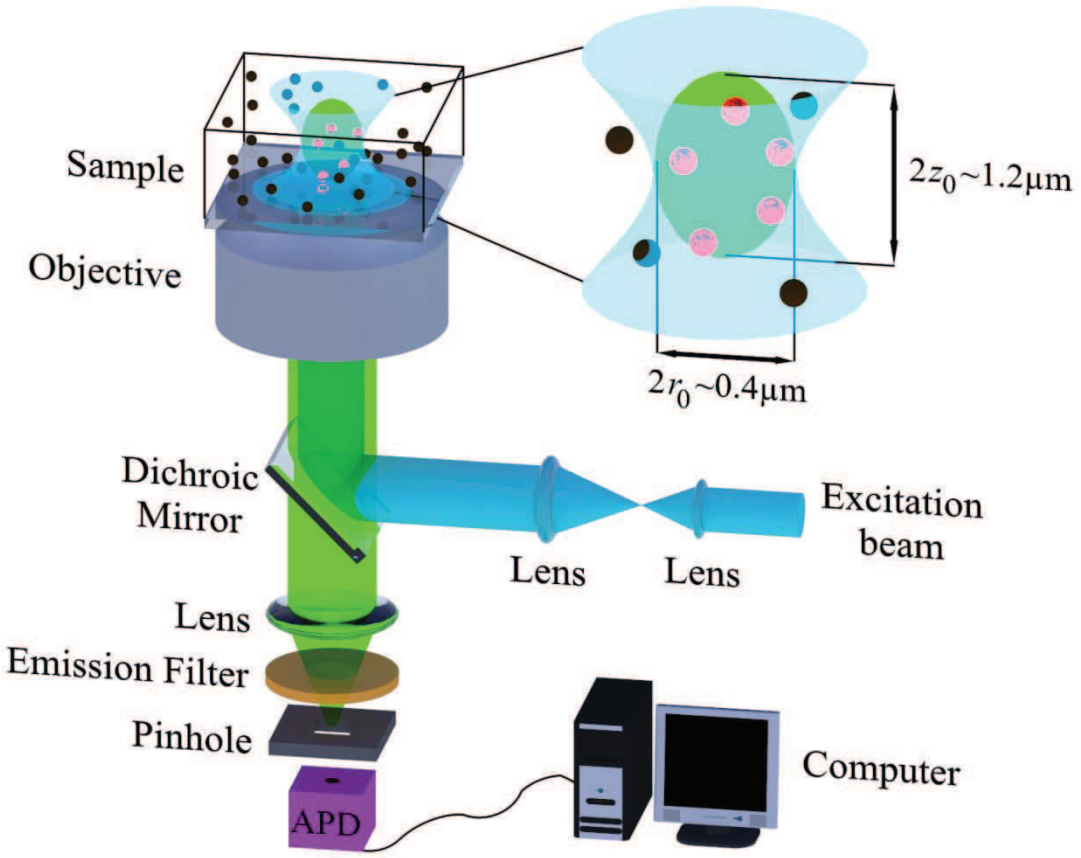

Figure 1.43 Schematic diagram of fluorescence correlation spectroscopy setup. Adapted from http://www.mpip-mainz.mpg.de/62430/Fluorescence_Correlation_Spectroscopy

Generally, FCS technique is based on confocal microscopy setup (Figure 1.43). The laser light, used as an excitation source, is sent through the objective lens to make a tiny focal volume (~1 fl). Fluorescence signal from the focal volume is collected by the same objective lens and filtered by a dichroic mirror. In order to remove the background fluorescence signal coming from out-of-focus region the confocal pinhole is placed. The detectors of high quantum yield are located in a detection part (*e.g,* avalanche photo diode), and the analysis of measured fluctuation of fluorescence signal is processed by either software or hardware.

Single molecule organic dyes, fluorescein proteins and nanoparticles are all suitable for FCS measurements. But the most crucial parameter for this purpose is photostability, as fluorophore have to withstand the enormous power in the laser focus (>100 kW/cm^2). For example, fluorescein possessing the moderate photostability is not a good flurophore for the FCS applications due to the possible unwanted artifacts, and it should be substituted with a specifically engineered dye Alexa488 (Molecular Probes) having similar characteristics such as absorption and emission and enhanced photostability. Other fluorescent markers, which are appropriate for the FCS measurements are rhodamines such as Rhodamine Green, TMR, Rhodamine B and 6G, and cyanines (Cy2, Cy3, Cy5).

The FCS method is particularly adapted for studying nanoparticles, because it can provide simultaneously the information about particle size (through correlation time), particle concentration and single particle brightness.[155] The latter, being a critical parameter for fluorescence imaging, cannot be measured with commonly used dynamic light scattering (DLS). Moreover, in contrast to DLS, FCS allows characterization of particle properties directly in biological media, such as serum and cell lysates. Importantly, FCS can estimate the stability and leakage of the loaded dyes form the particles by monitoring the particle concentration. This method becomes also essential when small NPs are studied at very low concentrations, which are not accessible by DLS techniques. The main limitations of FCS with respect to DLS are that it can study only fluorescent NPs and it cannot operate at very high NPs concentrations. In conclusion, FCS appears as powerful method to characterize NPs, which can be considered as complementary to the other techniques described above.

References

(1) Lakowicz, J. R. *Principles of Fluorescence Spectroscopy, 3rd ed.*; Springer, New York, 2006.

(2) Fleming, G. R.; Knight, A. W. E.; Morris, J. M.; Morrison, R. J. S.; Robinson, G. W. *Journal of the American Chemical Society* **1977**, *99*, 4306.

(3) Neckers, D. C. *Journal of Photochemistry and Photobiology a-Chemistry* **1989**, *47*, 1.

(4) Lavis, L. D.; Raines, R. T. *Acs Chemical Biology* **2008**, *3*, 142.

(5) Stokes, G. G. *Phil. Trans. R. Soc. London* **1852**, *142*, 463−562.

(6) Denk, W.; Svoboda, K. *Neuron* **1997**, *18*, 351.

(7) Bright, F. V.; Munson, C. A. *Analytica Chimica Acta* **2003**, *500*, 71.

(8) Owicki, J. C. *Journal of Biomolecular Screening* **2000**, *5*, 297.

(9) Kiyose, K.; Kojima, H.; Nagano, T. *Chemistry-an Asian Journal* **2008**, *3*, 506.

(10) Azuma, E.; Nakamura, N.; Kuramochi, K.; Sasamori, T.; Tokitoh, N.; Sagami, I.; Tsubaki, K. *Journal of Organic Chemistry* **2012**, *77*, 3492.

(11) Grimm, J. B.; Heckman, L. M.; Lavis, L. D. In *Fluorescence-Based Biosensors: From Concepts to Applications*; Morris, M. C., Ed. 2013; Vol. 113, p 1.

(12) Forster, T. *Discuss. Faraday Soc.* **1959**, *No. 27*, 7.

(13) Stryer, L.; Haugland, R. P. *Proceedings of the National Academy of Sciences of the United States of America* **1967**, *58*, 719.

(14) Stryer, L. *Annual Review of Biochemistry* **1978**, *47*, 819.

(15) Lim, C. S.; Miller, J. N.; Bridges, J. W. *Analytica Chimica Acta* **1980**, *114*, 183.

(16) Sapsford, K. E.; Berti, L.; Medintz, I. L. *Angewandte Chemie-International Edition* **2006**, *45*, 4562.

(17) Forster, T. *Ann. Physik [6 Folge]* **1948**, *2*, 55.

(18) Forster, T. *Z. Naturforsch.* **1949**, *4a*, 321.

(19) K. E. Sapsford, L. B., I. L. Medintz *Minerva Biotecnologica* **2005**, *16*, 253.

(20) Dosremedios, C. G.; Moens, P. D. J. *Journal of Structural Biology* **1995**, *115*, 175.

(21) Schobel, U.; Egelhaaf, H. J.; Brecht, A.; Oelkrug, D.; Gauglitz, G. *Bioconjugate Chemistry* **1999**, *10*, 1107.

(22) Lillo, M. P.; Szpikowska, B. K.; Mas, M. T.; Sutin, J. D.; Beechem, J. M. *Biochemistry* **1997**, *36*, 11273.

(23) Qu, Q.; Sharom, F. J. *Biochemistry* **2001**, *40*, 1413.

(24) Zhang, J.; Campbell, R. E.; Ting, A. Y.; Tsien, R. Y. *Nature Reviews Molecular Cell Biology* **2002**, *3*, 906.

(25) Hemmilä, I. A. *Applications of Fluorescence in Immunoassays* Wiley: New York, 1991.

(26) Boonacker, E.; Van Noorden, C. J. F. *Journal of Histochemistry & Cytochemistry* **2001**, *49*, 1473.

(27) Frangioni, J. V. *Current Opinion in Chemical Biology* **2003**, *7*, 626.

(28) Goddard, J. P.; Reymond, J. L. *Curr. Opin. Biotechnol.* **2004**, *15*, 314.

(29) Giepmans, B. N. G.; Adams, S. R.; Ellisman, M. H.; Tsien, R. Y. *Science* **2006**, *312*, 217.

(30) Valeur, B. *Molecular Fluorescence: Principles and Applications*; Wiley-VCH: Weinheim, 2001.

(31) Sadaghiani, A. M.; Verhelst, S. H. L.; Bogyo, M. *Current Opinion in Chemical Biology* **2007**, *11*, 20.

(32) Johnsson, N.; Johnsson, K. *Acs Chemical Biology* **2007**, *2*, 31.

(33) Waggoner, A. *Current Opinion in Chemical Biology* **2006**, *10*, 62.

(34) Baeyer, A. *Ber. Dtsch. Chem. Ges.* **1871**, *4*, 555.

(35) Haugland, R. P., Spence, M. T. Z., Johnson, I. D., and Basey, A. *The Handbook: A Guide to Fluorescent Probes and Labeling Technologies,10th ed.*; Molecular Probes: Eugene, OR, 2005.

(36) Johnson, I. *Histochemical Journal* **1998**, *30*, 123.

(37) Drexhage, K. H. *Structure and Properites of Laser Dyes. In Dye Lasers, 2nd ed.*; Springer-Verlag: Berlin, 1977.

(38) Karstens, T.; Kobs, K. *Journal of Physical Chemistry* **1980**, *84*, 1871.

(39) Treibs, A.; Kreuzer, F. H. *Justus Liebigs Ann. Chem.* **1968**, *718*, 208.

(40) Karolin, J.; Johansson, L. B. A.; Strandberg, L.; Ny, T. *Journal of the American Chemical Society* **1994**, *116*, 7801.

(41) Loudet, A.; Burgess, K. *Chemical reviews* **2007**, *107*, 4891.

(42) Ulrich, G.; Ziessel, R.; Harriman, A. *Angewandte Chemie-International Edition* **2008**, *47*, 1184.

(43) Boens, N.; Leen, V.; Dehaen, W. *Chemical Society Reviews* **2012**, *41*, 1130.

(44) Ziessel, R.; Ulrich, G.; Harriman, A. *New Journal of Chemistry* **2007**, *31*, 496.

(45) Zhao, W. L.; Carreira, E. M. *Angewandte Chemie-International Edition* **2005**, *44*, 1677.

(46) Zhao, W.; Carreira, E. M. *Chemistry-a European Journal* **2006**, *12*, 7254.

(47) Qian, G.; Wang, Z. Y. *Chemistry-an Asian Journal* **2010**, *5*, 1006.

(48) Mishra, A.; Behera, R. K.; Behera, P. K.; Mishra, B. K.; Behera, G. B. *Chemical reviews* **2000**, *100*, 1973.

(49) Lewis, G. N.; Calvin, M. *Chem. Rev.* **1939**, *25*, 273.

(50) Mujumdar, R. B.; Ernst, L. A.; Mujumdar, S. R.; Lewis, C. J.; Waggoner, A. S. *Bioconjugate Chemistry* **1993**, *4*, 105.

(51) Waggoner, A. *Biochemical Spectroscopy* **1995**, *246*, 362.

(52) Mujumdar, S. R.; Mujumdar, R. B.; Grant, C. M.; Waggoner, A. S. *Bioconjugate Chemistry* **1996**, *7*, 356.

(53) Brand, L.; Eggeling, C.; Zander, C.; Drexhage, K. H.; Seidel, C. A. M. *Journal of Physical Chemistry A* **1997**, *101*, 4313.

(54) Lavis, L. D.; Raines, R. T. *Acs Chemical Biology* **2014**, *9*, 855.

(55) Shimomura, O.; Johnson, F. H.; Saiga, Y. *Journal of cellular and comparative physiology* **1962**, *59*, 223.

(56) Heim, R.; Prasher, D. C.; Tsien, R. Y. *Proceedings of the National Academy of Sciences of the United States of America* **1994**, *91*, 12501.

(57) Ormo, M.; Cubitt, A. B.; Kallio, K.; Gross, L. A.; Tsien, R. Y.; Remington, S. J. *Science* **1996**, *273*, 1392.

(58) Tsien, R. Y.; Miyawaki, A. *Science* **1998**, *280*, 1954.

(59) Matz, M. V.; Fradkov, A. F.; Labas, Y. A.; Savitsky, A. P.; Zaraisky, A. G.; Markelov, M. L.; Lukyanov, S. A. *Nature Biotechnology* **1999**, *17*, 969.

(60) Shaner, N. C.; Patterson, G. H.; Davidson, M. W. *Journal of Cell Science* **2007**, *120*, 4247.

(61) Flors, C.; Hotta, J.-i.; Uji-i, H.; Dedecker, P.; Ando, R.; Mizuno, H.; Miyawaki, A.; Hofkens, J. *Journal of the American Chemical Society* **2007**, *129*, 13970.

(62) Habuchi, S.; Ando, R.; Dedecker, P.; Verheijen, W.; Mizuno, H.; Miyawaki, A.; Hofkens, J. *Proceedings of the National Academy of Sciences of the United States of America* **2005**, *102*, 9511.

(63) Lakowicz, J. R.; Balter, A. *Biophysical Chemistry* **1982**, *16*, 117.

(64) Birks, J. B. *Photophysics of aromatic molecules*; John Wiley & Sons: New York, London, 1970.

(65) Ogawa, M.; Kosaka, N.; Choyke, P. L.; Kobayashi, H. *Acs Chemical Biology* **2009**, *4*, 535.

(66) Zhelev, Z.; Ohba, H.; Bakalova, R. *Journal of the American Chemical Society* **2006**, *128*, 6324.

(67) Bakalova, R.; Zhelev, Z.; Aoki, I.; Ohba, H.; Imai, Y.; Kanno, I. *Anal. Chem.* **2006**, *78*, 5925.

(68) Tang, C. W.; Vanslyke, S. A. *Applied Physics Letters* **1987**, *51*, 913.
(69) Mei, J.; Hong, Y.; Lam, J. W. Y.; Qin, A.; Tang, Y.; Tang, B. Z. *Advanced Materials* **2014**, *26*, 5429.
(70) Demchenko, A. P. *Introduction to Fluorescence Sensing, 2nd ed.*; Springer, 2015.
(71) Johansson, M. K.; Cook, R. M. *Chemistry-a European Journal* **2003**, *9*, 3466.
(72) Bhattacharyya, K.; Chowdhury, M. *Chemical reviews* **1993**, *93*, 507.
(73) Jones, R. M.; Lu, L. D.; Helgeson, R.; Bergstedt, T. S.; McBranch, D. W.; Whitten, D. G. *Proceedings of the National Academy of Sciences of the United States of America* **2001**, *98*, 14769.
(74) Zhou, Q.; Swager, T. M. *Journal of the American Chemical Society* **1995**, *117*, 12593.
(75) Davydov, A. S. *Theory of molecular excitons (Translated by M. Kasha and M. Oppenheimer)*; McGraw-Hill: New York, 1962.
(76) Kasha, M.; Rawls, H. R.; El-Bayoumi, M. A. *Pure Appl. Chem.* **1965**, *11*, 371.
(77) Wuerthner, F.; Kaiser, T. E.; Saha-Moeller, C. R. *Angew. Chem., Int. Ed.* **2011**, *50*, 3376.
(78) Ohno, O.; Kaizu, Y.; Kobayashi, H. *Journal of Chemical Physics* **1993**, *99*, 4128.
(79) Rotomskis, R.; Augulis, R.; Snitka, V.; Valiokas, R.; Liedberg, B. *Journal of Physical Chemistry B* **2004**, *108*, 2833.
(80) Wurthner, F. *Chemical Communications* **2004**, 1564.
(81) Yagai, S.; Seki, T.; Karatsu, T.; Kitamura, A.; Wuerthner, F. *Angewandte Chemie-International Edition* **2008**, *47*, 3367.
(82) Klymchenko, A. S. *J. Nanosci. Lett.* **2013**, *3*, 21/1.
(83) Luo, J. D.; Xie, Z. L.; Lam, J. W. Y.; Cheng, L.; Chen, H. Y.; Qiu, C. F.; Kwok, H. S.; Zhan, X. W.; Liu, Y. Q.; Zhu, D. B.; Tang, B. Z. *Chemical Communications* **2001**, 1740.
(84) Tang, B. Z.; Zhan, X. W.; Yu, G.; Lee, P. P. S.; Liu, Y. Q.; Zhu, D. B. *Journal of Materials Chemistry* **2001**, *11*, 2974.
(85) Chen, J. W.; Xu, B.; Ouyang, X. Y.; Tang, B. Z.; Cao, Y. *Journal of Physical Chemistry A* **2004**, *108*, 7522.
(86) Chen, J. W.; Law, C. C. W.; Lam, J. W. Y.; Dong, Y. P.; Lo, S. M. F.; Williams, I. D.; Zhu, D. B.; Tang, B. Z. *Chemistry of Materials* **2003**, *15*, 1535.
(87) Hong, Y.; Lam, J. W. Y.; Tang, B. Z. *Chemical Communications* **2009**, 4332.
(88) Hong, Y. N.; Lam, J. W. Y.; Tang, B. Z. *Chemical Society Reviews* **2011**, *40*, 5361.
(89) Hu, R.; Leung, N. L. C.; Tang, B. Z. *Chemical Society Reviews* **2014**, *43*, 4494.
(90) Zhang, S.; Qin, A.; Sun, J.; Tang, B. *Progress in Chemistry* **2011**, *23*, 623.
(91) Liu, J.; Lam, J. W. Y.; Tang, B. Z. *Journal of Inorganic and Organometallic Polymers and Materials* **2009**, *19*, 249.
(92) Zhao, Z.; Lam, J. W. Y.; Tang, B. Z. *Journal of Materials Chemistry* **2012**, *22*, 23726.
(93) Ding, D.; Li, K.; Liu, B.; Tang, B. Z. *Acc. Chem. Res.* **2013**, *46*, 2441.
(94) Chi, Z.; Zhang, X.; Xu, B.; Zhou, X.; Ma, C.; Zhang, Y.; Liu, S.; Xu, J. *Chemical Society Reviews* **2012**, *41*, 3878.
(95) Zhao, G.; Shi, C.; Guo, Z.; Zhu, W.; Zhu, S. *Chinese Journal of Organic Chemistry* **2012**, *32*, 1620.
(96) Fan, X.; Sun, J.; Wang, F.; Chu, Z.; Wang, P.; Dong, Y.; Hu, R.; Tang, B. Z.; Zou, D. *Chemical Communications* **2008**, 2989.
(97) Li, S.; Wang, Q.; Qian, Y.; Wang, S.; Li, Y.; Yang, G. *Journal of Physical Chemistry A* **2007**, *111*, 11793.
(98) Luo, J.; Song, K.; Gu, F. L.; Miao, Q. *Chemical Science* **2011**, *2*, 2029.
(99) Li, Z.; Qin, A. J. *Natl Sci Rev* **2014**, *1*, 22.
(100) Ekimov, A. I.; Onushchenko, A. A. *Jetp Letters* **1981**, *34*, 345.
(101) Brus, L. *Journal of Physical Chemistry* **1986**, *90*, 2555.
(102) Alivisatos, A. P. *Abstracts of Papers of the American Chemical Society* **1999**, *218*, U296.

(103) Dabbousi, B. O.; RodriguezViejo, J.; Mikulec, F. V.; Heine, J. R.; Mattoussi, H.; Ober, R.; Jensen, K. F.; Bawendi, M. G. *Journal of Physical Chemistry B* **1997**, *101*, 9463.

(104) Talapin, D. V.; Rogach, A. L.; Kornowski, A.; Haase, M.; Weller, H. *Nano Letters* **2001**, *1*, 207.

(105) Biju, V.; Itoh, T.; Anas, A.; Sujith, A.; Ishikawa, M. *Analytical and Bioanalytical Chemistry* **2008**, *391*, 2469.

(106) Murray, C. B.; Norris, D. J.; Bawendi, M. G. *Journal of the American Chemical Society* **1993**, *115*, 8706.

(107) Peng, X. G.; Wickham, J.; Alivisatos, A. P. *Journal of the American Chemical Society* **1998**, *120*, 5343.

(108) Hines, M. A.; Guyot-Sionnest, P. *Journal of Physical Chemistry* **1996**, *100*, 468.

(109) Medintz, I. L.; Uyeda, H. T.; Goldman, E. R.; Mattoussi, H. *Nature Materials* **2005**, *4*, 435.

(110) Pellegrino, T.; Manna, L.; Kudera, S.; Liedl, T.; Koktysh, D.; Rogach, A. L.; Keller, S.; Radler, J.; Natile, G.; Parak, W. J. *Nano Letters* **2004**, *4*, 703.

(111) Wegner, K. D.; Hildebrandt, N. *Chemical Society Reviews* **2015**, *44*, 4792.

(112) Zhu, M. Q.; Chang, E.; Sun, J. T.; Drezek, R. A. *Journal of Materials Chemistry* **2007**, *17*, 800.

(113) Sperling, R. A.; Parak, W. J. *Therapeutic Innovation & Regulatory Science* **2013**, *47*, 1333.

(114) Jones, M.; Nedeljkovic, J.; Ellingson, R. J.; Nozik, A. J.; Rumbles, G. *Journal of Physical Chemistry B* **2003**, *107*, 11346.

(115) Hohng, S.; Ha, T. *Journal of the American Chemical Society* **2004**, *126*, 1324.

(116) Fomenko, V.; Nesbitt, D. J. *Nano Letters* **2008**, *8*, 287.

(117) Hollingsworth, J. A. *Chemistry of Materials* **2013**, *25*, 1318.

(118) Michalet, X.; Pinaud, F. F.; Bentolila, L. A.; Tsay, J. M.; Doose, S.; Li, J. J.; Sundaresan, G.; Wu, A. M.; Gambhir, S. S.; Weiss, S. *Science* **2005**, *307*, 538.

(119) Shibata, S.; Taniguchi, T.; Yano, T.; Yamane, M. *Journal of Sol-Gel Science and Technology* **1997**, *10*, 263.

(120) Tapec, R.; Zhao, X. J. J.; Tan, W. H. *Journal of Nanoscience and Nanotechnology* **2002**, *2*, 405.

(121) van Blaaderen, A.; Vrij, A. *Langmuir* **1992**, *8*, 2921.

(122) Bonacchi, S.; Genovese, D.; Juris, R.; Montalti, M.; Prodi, L.; Rampazzo, E.; Zaccheroni, N. *Angewandte Chemie-International Edition* **2011**, *50*, 4056.

(123) Yamauchi, H.; Ishikawa, T.; Kondo, S. *Colloids and Surfaces* **1989**, *37*, 71.

(124) Bagwe, R. P.; Yang, C. Y.; Hilliard, L. R.; Tan, W. H. *Langmuir* **2004**, *20*, 8336.

(125) Zhao, X. J.; Bagwe, R. P.; Tan, W. H. *Advanced Materials* **2004**, *16*, 173.

(126) Wang, L.; Tan, W. H. *Nano Letters* **2006**, *6*, 84.

(127) Das, S.; Jain, T. K.; Maitra, A. *Journal of Colloid and Interface Science* **2002**, *252*, 82.

(128) Rio-Echevarria, I. M.; Tavano, R.; Causin, V.; Papini, E.; Mancin, F.; Moretto, A. *Journal of the American Chemical Society* **2011**, *133*, 8.

(129) Zanarini, S.; Rampazzo, E.; Bonacchi, S.; Juris, R.; Marcaccio, M.; Montalti, M.; Paolucci, F.; Prodi, L. *Journal of the American Chemical Society* **2009**, *131*, 14208.

(130) Vijayasree, N.; Haritha, K.; Subhash, V.; Rao, K. R. S. S. *Research Journal of Biotechnology* **2009**, *4*, 61.

(131) Yan, J. L.; Estevez, M. C.; Smith, J. E.; Wang, K. M.; He, X. X.; Wang, L.; Tan, W. H. *Nano Today* **2007**, *2*, 44.

(132) Ray, S. C.; Saha, A.; Jana, N. R.; Sarkar, R. *Journal of Physical Chemistry C* **2009**, *113*, 18546.

(133) Wang, X.; Cao, L.; Yang, S. T.; Lu, F. S.; Meziani, M. J.; Tian, L. L.; Sun, K. W.; Bloodgood, M. A.; Sun, Y. P. *Angewandte Chemie-International Edition* **2010**, *49*, 5310.

(134) Bhunia, S. K.; Saha, A.; Maity, A. R.; Ray, S. C.; Jana, N. R. *Scientific Reports* **2013**, *3*.

(135) Kong, B.; Zhu, A. W.; Ding, C. Q.; Zhao, X. M.; Li, B.; Tian, Y. *Advanced Materials* **2012**, *24*, 5844.

(136) Luo, P. J. G.; Sahu, S.; Yang, S. T.; Sonkar, S. K.; Wang, J. P.; Wang, H. F.; LeCroy, G. E.; Cao, L.; Sun, Y. P. *Journal of Materials Chemistry B* **2013**, *1*, 2116.

(137) Sun, Y. P.; Zhou, B.; Lin, Y.; Wang, W.; Fernando, K. A. S.; Pathak, P.; Meziani, M. J.; Harruff, B. A.; Wang, X.; Wang, H. F.; Luo, P. J. G.; Yang, H.; Kose, M. E.; Chen, B. L.; Veca, L. M.; Xie, S. Y. *Journal of the American Chemical Society* **2006**, *128*, 7756.

(138) Zhang, X. Y.; Wang, S. Q.; Zhu, C. Y.; Liu, M. Y.; Ji, Y.; Feng, L.; Tao, L.; Wei, Y. *Journal of Colloid and Interface Science* **2013**, *397*, 39.

(139) Essner, J. B.; Laber, C. H.; Ravula, S.; Polo-Parada, L.; Baker, G. A. *Green Chemistry* **2015**.

(140) An, B. K.; Kwon, S. K.; Jung, S. D.; Park, S. Y. *J. Am. Chem. Soc.* **2002**, *124*, 14410.

(141) Bertorelle, F.; Lavabre, D.; Fery-Forgues, S. *Journal of the American Chemical Society* **2003**, *125*, 6244.

(142) Badre, S.; Monnier, V.; Meallet-Renault, R.; Dumas-Verdes, C.; Schmidt, E. Y.; Mikhaleva, A. b. I.; Laurent, G.; Levi, G.; Ibanez, A.; Trofimov, B. A.; Pansu, R. B. *Journal of Photochemistry and Photobiology a-Chemistry* **2006**, *183*, 238.

(143) Parthasarathy, V.; Fery-Forgues, S.; Campioli, E.; Recher, G.; Terenziani, F.; Blanchard-Desce, M. *Small* **2011**, *7*, 3219.

(144) Yao, H.; Yamashita, M.; Kimura, K. *Langmuir* **2009**, *25*, 1131.

(145) Yao, H.; Ashiba, K. *RSC Adv.* **2011**, *1*, 834.

(146) Lamere, J.-F.; Saffon, N.; Dos Santos, I.; Fery-Forgues, S. *Langmuir* **2010**, *26*, 10210.

(147) Rao, J. P.; Geckeler, K. E. *Progress in Polymer Science* **2011**, *36*, 887.

(148) Schubert, S.; Delaney, J. T.; Schubert, U. S. *Soft Matter* **2011**, *7*, 1581.

(149) Duncan, R.; Richardson, S. C. W. *Molecular Pharmaceutics* **2012**, *9*, 2380.

(150) Delplace, V.; Couvreur, P.; Nicolas, J. *Polymer Chemistry* **2014**, *5*, 1529.

(151) Landfester, K.; Musyanovych, A.; Mailander, V. *Journal of Polymer Science Part a-Polymer Chemistry* **2010**, *48*, 493.

(152) Wagh, A.; Jyoti, F.; Mallik, S.; Qian, S.; Leclerc, E.; Law, B. *Small* **2013**, *9*, 2129.

(153) Wagh, A.; Qian, S. Y.; Law, B. *Bioconjugate Chemistry* **2012**, *23*, 981.

(154) Reisch, A.; Didier, P.; Richert, L.; Oncul, S.; Arntz, Y.; Mely, Y.; Klymchenko, A. S. *Nature Communications* **2014**, *5*.

(155) Trofymchuk, K.; Reisch, A.; Shulov, I.; Mély, Y.; Klymchenko, A. S. *Nanoscale* **2014**, *6*, 12934.

(156) Grazon, C.; Rieger, J.; Meallet-Renault, R.; Charleux, B.; Clavier, G. *Macromolecules* **2013**, *46*, 5167.

(157) Antonietti, M.; Basten, R.; Lohmann, S. *Macromolecular Chemistry and Physics* **1995**, *196*, 441.

(158) Candau, F.; Pabon, M.; Anquetil, J. Y. *Colloids and Surfaces a-Physicochemical and Engineering Aspects* **1999**, *153*, 47.

(159) Robin, M. P.; O'Reilly, R. K. *Polymer International* **2015**, *64*, 174.

(160) Merian, J.; Gravier, J.; Navarro, F.; Texier, I. *Molecules* **2012**, *17*, 5564.

(161) Delmas, T.; Piraux, H.; Couffin, A. C.; Texier, I.; Vinet, F.; Poulin, P.; Cates, M. E.; Bibette, J. *Langmuir* **2011**, *27*, 1683.

(162) Gravier, J.; Navarro, F. P.; Delmas, T.; Mittler, F.; Couffin, A. C.; Vinet, F.; Texier, I. *Journal of Biomedical Optics* **2011**, *16*.

(163) Kilin, V. N.; Anton, H.; Anton, N.; Steed, E.; Vermot, J.; Vandamme, T. E.; Mely, Y.; Klymchenko, A. S. *Biomaterials* **2014**, *35*, 4950.

(164) Cormode, D. P.; Jarzyna, P. A.; Mulder, W. J. M.; Fayad, Z. A. *Advanced Drug Delivery Reviews* **2010**, *62*, 329.

(165) Ng, K. K.; Lovell, J. F.; Zheng, G. *Accounts of Chemical Research* **2011**, *44*, 1105.

(166) Cao, W. G.; Ng, K. K.; Corbin, I.; Zhang, Z. H.; Ding, L. L.; Chen, J.; Zheng, G. *Bioconjugate Chemistry* **2009**, *20*, 2023.

(167) Zheng, G.; Chen, J.; Li, H.; Glickson, J. D. *Proceedings of the National Academy of Sciences of the United States of America* **2005**, *102*, 17757.

(168) Zheng, X. H.; Xing, D.; Zhou, F. F.; Wu, B. Y.; Chen, W. R. *Molecular Pharmaceutics* **2011**, *8*, 447.

(169) Kirchherr, A. K.; Briel, A.; Mader, K. *Molecular Pharmaceutics* **2009**, *6*, 480.

(170) Deissler, V.; Ruger, R.; Frank, W.; Fahr, A.; Kaiser, W. A.; Hilger, I. *Small* **2008**, *4*, 1240.

(171) Sandanaraj, B. S.; Gremlich, H. U.; Kneuer, R.; Dawson, J.; Wacha, S. *Bioconjugate Chemistry* **2010**, *21*, 93.

(172) Portnoy, E.; Lecht, S.; Lazarovici, P.; Danino, D.; Magdassi, S. *Nanomedicine-Nanotechnology Biology and Medicine* **2011**, *7*, 480.

(173) Proulx, S. T.; Luciani, P.; Derzsi, S.; Rinderknecht, M.; Mumprecht, V.; Leroux, J. C.; Detmar, M. *Cancer Research* **2010**, *70*, 7053.

(174) Lovell, J. F.; Jin, C. S.; Huynh, E.; Jin, H. L.; Kim, C.; Rubinstein, J. L.; Chan, W. C. W.; Cao, W. G.; Wang, L. V.; Zheng, G. *Nature Materials* **2011**, *10*, 324.

(175) Tuncel, D.; Demir, H. V. *Nanoscale* **2010**, *2*, 484.

(176) Feng, L. H.; Zhu, C. L.; Yuan, H. X.; Liu, L. B.; Lv, F. T.; Wang, S. *Chemical Society Reviews* **2013**, *42*, 6620.

(177) Kurokawa, N.; Yoshikawa, H.; Hirota, N.; Hyodo, K.; Masuhara, H. *Chemphyschem* **2004**, *5*, 1609.

(178) Wu, C. F.; Jin, Y. H.; Schneider, T.; Burnham, D. R.; Smith, P. B.; Chiu, D. T. *Angewandte Chemie-International Edition* **2010**, *49*, 9436.

(179) Petkau, K.; Kaeser, A.; Fischer, I.; Brunsveld, L.; Schenning, A. P. H. J. *Journal of the American Chemical Society* **2011**, *133*, 17063.

(180) Zhang, X.; Chen, Z. J.; Wurthner, F. *Journal of the American Chemical Society* **2007**, *129*, 4886.

(181) Olivier, J. H.; Widmaier, J.; Ziessel, R. *Chemistry-a European Journal* **2011**, *17*, 11709.

(182) Wurthner, F.; Kaiser, T. E.; Saha-Moller, C. R. *Angewandte Chemie-International Edition* **2011**, *50*, 3376.

(183) Langhals, H. *Helvetica Chimica Acta* **2005**, *88*, 1309.

(184) Langhals, H.; Ismael, R.; Yuruk, O. *Tetrahedron* **2000**, *56*, 5435.

(185) Langhals, H. *New Journal of Chemistry* **2008**, *32*, 21.

(186) Weil, T.; Vosch, T.; Hofkens, J.; Peneva, K.; Mullen, K. *Angewandte Chemie-International Edition* **2010**, *49*, 9068.

(187) Zhang, X.; Rehm, S.; Safont-Sempere, M. M.; Wurthner, F. *Nature Chemistry* **2009**, *1*, 623.

(188) Dudek, S. P.; Pouderoijen, M.; Abbel, R.; Schenning, A. P. H. J.; Meijer, E. W. *Journal of the American Chemical Society* **2005**, *127*, 11763.

(189) Abbel, R.; Schenning, A. P. H. J.; Meijer, E. W. *Journal of Polymer Science Part a-Polymer Chemistry* **2009**, *47*, 4215.

(190) Abbel, R.; van der Weegen, R.; Meijer, E. W.; Schenning, A. P. H. J. *Chemical Communications* **2009**, 1697.

(191) Suk, J.; Cheng, J. Z.; Wong, K. T.; Bard, A. J. *Journal of Physical Chemistry C* **2011**, *115*, 14960.

(192) Fan, G.; Lin, Y. X.; Yang, L.; Gao, F. P.; Zhao, Y. X.; Qiao, Z. Y.; Zhao, Q.; Fan, Y. S.; Chen, Z. J.; Wang, H. *Chemical Communications* **2015**, *51*, 12447.

(193) Casuso, I.; Rico, F.; Scheuring, S. *Journal of Molecular Recognition* **2011**, *24*, 406.

(194) Garcia-Negrete, C. A.; de Haro, M. C. J.; Blasco, J.; Soto, M.; Fernandez, A. *Analyst* **2015**, *140*, 3082.

(195) Tanaka, N. *Science and Technology of Advanced Materials* **2008**, *9*.
(196) Erni, R.; Rossell, M. D.; Kisielowski, C.; Dahmen, U. *Physical Review Letters* **2009**, *102*.
(197) O'Keefe, M. A.; Shao-Horn, Y. *Microsc Microanal* **2004**, *10*, 86.
(198) Yang, S.-H.; Croguennec, L.; Delmas, C.; Nelson, E. C.; O'Keefe, M. A. *Nat. Mater.* **2003**, *2*, 464.
(199) O'Keefe, M. A.; Allard, L. F.; Blom, D. A. *J Electron Microsc (Tokyo)* **2005**, *54*, 169.

Aim of the PhD thesis

Based on the literature overview above, it is clear that preparation of fluorescence organic nanoparticles characterized by small size and high brightness, comparable or better than inorganic particles, remains a challenge. The aim of my thesis project is to develop new strategies for preparation of ultrabright fluorescent organic nanoparticles featuring 5-20 nm size and to evaluate their properties and applicability to biological imaging. In this work, we followed four strategies. The first one is the encapsulation of highly lipophilic dyes into lipid nano-droplets. The second one is the assembly of nanoparticles from cationic dyes in the presence of bulky hydrophobic counterions. The third one is based on the amphiphiles of cationic dyes, where bulky hydrophobic counterion ensures formation of small and bright fluorescent micelles. Finally, the forth one is based on micelles of amphiphilic calixarenes which are cross-linked by fluorescent cross-linkers. The final fourth approach presents the highest level of complexity that combines assembly of ultra-small nanoparticles with their cross-linking that ensures high stability of the obtained NPs in biological applications. Each strategy is presented in a separate chapter, where an extended summary is followed by corresponding article or manuscript.

2. RESULTS AND DISCUSSION

2.1 Highly lipophilic fluorescent dyes in nano-emulsions: towards bright non-leaking nano-droplets

Lipid nanodroplets attracted attention of researchers as potential tools for bioimaging and drug delivery purposes as they are injectable into a blood, biodegradable and composed of non-toxic materials. They can be readily prepared in the large quantities by nano-emulsification of oil (medium chain triglyceride, such as labrafac) and surfactant (based on PEGylated and alkyl chains, such as solutol) (Fig. 2.1.1). To achieve high fluorescence brightness, the nano-droplets have to be heavily loaded with the dyes avoiding fluorescence self-quenching and release (leakage) of the encapsulated dyes from the nano-droplets in biological media. However, the latter problems were not systematically addressed in the literature. In our work, to overcome these problems we have designed highly lipophilic fluorescent derivatives of 3-alkoxyflavone and Nile Red dyes, by introducing three medium length alkyl chains per dye. Their chemical structure is close to that of the labrafac oil used in the droplet core, which we expected would ensure their efficient encapsulation. Indeed, these dyes were readily encapsulated into the lipophilic oil core and provided excellent stability of obtained nano-emulsion at very high dye concentrations in the oil core (up to 10 wt%). In contrast, parent dye Nile Red gave stable fluorescent nano-droplets only at concentrations around 0.1 wt%. Despite the high loading, the new dyes kept high fluorescence quantum yield, thus providing high brightness of the nano-droplets, which we explain by the dye bulky structure preventing self-quenching of fluorophores through π-π stacking.

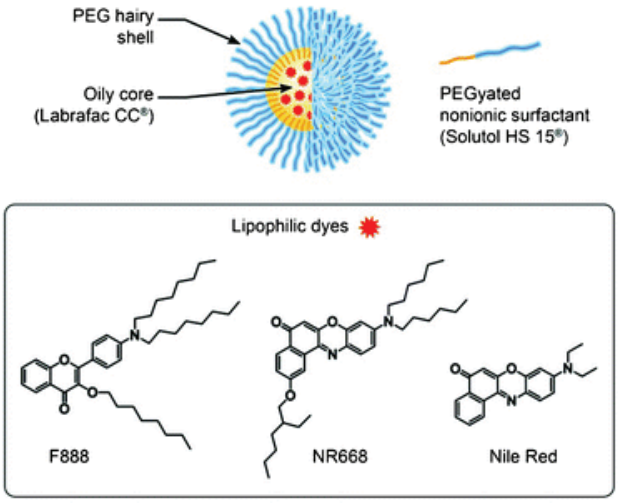

Figure 2.1.1 Schematic presentation of a nano-droplet and chemical structure of the new lipophilic dyes used for encapsulation. Nile Red was used as a reference for characterizing the release properties.

Moreover, simultaneous encapsulation of both F888 and NR668 dyes at high concentrations within nano-droplets enabled observation of Förster resonance energy transfer (FRET). As FRET depends strongly on the dye-dye distance, we used it to study the dye leakage in 10% serum, which is a model biological medium. We found that nano-droplets containing F888 and NR668 did not show significant changes in the presecence of serum for hours at 37°C. In sharp contrast, parent Nile Red, used in combination with F888, showed rapid release into serum that was observed as loss of the FRET signal. According to Fluorescence Correlation Spectroscopy (FCS), the nano-droplet brightness and concentration changed very slowly in the case of new Nile Red derivative NR668 in the serum-containing medium, which confirmed absence of fast release of this dye into the biological medium. Again, unmodified Nile Red dye, used as the reference in our experiments, leaked immediately, as the particle number increased and the particle brightness decreased immediately after addition of these nano-droplets to 10% serum. This strong difference in the leakage studies between modified and unmodified Nile Red dyes was confirmed by in vitro cellular studies as well as by in vivo angiography imaging on zebrafish model. In the latter experiments, the nano-droplets loaded with NR668 remained stable in the blood circulation, while the unmodified Nile Red leaked rapidly from the droplets distributing all over the animal body (Fig. 2.1.2). This study shows that our specific design of dye molecules works well for obtaining bright nano-droplets without dye leakage, suggesting their promising use as new efficient and stable optical contrast agents *in vitro* and *in vivo*. The results of these studies were published in the article: Andrey S. Klymchenko, Emilie Roger, Nicolas Anton, Halina Anton, Ievgen Shulov, Julien Vermot, Yves Mely and Thierry F. Vandamme. ''Highly lipophilic fluorescent dyes in nano-emulsions: towards bright non-leaking nano-droplets" RSC Advances, 2012, 2, 11876-11886.

The full description of this work can be found in this article enclosed below.

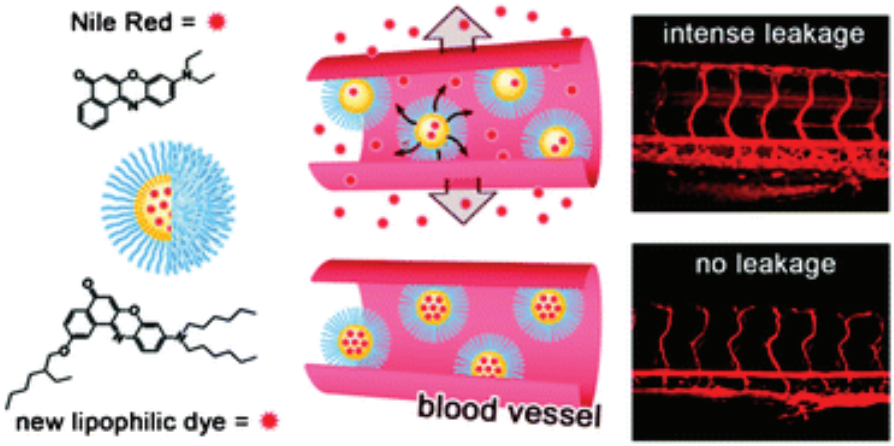

Figure 2.1.2 Schematic presentation of retention of new Nile Red derivative encapsulated into lipid nanodroplets as compared to a leakage process observed in case of use of unmodified Nile Red.

PUBLICATION №1

Highly lipophilic fluorescent dyes in nano-emulsions: towards bright non-leaking nano-droplets

View Article Online / Journal Homepage / Table of Contents for this issue
Dynamic Article Links

RSC Advances

Cite this: *RSC Advances*, 2012, **2**, 11876–11886

www.rsc.org/advances

PAPER

Highly lipophilic fluorescent dyes in nano-emulsions: towards bright non-leaking nano-droplets†

Andrey S. Klymchenko,‡*[a] Emilie Roger,‡[b] Nicolas Anton,[b] Halina Anton,[ac] Ievgen Shulov,[a] Julien Vermot,[c] Yves Mely§[a] and Thierry F. Vandamme§[b]

Received 24th July 2012, Accepted 28th September 2012
DOI: 10.1039/c2ra21544f

Dye-loaded lipid nano-droplets present an attractive alternative to inorganic nanoparticles, as they are composed of non-toxic biodegradable materials and are easy to prepare. However, to achieve high fluorescence brightness, the nano-droplets have to be heavily loaded with the dyes avoiding fluorescence self-quenching and release (leakage) of the encapsulated dyes from the nano-droplets in biological media. In the present work, we have designed highly lipophilic fluorescent derivatives of 3-alkoxyflavone (F888) and Nile Red (NR668) that can be encapsulated in the lipophilic core of stable nano-emulsion droplets at exceptionally high concentrations in the oil core, *i.e.* up to 170 mM and 17 mM, respectively, corresponding to ~830 and 80 dyes per 40 nm droplet. Despite this high loading, these dyes keep high fluorescence quantum yields and thus, provide high nano-droplet brightness, probably due to their bulky structure preventing self-quenching. Moreover, simultaneous encapsulation of both dyes at high concentrations in single nano-droplets allows the observation of FRET. FRET and fluorescence correlation spectroscopy (FCS) studies showed that NR668 release in the serum-containing medium is very slow, while the reference hydrophobic dye Nile Red leaks immediately. This drastic difference in the leakage profile between NR668 and Nile Red was confirmed by *in vitro* cellular studies as well as by *in vivo* angiography imaging on zebrafish models, where the NR668-loaded nano-droplets remained in the blood, while the parent Nile Red leaked rapidly from the droplets distributing all over the animal body. This study suggests new molecular design strategies for obtaining bright nano-droplets without dye leakage and their use as efficient and stable optical contrast agents *in vitro* and *in vivo*.

1 Introduction

Nanoscale delivery systems represent a rapidly expanding research field, which shows strong promise for the development of new clinical and diagnostic tools. These systems include polymeric and lipid-based nanocarriers such as nanoparticles, liposomes, micelles as well as inorganic nanoparticles.[1–4] According to their composition and morphology, hydrophobic or hydrophilic molecules can be encapsulated. While nanocarriers encapsulating drugs serve as therapeutic tools, those encapsulating contrast agents can function as diagnostic imaging tools.[1,3] Of particular interest are nanoparticles encapsulating fluorescent agents, which offer great potential in biomedical *in vitro* or *in vivo* imaging.[3–6] Fluorescence imaging appears as an attractive tool for preclinical studies, since it does not require specific handling and relies on relatively inexpensive hardware in comparison with magnetic resonance imaging (MRI), X-rays, positron emission tomography (PET) or single photon emission computed tomography (SPECT).[7–9]

Different types of fluorescent probes are already used in biological and medical research: organic dyes and inorganic nanoparticles. Unlike organic dyes, inorganic nanoparticles such as quantum dots (QDs)[6,10,11] and dye-doped silica nanoparticles[12–14] display exceptional brightness and photostability. However, the toxicity and fate of silica nanoparticles and QDs are hard to estimate, due to their composition of toxic elements (cadmium, selenium, indium, *etc*) and their lack of biodegradability.[15,16] On the other hand, organic dyes show good biocompatibility but their brightness is limited. Therefore, encapsulation of organic dyes in organic nanocarriers opens an attractive possibility to develop biocompatible fluorescent nanoparticles. Different structures of lipid-based nanocarriers have already been developed for therapy or imaging, such as

[a]*Laboratoire de Biophotonique et Pharmacologie, UMR 7213 CNRS, Université de Strasbourg, Faculté de Pharmacie, 74, Route du Rhin, 67401 ILLKIRCH, France. E-mail: andrey.klymchenko@unistra.fr*
[b]*Laboratoire de Conception et Application de Molecules Bioactives, UMR CNRS 7199, Université de Strasbourg, Faculté de Pharmacie, 74, Route du Rhin, 67401 ILLKIRCH, France*
[c]*IGBMC (Institut de Génétique et de Biologie Moléculaire et Cellulaire), Inserm U964, CNRS UMR7104, Université de Strasbourg, 1 rue Laurent Fries, 67404 ILLKIRCH, France*
† Electronic Supplementary Information (ESI) available. See DOI: 10.1039/c2ra21544f
‡ Equal contribution to the work.
§ Last co-authors

liposomes,[17,18] nano-emulsions,[19–22] nanocapsules,[23,24] micro-emulsions,[25] solid lipid nanoparticles (SLN)[26] and peptide–lipid nanoparticles.[27] Among them, lipid nano-emulsions, represented by nano-objects with a liquid core (nano-droplets), are of particular interest for the construction of fluorescent nano-carriers. Indeed, the oily core of nano-droplets is a perfect reservoir for the encapsulation of lipophilic dyes, where they can distribute in a rather homogeneous manner.[23,28] As a vast majority of fluorescent dyes are well-characterized in solution, their solubilization in the oil core could enable the generation of nano-carriers with desired fluorescent properties, notably absorption and emission color, brightness, fluorescence lifetime, *etc.* This is an advantage compared to dye-doped nanoparticles with a solid core, because the fluorescent properties of dyes in the solid state are much less known and difficult to predict. Moreover, the other advantage of nano-carriers with a liquid core is the simple and rapid procedure for their preparation based on spontaneous nano-emulsification,[20–22] where the size and composition of the nano-droplets can be easily controlled. Finally, nano-emulsions are usually composed of non-toxic components,[22,24] which are biodegradable and/or readily eliminated from the animal body.

The high loading of nanoparticles with dyes is an attractive approach as one can obtain particles with exceptional brightness, comparable or even superior to QDs and silica nanoparticles.[29] Though the idea seems to be simple, its realization for nano-emulsion droplets is not easy, as several key problems have to be resolved. Firstly, organic dyes at high concentrations tend to aggregate, resulting in fluorescence self-quenching.[29–31] Secondly, most fluorophores are poorly soluble in apolar oils, and thus do not allow high loading in lipid nanocarriers. Third, encapsulated dyes may leak from the nanocarriers into biological media. While dye-doped nanoparticles based on silica[14,32,33] and polymers[29] show high stability against dye leakage due to their solid matrix, the stability of nano-emulsion droplets against leakage is limited. Indeed, nano-emulsions are dynamic systems, which usually release their lipophilic content rather rapidly on a timescale ranging from minutes to hours depending on the encapsulated molecule.[34,35] Therefore, examples of fluorescent lipid nanocarriers containing liquid lipid cores are rare. In one recent work, Texier and coworkers prepared lipid nanocarriers encapsulating cyanine dyes bearing long hydrophobic chains.[23] The authors encapsulated up to 53 molecules per particle of 35 nm diameter, which corresponded to a 1 mM concentration of the dye in the oil. They showed that at this high concentration in the oily core of the nano-droplets, the dye preserved its efficient fluorescence, allowing successful cellular and *in vivo* animal imaging.[36] However, no leakage studies in biological media were performed in this work.

In the present work, we designed new fluorescent dyes based on 3-alkoxyflavone[37] and Nile Red[38,39] which can be encapsulated at exceptionally high concentrations, *i.e. ca.* 170 and 17 mM, respectively, in the oily core of the nano-droplets. In spite of this high loading, the dyes remain highly fluorescent within the nano-droplets. In addition, this high loading enabled Förster Resonance Energy Transfer (FRET) between two different dyes in the same droplet. Using FRET and fluorescence correlation spectroscopy (FCS) we showed that the leakage of our new dyes into a biological medium (serum) is very slow compared to the rapid leakage of Nile Red, which was taken as a reference of a hydrophobic dye. Finally, clearly different leakage profiles for the new and the reference dyes were observed when the nano-droplets were added to living cells in culture or injected into zebra fish. Thus, for the first time, fluorescent nano-emulsion droplets stable against the leakage of encapsulated dye into biological media are shown.

2 Materials and methods

2.1 Materials

All chemicals and solvents for synthesis were from Sigma-Aldrich. Solutol HS15® (mixture of free polyethylene glycol 660 and polyethylene glycol 660 hydroxystearate) from BASF (Ludwigshafen, Germany) was a kind gift from Laserson (Etampes, France), Labrafac CC® (medium chain triglycerides) was obtained from Gattefossé (Saint-Priest, France). Ultrapure® water was obtained using a MilliQ® filtration system (Millipore, Saint-Quentin-en-Yvelines, France). Culture reagents were obtained from Sigma (St. Louis, USA), Lonza (Verviers, Belgium) and Gibco-Invitrogen (Grand Island, USA).

4′-Dioctylamino-3-octyloxyflavone (F888). 100 mg (0.21 mmol) of 4′-(*N*,*N*-dioctylamino)-3-hydroxyflavone, which was prepared as described elsewhere,[40] was dissolved in 10 ml of dry methanol. Then, 191 µl (1.05 mmol) of 1-iodooctane and 60 mg (0.42 mmol) of potassium carbonate were added. The resulting mixture was refluxed overnight under an inert atmosphere. Solvent was removed under reduced pressure. The obtained residue was purified by TLC plate chromatography on silica gel (EtOAc : heptane, 1 : 9 as the eluent) to give the product (100 mg, 81%) as a yellow oil. ^{1}H NMR ($CDCl_3$, 400 MHz): δ 8.23 (dd, J1 = 8.0 Hz, J2 = 1.7 Hz, 1H), 8.08 (d, J = 9.3 Hz, 2H), 7.61 (ddd, J1 = 8.8 Hz, J2 = 7.0 Hz, J3 = 1.7 Hz, 1H), 7.47 (dd, J1 = 8.8 Hz, J2 = 1.1 Hz, 1H), 7.34 (ddd, J1 = 8.0 Hz, J2 = 7.0 Hz, J3 = 1.1 Hz, 1H), 6.68 (d, J = 9.3 Hz, 2H), 4.03 (t, J = 6.8 Hz, 2H), 3.33 (m, 4H), 1.77 (m, 2H), 1.62 (m, 4H), 1.28 (m, 30H), 0.87 (m, 9H). HRMS: (*m*/*z*): ESI, calcd for $C_{39}H_{60}NO_3^+$ 590.4573; found $[M+1]^+$ 590.4575.

9-Dihexylamino-2-hydroxy-benzo[a]phenoxazin-5-one (NR66). NR66 was synthesized using the same protocol as for 9-diethylamino-2-hydroxy-benzo[a]phenoxazin-5-one[41] starting from 3-dihexylaminophenol. Dark green solid, yield 50%. ^{1}H NMR (300 MHz, DMSO-d6): δ 10.38 (s, 1H), 7.95 (d, 1H), 7.86 (d, 1H), 7.55 (d, 1H), 7.07 (dd, 1H), 6.74 (dd, 1H), 6.56 (d, 1H), 6.13 (s, 1H), 3.40 (t, 4H), 1.54 (m, 4H), 1.40–1.20 (m, 12H), 0.86 (t, 6H). LCMS (*m*/*z*): MM-ES+APCI, found $[M+1]^+$ 447.2 (calcd for $C_{28}H_{35}N_2O_3^+$ 447.2).

9-Dihexylamino-2-(2-ethyl-hexyloxy)-benzo[a]phenoxazin-5-one (NR668). 100 mg of NR66, 65 mg of 2-ethylhexyl bromide and 62 mg of potassium carbonate were mixed in 10 ml of acetonitrile. The mixture was refluxed under stirring for 24 h. Then, the solvent was removed in vacuum and the product was purified on a silica gel column (EtOAc : heptane, 2 : 8 as the eluent). ^{1}H NMR ($CDCl_3$, 400 MHz): δ 8.14 (d, J = 8.8 Hz, 1H), 7.97 (d, J = 2.5 Hz, 1H), 7.52 (d, J = 9.0 Hz, 1H), 7.09 (dd, J = 8.8 Hz, J2 = 2.5 Hz, 1H), 6.55 (dd, J = 9.0 Hz, J2 = 2.5 Hz, 1H),

6.33 (d, J = 2.5 Hz, 1H), 6.25 (s, 1H), 3.98 (dd, J = 5.6 Hz, J2 = 1.4 Hz, 2H), 3.29 (m, 4H), 1.70–1.75 (m, 1H), 1.35–1.53 (m, 6H), 1.28 (m, 18H), 0.81–0.95 (m, 12H). HRMS: (m/z): ESI, calcd for $C_{36}H_{51}N_2O_3^+$ 559.3901; found $[M+1]^+$ 559.3903.

2.2 Formulation and characterization of nano-emulsions

Nano-emulsions were prepared by spontaneous nano-emulsification. Briefly, the fluorescent dyes were solubilised in Labrafac® CC. Then, Solutol® HS 15 was added and the mixture was homogenized under magnetic stirring at 90 °C. Nano-emulsions were formed by adding ultrapure water. Two sizes of nano-droplets were prepared by varying the proportions between the different components (Table 1).

The size distribution of the nano-emulsions was determined by dynamic light scattering on a Zetasizer® Nano series DTS 1060 (Malvern Instruments S.A., Worcestershire, UK) and by FCS (home-built setup, see below).

2.3 Cell culture preparations

HeLa cells were cultured in Dulbecco's modified Eagle medium (D-MEM, high glucose, Gibco-invitrogen) supplemented with 10% (v/v) fetal bovine serum (FBS, Lonza), 1% antibiotic solution (penicillin-streptomycin, Gibco-invitrogen) in a humidified incubator with 5% CO_2/95% air atmosphere at 37 °C. Cells plated on a 75 cm^2 flask at a density of 10^6 cells/flask were harvested at 80% confluence with trypsin–EDTA (Sigma) and seeded onto a chambered coverglass (IBiDi) at a density of 0.1 × 10^6 cells/IBiDi.

After 24 h, cells in the IBiDi dishes were washed with PBS (phosphate buffer saline) (Lonza). Then, a solution of dye-loaded nano-droplets diluted at 1 : 1000 in Opti-MEM was added. In control experiments, cells were incubated in 0.33 μM Nile Red solution in Opti-MEM, which was obtained by addition of an aliquot of Nile Red in DMSO to Opti-MEM (final DMSO concentration was ~0.1%). Microscopy images were taken after 15 min or 1 h of incubation at 37 °C with the nano-droplets and 15 min in the case of Nile Red alone.

2.4 Fluorescence spectroscopy and microscopy

Absorption and fluorescence spectra were recorded on a Cary 4 spectrophotometer (Varian) and a Fluorolog (Jobin Yvon, Horiba) spectrofluorometer, respectively. Fluorescence emission spectra were recorded at room temperature with 390 and 520 nm excitation wavelengths for F888- and NR668-loaded nano-droplets, respectively. All fluorescence measurements were done using solutions with absorbance ⩽ 0.1. Fluorescence quantum yields (QY) of F888- and NR668-loaded nano-droplets were measured using, respectively, 4′-dimethylamino-3-hydroxyflavone in ethanol (QY = 29%),[42] and Nile Red in ethanol (QY = 52%),[43] as reference. Fluorescence images were taken on a Leica DMIRE2 inverted microscope equipped with a Leica DC350FX CCD camera and a thermostated chamber (Life Imaging Services, Basel Switzerland) for maintaining the temperature at 37 °C. A 63× HCX PLAPO (1.32 NA) objective and a Cy3 filter cube (excitation 535/50 nm, emission 610/75 nm) were used. The size of the images was systematically 140 × 105 μm.

Table 1 Composition of the two prepared batches of nano-emulsions

	Formulations	
Components	A (d ~ 20 nm)	B (d ~ 40 nm)
Labrafac CC®	0.04 g	0.07 g
Solutol HS 15®	0.16 g	0.13 g
MilliQ® water	460 μl	460 μl

2.5 Fluorescence correlation spectroscopy (FCS) and data analysis

FCS measurements were performed on a two-photon platform including an Olympus IX70 inverted microscope, as described previously.[44] Two-photon excitation at 780 nm (5 mW laser output power) was provided by a mode-locked Tsunami Ti : sapphire laser pumped by a Millenia V solid state laser (Spectra Physics). The measurements were carried out in an eight-well Lab-Tek II coverglass system, using a 300 μL volume per well. The focal spot was set about 20 μm above the coverslip. The normalized autocorrelation function, G(τ) was calculated online by an ALV-5000E correlator (ALV, Germany) from the fluorescence fluctuations, $\delta F(t)$, by $G(\tau) = \langle \delta F(t)\delta F(t+\tau)\rangle / \langle F(t)\rangle^2$ where $\langle F(t)\rangle$ is the mean fluorescence signal, and τ is the lag time. Assuming that lipid nano-droplets diffuse freely in a Gaussian excitation volume, the correlation function, G(τ), calculated from the fluorescence fluctuations was fitted according to Thompson:[45]

$$G(\tau) = \frac{1}{N}\left(1+\frac{\tau}{\tau_d}\right)^{-1}\left(1+\frac{1}{S^2}\frac{\tau}{\tau_d}\right)^{-1/2}$$

where τ_d is the diffusion time, N is the mean number of fluorescent species within the two-photon excitation volume, and S is the ratio between the axial and lateral radii of the excitation volume. The excitation volume is about 0.34 fL and S is about 3 to 4. Typical data recording times were 10 min, using dye-loaded lipid nano-droplets diluted 1 : 10 000 from the originally prepared nano-emulsion. Using 6-carboxytetramethylrhodamine (TMR from Sigma-Aldrich) in water as a reference (D_{TMR} = 421 $\mu m^2\ s^{-1}$),[46] the diffusion coefficient, D_{exp}, of the lipid nano-droplets was calculated by: $D_{exp} = D_{TMR} \times \tau_{d(TMR)}/\tau_{d(droplets)}$ where $\tau_{d(TMR)}$ and $\tau_{d(droplets)}$ are the measured correlation times for TMR and lipid nano-droplets, respectively. The hydrodynamic diameter, d, of the nano-droplets was calculated with the Stokes–Einstein equation: $d = 2k_bT/6\pi\eta D_{exp}$, where k_b is the Boltzmann constant, T is the absolute temperature (293 K) and η is the viscosity of the solution (1 cP). The nano-droplet concentration was calculated from the droplet number by: $C_{droplets} = N_{droplets}/N_{TMR} \times C_{TMR}$, using a TMR concentration of 50 nM.

2.6 Dye release studies

The release of the dye was estimated using Förster resonance energy transfer (FRET) between two encapsulated dyes and FCS with one encapsulated dye. The release of the dyes from the nano-droplets was performed in water, cell culture medium (Opti-MEM, Gibco-invitrogen) in the absence or presence of 10% of fetal bovine serum (FBS). In both studies the nano-droplets were diluted 10 000-times from the original formulation into the medium of interest. In the FRET studies nano-droplets encapsulating 0.5% of F888 (with respect to Labrafac CC®) as energy donor and 0.5 wt.% of Nile Red or NR668 as energy acceptor were used. The first fluorescence spectra were measured

after 3 min incubation at RT. Then, samples were incubated for 1 h, 3 h and 6 h at 37 °C. The donor in the nano-droplets was excited at 390 nm. FRET was quantified as the fluorescence intensity ratio between the maximum of the donor (450 nm) and acceptor (590 nm). The fluorescence spectra were systematically corrected from the spectrum in the blank media. In the other study the release was evaluated by FCS as the brightness (the photon count rate per droplet) and apparent concentration of the emissive species. If the dye is released from the nano-droplets the brightness decreases, while the apparent concentration of the emissive species increases. The nano-emulsions prepared in water were measured 5 min after dilution in the corresponding media at room temperature or after incubation in these media at 37 °C for 1 h or 6 h.

2.7 *In vivo* imaging on zebrafish

Zebrafish were kept at 28 °C and bred under standard conditions. The transgenic line, *Tg(fli1:eGFP)*^{y1},[47] expressing eGFP specifically in the endothelial cells, was used in order to visualize the vasculature. For the angiography, the embryos, 3 days after fertilization, were anaesthetized in egg water containing 0.04% tricaine and 0.05% phenyl thiourea (Sigma-Aldrich) and immobilized in 0.8% low melting point agarose (Sigma). The injections were performed using a Nanoject microinjector (Drummond Scientific, Broomal, PA, USA). The glass capillary was filled with NR668-loaded nano-emulsions (1 wt.% in oil) of the nano-droplets solution in 5 mM HEPES and 2.3 nL were injected in the sinus venosus of the embryos. The nano-emulsion was immediately distributed in all the vasculature. The injected embryos were placed on the microscope stage and imaged within 5 min after injection. Intravital confocal microscopy was performed on a Leica SP5 fixed stage direct microscope with a 25× (NA 0.95) and 10× (NA 0.3) water immersion objectives. 488 nm argon laser line was used to excite both eGFP and the Nile Red dyes, and their emission was detected by two separate PMTs in the spectral range 500–530 nm and 620–650 nm, respectively. At these conditions, no cross-talk between the channels was observed. Confocal z-stacks and time lapses were recorded and treated by the ImageJ software (rsbweb.nih.gov/ij/). The embryos were imaged during one hour post injection and no toxicity due to the injection or to the illumination was observed. All experiments performed with zebrafish complied with the European directive 86/609/CEE and IGBMC guidelines validated by the regional committee of ethics.

3 Results and discussion

3.1 Design of fluorescent dyes

In order to achieve high dye loading and its low leakage from the nano-droplets, the fluorescent dyes have to be designed with highly lipophilic functions. Therefore, the dye should be a neutral apolar molecule bearing as many apolar hydrophobic groups as possible. Using bulky hydrophobic groups should further improve the dye solubility and prevent dye aggregation at high concentrations. Two dyes, F888 and NR668, were synthesized (Fig. 1), both featuring three alkyl chains of 6–8 carbon atoms. This medium chain length is a compromise between very long alkyl chains presenting poor solubility and very short ones featuring insufficient hydrophobicity. Moreover, the chain length of the dyes matches perfectly with that of fatty acid residues of Labrafac CC® (caprylic/capric triglyceride), which is expected to dissolve the dyes in the nano-droplet core. F888 is a 3-hydroxyflavone derivative with two octyl chains at the 4′-nitrogen and one octyl chain at the 3-OH group. This fluorophore was selected because it is neutral and apolar, showing absorption and emission in the blue region of the visible spectrum.[37] Moreover, F888 should have no tendency to aggregate as the aromatic moiety of this dye is not perfectly flat due to the steric hindrance between the 2-aryl and 3-alkoxy group. NR668 is a Nile Red[38,39] derivative also bearing three alkyl chains. As this dye presents a perfectly flat aromatic structure, one bulky alkyl group was used in order to minimize its π-stacking aggregation.

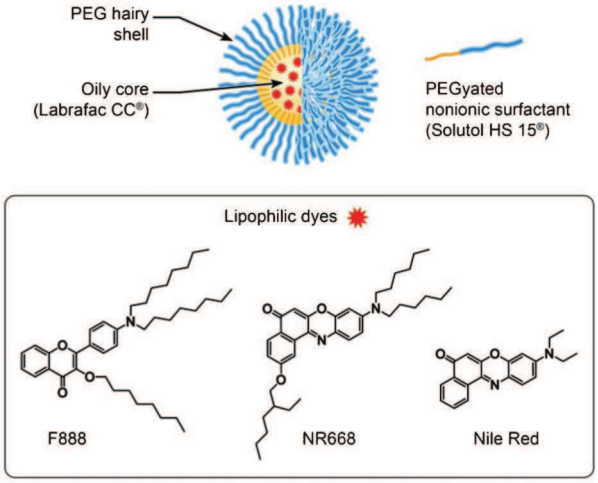

Fig. 1 Schematic presentation of a nano-droplet and chemical structure of the new lipophilic dyes used for encapsulation. Nile Red was used as a reference for characterizing the release properties.

3.2 Nano-droplet preparation

In the first step, solutions of the new dyes in Labrafac CC® were prepared. F888 is a viscous oil, and is readily miscible in Labrafac CC® allowing the preparation of a 10 wt.% (170 mM) solution (higher concentrations were not tested). In the case of NR668, which is a solid, the solubility was lower. Several hours of vortex at 80 °C were needed to obtain a clear solution of 5 wt.% (90 mM) solution in Labrafac CC®, which did not show any precipitation after cooling. Nevertheless, NR668 was much more soluble than the parent Nile Red. Indeed, to prepare 0.1 and 0.5 wt.% of Nile Red in Labrafac CC®, a co-solvent (acetone) has to be used and then evaporated just before the preparation of the nano-emulsion. The obtained solutions in Labrafac CC® were used for preparing the dye-loaded nano-emulsion droplets. Different methods are described in the literature for the preparation of the nano-emulsions, ranging from high energy methods using specific devices[24] (sonifiers, high pressure homogenizers), to low-energy nano-emulsification[24,48,49] using the self-assembling properties of surfactants. Herein, we choose to follow one of the simplest methods, spontaneous nano-emulsification,[48] for which the nano-emulsion is generated as a result of mixing of two phases: (i) oil

solubilizing lipophilic dye and surfactants (beforehand homogenized and maintained at 90 °C), and (ii) pure MilliQ® water (at room temperature). After their mixing, stable monodisperse nano-emulsions are immediately formed. This protocol was already described for Labrafac CC® (as an oil core) and Solutol HS15® (as a surfactant).[48] Moreover, this process can be easily controlled since notably, the nano-droplets size is directly linked to the surfactant-to-oil ratio.[48,50] Generally recognized as safe (GRAS) ingredients, such as Labrafac CC® (medium chain triglycerides) and Solutol HS15® (*i.e.* PEG-660-hydroxystearate), were selected for the formulation of the nano-emulsions of this study. These GRAS ingredients are compatible with parenteral administration (*i.e.* injectable) in humans.

Dynamic light scattering measurements for two representative formulations A and B (Table 1) provided narrow size distributions centered around 23 nm and 43 nm diameter, respectively (henceforth called 20- and 40 nm nano-droplets).

Importantly, the sizes of the nano-droplets encapsulating 10 wt.% of F888 or 5 wt.% of NR668 (concentrations in the oil) were identical to the sizes of the blank ones (Table 2). Moreover, the presence of the dyes did also not affect the polydispersity and surface charge of the droplets. It follows that the high dye loading does not influence the physicochemical properties of the oil and thus, the formulation process. Importantly, the nano-droplets remained unchanged after 3 months of storage at 4 °C in the dark, in agreement with the high stability of nano-emulsions.[20,21] In contrast, droplets containing 0.5 wt.% of Nile Red showed precipitation of the dye after 1 week of storage at 4 °C. To summarize, we obtained stable nano-emulsions encapsulating F888 and NR668 at exceptionally high concentrations, higher by a few orders of magnitude compared to those reported for cyanine dyes.[23]

3.3 Fluorescence properties

The absorption and fluorescence properties of the obtained droplets were then studied and compared to those for diluted solutions of the dyes (absorbance around 0.1) in neat organic solvents and Labrafac CC®. The absorption spectra of both F888 and NR668 in the nano-droplets were similar to those in neat Labrafac CC® and organic solvents (Table 3). This indicates that both F888 and NR668 do not form specific aggregates in the Labrafac CC® core of the nano-emulsion droplets, which would significantly affect their spectra. The nano-droplets are highly fluorescent, showing a single emission band. For F888 at 1 wt.% and 10 wt.% contents, the emission maximum is red-shifted by 8 and 17 nm with respect to that in neat Labrafac CC® (Table 3). As 3-alkoxychromones show fluorescence solvatochromism (Table 2)[37], these red shifts could be attributed to a somewhat increased environment polarity of the dye in the oil core of the nano-droplet compared to the neat oil. However, these shifts are relatively small compared to the 56 nm red-shift observed on changing the solvent from apolar dioxane to polar ethanol (Fig. 2). Therefore, the dye appears well encapsulated in the Labrafac CC® containing core and does not experience the polar environment of water or Solutol HS15®. The larger red-shift observed for higher loading (10 wt.%) could be related to some fraction of the dyes being located at the more polar regions of the droplet, probably within the water–oil interface occupied by Solutol HS 15®. On the other hand, the fluorescence quantum yield of F888 loaded in the nano-emulsion droplets remains very high for any droplet size, close to the one in neat organic solvents and Labrafac CC® (Table 3). A decrease in the quantum yields is observed in the following sequence:

Table 2 Physicochemical characteristics of the lipid nano-emulsions, encapsulating different dyes[a]

Formulation	Dye	[Dye] (%)	d_h, nm	PDI	ξ, mV
A	—	0	22	0.21	−4.8
B	—	0	45	0.13	−8.3
A	F888	10	24	0.08	−5.2
B	F888	10	40	0.07	−4.5
B	F888	1	46	0.11	−13.5
B	NR668	5	36	0.03	−6.3
B	NR668	1	43	0.10	−12.5
B	Nile Red	0.5	45	0.10	−10.1
B	Nile Red	0.1	48	0.17	−7.2

[a] [Dye] is the initial dye concentration in Labrafac CC® used for the nano-droplet preparation. d_h is the hydrodynamic diameter, PDI is the polydispersity index, and ξ is the zeta potential. The errors for d_h and ξ values were ±2 nm and ±10%, respectively.

Table 3 The absorption and fluorescence properties of the dyes in organic solvents and in lipid nano-emulsions[a]

Dye	Samples	Abs max, nm	Fluo max, nm	QY (%)
F888	20 nm-10%	390	466	78
	40 nm-10%	390	464	72
	40 nm-1%	388	455	87
	Labrafac®	387	447	91
	Dioxane	385	454	65
	Ethanol	400	510	48
NR668	40 nm-1%	526	592	60
	40 nm-5%	523	610	13
	Labrafac®	526	580	61
	Dioxane	518	575	84
	Ethanol	550	631	42
NR	40 nm-0.1%	530	599	73
	Labrafac®	526	581	78
	Dioxane	520	575	91
	Ethanol	550	626	52

[a] Abs max (nm) and Fluo max (nm) are the absorption and fluorescence maxima; QY (%) is fluorescence quantum yield.

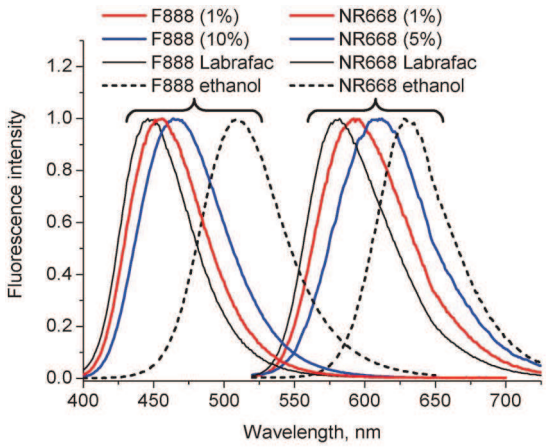

Fig. 2 Fluorescence spectra of F888 and NR668 in nano-emulsions, neat Labrafac CC® oil and ethanol.

Labrafac CC® > 1 wt.% droplets > 10 wt.% droplets, but it is relatively small, indicating that the concentration-dependent self-quenching of F888 is almost negligible even at 10 wt.% concentration. This indicates that the 40 nm droplets containing 10 wt.% of F888 in their core contain a large quantity of highly fluorescent dye molecules, which should make the nano-droplet extremely bright.

In the case of NR668, being encapsulated at 1 wt.%, its maximum emission wavelength and its quantum yield are close to those in neat Labrafac CC® (Table 3). In contrast, at 5 wt.% in the nano-droplets, the emission maximum is 30 nm red-shifted with respect to Labrafac CC®, which is significant compared to the 50 nm polarity effect (dioxane-ethanol) observed for this dye (Fig. 2). This red shift suggests that at this high loading some part of the dye is probably exposed to the more polar environment at the interface occupied by Solutol HS15®. However, we also cannot exclude that at high concentrations, NR668 molecules form aggregates with red-shifted emission. The quantum yield of 5 wt.% NR668 nano-droplets is much lower than the one in Labrafac CC® (Table 3), so that at this high loading, NR668 is likely self-quenched.

As the nano-droplets loaded with the parent Nile Red at 0.5 wt.% were not stable enough, only 0.1 wt.% Nile Red-loaded nano-emulsions were characterized. While their fluorescence quantum yield was high, their emission spectrum was broader and considerably red-shifted with respect to that in Labrafac CC® (Table 2, Figure 1S† in the ESI), indicating that this fluorophore is probably present both in the core and at the water–oil interface of the droplets. It should be noted that the fraction of Nile Red in water for the present experimental conditions was negligible, because the absorption spectrum of the Nile Red-loaded nano-droplets is close to that of Nile Red in Labrafac CC® without visible contribution of the red-shifted band of this dye in water (Figure S2† in the ESI).

Then, we further characterized our best nano-emulsion–dye formulations by fluorescence correlation spectroscopy (FCS). This technique measures the diffusion of the fluorescent species through the two-photon excitation volume, providing information about their number, size and brightness.[44–46] The auto-correlation curves of the dye-loaded nano-emulsions (Fig. 3) could be well-fitted with only one correlation time, giving a droplet size (Table 4) in excellent agreement with that measured by DLS (Table 2). Moreover, FCS further indicated that no other fluorescent species, such as large aggregates or small micelles, are present in solution. FCS also allows the estimation of the photon count rate per droplet (*i.e.* brightness), which we calculated with respect to that of 6-carboxytetramethylrhodamine (TMR) in water, used as a reference. The 20 and 40 nm droplets prepared with 10 wt.% of F888 were 22 and 205 times as bright as TMR, while 40 nm droplets with 1 wt.% of NR668 were 21 times as bright (Fig. 3). Thus, the obtained lipid nano-droplets showed a remarkable brightness. Moreover, FCS allowed us to recalculate the concentration of the droplets in the 1 : 10 000 diluted nano-emulsion (from original formulation), giving 9.8, 1.8 and 2.2 nM concentrations for 20 nm F888, 40 nm F888 and 40 nm NR668 droplets, respectively (Table 4). Meantime, based on the absorption data, we can estimate that the dye concentration in the 1 : 10 000 diluted nano-emulsion is 1130, 1500 and 180 nM, respectively. Thus, on average 115, 830 and 80 molecules are present in 20 nm F888, 40 nm F888 and 40 nm NR668 droplets, respectively. Thus, our simple protocol using new hydrophobic dyes provides highly fluorescent nano-droplets encapsulating a large number of hydrophobic dyes. Due to this high loading, these nano-droplets are much brighter than TMR in water.

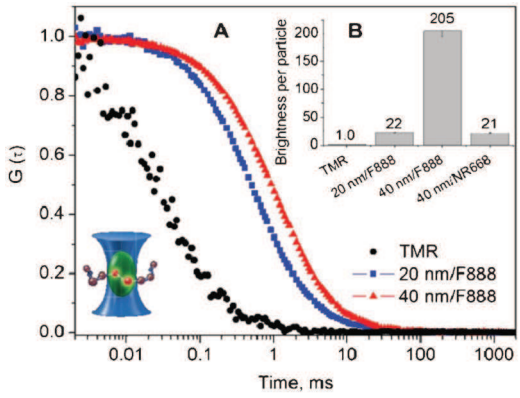

Fig. 3 Typical examples of FCS correlation curves (A) and obtained nano-droplet brightness (B) for dye-loaded nano-emulsions compared to TMR, used as reference. Inset: principle of FCS measurements.

3.4 Observation of FRET inside the nano-droplets

FRET is a powerful tool for the characterization of molecular interactions and monitoring the integrity of the nano-objects. Since efficient FRET requires short distances between the donor and acceptor fluorophores (2–10 nm), one should achieve concentrations in the mM range to realize FRET inside the nano-droplets. As we succeeded to load the nano-droplets with high concentrations of the dyes, we tested the possibility to obtain FRET inside them. The F888 and NR668 dyes are a perfect FRET couple, because the emission maximum of F888 in the nano-droplets is very close to the absorption maximum of NR668 (Table 3). The calculated Förster distance R_0 for the F888–NR668 couple in Labrafac CC® is 7.0 nm. In order to avoid the use of a complex model based on FRET with multiple acceptors, we estimated the minimal concentration needed to achieve a distance between the donor and acceptor corresponding to $2 \times R_0 = 14$ nm. Assuming a simple geometrical model, where the dye molecules are organized in solution as cubic lattices separated by 14 nm distance, the average free volume per dye molecule in solution is $(14\ \text{nm})^3 = 2744\ \text{nm}^3$, which corresponds to a total concentration of both donor and acceptor of 0.60 mM. Thus, in the case of a 1 : 1 molar ratio donor and acceptor, the minimal concentration of each partner, at which the distance between donor and acceptor is 14 nm, should be around 0.30 mM. To verify experimentally the existence of FRET at different concentrations of dyes, we prepared nano-droplets containing both dyes at equimolar ratio, ranging from 0.02% (0.36 mM) up to 0.5% (9 mM), where NR668 still keeps invariant fluorescence properties. The fluorescence spectra were obtained by exciting the donor at 390 nm. Nano-droplets containing 0.02 wt.% of both dyes showed almost exclusive emission of the F888 dye (Fig. 4), indicating that, in line with our estimations, FRET is almost undetectable in these conditions. This result also shows that the direct excitation of the acceptor at

Table 4 FCS data for dye-loaded nano-emulsions[a]

Formulation	Dye	[Dye] (%)	τ, ms	d_h, nm	Brightness	[Droplets], nM	Dyes/droplet
A	F888	10	0.808	21	22	9.8	115
B	F888	10	1.54	42	205	1.8	830
B	NR668	1	1.51	43	21	2.2	80
B	Nile Red	0.1	1.35	39	2.0	2.25	8

[a] τ is the correlation time (for TMR, it was 0.035 ms); brightness is the ratio of photon count rate per droplet with respect to TMR; [Droplets] is the droplet concentration, estimated from FCS data (see Materials and Methods).

390 nm is very low. In contrast, for dye concentrations above 0.1 wt.% (1.8 mM), the relative intensity of the long-wavelength band (acceptor) progressively increases (Fig. 4), while the donor fluorescence drops, evidencing an increase in the efficiency of FRET from F888 to NR668. At 0.2 wt.% (3.6 mM) and 0.5 wt.% (9 mM) of the dyes, FRET efficiencies estimated from the changes in the donor intensity were approx. 45 ± 10% and 65 ± 10%, respectively. When nano-droplets were prepared from 0.5 wt.% of F888 and Nile Red, a similar FRET efficiency was achieved (approx. 75 ± 10%). To the best of our knowledge, this is one of the first reports where FRET inside lipid nano-droplets was performed. Only one recent report showed FRET in the liquid core of lipid nano-carriers, though somewhat lower concentrations (<4 mM) of the donor and acceptor partners were used.[51] Observation of the highly efficient FRET inside the nano-droplet core became possible in the present work because of the exceptionally high loading of the droplets with both donor and acceptor dyes.

3.5 Studies of dye release in biological media

Though FRET is a well-established technique to monitor proximity between the fluorophores in biomolecules, it has never been applied so far for monitoring the dye leakage from nano-droplets. Using our FRET nano-emulsions, we could easily test through the changes in FRET efficiency whether the dyes remain inside the droplets or leak to the bulk solution. Serum, which is present in cell culture media, binds readily hydrophobic molecules[52–55] and could therefore extract hydrophobic dyes from the droplets and thus affect the FRET signal inside the nano-droplets. The FRET nano-droplets containing F888 as the FRET donor and NR668 (0.5 wt.%) or Nile Red (0.5 wt.%) as the acceptor were incubated in different media: water, Opti-MEM (a common cellular medium used for fluorescence imaging), and Opti-MEM with 10 wt.% serum (Opti-MEM+FBS). Almost no changes in the fluorescence spectra were observed when the F888–NR668 nano-droplets were incubated with Opti-MEM or Opti-MEM+FBS for 3 min at room temperature (Fig. 5B and C). In sharp contrast, the F888–Nile Red-loaded nano-droplets incubated in the same conditions showed an increase of the donor fluorescence intensity along with a decrease of the fluorescence intensity of the acceptor (Fig. 5A and C). This result indicates a strong decrease in the

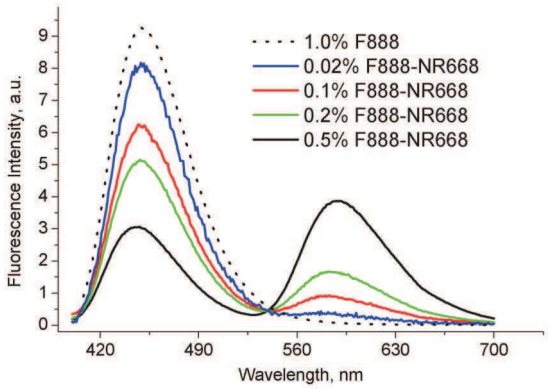

Fig. 4 Observation of FRET inside lipid nano-droplets at different concentrations of donor (F888) and acceptor (NR668), encapsulated at a 1 : 1 molar ratio. The dotted line corresponds to nano-droplets containing only the donor. The fluorescence spectra were recorded at 390 nm excitation wavelength. To compare the spectra, their absolute fluorescence intensity was divided by the F888 concentration.

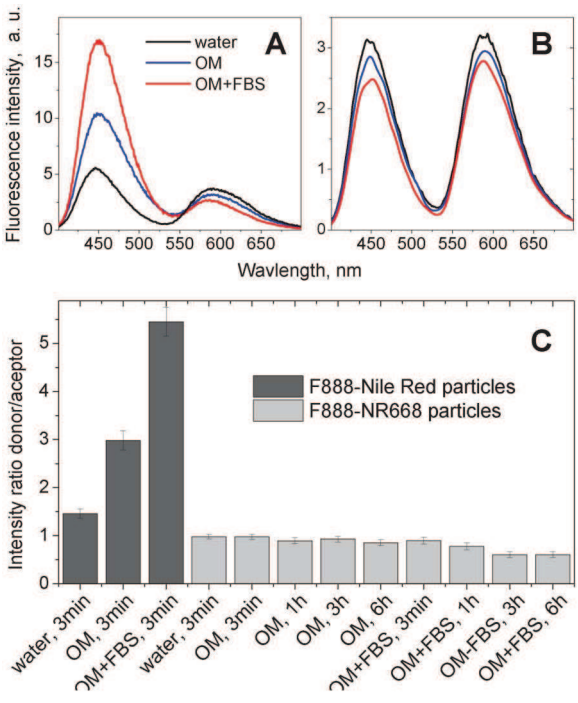

Fig. 5 Investigation by FRET of the dye release from the lipid nano-droplets in different media: water, Opti-MEM (OM) and Opti-MEM with 10 vol.% FBS (OM+FBS). Droplets encapsulating 0.5% of F888 (with respect to Labrafac CC®) as energy donor and 0.5 wt.% of Nile Red (A) or NR668 (B) as energy acceptor were used. The nano-droplets were diluted 10 000-times from the original formulation into the medium of interest. The first fluorescence spectra were measured after 3 min incubation at RT (A and B). Then, samples were incubated for 1 h, 3 h and 6 h at 37 °C. FRET was quantified as the fluorescence intensity ratio between the maximum of the donor (450 nm) and acceptor (590 nm) (C). The donor in the nano-droplets was excited at 390 nm.

FRET efficiency and thus, a rapid release of Nile Red from the lipid nano-droplets in the presence of biological media. The effect is stronger in the case of Opti-MEM+FBS, emphasizing the contribution of the serum in the dye release. Compared to Nile Red, the negligible release observed for NR668 is likely a consequence of its much higher lipophilicity. To further characterize the NR668-containing nano-emulsions, we incubated them in the same media for 1, 3, and 6 h at 37 °C. In Opti-MEM, no change in the intensity ratio of the donor–acceptor was observed, while in Opti-MEM+FBS a small decrease in this ratio was detected (Fig. 5C). Thus, the nano-emulsion appears highly stable against the dye release in Opti-MEM even for long incubation times at 37 °C. In the presence of Opti-MEM+FBS medium, the observed small changes cannot be related to dye release, which would result in the opposite effect (*i.e.* increase in the donor–acceptor intensity ratio), and probably result from other processes such as the adsorption of serum components on the nano-droplets.

Since dye release in the presence of serum should affect the nano-droplet brightness and the quantity of emissive species in solution, FCS appears as an appropriate complementary method for monitoring the dye release. In these experiments, 40 nm droplets with 1 wt.% NR668 were compared with droplets of the same size containing 0.1 wt.% of the parent Nile Red. All the FCS data obtained in these experiments fitted well to a single-component model. Within the course of incubation (5 min, 1 h and 6 h), the Nile Red-loaded nano-droplets in Opti-MEM without serum showed a progressive drop in their fluorescence brightness, accompanied by a strong increase in the apparent concentration of emissive species (Fig. 6). Moreover, the brightness of the nano-droplets was observed to drop >10-fold immediately after diluting the nano-emulsion in water or Opti-MEM containing 10 wt.% of serum, while no changes were observed for longer incubation times. This drop is accompanied by a strong (>25-fold) increase in the apparent concentration of emissive species, again with no changes for longer incubation times (Fig. 6). The observed changes can be clearly connected with the release of Nile Red from the lipid nano-droplets. Indeed, the leaked dye likely binds the components of the medium and produces the observed increase in the apparent concentration of emissive species, while decreasing the brightness of the lipid nano-droplets. The dye release is particularly fast in the presence of serum, which contains proteins that can strongly bind hydrophobic dyes (serum albumins in particular).[52–55] As the leaked dye probably binds to the proteins and/or lipoproteins of the serum, the size of the new emissive species should not drastically differ from the nano-droplet size, thus explaining the good fit of the FCS curves to a one-component model. Nevertheless, the goodness of the fit to the one-component model decreased significantly for Nile Red nano-droplets in the presence of serum (as can be seen from the larger experimental errors in Fig. 6), indicating an increased heterogeneity of the emissive species, as a consequence of the Nile Red leakage from the nano-droplets. Remarkably, nano-droplets encapsulating 1 wt.% of NR668 did not show any changes in Opti-MEM medium even after 6 h of incubation. In the presence of serum, a relatively slow decrease in the droplet brightness was observed, with about a 2-fold change after incubation for 6 h at 37 °C, which is accompanied by an almost negligible change in the apparent concentration of the emissive species (Fig. 6). Thus, the FCS results confirmed that the nano-droplets encapsulating NR668 are relatively stable in biological media, while Nile Red shows a strong tendency to leak from the droplets in Opti-MEM and particularly in Opti-MEM with serum. These conclusions are fully in line with our FRET results, suggesting that the new Nile Red derivative NR668 bearing three long hydrophobic chains enables both a strong improvement in the dye encapsulation level and an increased nano-droplet stability against dye release in biological media as compared to the parent Nile Red. These three long chains increase the dye hydrophobicity strongly (estimated logP = 9.22 and 2.98 for NR668 and Nile Red, respectively), which decreases its escape drastically from the apolar core of the nano-droplets. The observation of the fast release of Nile Red in our studies corroborates with previous studies showing that other lipophilic molecules can leak from nano-emulsions on the time scale of minutes.[34,35]

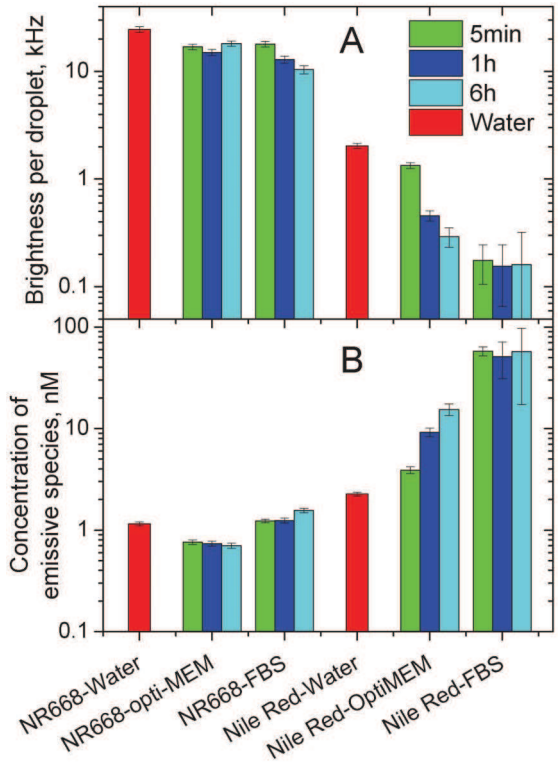

Fig. 6 Dye release studies by FCS. (A) Brightness and apparent concentration (B) of emissive species in water and in biological media determined from FCS data. Brightness is the photon count rate per droplet. The nano-emulsions prepared in water were measured 5 min after dilution in the indicated media at room temperature or after incubation in these media at 37 °C for 1 h or 6 h. Data in water, measured 5 min after dilution at room temperature, are presented for comparison.

3.6 Interaction with living cells

To further evaluate our highly fluorescent nano-droplets, we addressed their possible binding and internalization into living cells. Nano-droplets loaded with NR668 (1 wt.%) or Nile Red (0.1 wt.%) were added to living cells (in Opti-MEM without serum) and fluorescence images were recorded after different incubation times (Fig. 7A to D). It can be seen that the cells

remained non-fluorescent after incubation with NR668 nano-droplets (Fig. 7C and D). This observation is similar to that reported before for cyanine-dye loaded nanoparticles,[36] and is probably connected with the PEGylated surface of the nano-droplets that likely inhibits the cellular uptake of the nanocarriers.[56,57] NR668 alone was not tested with cells as it is absolutely insoluble in water. In contrast, cells incubated with Nile Red-loaded nano-droplets showed a clear spotted fluorescence inside the cells that increases with time (Fig. 7A and B). A very similar result is observed when Nile Red is added alone to the cells (see Fig. S3†in the ESI) showing fluorescent dots, which correspond to intracellular lipid droplets according to previous studies.[26] As nano-droplets do not enter the cells, the observed intracellular fluorescence is likely due to the release of the Nile Red dye from the droplets inside the cells. Thus, the cellular studies are fully in line with the FRET and FCS data showing the fast leakage of Nile Red into the Opti-MEM medium with serum, and its absence for NR668. These observations are very important, as Nile Red is commonly used for tracking the internalization of various nanostructures, including lipid nano-emulsions or nanoparticles inside the cells. Therefore, Nile Red should be used with great care, as it can lead to artifacts related to dye release. Evidently, NR668 appears much more suitable for monitoring the interaction of lipid-based nanocarriers with cells, as no dye release artifacts are observed with this dye.

3.7 *In vivo* imaging on zebrafish

In order to confirm the suitability of the NR668-loaded nano-droplets for biological imaging and verify the dye leakage *in vivo*, we performed microangiography experiments on living zebra fish embryos. A 2.3 nL volume of the Nile Red- or NR668-containing nano-emulsions was injected in the sinus venosus of the embryos, a sac that collects blood from the veins at the entry of the heart. Fig. 8 shows a general view of the whole embryo vasculature and a zoomed in view of the trunk region. To confirm the specificity of labeling within the vascular network, we injected the nano-emulsions into a transgenic line expressing eGFP specifically in the endothelial cells (*Tg*(*fli1*:*eGFP*)^{y1}).[47] The endothelial cells, which constitute the vessel walls, expressing the eGFP are visualized in the green channel and the nano-droplets in the red one. Both types of nano-droplets were immediately distributed in the entire vascular system. However, the labeling patterns showed very different characteristics within the 5–30 min period after injection. 30 min after injection of the Nile Red-containing nano-emulsion, the dye diffused and accumulated in the endothelial cells, as can be seen from the co-localized green fluorescence from the endothelial cells and the red one of the dye (Fig. 8A–C). Moreover, a diffuse labeling of the surrounding tissues was also observed, indicating a fast spreading of Nile Red over the animal body (Fig. 8B).

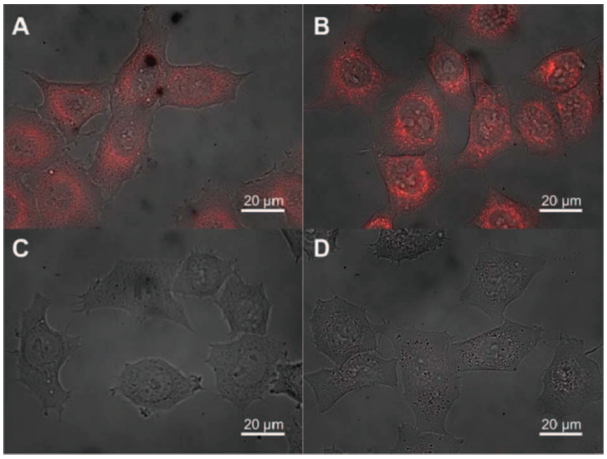

Fig. 7 Combined fluorescence and transmission images of HeLa cells incubated with 40 nm nano-droplets containing 0.1 wt.% of Nile Red (A and B) or 1 wt.% of NR668 (C and D) for different lengths of time: 15 min (A and C) and 2 h (B and D).

In contrast, NR688 was detected exclusively in the lumen of the vessels, as shown in Fig. 8E. No labeling of the endothelial cells was visible 30 min after injection with the nano-emulsion, as the interior of the blood vessels and the endothelial cells are distinctly colored in red and green, without co-localization (Fig. 8F). Thus, in contrast to the nano-droplets loaded with the parent Nile Red, no dye leakage was observed in the blood circulation system with the NR668-loaded nano-droplets within the observation time. This stability of the NR688 nano-emulsion represents an important advantage for microangiography experiments typically performed by injecting fluorescent microbeads[58] or QDs.[59] In both cited studies, a relatively fast accumulation of the fluorescent particles in the endothelial cells was observed. This labeling of the endothelium can be bothering when a precise delimitation of the lumen is needed, for example during the lumenization of newly formed vessels or vessel fusion during the developmental processes.[60] In this context, the NR688-containing nano-droplets represent an imaging tool perfectly adapted for microangiography experiments. Other *in vivo* studies on similar Labrafac CC®–Solutol HS15® nano-carrier systems showed sufficiently long circulation half-life in the blood stream of Wistar rats (over 2h),[61] which showed the potential of these systems for targeted labeling and long-time observations.

This important result together with the FRET, FCS and cellular studies indicates that the modified Nile Red dye NR668 not only allows the fabrication of highly fluorescent nano-droplets, stable against self-quenching, but also prevents dye leakage in biological media. This latter point allows the successful application of the obtained fluorescence nano-droplets to *in vivo* imaging, avoiding experimental artifacts related to dye leakage.

4 Conclusions

We designed highly lipophilic fluorescent dyes based on 3-alkoxyflavone (F888) and Nile Red (NR668) that can be encapsulated inside the hydrophobic core of lipid nano-emulsion droplets at exceptionally high concentrations (up to 170 mM and 830 dyes per 40 nm droplet for one of the dyes). Due to their bulky nature, these dyes maintained a high fluorescence quantum yield with low self-quenching even at this high loading, allowing the preparation of very bright fluorescent nano-droplets. Moreover, high loading allowed us to realize FRET between two different dyes inside the nano-droplets. FRET and fluorescence correlation spectroscopy (FCS) studies showed that NR668 release in the presence of serum is very slow, while the

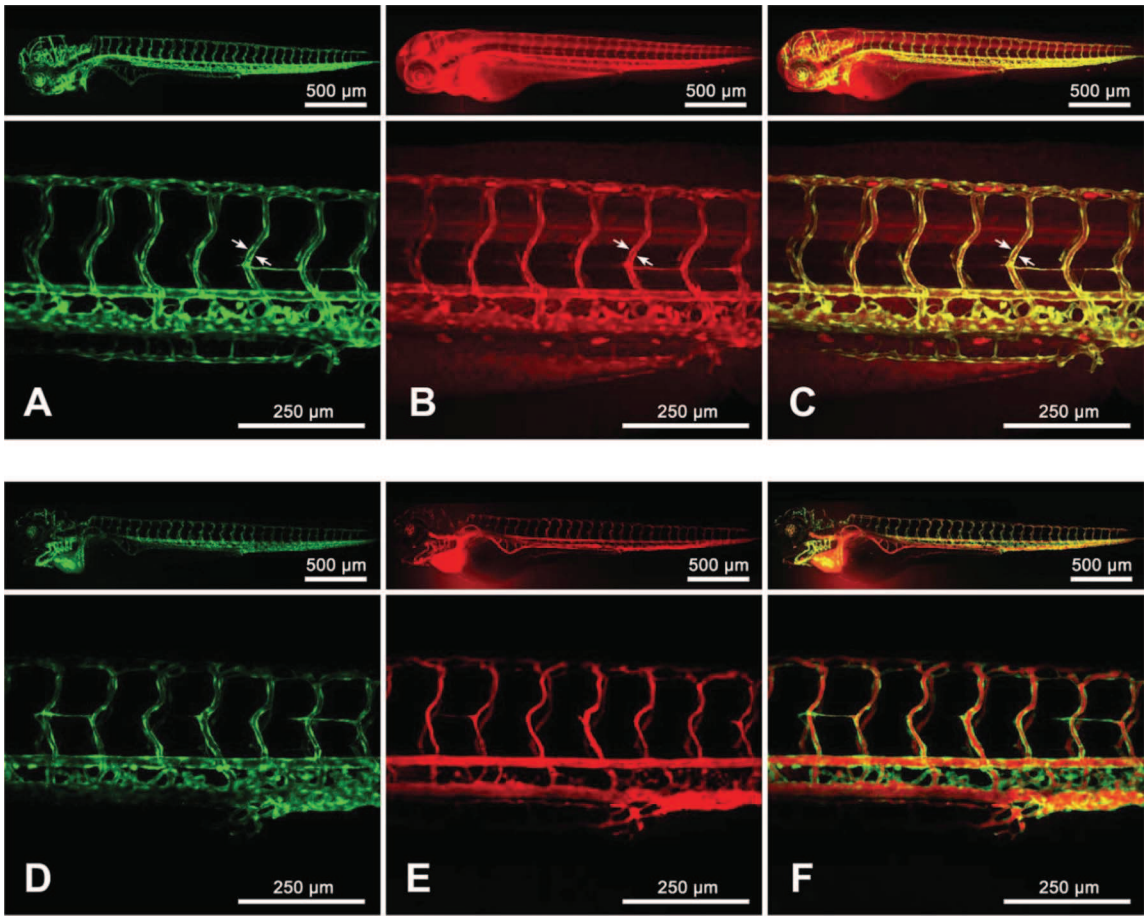

Fig. 8 Zebrafish microangiography using nano-droplets containing 0.1 wt.% of Nile Red (A, B and C) or 1 wt.% of NR668 (D, E and F) with the *Tg*(*fli1*:*eGFP*)^{y1} line. 3 days post fertilization, the living zebrafish embryos were injected with 2.3 nL of nano-emulsions diluted twice in HEPES buffer (pH 7.4) and imaged with a confocal microscope. The images present the global view (upper panels) and a zoomed in view of the trunk vasculature (lower panels). The images in green (A and D) present endothelial cells expressing eGFP, while in red—fluorescence of Nile Red (B) and NR668 (E), 30 min after injection of the nano-emulsion. The arrows show the endothelial cells. The merged image (C) shows the localization of Nile Red in the endothelium and the global diffuse labeling of the entire embryo, while the merged image (F) shows no co-localization of NR688 with the endothelial cells.

reference hydrophobic dye Nile Red leaks immediately. This drastic difference in the leakage profile between NR668 and Nile Red was confirmed by *in vitro* cellular studies. Finally, *in vivo* imaging in zebrafish showed perfect applicability of NR668-loaded nano-droplets for microangiography, while Nile Red-based droplets showed rapid diffusion of the dye to the endothelial cells of the vessels and to other tissues. Thus, the present work shows that to obtain efficient optical probes for *in vitro* and *in vivo* imaging based on nano-droplets, the problem of dye leakage from the nano-droplets in different biological media (serum, living cells and small animals) has to be resolved, and it suggests a path to bright and non-leaking lipid nano-carriers.

Acknowledgements

This work was supported by CNRS, Université de Strasbourg, ANR JCJC (ANR-11-JS07-014-01), INSERM, FRM, HFSP and Marie Curie FP7. The financial support of IS from the French Embassy and University of Strasbourg is acknowledged. We thank to D. Dujardin and R. Vauchelles from the PIQ imaging platform for help with the fluorescence imaging. L. Richert and V. Kilin are acknowledged for their help with the FCS measurements.

References

1 I. Brigger, C. Dubernet and P. Couvreur, *Adv. Drug Delivery Rev.*, 2002, **54**, 631.
2 D. Horn and J. Rieger, *Angew. Chem., Int. Ed.*, 2001, **40**, 4330.
3 M. Liong, J. Lu, M. Kovochich, T. Xia, S. G. Ruehm, A. E. Nel, F. Tamanoi and J. I. Zink, *ACS Nano*, 2008, **2**, 889.
4 P. Sharma, S. Brown, G. Walter, S. Santra and B. Moudgil, *Adv. Colloid Interface Sci.*, 2006, **123–126**, 471.
5 J. Lu, M. Liong, J. I. Zink and F. Tamanoi, *Small*, 2007, **3**, 1341.
6 X. H. Gao, Y. Y. Cui, R. M. Levenson, L. W. K. Chung and S. M. Nie, *Nat. Biotechnol.*, 2004, **22**, 969.
7 S. Keereweer, J. D. Kerrebijn, P. B. van Driel, B. Xie, E. L. Kaijzel, T. J. Snoeks, I. Que, M. Hutteman, J. R. van der Vorst, J. S. Mieog, A. L. Vahrmeijer, C. J. van de Velde, R. J. Baatenburg de Jong and C. W. Lowik, *Mol. Imaging Biol.*, 2011, **13**, 199.
8 K. Licha and C. Olbrich, *Adv. Drug Delivery Rev.*, 2005, **57**, 1087.
9 J. Rao, A. Dragulescu-Andrasi and H. Yao, *Curr. Opin. Biotechnol.*, 2007, **18**, 17.
10 I. L. Medintz, H. T. Uyeda, E. R. Goldman and H. Mattoussi, *Nat. Mater.*, 2005, **4**, 435.

11 R. Gill, M. Zayats and I. Willner, *Angew. Chem., Int. Ed.*, 2008, **47**, 7602.
12 S. Santra, K. Wang, R. Tapec and W. Tan, *J. Biomed. Opt.*, 2001, **6**, 160.
13 E. B. Cho, D. O. Volkov and I. Sokolov, *Small*, 2010, **6**, 2314.
14 S. Bonacchi, D. Genovese, R. Juris, M. Montalti, L. Prodi, E. Rampazzo and N. Zaccheroni, *Angew. Chem., Int. Ed.*, 2011, **50**, 4056.
15 R. Hardman, *Environ. Health Perspect.*, 2006, **114**, 165.
16 J. L. Pelley, A. S. Daar and M. A. Saner, *Toxicol. Sci.*, 2009, **112**, 276.
17 V. P. Torchilin, *Nat. Rev. Drug Discovery*, 2005, **4**, 145.
18 K. T. Plajnsek, S. Pajk, B. Govedarica, S. Pecar, S. Srcic and J. Kristl, *Int. J. Pharm.*, 2011, **416**, 384.
19 M. M. Fryd and T. G. Mason, *Annu. Rev. Phys. Chem.*, 2012, **63**, 493.
20 N. Anton, J. P. Benoit and P. Saulnier, *J. Controlled Release*, 2008, **128**, 185.
21 N. Anton and T. F. Vandamme, *Pharm. Res.*, 2011, **28**, 978.
22 D. J. McClements, *Soft Matter*, 2012, **8**, 1719.
23 I. Texier, M. Goutayer, A. Da Silva, L. Guyon, N. Djaker, V. Josserand, E. Neumann, J. Bibette and F. Vinet, *J. Biomed. Opt.*, 2009, **14**, 054005.
24 B. Heurtault, P. Saulnier, B. Pech, J. E. Proust and J. P. Benoit, *Pharm. Res.*, 2002, **19**, 875.
25 P. P. Constantinides, M. V. Chaubal and R. Shorr, *Adv. Drug Delivery Rev.*, 2008, **60**, 757.
26 S. A. Wissing, O. Kayser and R. H. Muller, *Adv. Drug Delivery Rev.*, 2004, **56**, 1257.
27 Z. Zhang, J. Chen, L. Ding, H. Jin, J. F. Lovell, I. R. Corbin, W. Cao, P. C. Lo, M. Yang, M. S. Tsao, Q. Luo and G. Zheng, *Small*, 2010, **6**, 430.
28 R. V. Tikekara and N. Nitin, *Soft Matter*, 2011, **7**, 8149.
29 A. Wagh, S. Y. Qian and B. Law, *Bioconjugate Chem.*, 2012, **23**, 981.
30 B. Law, A. Curino, T. H. Bugge, R. Weissleder and C. H. Tung, *Chem. Biol.*, 2004, **11**, 99.
31 H. Patel, C. Tscheka and H. Heerklotz, *Soft Matter*, 2009, **5**, 2849.
32 A. S. Al Dwayyan, S. M. H. Qaid, M. A. Majeed Khan and M. S. Al Salhi, *Opt. Mater.*, 2012, **34**, 761.
33 R. Tapec, X. J. Zhao and W. Tan, *J. Nanosci. Nanotechnol.*, 2002, **2**, 405.
34 D. J. McClements and Y. Li, *Adv. Colloid Interface Sci.*, 2010, **159**, 213.
35 A. K. Li, Y. McClements and D. J. H. Xiao, *Food Chem.*, 2012, **132**, 799.
36 M. Goutayer, S. Dufort, V. Josserand, A. Royere, E. Heinrich, F. Vinet, J. Bibette, J. L. Coll and I. Texier, *Eur. J. Pharm. Biopharm.*, 2010, **75**, 137.
37 O. A. Kucherak, L. Richert, Y. Mély and A. S. Klymchenko, *Phys. Chem. Chem. Phys.*, 2012, **14**, 2292.
38 P. Greenspan, E. P. Mayer and S. D. Fowler, *J. Cell Biol.*, 1985, **100**, 965.
39 G. Diaz, M. Melis, B. Batetta, F. Angius and A. M. Falchi, *Micron*, 2008, **39**, 819.
40 T. Ozturk, A. S. Klymchenko, A. Capan, S. Oncul, S. Cikrikci, S. Taskiran, B. Tasan, F. B. Kaynak, S. Ozbey and A. P. Demchenko, *Tetrahedron*, 2007, **63**, 10290.
41 O. A. Kucherak, S. Oncul, Z. Darwich, D. A. Yushchenko, Y. Arntz, P. Didier, Y. Mely and A. S. Klymchenko, *J. Am. Chem. Soc.*, 2010, **132**, 4907.
42 S. M. Ormson, R. G. Brown, F. Vollmer and W. Rettig, *J. Photochem. Photobiol., A*, 1994, **81**, 65.
43 M. L. Deda, M. Ghedini, I. Aiello, T. Pugliese, F. Barigelletti and G. Accorsi, *J. Organomet. Chem.*, 2005, **690**, 857.
44 J. P. Clamme, J. Azoulay and Y. Mely, *Biophys. J.*, 2003, **84**, 1960.
45 N. L. Thompson, in *Topics in Fluorescence Spectroscopy Techniques*, ed. J. R. Lakowicz, Plenum Press, New York, 1991, vol. **1**, p. 337.
46 P. Didier, J. Godet and Y. Mely, *J. Fluoresc.*, 2009, **19**, 561.
47 N. D. Lawson and B. M. Weinstein, *Dev. Biol.*, 2002, **248**, 307.
48 N. Anton and T. F. Vandamme, *Int. J. Pharm.*, 2009, **377**, 142.
49 N. T. Huynh, C. Passirani, P. Saulnier and J. P. Benoit, *Int. J. Pharm.*, 2009, **379**, 201.
50 T. F. Vandamme and N. Anton, *Int. J. Nanomed.*, 2010, **5**, 867.
51 J. Gravier, F. P. Navarro, T. Delmas, F. Mittler, A. C. Couffin, F. Vinet and I. Texier, *J. Biomed. Opt.*, 2011, **16**, 096013.
52 A. Sulkowska, *J. Mol. Struct.*, 2002, **614**, 227.
53 F. Kratz and U. Beyer, *Drug Delivery*, 1998, **5**, 281.
54 S. Li, W. C. Tseng, D. Beer Stolz, S. P. Wu, S. C. Watkins and L. Huang, *Gene Ther.*, 1999, **6**, 585.
55 C. Dufour and O. Dangles, *Biochim. Biophys. Acta, Gen. Subj.*, 2005, **1721**, 164.
56 S. Mishra, P. Webster and M. E. Davis, *Eur. J. Cell Biol.*, 2004, **83**, 97.
57 J. Xie, C. Xu, N. Kohler, Y. Hou and S. Sun, *Adv. Mater.*, 2007, **19**, 3163.
58 B. M. Weinstein, D. L Stemple, W. Driever and M. C. Fishman, *Nat. Med.*, 1995, **1**, 1143.
59 S. Rieger, R. P. Kulkarni, D. Darcy, S. E. Fraser and R. W. Köster, *Dev. Dyn.*, 2005, **234**, 670.
60 E. Ellertsdóttir, A. Lenard, Y. Blum, A. Krudewig, L. Herwig, M. Affolter and H. G. Belting, *Dev. Biol.*, 2010, **341**, 56.
61 F. Lacoeuille, F. Hindre, F. Moal, J. Roux, C. Passirani, O. Couturier, P. P. Cales, J. J. Le Jeune, A. Lamprecht and J. P. Benoit, *Int. J. Pharm.*, 2007, **344**, 143.

2.2 Fluorinated counterion-enhanced emission of rhodamine aggregates: ultrabright nanoparticles for bioimaging and light-harvesting

Fluorescent dye nanoparticles are highly attractive systems, because they are composed exclusively of fluorescent molecules. This means a high concentration of fluorophores per volume compared to dye-loaded lipid nano-droplets described above, where dyes are diluted inside the oil core. If the quenching of fluorophores can be suppressed or significantly reduced in such systems, they can achieve much higher brightness compared to dye-loaded NPs. Recent work in our group showed that octadecyl rhodamine B with per-fluorinated tetraphenylborate counterion showed minimized self-quenching after encapsulation into polymer NPs.[1] Moreover, a unique behavior of collective on/off switching (blinking) of these NPs was observed, which suggested that the dyes are organized in form of domains inside polymer matrix where the dyes are strongly coupled. Therefore, we hypothesized that pure alkyl rhodamine B salts with tetraphenyl borate counterions could also be highly emissive, as it was shown before by groups of Yao and Warner on other types of dyes and counterions.[2] Here, we present our findings on NPs prepared from a series rhodamine B lipophilic ester derivatives bearing alkyl chain with different length and series of tetraphenylborate counterions by nanoprecipitation approach (Fig. 2.2.1). The alkyl function was varied in rhodamine B ester in order to modulate the lipophilicity and the strength of hydrophobic interactions in the dye-counterion pair. We also explored the effect of tetraphenylborate counterion structure, especially its fluorination level, on properties of nanoparticles. We have assumed that the size and structure of counterions may influence the organization of "ionic liquid type" dye pairs forming nanoparticle core, as the size of the counterion changes the inter-fluorophore distance.

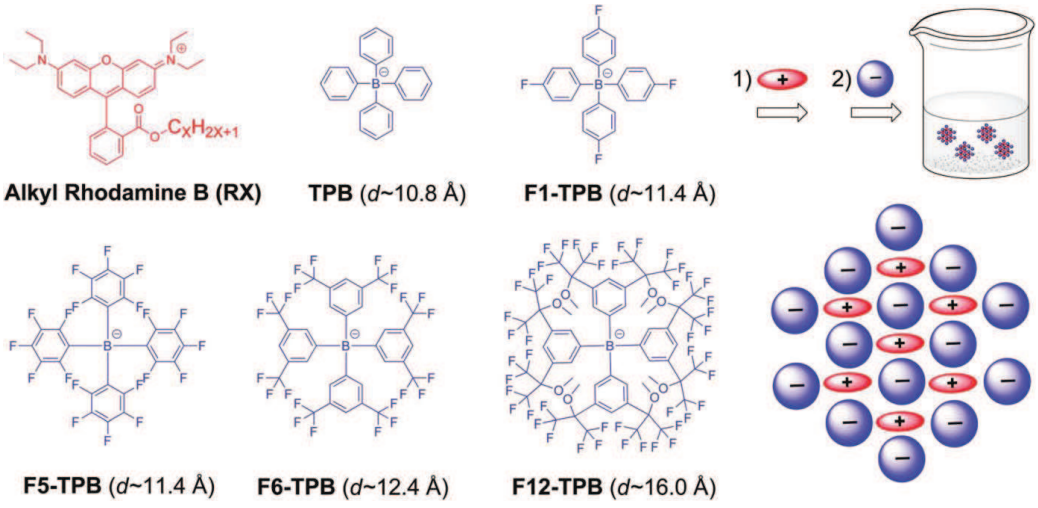

Figure 2.2.1. Chemical structures of the rhodamine B derivatives (RX, X varied from 2 to 18) and tetraphenylborate counterions with increasing fluorination level: from non-fluorinated (TPB) to 12 fluorines (F12-TPB) per phenyl ring.

Before the addition of counterions, all studied rhodamine derivatives, except most hydrophobic octadecyl rhodamine B iodide, were found to be well soluble at micromolar concentration and no precipitation was observed. Then, NPs were prepared by an addition of 10-fold counterion excess to a one micromolar solution of the rhodamine derivative in water. Based on examination of the absorption spectra, we have concluded that increase in the fluorination of tetraphenylborate counterion significantly reduced the H-aggregate formation of rhodamine B derivatives (Fig. 2.2.2A). Some decrease in the H-aggregation was also observed with increase in the length of the alkyl chain in the rhodamine structure (Figure 2.2.2B).

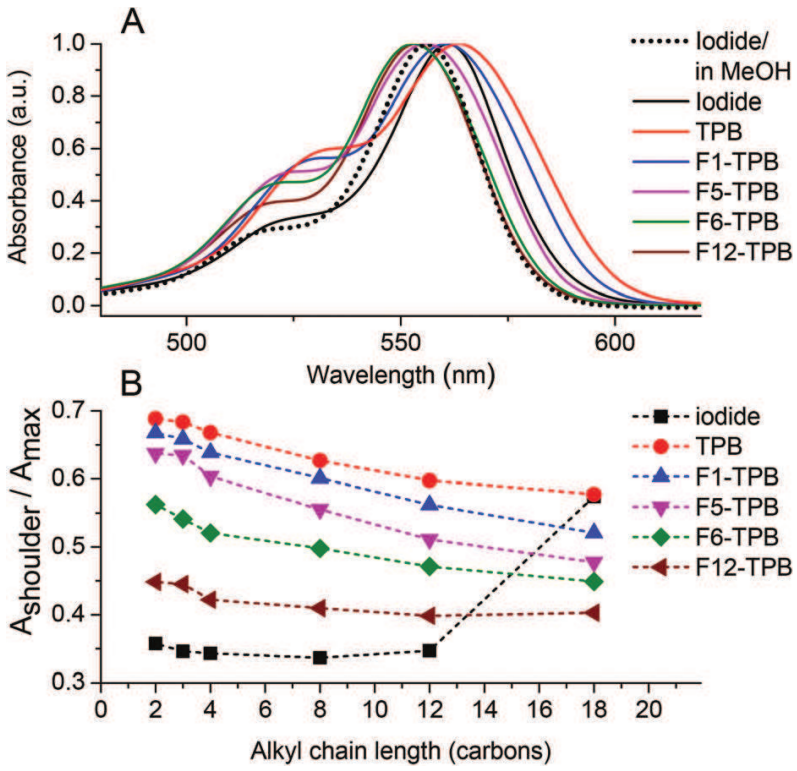

Figure 2.2.2 Effect of counterion fluorination and alkyl chain length on the absorption spectra of alkyl rhodamines B in water. (A) Normalized absorption spectra of R12 NPs with different TPB counterions and comparison to R12 iodide in water. (B) Absorbance ratio of the short-wavelength shoulder to the maximum for different alkyl chains and counterions.

The AFM and DLS measurements suggested that the obtained NPs were about 20-40 nm in size, except F5-TPB particles that had a size of 11 nm. The excess of counterion forms the nanoparticle shell and also provides the negative charge for the nanoparticle surface, which has been verified by Zeta potential measurements. The large value of Zeta potential corroborated with the observed good colloidal stability against precipitation and also can explain the small size of NPs.

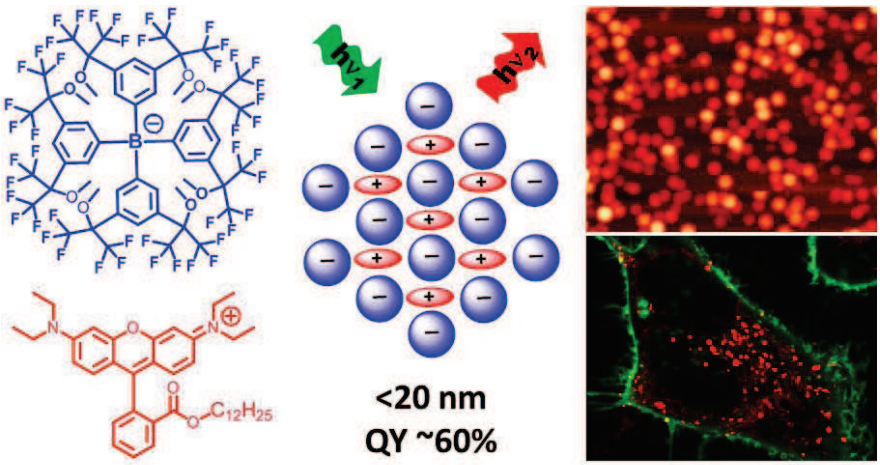

Figure 2.2.3. Some properties of NPs composed of dodecyl rhodamine B and highly fluorinated counterion. Panel at the top right shows AFM image, while at the bottom right shows confocal image of the cell staining with NPs (red) and plasma membrane tracker (green).

Fluorescence studies showed that increase in the level of fluorination produced a systematic increase in a fluorescence quantum efficiency, which grows in the following order: TPB <F1-TPB ≪ F5-TPB < F6-TPB < F12-TPB. This result matched perfectly the lower H-aggregation observed in the absorption spectra.

We also found that the counterions had an influence on the spectral shape of the emission of obtained NPs. The emission band of NPs became narrower compared to free rhodamine in solution, which meant that highly fluorinated TPB counterions not only reduced the H-aggregate formation inside NPs but also created a rigid environment for the rhodamine dyes. Moreover, in our NPs we observed extremely low value of fluorescence anisotropy (*i.e.,* ~0.01) compared to the free rhodamine B iodides in water. This likely corresponds to the fast excitation energy migration rather that dye movement inside NPs.

Further, we used FCS to obtain information about the size, single particle brightness, and concentration of our NPs. The measured hydrodynamic diameters of 14 and 19 nm were found in accordance with a data obtained by AFM for the F5-TPB and F12-TPB respectively. The brightness of F5-TPB and F12-TPB NPs were respectively 340 and 540 times higher than a single rhodamine B dye in solution. According to the wide-field fluorescence microscopy, our brightest NPs of F12-TPB appeared to be as bright as FluoroSpheres® 535/575 and ~40-fold brighter than QD-585. Interestingly, nearly half of F5-TPB NPs exhibited remarkable feature of rapid blinking that can be referred to the fast excitation energy migration through the dyes, which ended up with a dark state of the particle. In contrast, the blinking behavior was not present in F12-TPB particles, which showed

relatively stable fluorescence signal with some weak fluctuations that corresponded to the particle movements inside the gel on the focal plane. Thus, we concluded that the level of fluorination played essential role in the blinking behavior as well as in photostability of the whole particle.

As a large number of fluorescent dyes strongly coupled by fast excitation energy migration were present inside our NPs, we assumed that this system can act as a light-harvesting antenna in the presence of an energy acceptor. To confirm this idea we encapsulated Cy5-derivative (C2-Cy5), which is able to harvest the light from the rhodamine donors, inside our most representative examples of NPs, the salts of R12 with F5-TPB and F12-TPB counterions. We found that the most fluorinated counterion F12-TPB displayed remarkably high antenna effect of 200. This striking result indicated that almost all the energy of the donors of single NP was efficiently transferred to a single energy acceptor (C2-Cy5), which proved our assumption about light-harvesting properties of this system.

Finally, we investigated whether our fluorescent NPs are able to enter and retain their integrity inside living cells (HeLa), which are most crucial parameters for applying NPs in cellular imaging. Our confocal imaging studies showed that NPs with the most fluorinated counterion were rather stable after entry into living cells (Fig. 2.2.3), while NPs built from less fluorinated NPs disassembled after 1h and their released dye accumulated in the mitochondria. We can conclude that in our NPs the counterion fluorination significantly increases the particle intracellular stability, which is probably due to super-hydrophobic properties of the fluorinated compounds.

Overall, the counterion fluorination and steric hinderance is crucial for correct ordering of dyes in solid state without aggregation-caused quenching. It enables preparation of NPs with high fluorescence brightness and photostability, narrow-band emission, fast energy transfer and high intracellular stability. We believe that these findings will facilitate the route the next generation of fluorescent nanomaterials for various applications, especially, bioimaging and light harvesting. The results of these studies were published in the article: Shulov I., Oncul S., Reisch A., Arntz Y., Collot M., Mely Y., Klymchenko A.S. Fluorinated counterion-enhanced emission of rhodamine aggregates: ultrabright nanoparticles for bioimaging and light-harvesting. Nanoscale. 2015, 7, 18198-18210.
The full description of this work can be found in this article enclosed below.

References

(1) Reisch, A.; Didier, P.; Richert, L.; Oncul, S.; Arntz, Y.; Mely, Y.; Klymchenko, A. S. *Nature Communications* **2014**, *5*.

(2) (a) Yao, H.; Ashiba, K. *RSC Adv.* **2011**, *1*, 834. (b) Bwambok, D. K.; El-Zahab, B.; Challa, S. K.; Li, M.; Chandler, L.; Baker, G. A.; Warner, I. M. *ACS Nano* **2009**, *3*, 3854.

PUBLICATION №2

Fluorinated counterion-enhanced emission of rhodamine aggregates: ultrabright nanoparticles for bioimaging and light-harvesting

Nanoscale

PAPER

View Article Online
View Journal | View Issue

Cite this: *Nanoscale*, 2015, **7**, 18198

Fluorinated counterion-enhanced emission of rhodamine aggregates: ultrabright nanoparticles for bioimaging and light-harvesting†

Ievgen Shulov,[a,b] Sule Oncul,[a,c] Andreas Reisch,[a] Youri Arntz,[a] Mayeul Collot,[a] Yves Mely[a] and Andrey S. Klymchenko*[a]

Received 23rd July 2015,
Accepted 26th September 2015

DOI: 10.1039/c5nr04955e

www.rsc.org/nanoscale

The key to ultrabright fluorescent nanomaterials is the control of dye emission in the aggregated state. Here, lipophilic rhodamine B derivatives are assembled into nanoparticles (NPs) using tetraphenylborate counterions with varied fluorination levels that should tune the short-range dye ordering. Counterion fluorination is found to drastically enhance the emission characteristics of these NPs. Highly fluorinated counterions produce 10–20 nm NPs containing >300 rhodamine dyes with a fluorescence quantum yield of 40–60% and a remarkably narrow emission band (34 nm), whereas, for other counterions, aggregation caused quenching with a weak broad-band emission is observed. NPs with the most fluorinated counterion (48 fluorines) are ~40-fold brighter than quantum dots (QD585 at 532 nm excitation) in single-molecule microscopy, showing improved photostability and suppressed blinking. Due to exciton diffusion, revealed by fluorescence anisotropy, these NPs are efficient FRET donors to single cyanine-5 acceptors with a light-harvesting antenna effect reaching 200. Finally, NPs with the most fluorinated counterion are rather stable after entry into living cells, in contrast to their less fluorinated analogue. Thus, the present work shows the crucial role of counterion fluorination in achieving high fluorescence brightness and photostability, narrow-band emission, efficient energy transfer and high intracellular stability of nanomaterials for light harvesting and bioimaging applications.

Introduction

Designing brightly fluorescent nanomaterials is the key step for obtaining fluorescent nanoparticles (NPs) for imaging applications.[1,2] Quantum dots are considered as the brightest materials among inorganic NPs, since their cores of ~5 nm diameter can exhibit extinction coefficients up to 10^6 M^{-1} cm^{-1} together with high quantum yields (40–100%).[3,4] However, for imaging applications, QDs require a robust water-compatible shell, which makes them much larger with a hydrodynamic radius usually around 15–25 nm. On the other hand, it is well known that organic dyes present an even higher capacity to absorb photons, with extinction coefficients of 10^5–3×10^5 M^{-1} cm^{-1} for molecules with a size of only ~1 nm and that they also emit with high quantum yields (20–100%).[5] Hence, the organization of organic dyes in the form of water-compatible NPs should lead to nanomaterials with comparable or better brightness than QDs of the same size. Moreover, these organic fluorescent nanomaterials are potentially biodegradable in contrast to QDs, making them particularly attractive for biomedical imaging applications.[1,2] Several organic systems have already been developed: conjugated polymer NPs,[6,7] dye-doped polymer NPs[8–14] and dye-based NPs.[10,11,15–17] Conjugated polymer NPs are probably the brightest organic nanomaterials,[6,18,19] but, they lack biodegradability, due to their polymer backbone made from carbon–carbon bonds. Dye-based NPs are of particular interest because of their very high density of fluorophores per volume compared to dye-doped (blended) systems, where the dye is diluted in a matrix. However, the major problem of dye-based particles is aggregation-caused quenching (ACQ), originated from aggregation of usually flat fluorophores into non-fluorescent pi-stacked structures (H-aggregates).[20,21] In recent years, several solutions to the ACQ problem were proposed, where fluorophores exhibit unique arrangements in the solid phase, so that self-quenching is prevented.[11,17,22] The first one exploits

[a]*Laboratoire de Biophotonique et Pharmacologie, UMR 7213 CNRS, Université de Strasbourg, Faculté de Pharmacie, 74, Route du Rhin, 67401 ILLKIRCH Cedex, France. E-mail: andrey.klymchenko@unistra.fr; Tel: +33 368 85 42 55*
[b]*Organic Chemistry Department, Chemistry Faculty, Taras Shevchenko National University of Kyiv, 01601 Kyiv, Ukraine*
[c]*Department of Biophysics, School of Medicine, Istanbul Medeniyet University, 34700 Istanbul, Turkey*
†Electronic supplementary information (ESI) available: Additional data on synthesis of rhodamine B derivatives, AFM and excitation spectra of NPs. See DOI: 10.1039/c5nr04955e

the phenomenon of aggregation induced emission (AIE),[23–25] where non-radiative pathways due to internal rotations are prevented after aggregation of the fluorophores in the form of distorted H- or J-aggregates. The second approach is to couple bulky groups to the fluorophore, as it was shown for BODIPY,[26] fluorene[27] and push–pull triphenylamine[28] derivatives. The third approach utilizes dye salts with bulky counterions, so-called non-coordinating ions,[29] which serve as spacers for ionic dyes inside NPs.[30,31] Warner *et al*. named this type of salts "frozen ionic liquids",[30] because they presented intermediate properties between ordered crystals and disordered liquids, while Yao *et al*. called "ion-association" the process to form NPs from these salts.[32] This approach was mainly applied to cyanines,[31,33–35] using different counterions, such as bis(trifluoromethanesulfonyl)imide, bis(pentafluoroethanesulfonyl)imide,[33] bis(2-ethylhexyl)sulfosuccinate[30] and tetraphenylborate derivatives.[31,36] Many of these counterions contain fluorine atoms, but so far there has been no systematic study showing the importance of counterion fluorination on the emission properties of the ion-associated (we will call them counterion-assembled) NPs. The role of fluorine is particularly important, because fluorinated groups exhibit strong electron withdrawing and super-hydrophobic properties, orthogonal to aqueous and organic species.[37–39] Highly fluorinated, or fluorous compounds, were successfully used in molecular electronics[40–43] as well as *in vivo* for imaging and oxygen delivery.[44–46] Importantly, fluorination was also reported to improve the characteristics of photovoltaic materials,[47,48] and fluorescent properties of dyes[49] and nanomaterials.[50,51] On the other hand, the single particle emission performance of counterion-assembled NPs has not been sufficiently addressed, so it remains unclear, whether these systems can really compete with QDs. Rhodamine derivatives are probably the most interesting dyes for constructing ultrabright nanomaterials, because of their high extinction coefficient, excellent quantum yields (40–100%) and photostability.[5,52] Recently, we showed that self-quenching of rhodamines in a polymer matrix can be strongly reduced using perfluorinated tetraphenylborate, though this was not the case with all tetraphenyl-borate derivatives.[9] Moreover, we showed that these systems presented exceptional collective behavior, suggesting that the rhodamine molecules were assembled by the counterions inside the polymer matrix into a unique arrangement.

In the present work, we prepared NPs through nano-precipitation of rhodamine B derivatives bearing different alkyl chains with tetraphenylborate counterions containing different numbers of fluorine atoms (0 to 12 per phenyl). We found that fluorination of the counterion drastically enhanced the characteristics of rhodamine NPs: increased the fluorescence quantum yield, narrowed the emission band in comparison to the dye in solution, enhanced the brightness and photostability at the single-particle level and finally improved the stability of the NPs inside living cells. As a result, for the most fluorinated counterion, we obtained NPs of 20 nm size with a brightness corresponding to >300 rhodamine molecules and a quantum yield of 60% (extinction coefficient × quantum yield = 2.4×10^7 M^{-1} cm^{-1}). Single molecule microscopy suggested that they were 40-fold brighter than QDs of similar color (QD585 at 532 nm excitation) and comparable hydrodynamic diameter. The obtained NPs were found promising for light-harvesting and bioimaging applications.

Results

Dyes and counterions

Alkyl rhodamine B was selected as a cationic dye, for which the length of the alkyl chain was varied from 2 (R2) to 18 (R18) (Fig. 1). Variation of the length of the alkyl chain may influence the organization and mode of interaction with the hydro-

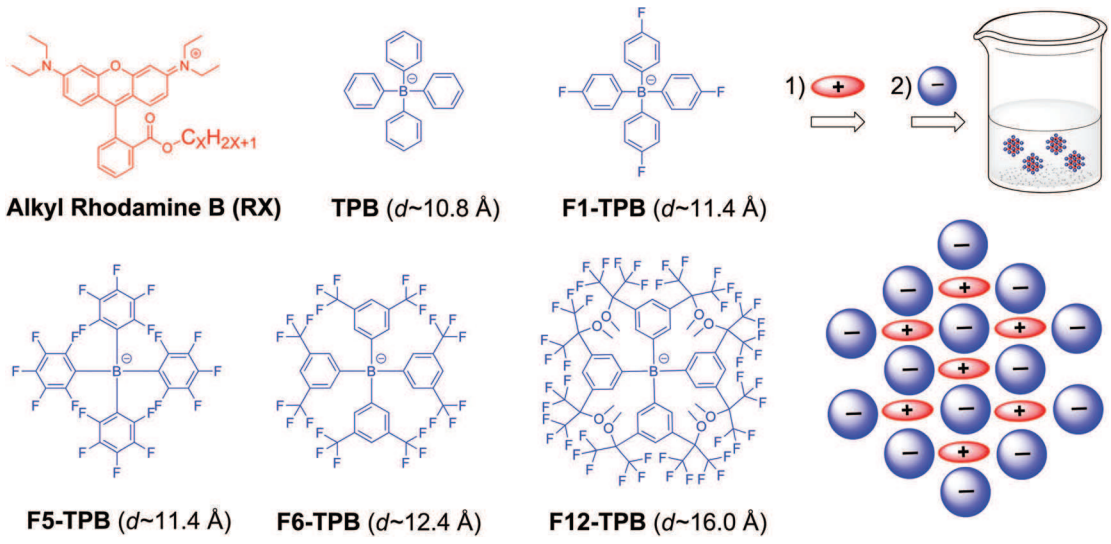

Fig. 1 Chemical structures of the rhodamine B derivatives (*RX*, *X* varies from 2 to 18) and the different tetraphenylborate counterions used in this work.

phobic counterion. As counterions, we selected five bulky anions with increasing fluorination level: from non-fluorinated (TPB) to 12 fluorines (F12-TPB) per phenyl ring (Fig. 1). In addition to the number of fluorine groups, these ions differ by size, with the nonfluorinated TPB being the smallest (~1.08 nm diameter), while F12-TPB being the largest (~1.6 nm diameter). We hypothesized that the level of fluorination and the size of the counterion could change the molecular arrangement of the dyes and vary the inter-fluorophore distance.

Ion-association: formation of NPs

In the ion-association method for preparation of fluorescent NPs, the hydrophobic cation and anion dissolved in water are mixed together to form insoluble salts that may precipitate in the form of NPs.[30–33] Primarily, we checked whether our alkyl-rhodamines are well soluble in water at micromolar concentrations and do not form aggregates without the hydrophobic counterion. The absorption spectrum of dodecyl-rhodamine B (R12) iodide in water was composed of one band with the maximum centered at 561 nm with a relatively low-intensity short-wavelength shoulder located ~30 nm from the maximum similar to that in methanol (Fig. 2A). Earlier studies showed that, the relative intensity of this shoulder, being low in molecular form, increases drastically on the formation of non-fluorescent H-aggregates.[9] Hence, in aqueous medium R12 probably remains in the molecular form. The same behavior was observed for all rhodamines with alkyl chain lengths ≤12, where the relative intensity of the short-wavelength shoulder was $A_{shoulder}/A_{maximum}$ = 0.34–0.36 (Fig. 2B). By contrast, the most hydrophobic derivative R18 iodide in water showed a much larger relative intensity of the short-wavelength shoulder (0.57, Fig. 2B and S1†), suggesting the formation of H-aggregates, where the R18 dyes are pi-stacked.

Then, we studied the formation of NPs by ion-association. To this end, we mixed an alkyl rhodamine B derivative in water (1 μM) with a 10-fold molar excess of the corresponding borate counterion. In the presence of the non-fluorinated TPB counterion, the band maximum of R12 was red-shifted and the short-wavelength shoulder increased compared to iodide as a counterion, indicating that the dyes aggregate in the presence of this counterion (Fig. 2A). This phenomenon was observed for all rhodamine B derivatives with alkyl chain lengths ≤12, as can be seen from the high short-wavelength shoulder in the presence of TPB (Fig. 2B). In the case of R18, which was already aggregated in water, the addition of TPB did not change this ratio significantly. The nature of the borate counterion had an important influence on the absorption spectra of the dyes. Indeed, the contribution of the short-wavelength shoulder decreased with increasing TPB fluorination: TPB > F1-TPB > F5-TPB > F6-TPB > F12-TPB. Thus, higher fluorination of TPB decreased H-aggregation of rhodamine B fluorophore in these assemblies. Moreover, the band maximum shifted to the blue with increasing counterion fluorination. As a result for F6-TPB and F12-TPB counterions, the absorption maximum of the dye was blue shifted by *ca.* 8 nm with respect to that in water. This shift originates probably from the unique super-hydrophobic fluorinated environment of the dye within the aggregates. It should be also noted that with most counterions, an increase in the length of the alkyl chain decreased the fraction of H-aggregates (Fig. 2B).

Dynamic light scattering (DLS) data showed that R12 in the presence of hydrophobic counterions forms relatively small particles with TPB and F1-TPB counterions (~25 nm), but a bit larger ones (32–50 nm) with highly fluorinated counterions, F5-TPB, F6-TPB and F12-TPB (Table 1). However, we suspected that DLS data for NPs built from highly fluorinated counterions were biased because of their strong fluorescence (see below). Therefore, we additionally studied all NPs by atomic force microscopy (AFM). We found that R12 salts with

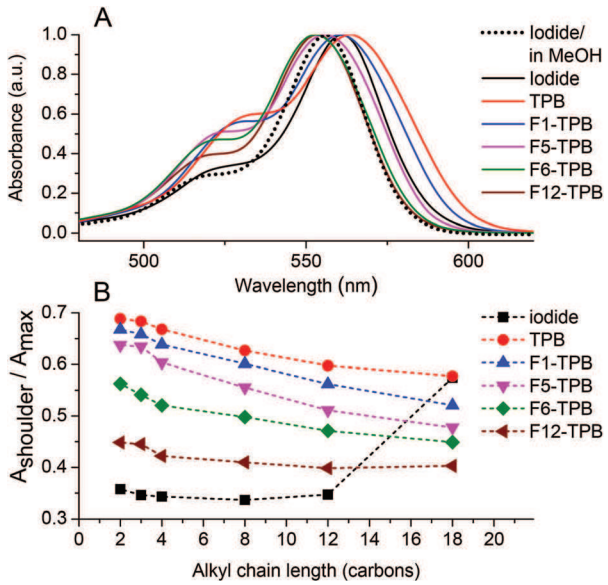

Fig. 2 Effect of counterion fluorination and alkyl chain length on the absorption spectra of alkyl rhodamines B in water. (A) Normalized absorption spectra of R12 NPs with different TPB counterions and comparison to R12 iodide in water. (B) Absorbance ratio of the short-wavelength shoulder to the maximum for different alkyl chains and counterions.

Table 1 Hydrodynamic diameter and zeta potential by DLS and diameter by AFM of NPs assembled from R12 with different hydrophobic counterions

Counterion	Diameter (nm)	Polydispersity (PDI)	Zeta potential (mV)	Diameter (AFM)[b] (nm)
TPB	25 (±1)	0.19	−51 (±5)	22 (±2)
F1-TPB	26 (±1)	0.15	−52 (±3)	22 (±2)
F5-TPB[a]	25 (±2)	0.17	−58 (±8)	11 (±1)
F6-TPB[a]	40 (±2)	0.19	−80 (±7)	21 (±2)
F12-TPB[a]	45 (±2)	0.16	−74 (±4)	21 (±2)

[a] The values obtained for these NPs by DLS are probably affected by their efficient fluorescence. [b] Diameter was obtained from height AFM measurements.

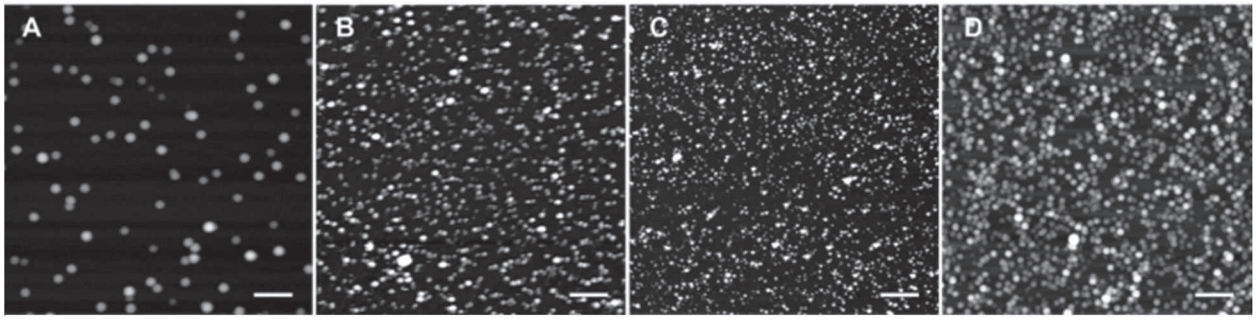

Fig. 3 Atomic force microscopy of NPs assembled from R12 with fluorinated counterions TPB (A), F1-TPB (B), F5-TPB (C) and F12-TPB (D). The imaging was done in the liquid phase with 10–100 mM $CaCl_2$ (B). Scale bar is 500 nm. Particle diameter was estimated from the height measurements, because the measured lateral dimensions of NPs depended on the AFM tip geometry.

different counterions form NPs of 21–22 nm diameter, except F5-TPB giving 11 nm NPs (Table 1, and Fig. 3, S2, S3†). Importantly, these NPs presented very high negative zeta potentials between −51 and −74 mV (Table 1). The zeta potential decreased from +70 to −51 mV, when the ratio of TPB/R12 increased from 1 to 10 (Fig. S4†). This suggests that the negative surface charge originates from the adsorption of the excess of borate counterions at the particle surface. The latter create a negatively charged protection shell that can explain the formation of small NPs.

We then verified whether these NP suspensions of R12 salts with different counterions are stable over time. To this end, we studied the absorbance values of these suspensions in plastic cuvettes as a function of time. The decrease in the absorbance value depended clearly on the fluorination level: iodide ~ TPB > F1-TPB > F5-TPB ~ F6-TPB (Fig. 4). As the shape of the absorption spectra for these counterions remained unchanged with time, we could conclude that the decrease in the absorption, observed mainly for non-fluorinated counterions, was related to sedimentation of the particles and their adsorption on the walls of the cuvette. On the other hand the most fluorinated one F12-TPB showed an increase in the absorbance with time, especially in the first 1 h. This initial rapid increase in absorbance was associated with a decrease in the short-wavelength shoulder (data not shown), probably reflecting the "maturation" of the NPs towards minimum dye H-aggregation. This maturation was observed only for F12-TPB, probably because this large counterion requires more time to stably assemble with the R12 dye. Overall, we could conclude that the increase in counterion fluorination improved the stability of suspensions of NPs against sedimentation and adsorption to the walls of the plastic cuvette. For the most promising NPs (R12/F12-TPB) the stability was tested at different biologically relevant pH. In the pH range of 5.0–9.0 within 24 h, absorption measurements suggested no signs of sedimentation of NPs, while DLS showed no significant variations in their size (Fig. S5†).

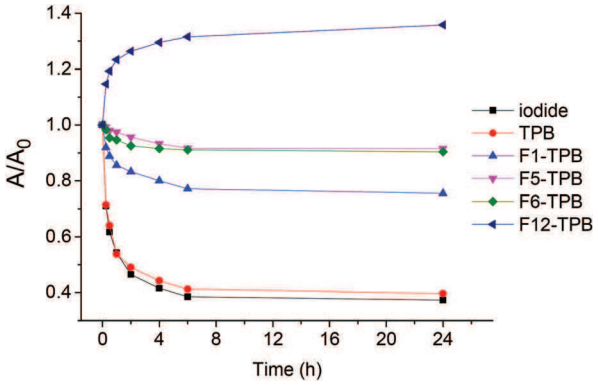

Fig. 4 Maturation and stability of NPs assembled from R12 dye with different counterions in plastic cuvettes measured by the absorbance at the maximum. Concentrations of R12 and TPB counterions were 1 μM and 10 μM, respectively.

Fluorescence properties of NPs

Encouraged by the AFM and stability data, we next studied the effect of counterions on the NPs' fluorescence properties. The fluorescence quantum yield (QY) of NPs showed a remarkable variation as a function of the counterion. Iodide derivatives with a chain length from 2 to 12 showed high QY in water, in agreement with highly efficient fluorescence of the molecular form of rhodamine B in water (Fig. 5). By contrast, R18 bearing a long C18 alkyl chain, showed a very low QY, which is clearly due to the aggregation-induced self-quenching in water, in line with the absorption spectral data. While non-fluorinated TPB induced strong quenching with QY values <1% for all dyes, an increase in the fluorination level of TPB produced a systematic increase in the quantum yield: TPB < F1-TPB ≪ F5-TPB < F6-TPB < F12-TPB (Fig. 5). As a result, the QY values for F12-TPB were 2-fold larger than those in water, reaching >60%. This increase in QY for counterions with higher fluorination correlated perfectly with the decrease in the H-aggregation state of rhodamine B suggested by absorption spectroscopy. The length of the alkyl chains on rhodamine B had some influence on QYs only for the TPB counterions with intermediate fluorination levels, F5-TPB and F6-TPB, where the QY values increased for the longer alkyl chains (Fig. 5).

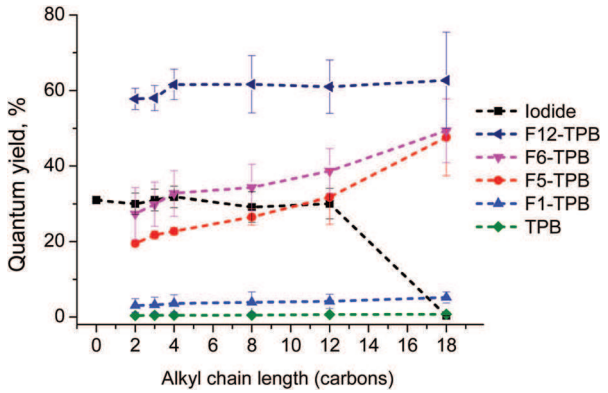

Fig. 5 Fluorescence quantum yields of NPs assembled from alkyl rhodamine B derivatives with different counterions in water. Rhodamine B in water was used as a reference for the quantum yield measurements (QY = 31%).[53]

The nature of the counterion also influenced the spectral shape of the emission of the obtained NPs. We found that the emission maximum shifted to the blue and the long-wavelength shoulder decreased with increasing TPB fluorination level (Fig. 6A). The emission spectra resembled closely to the mirror-image of the absorption spectra. The striking observation was that the emission band narrowed significantly with an increase in the fluorination level (Fig. 6B). Thus, in comparison to R12 iodide in water, the FWHM of the salts with F5-TPB and F12-TPB decreased from 41 nm to 34 nm. A similar tendency was observed for rhodamine B with other alkyl chain lengths. The sharper emission bands may indicate that highly fluorinated TPB counterions not only decrease the H-aggregation inside NPs but also create a rigid environment for the rhodamine dyes.

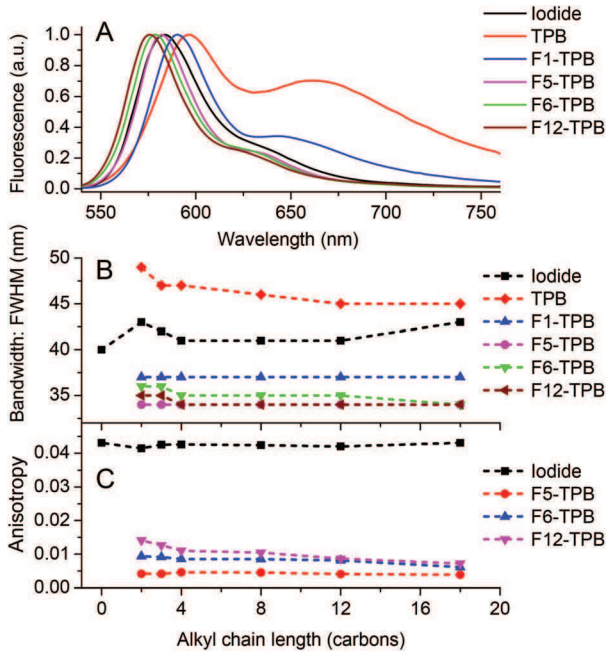

Fig. 6 Effect of the counterion fluorination and the chain length of alkyl rhodamine B on the fluorescence properties of NPs. (A) Normalized fluorescence spectra of R12 with different counterions in water. (B) Full width at half maximum (FWHM) for rhodamine B dyes with alkyl chains of different lengths with different counterions. (C) Fluorescence anisotropy of alkyl rhodamine B dyes in the presence of selected fluorinated counterions.

Fluorescence anisotropy is a measure of the polarization of the emitted light with respect to polarized excitation and is normally used to access the mobility of the fluorophore in a given environment. However, this value can be strongly altered when the excitation energy migrates through dyes exhibiting different orientations within dye assemblies.[54–56] Here, we studied the fluorescence anisotropy of alkyl rhodamine B salts that exhibited high fluorescence QYs, because quenching produces deviation of the anisotropy upwards. All rhodamine B iodides showed an anisotropy value around 0.041–0.043, which is typical for Rhodamine B in water. By contrast, the rhodamine salts with fluorinated TPB, expected to be in the form of NPs, exhibited 5–10-fold lower anisotropy values (Fig. 6C). As the fluorophore rotation inside NPs should be much slower compared to that in water, the low anisotropy values are likely due to very fast energy migration inside NPs. This is not surprising, as the distance between the fluorophores is controlled by the size of the TPB counterions, and thus, varies between 1 and 2 nm. Taking into account that the Förster radius for homo-FRET of alkyl rhodamine B is 5.2 nm,[9] the excitation energy should undergo very fast transfer between the dyes at distances around 1 nm, efficiently depolarizing the emission of the NPs. These results are in line with the low anisotropy values described earlier for polymer NPs encapsulating a salt of R18 with F5-TPB, where energy migration was suggested to occur on a time scale below 30 ps.[9] Remarkably, the anisotropy values increased with increasing fluorination level: F5-TPB < F6-TPB < F12-TPB, suggesting that energy migration is likely the slowest with the F12-TPB counterion. We can hypothesize that F12-TPB, being larger than F5-TPB, should further separate the fluorophores and thus, slow down the energy migration. Alternatively, in the case of F12-TPB, the dyes may have some levels of preferential orientation, which could also contribute to the observed slightly higher values of anisotropy.

Single-particle fluorescence

We then took the most representative ion pairs, R12/F5-TPB and R12/F12-TPB and studied their fluorescence properties at the single particle level. First, we used fluorescence correlation spectroscopy, which is a powerful method to characterize simultaneously the size, brightness and concentration of NPs.[57,58] The correlation times obtained for R12 salts with F5-TPB and F12-TPB were 0.60 and 0.82 ms, which corresponded to NPs of 14 and 19 nm hydrodynamic diameters, respectively (Table 2). These data are in line with our observations by AFM (Table 1). The corresponding single particle brightnesses for these NPs were 340 and 540 equivalents of single rhodamine B dyes in solution. To understand this exceptional brightness of the

Table 2 FCS and single particle microscopy data on NPs assembled from R12 with F5-TPB or F12-TPB in comparison to FluoroSpheres® (FS-28) and QD-585[a]

	R12/F5-TPB	R12/F12-TPB	FS-28	QD-585
Number	0.88 ± 0.1	1.0 ± 0.2	2.5 ± 0.3	0.57 ± 0.05
τ_{corr}	0.60 ± 0.05	0.82 ± 0.08	1.5 ± 0.1	0.98 ± 0.08
Size, nm	14 ± 2	19 ± 3	38 ± 1	22 ± 2
Bri/TMR	310 ± 40	500 ± 100	8 ± 2	780 ± 90
Bri/RhB	340 ± 40	540 ± 100	8 ± 2	850 ± 100
Conc.,nM	3.1 ± 0.4	3.4 ± 0.7	9.4 ± 0.4	1.8 ± 0.3
Dyes/NP	340 ± 50	320 ± 90	—	—
SP-bri	10 ± 1	40 ± 4	36 ± 5	1.0 ± 0.1

[a] FCS and single particle measurements used two-photon and one-photon excitation, respectively. Number is the number of emissive species per excitation volume; τ_{corr} is the correlation time; size is the hydrodynamic diameter; Bri/RhB is the brightness with respect to one molecule of rhodamine B; Conc. is the concentration of emissive species; dyes/NP is the estimated number of R12 dyes per particle. SP-bri is the single-particle brightness based on the photon count obtained from the wide field fluorescence microscopy images of NPs in a gel. The relative values with respect to QD-585 are given.

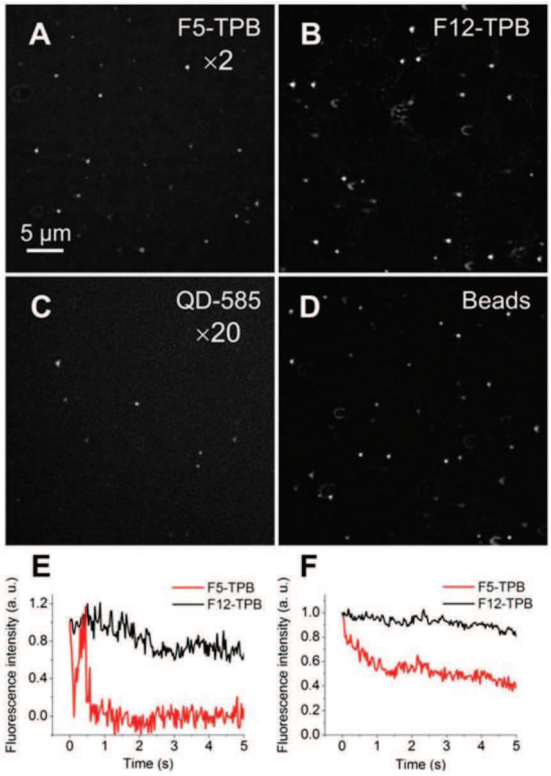

Fig. 7 Wide-field fluorescence microscopy images of counterion-assembled NPs, polystyrene beads and QDs in polyvinyl alcohol gel. Images of NPs assembled from R12 with F5-TPB (A) and F12-TPB (B), compared to QD-585 (C) and polystyrene beads, FluoroSpheres® 535/575 (D). For better visibility, the signal in panels (A) and (C) was amplified 2 and 20-fold, respectively. (E) Representative single-particle emission transients showing turn-off of the F5-TPB NPs and only weak fluctuations for F12-TPB. (F) Dependence of the average fluorescence intensity of NPs with time. The emission of NPs was observed under continuous illumination at 532 nm, with a power of 1 W cm^{-2}.

NPs, we estimated the number of dyes per NPs. We first did an estimation based on the size of NPs assuming the core size (without a monolayer of the TPB counterions of ~1 nm) of 12 and 17 nm for F5-TPB and F12-TPB, respectively and taking the core density of 1 g ml^{-1}. In this case, the numbers of R12 dyes should be ~420 and ~650 for F5-TPB and F12-TPB, respectively. In the alternative approach using FCS, we measured the particle concentrations of 3.1 and 3.4 nM for F5-TPB and F12-TPB, respectively. Then, knowing that the total concentration of R12 in solution is 1 μM, we could estimate the number of R12 dyes per particle to be 340 and 320 for F5-TPB and F12-TPB counterions, respectively, which is in reasonable agreement with theoretical estimations based on the particle size. In the case of F5-TPB, the QY of dyes inside the NPs is close to that of rhodamine B in solution, so that the brightness corresponds well to the number of R12 per particle. In the case of F12-TPB, the QY of the dye in the NPs was nearly double, which explains the nearly twice as high brightness of the corresponding NPs. In comparison to commercial polystyrene NPs of similar color (FluoroSpheres® 535/575, FS-28, Table 2), our particles were 50–70 fold brighter while being of smaller size. In contrast, they were a bit less bright than QD585, likely as a result of the exceptionally high two-photon absorption cross-section of QDs,[3] as compared to FluoroSpheres® and our NPs.

In the second approach, we diluted our R12/F5-TPB and R12/F12-TPB NPs in polyvinyl alcohol gels and imaged single particles using wide-field fluorescence microscopy, with one-photon excitation. The data were directly compared to commercial FluoroSpheres® 535/575 and QD-585. We found that our NPs appeared as bright dots with an about 4-fold higher average intensity for F12-TPB NPs as compared to F5-TPB NPs, which is in line with the higher QY and FCS brightness of the former. Moreover, F12-TPB NPs were as bright as FluoroSpheres® and ~40-fold brighter than QD-585 (Table 2 and Fig. 7). According to FCS, the number of R12 dyes per F12-TPB NPs is 320, so that their total brightness is $N \times \varepsilon \times QY = 320 \times 125\,000 \times 0.6 = 2.4 \times 10^7\ M^{-1}\ cm^{-1}$. When excited at 532 nm, this value is slightly lower: $320 \times 57\,000 \times 0.6 = 1.1 \times 10^7\ M^{-1}\ cm^{-1}$. On the other hand, FCS suggests that the brightness of R12/F12-TPB NPs corresponds to that of 540 rhodamine B molecules in solution. This should be valid for both two-photon and single photon excitation as our NPs are composed of the same rhodamine B fluorophore. Therefore, the estimated brightness of our NPs excited at 532 nm is $N \times \varepsilon(532) \times QY = 540 \times 57\,000\ M^{-1}\ cm^{-1} \times 0.31 = 9.5 \times 10^6\ M^{-1}\ cm^{-1}$, which is very close to that estimated from the number of dye particles. In contrast, the brightness of QD-585 at 532 nm (one-photon) excitation is $\varepsilon \times QY = 310\,000\ M^{-1}\ cm^{-1} \times 0.67 = 2.1 \times 10^5\ M^{-1}\ cm^{-1}$ and thus, >45-fold less bright than our counterion-assembled NPs. Thus, the experimental difference in brightness obtained by microscopy confirms the theoretical estimations. The other remarkable feature was that ~50% of NPs built from F5-TPB showed rapid blinking that ended up with a dark state of the particles (Fig. 7E). Previously, we showed a similar phenomenon for PLGA NPs loaded with a

similar dye (R18) with the same F5-TPB counterion and assigned it to fast excitation energy migration through the dyes.[9] However, some heterogeneity in the particle behavior was observed, so that the averaged curve obtained from multiple particles of the image showed a smoother drop in the fluorescence, with nevertheless a loss of ~50% of initial intensity within 2 seconds (Fig. 7F). By contrast, F12-TPB did not show blinking behavior, with only a few exceptions, as we could see from the relatively stable and only weakly fluctuating fluorescence (mainly due to slow particle diffusion within the gel) at the single particle level (Fig. 7E). Moreover, the averaged ensemble fluorescence of NPs showed a much slower decrease as a function of time (Fig. 7F), *i.e.* much higher photostability compared to F5-TPB NPs. This striking result shows that the level of fluorination and/or the larger size of the counterion can modulate the blinking and photostability of the whole particle.

Application for light harvesting

As our counterion-assembled NPs contain a large number of fluorescent dyes, which are strongly coupled by energy transfer, we hypothesized that they could be very efficient energy donors, similar to light-harvesting complexes.[59–62] To check this idea, we encapsulated an energy acceptor Cy-derivative (C2-Cy5) inside our most interesting salts of R12 with F5-TPB and F12-TPB. As the cyanine dye is also cationic, we expected that it can efficiently co-precipitate forming blended NPs with R12 (Fig. 8). Increasing the C2-Cy5 concentration produced a sequential increase in the acceptor emission, accompanied by a decrease in the donor fluorescence (Fig. 8 and S6†). For F12-TPB, >50% FRET efficiency was already observed at a donor/acceptor ratio of 1000/1, which is outstanding (Fig. 8B). In the case of F5-TPB, somewhat higher acceptor concentrations were needed to reach >50% FRET. In both cases at a 200/1 donor/acceptor ratio, where statistically each NP should contain at least one C2-Cy5 acceptor, the FRET efficiency was 60 and 80% for F5-TPB and F12-TPB, respectively. To quantify the antenna effect, we recorded the excitation spectra of the donor and acceptor by detecting the emission of the acceptor (Fig. S6 and S7†). The antenna effect (AE) was then expressed as the ratio of the maximal excitation intensity of the donor to that of the acceptor.[63] For F12-TPB the value of the antenna effect reached 200 at the donor/acceptor ratio of 1000/1, though for F5-TPB the effect was 2-fold smaller. The theoretical value of the antenna effect could be calculated as AE = $(n_D\varepsilon_D E)/(n_A\varepsilon_A)$, where n_D and n_D are the numbers of donors and acceptors, respectively, per particle, ε_D and ε_A are the extinction coefficients of donors and acceptors, respectively, and E is the FRET efficiency. For F12-TPB NPs at a donor acceptor ratio of 1000/1, we assume that the NPs containing ~320 R12 donors (from FCS) would contain only one C2-Cy5 acceptor. Then the formula above gives AE ≈ 91, which is somewhat lower than that experimentally observed. It is possible that the real number of R12 dyes per F12-TPB particle is higher as for instance suggested from geometrical estimation (~650), which could explain the observed high AE values. In any case, our results indicate that nearly all the energy of the donors of one NP was efficiently transferred to a single C2-Cy5-acceptor. Importantly, the QY values of C2-Cy5 inside the dye NPs for donor/acceptor ratios of 1/1000–1/200 was around 30 and 50% for F5-TPB and F12-TPB counterions, respectively, and thus, similar or even higher than that in methanol (Fig. S9†). These data show that these NPs can readily encapsulate other cationic dyes at small quantities, ensuring their efficient fluorescence, especially for the most fluorinated F12-TPB counterion.

Application for cellular imaging

Finally, we explored whether the obtained NPs can be applied to cellular imaging. In particular, we were interested in the

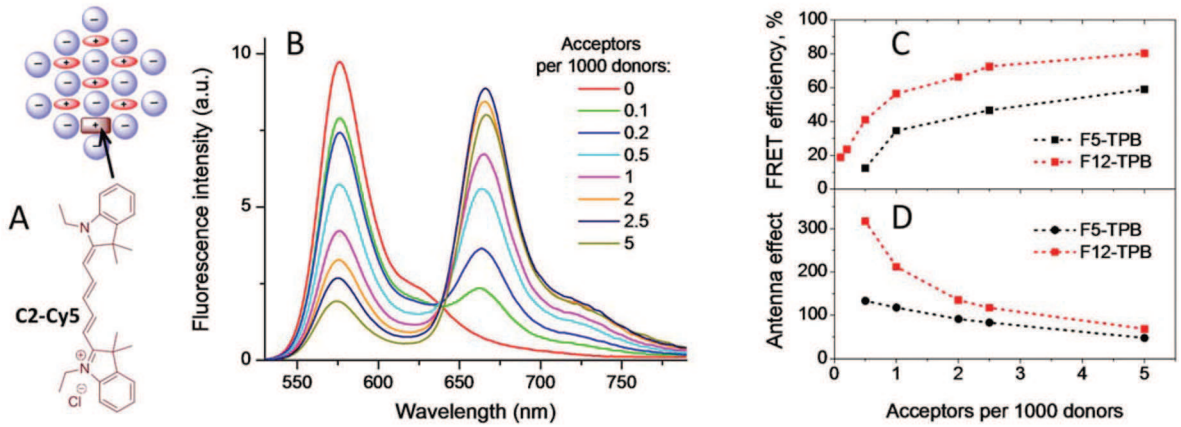

Fig. 8 FRET from R12-based counterion-assembled NPs to C2-Cy5 acceptor. (A) Chemical structure of the C2-Cy5 acceptor and its encapsulation into counterion-assembled NPs. (B) Fluorescence spectra of R12 NPs with F12-TPB counterion containing different amounts of C2-Cy5 acceptor dye. Excitation wavelength was 520 nm. (C) FRET efficiency calculated from the donor fluorescence for NPs with F5-TPB and F12-TPB counterions at different acceptor concentrations. (D) Antenna effect calculated from the excitation spectra (ratio of donor intensity maximum to the acceptor intensity maximum emission was detected at 680 nm) for NPs with two different counterions.

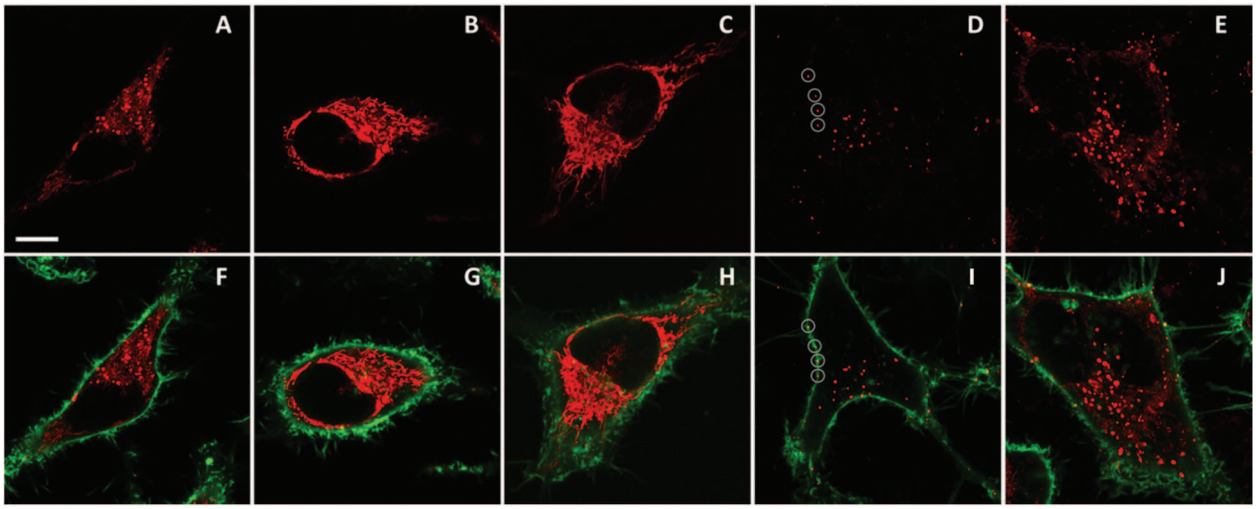

Fig. 9 Fluorescence imaging of counterion-assembled NPs in HeLa cells. NPs prepared from R12 salts with F5-TPB (A, B, F, G) or F12-TPB (D, E, I, J) were incubated for 1 h (A, F, D, I) and 6 h (B, G, E, J) at 37 °C. Control R12 iodide dye was incubated with cells for 1h (C, H). Circles in panels (D) and (I) highlight NPs localized at the plasma membrane. Upper panels (in red) present images of NPs using an excitation at 561 nm and a detection range of 567–700 nm, while lower panels present images of both NPs (red) and the plasma membrane marker WGA-AlexaFluor®488 (green). The latter was observed using an excitation at 488 nm and a detection range of 503–550 nm. To enable the comparison of the intensities in the red channel, the imaging conditions were the same in all cases except for panel (B), where the scale was extended 3-fold (due to much higher signal). When added to the cells, the NPs were diluted to a final R12 concentration of 50 nM. Scale bar is 10 μm.

ability of the particles to enter cells and to retain their integrity. To this end, we incubated representative NPs (R12 salt with F5-TPB and F12-TPB counterions) with HeLa cells and imaged the cells using confocal fluorescence microscopy. Both types of NPs could enter the cells, but their behavior was surprisingly different. We found that after 1 h of incubation, NPs based on F5-TPB showed intracellular fluorescence in the form of dots and diffuse fluorescence (Fig. 9A and F). After 6 h of incubation, only a diffuse yet structured fluorescence pattern was observed (Fig. 9B and G). To verify whether this pattern originates from the released R12 dyes, we incubated HeLa cells for 1 h with a water soluble R12 iodide. In this case, a very similar fluorescence pattern was observed, which corresponds probably to intracellular organelles (Fig. 9C and H). Furthermore, co-staining with Mito-Tracker Green® showed a perfect colocalization with R12 iodide (Fig. S10†), indicating that the cationic dye accumulated in the mitochondria.

Thus, our data showed that NPs based on F5-TPB could enter the cells on a time scale of hours and then disassemble, releasing the R12 dyes. In sharp contrast, after 1 h of incubation, NPs based on F12-TPB showed exclusively dotted fluorescence patterns (Fig. 9D and J) both inside the cells and at the level of the plasma membranes. After 6 h of incubation, the intracellular fluorescence markedly increased, mainly in the form of dots, indicating an accumulation of NPs inside the cells (Fig. 9E and J). However, some diffuse intracellular fluorescence also appeared, suggesting a partial release of R12 dyes from NPs. Nevertheless, it is clear that NPs built from F12-TPB counterions are far more stable in cells than those built from F5-TPB. The higher stability seems to correlate with the higher fluorination of the F12-TPB counterion, which should make NPs more "inert" with respect to biological media.

Discussion

Previous studies by the groups of Warner and Yao suggested the ion-association method for the preparation of NPs from cationic dyes and hydrophobic counterions.[30,31] Here, for the first time, effects of the fluorination of the bulky hydrophobic counterion and the hydrophobicity of the cationic dye were studied in order to find the brightest possible nanomaterials. Though we observed that longer alkyl chains (*i.e.* higher hydrophobicity) decreased the dye H-aggregation and improved fluorescence quantum yields, this effect was relatively weak. On the other hand, a clear-cut improvement of the NPs' fluorescence properties was observed on increase in the counterion fluorination. While the non-fluorinated bulky counterion (TPB) produced strongly quenched NPs, the most fluorinated counterion (F12-TPB) improved the QY values ~100-fold up to 60%. QY values grew sequentially with the fluorination level and this was accompanied by a gradual decrease in the H-aggregation of the dyes. Remarkably, fluorination also influenced the width of the emission band, so that for the most fluorinated counterion the emission band was even sharper than for rhodamine B in solution. We also showed that the NPs assembled from the most fluorinated F12-TPB present the highest brightness and photostability at the single particle level. Fluorinated counterions such as F1-TPB,[31,32,36] bis(tri-

fluoromethanesulfonyl)imide and bis(pentafluoroethanesulfonyl)imide[33] were used previously to prepare fluorescent NPs, however, the role of fluorine in these ions to control NPs' fluorescence was not clarified. Few reports showed the role of fluorinated environment for improving the fluorescence properties of dyes. One report showed that perfluorinated solvents could decrease the dye photobleaching and vibrational quenching.[49] Another one showed the improvement of dye brightness in fluorinated emulsions,[50] and dye-assembled nanomaterials.[51] Here, we found that a gradual increase in the fluorination of the counterion improves a bunch of fluorescence characteristics of the ionic dye: it minimizes H-aggregation, increases fluorescence quantum yield, sharpens the emission bands, and improves single particle brightness and photostability.

An important finding of the present work is the excellent single particle performance of counterion-assembled NPs. So far, only bulk solution properties of this type of NPs have been reported,[31,33–35] and these cannot be directly extrapolated to the particle performance under the microscope. In this respect, we have clearly shown that our counterion-assembled NPs based on fluorinated counterions are much brighter than QDs under single photon excitation. Thus, we showed here that the organic particles of 19 nm hydrodynamic radius (R12/F12-TPB) are ~40-fold brighter than inorganic semiconductor particles of similar size (~20 nm). However, if the fluorescent cores are compared, the brightness per volume is comparable, as the size of the QD core (3–8 nm) is much smaller than its hydrodynamic size that includes all the necessary shells.[64,65] Indeed, the size of the QD 585 core is ~5 nm, so that its volume is 14- and 39-fold smaller than that of F5-TPB (12 nm) and F12-TPB (17 nm) NPs, respectively, in line with the difference in brightness with our organic NPs. In this respect, the key advantage of the counterion-assembled NPs is their capacity to be solubilized in water with a minimal size of the shell. In the present case, the shell of our NPs is just a monolayer of counterions (thickness ~1 nm), while QDs require, in addition to the thin ZnO shell, a 5–10 nm thick organic shell to retain the colloidal stability and highly emissive properties of their core in water.[3,66]

On the other hand, single particle measurements revealed some key differences between F5-TPB and F12-TPB, which were not detectable from bulk experiments. We found that NPs built from F5-TPB showed on/off switching (blinking). This phenomenon was previously described for PLGA NPs encapsulating R18 with the same counterion, and this phenomenon was assigned to the exceptional communication of the dyes due to fast exciton diffusion.[9] A similar blinking phenomenon was also reported for dendrites,[67] conjugated polymers[68] and J-aggregates,[69] which also present remarkable exciton diffusion behavior. Therefore we speculate that in the present case, light induces the formation of dark species of rhodamine B that can quench the whole ensemble of ~300 dyes. The fast energy migration for NPs based on F5-TPB was confirmed by the exceptionally low values of anisotropy, similar to those previously reported for PLGA NPs.[9] Remarkably, NPs based on the most fluorinated counterion F12-TPB showed almost no blinking behavior. Two reasons could be behind this dramatic difference between F5-TPB and F12-TPB. As we observe some increase in the anisotropy for F12-TPB, one could expect that the inter-fluorophore communication is slower with this counterion, which may thus make the blinking inefficient. However, this scenario is unlikely because F12-TPB NPs are even more efficient energy donors than F5-TPB NPs in our FRET experiments. Therefore, a more probable reason is that the higher fluorination and larger size of F12-TPB change the mode of R12 dye assembly favoring larger distances between the dyes within 1–2 nm range, which may prevent formation of the dark species.

Here, we found that our counterion-assembled NPs are exceptional FRET donors to single acceptors, with an antenna effect reaching 200, which is a rare observation. In other multichromophore systems, such as dye-doped silica NPs[70,71] and DNA nanostructures,[63,72] the efficient FRET was reported for significantly smaller number of donor dyes. The efficient FRET in counterion-assembled NPs was reported independently by the groups of Warner[73] and Yao,[74] though the phenomenon was not explained. As the particle size in the case of F12-TPB (19 nm according to FCS) is larger than the double Förster radius of the rhodamine B–C2-Cy5 pair ($2 \times R_0$ ~10 nm), the observed exceptional FRET efficiency and the antenna effect can be explained by ultrafast energy migration between the energy donors, until it is transferred to the acceptor. This is supported by our anisotropy data, as well as by the observation of on/off switching for F5-TPB NPs. Energy migration is considered as an important mechanism that ensures a high energy transfer efficiency from multiple donors to a single acceptor in light-harvesting systems[59–62] as well as in conjugated polymers[19] and some dye-doped nanostructures.[71] The present work suggests that this energy migration process can be behind the observed remarkably high FRET efficiency and antenna effect in counterion-assembled NPs.

The final aspect is the compatibility of the present NPs with the cellular environment. As these NPs are formed by self-assembly through non-covalent interactions, they may disassemble in the cells because of high dilution (20-fold with respect to the original formulation) and the interactions with the cellular components. F5-TPB NPs are indeed not sufficiently stable after entering the cells, as can be seen from the diffuse fluorescence inside the cells similar to that obtained with the free dye. Comparison with the free dye R12 iodide suggested that these particles, after entering the cells, likely disassemble, so that the released rhodamine dyes can accumulate in the mitochondria. This tropism of R12 for mitochondria is consistent with earlier reports showing that hydrophobic derivatives of rhodamines readily localize in the mitochondria, driven by the electric potential.[75,76] Moreover, a recent report showed similar mitochondrial staining without dotted fluorescence for cells incubated with counterion-assembled NPs of rhodamine 6G,[77] which confirms that these NPs have a tendency to disassemble inside the cells. Therefore, it is clear that R12/F5-TPB salt in pure form cannot be used for

cellular imaging but requires protection, for instance using a polymer, as we showed recently.[9] In contrast, NPs based on the most fluorinated counterion F12-TPB showed much higher stability than F5-TPB NPs, allowing observation of NPs inside cells on the time scale of hours. This shows that a high level of fluorination can prevent NPs form disassembly at high dilution in a complex biological environment. To the best of our knowledge, for the first time counterion-assembled NPs stable in a cellular context were prepared and the role of fluorination in the particle stability is described. This unique stabilization effect could be explained by the fact that perfluorinated compounds present orthogonal properties to both aqueous and hydrophobic environments.[37–39] Thus, fluorination probably decreases the affinity of the counterion to the hydrophobic sites in the cells and inhibits the interaction of the rhodamine dye with cellular compartments.

Experimental section

Sodium tetraphenylborate (≥99.5%), sodium tetrakis(4-fluorophenyl)borate dihydrate (≥97.0%), lithium tetrakis(pentafluorophenyl)borate ethyl etherate, sodium tetrakis[3,5-bis(trifluoromethyl)phenyl]borate, acetonitrile, tetrakis[3,5-bis(1,1,1,3,3,3-hexafluoro-2-methoxy-2-propyl)phenyl]borate (≥99.5%) were purchased from Sigma-Aldrich and used as received. Milli-Q water (Millipore) was used in all experiments. All starting materials for synthesis were purchased from Alfa Aesar and Sigma Aldrich or TCI Europe and used as received unless stated otherwise. NMR spectra were recorded on a Bruker Avance III 400 MHz spectrometer. Mass spectra were obtained using an Agilent Q-TOF 6520 mass spectrometer. Synthesis of alkyl-rhodamine B dyes is described in the ESI.†

Preparation of fluorescent NPs

The rhodamine B derivative was dissolved at 1 mM in DMSO. The concentration was measured by photometry using the extinction coefficient for all rhodamine B derivatives 125 000 M^{-1} cm^{-1} in methanol.[78] To prepare 1 μM of nanoparticle solution, 2 μL of 1 mM rhodamine B derivative stock solution was added quickly under stirring (shaking) using a micropipette to 2 mL of Milli-Q® water (Millipore). Then to the obtained solution a 10-fold excess of the corresponding borate solution (20 μL of 1 mM stock solution) was added quickly under stirring using a micropipette.

For the DLS measurements of nanoparticle suspension 5 μM dye concentration was used to obtain sufficient signal. To this end, 10 μL of 1 mM rhodamine B derivative stock solution was added quickly under stirring using a micropipette to a 1.9 mL of Milli-Q® water (Millipore). Then to the obtained solution 10-fold excess of the corresponding borate solution (100 μL of 1 mM stock solution) was added quickly under stirring using a micropipette. Zeta potential measurements were performed using 20 μM dye concentration.

For the DLS and AFM measurements, to remove possible aggregates the obtained solution of prepared nanoparticles was additionally filtered through a 0.1 μm PVDF NS "Ultrafree®-CL" centrifugal filter unit (Merck Millipore).

Optical spectroscopy

Absorption and emission spectra were recorded on a Cary 400 Scan UV-visible spectrophotometer (Varian) and a FluoroMax-4 spectrofluorometer (Horiba Jobin Yvon) equipped with a thermostated cell compartment, respectively. For standard recordings of fluorescence spectra, the excitation wavelength was set to 520 nm. The fluorescence spectra were corrected for detector response and lamp fluctuations. Fluorescence quantum yields were calculated using rhodamine B in water (QY = 31%)[53] with an absorbance of 0.1 at 520 nm as a reference. Hydrodynamic diameter and zeta-potential measurements were performed on a Zetasizer Nano series DTS 1060 (Malvern Instruments S.A.) with a laser source at 633 nm.

Other software

The calculations were performed using Hyperchem 8.0. The starting geometry of borate ions was subsequently optimized using a Polak–Ribière algorithm (conjugate gradient) under vacuum with a RMS gradient of 0.1 kcal $(A\ mol)^{-1}$. The resulting structures of counter-ions were relatively similar to each other and showed common features such as a symmetric arrangement.

AFM measurements

AFM measurements were performed using a Solver-Pro-M (NT-MDT) instrument. The measurements were performed in the liquid phase. Cantilevers were NSG03 (NT-MDT) with a tip curvature radius of 10 nm. The NPs were prepared as described before. To deposit NPs on the mica surface, 100 μL of 10–100 mM calcium chloride solution (depending on the counterion) was first incubated for 30 min. Then, the solution was removed with a filter paper and 100 μL of an undiluted suspension of NPs was deposited on the mica surface. After 30 min, the solution was removed using a filter paper and then replaced with 100 μL of 10–100 mM solution of calcium chloride. The obtained sample was imaged in the liquid phase, using the tapping mode (~37 kHz).

Fluorescence correlation spectroscopy (FCS) and data analysis

FCS measurements were performed on a two-photon platform including an Olympus IX70 inverted microscope, as described previously.[58] Two-photon excitation at 830 nm (1–5 mW laser output power) was provided using an InSight DeepSee laser (Spectra Physics). The measurements were carried out in an eight-well Lab-Tek II coverglass system, using a 300 μL volume per well. The focal spot was set about 20 μm above the coverslip. The normalized autocorrelation function, $G(\tau)$ was calculated online by using an ALV-5000E correlator (ALV, Germany) from the fluorescence fluctuations, $\delta F(t)$, by $G(\tau) = \langle \delta F(t) \delta F(t+\tau) \rangle / \langle F(t) \rangle^2$ where $\langle F(t) \rangle$ is the mean fluorescence signal, and τ is

the lag time. Assuming that lipid nano-droplets diffuse freely in a Gaussian excitation volume, the correlation function, $G(\tau)$, calculated from the fluorescence fluctuations was fitted according to Thompson:[79]

$$G(\tau) = \frac{1}{N}\left(1+\frac{\tau}{\tau_d}\right)^{-1}\left(1+\frac{1}{S^2}\frac{\tau}{\tau_d}\right)^{-1/2}$$

where τ_d is the diffusion time, N is the mean number of fluorescent species within the two-photon excitation volume, and S is the ratio between the axial and lateral radii of the excitation volume. The excitation volume is about 0.34 fL and S is about 3 to 4. Typical data recording time was 5 min, using freshly prepared PLGA NPs without further dilution. The measurements were done with respect to a reference 5(6)-carboxytetramethylrhodamine (TMR, from Sigma-Aldrich) in water. The hydrodynamic diameter, d, of NPs was calculated as: $d_{NPs} = \tau_{d(NPs)}/\tau_{d(TMR)} \times d_{TMR}$, where d_{TMR} is a hydrodynamic diameter of TMR (1.0 nm). The concentration of NPs was calculated from the number of species by: $C_{NPs} = N_{NPs}/N_{TMR} \times C_{TMR}$, using a TMR concentration of 50 nM.

Single-particle imaging

Counterion-assembled NPs were immobilized in polyvinyl alcohol (Aldrich) gel. 3 g of poly(vinyl alcohol) (M_w 89 000–98 000, 99+%) in 10 mL of degassed Milli-Q® water (Millipore) was stirred at 90–100 °C for two hours to obtain a homogeneous 30 wt% PVA gel. Then 300 μL of the PVA gel were added into a cell of the Lab-Tek® plate and immediately after 50 μL of 1 μM particle solution were injected into the PVA gel and mixed using the tip of the micropipette. Then the Lab-Tek® plate was kept for 5 h in a desiccator under vacuum. Quantum dots (QDot-585 streptavidin conjugate, Life Technologies) and FluoroSpheres® 535/575 (diameter 0.028 μm, carboxylate modified, Invitrogen) at ~6 pM concentration were immobilized and imaged in the same way. Single particle measurements were performed in the TIRF (Total Internal Reflection Fluorescence) mode on a home-made wide-field setup based on an Olympus IX-71 microscope with an oil immersion objective (NA = 1.49, 100×). A DPPS (Cobolt) continuous wave (CW) laser emitting at 532 nm was used for excitation. The laser intensity was set to 1 W cm^{-2} using a polarizer and a half-wave plate (532 nm). The fluorescence signal was recorded with an EMCCD (ImagEM Hamamatsu). The presented images were an average of the first 30 frames recorded with an acquisition time of 30.67 ms per frame.

Cellular studies

HeLa cells (ATCC® CCL-2) were grown in Dulbecco's modified Eagle's medium (DMEM, Gibco-Invitrogen), supplemented with 10% fetal bovine serum (FBS, Lonza) and 1% antibiotic solution (penicillin–streptomycin, Gibco-Invitrogen) at 37 °C under a humidified atmosphere containing 5% CO_2. Cells were seeded onto a chambered coverglass (IBiDi) at a density of 5×10^4 cells per well 24 h before the microscopy measurement. For imaging, the culture medium was removed and the attached cells were washed with Opti-MEM (Gibco-Invitrogen). Then, a freshly prepared solution of NPs (at 20-fold dilution of the original formulation, corresponding to ~50 nM dye) in Opti-MEM was added to the cells and incubated for different time periods. Cell membrane staining with wheat germ agglutinin-Alexa488 was done for 10 min at rt before the measurements. Fluorescence images were taken on a Leica TSC SPE confocal microscope. The microscope settings were: a 561 nm laser source with a 567–700 nm detection range for imaging counterion-assembled rhodamine NPs and 488 nm excitation with a 503–550 nm emission range for imaging the plasma membrane marker WGA-AlexaFluor®488 (green) or MitoTracker® green (Life Technologies).

Conclusion

In the present work, we prepared nanoparticles through aggregation of alkylated lipophilic rhodamine B derivatives with fluorinated tetraphenylborate counterions. It was found that fluorination degree of the counterion produced a profound effect on the fluorescence properties of NPs. Thus, for the most fluorinated counterion, we obtained rhodamine NPs with a quantum yield reaching 40–60% and their emission bandwidth was ~20% narrower than rhodamine B in organic solvents. Absorption spectra suggested that the fluorinated counterions prevent H-aggregation of rhodamines in the solid state, thus favoring enhanced emission. According to fluorescence correlation spectroscopy these NPs emit like 300–500 rhodamines together, so that their brightness should be around 2.4×10^7 M^{-1} cm^{-1} (extinction coefficient × quantum yield). This high brightness was confirmed by single molecule microscopy, where NPs with the most fluorinated counterion (48 fluorines) presented ~40-fold higher brightness than quantum dots (QD585 at 532 nm excitation). Remarkably, we also found that counterion with the highest fluorination favored higher photostability and suppressed blinking of the NPs. We hypothesize that the size of the counterion and its fluorination level should finely tune the spacing between dyes within 1–2 nm range that produce these drastic variations in the fluorescence properties. This short distance ensured fast exciton diffusion, revealed by fluorescence anisotropy, and efficient FRET to single cyanine-5 acceptors with a light-harvesting antenna effect reaching 200. Finally, our cellular studies showed that NPs with the most fluorinated counterion are rather stable after entry into living cells, while NPs built from the less fluorinated counterion disassembled after 1 h and their released dye accumulated in the mitochondria. Thus, the counterion fluorination is crucial for correct ordering of dyes in the solid state without aggregation-caused quenching. It enables the preparation of NPs with high fluorescence brightness and photostability, narrow-band emission, fast energy transfer and high intracellular stability. We believe that these findings will facilitate the route to next generation of nanomaterials for light harvesting and bioimaging applications.

Acknowledgements

I.S. acknowledges support from French Embassy. This work was supported by Université de Strasbourg (IdEX 2015, W15RAT68) and ERC Consolidator grant BrightSens 648528. We thank Pascal Didier and Frederic Przybilla for help with wide-field microscopy setup.

References

1 H.-S. Peng and D. T. Chiu, *Chem. Soc. Rev.*, 2015, **44**, 4699–4722.
2 M. Chen and M. Yin, *Prog. Polym. Sci.*, 2014, **39**, 365–395.
3 D. R. Larson, W. R. Zipfel, R. M. Williams, S. W. Clark, M. P. Bruchez, F. W. Wise and W. W. Webb, *Science*, 2003, **300**, 1434–1436.
4 W. W. Yu, L. H. Qu, W. Z. Guo and X. G. Peng, *Chem. Mater.*, 2003, **15**, 2854–2860.
5 L. D. Lavis and R. T. Raines, *ACS Chem. Biol.*, 2008, **3**, 142–155.
6 C. Wu and D. T. Chiu, *Angew. Chem., Int. Ed.*, 2013, **52**, 3086–3109.
7 C. Wu, B. Bull, C. Szymanski, K. Christensen and J. McNeill, *ACS Nano*, 2008, **2**, 2415–2423.
8 A. Wagh, S. Y. Qian and B. Law, *Bioconjugate Chem.*, 2012, **23**, 981–992.
9 A. Reisch, P. Didier, L. Richert, S. Oncul, Y. Arntz, Y. Mely and A. S. Klymchenko, *Nat. Commun.*, 2014, **5**, 4089.
10 K. Li and B. Liu, *Chem. Soc. Rev.*, 2014, **43**, 6570–6597.
11 J. Schill, A. P. H. J. Schenning and L. Brunsveld, *Macromol. Rapid Commun.*, 2015, **36**, 1306–1321.
12 X.-d. Wang, R. J. Meier and O. S. Wolfbeis, *Adv. Funct. Mater.*, 2012, **22**, 4202–4207.
13 K. Trofymchuk, A. Reisch, I. Shulov, Y. Mely and A. S. Klymchenko, *Nanoscale*, 2014, **6**, 12934–12942.
14 G. Sun, M. Y. Berezin, J. Fan, H. Lee, J. Ma, K. Zhang, K. L. Wooley and S. Achilefu, *Nanoscale*, 2010, **2**, 548–558.
15 H. Yao, *Springer Ser. Fluoresc.*, 2010, **9**, 285–304.
16 K. Li, Z. S. Zhu, P. Q. Cai, R. R. Liu, N. Tomczak, D. Ding, J. Liu, W. Qin, Z. J. Zhao, Y. Hu, X. D. Chen, B. Z. Tang and B. Liu, *Chem. Mater.*, 2013, **25**, 4181–4187.
17 S. Fery-Forgues, *Nanoscale*, 2013, **5**, 8428–8442.
18 J. Pecher and S. Mecking, *Chem. Rev.*, 2010, **110**, 6260–6279.
19 S. W. Thomas Iii, G. D. Joly and T. M. Swager, *Chem. Rev.*, 2007, **107**, 1339–1386.
20 M. Kasha, H. R. Rawls and M. A. El-Bayoumi, *Pure Appl. Chem.*, 1965, **11**, 371–392.
21 F. Würthner, T. E. Kaiser and C. R. Saha-Moller, *Angew. Chem., Int. Ed.*, 2011, **50**, 3376–3410.
22 G. Battistelli, A. Cantelli, G. Guidetti, J. Manzi and M. Montalti, *Wiley Interdiscip. Rev.: Nanomed. Nanobiotechnol.*, 2015, DOI: 10.1002/wnan.1351.
23 Y. Hong, J. W. Y. Lam and B. Z. Tang, *Chem. Soc. Rev.*, 2011, **40**, 5361–5388.
24 Y. Hong, J. W. Y. Lam and B. Z. Tang, *Chem. Commun.*, 2009, 4332–4353.
25 W. Qin, K. Li, G. Feng, M. Li, Z. Yang, B. Liu and B. Z. Tang, *Adv. Funct. Mater.*, 2014, **24**, 635–643.
26 T. T. Vu, S. Badre, C. Dumas-Verdes, J. J. Vachon, C. Julien, P. Audebert, E. Y. Senotrusova, E. Y. Schmidt, B. A. Trofimov, R. B. Pansu, G. Clavier and R. Meallet-Renault, *J. Phys. Chem. C*, 2009, **113**, 11844–11855.
27 K. Petkau, A. Kaeser, I. Fischer, L. Brunsveld and A. P. H. J. Schenning, *J. Am. Chem. Soc.*, 2011, **133**, 17063–17071.
28 E. Genin, Z. Gao, J. A. Varela, J. Daniel, T. Bsaibess, I. Gosse, L. Groc, L. Cognet and M. Blanchard-Desce, *Adv. Mater.*, 2014, **26**, 2258–2261.
29 I. Krossing and I. Raabe, *Angew. Chem., Int. Ed.*, 2004, **43**, 2066–2090.
30 D. K. Bwambok, B. El-Zahab, S. K. Challa, M. Li, L. Chandler, G. A. Baker and I. M. Warner, *ACS Nano*, 2009, **3**, 3854–3860.
31 H. Yao and K. Ashiba, *RSC Adv.*, 2011, **1**, 834–838.
32 T. Enseki and H. Yao, *Chem. Lett.*, 2012, **41**, 1119–1121.
33 A. N. Jordan, S. Das, N. Siraj, S. L. de Rooy, M. Li, B. El-Zahab, L. Chandler, G. A. Baker and I. M. Warner, *Nanoscale*, 2012, **4**, 5031–5038.
34 S. L. de Rooy, S. Das, M. Li, B. El-Zahab, A. Jordan, R. Lodes, A. Weber, L. Chandler, G. A. Baker and I. M. Warner, *J. Phys. Chem. C*, 2012, **116**, 8251–8260.
35 Z.-m. Ou, H. Yao and K. Kimura, *Bull. Chem. Soc. Jpn.*, 2007, **80**, 295–302.
36 H. Yao, M. Yamashita and K. Kimura, *Langmuir*, 2009, **25**, 1131–1137.
37 J. A. Gladysz, D. P. Curran and I. T. Horváth, *Handbook of Fluorous Chemistry*, Wiley-VHC, Weinheim, 2004.
38 I. T. Horváth, *Acc. Chem. Res.*, 1998, **31**, 641–650.
39 M. Cametti, B. Crousse, P. Metrangolo, R. Milani and G. Resnati, *Chem. Soc. Rev.*, 2012, **41**, 31–42.
40 M. L. Tang and Z. Bao, *Chem. Mater.*, 2011, **23**, 446–455.
41 J. M. Vincent, *Chem. Commun.*, 2012, **48**, 11382–11391.
42 R. Schmidt, M. M. Ling, J. H. Oh, M. Winkler, M. Könemann, Z. Bao and F. Würthner, *Adv. Mater.*, 2007, **19**, 3692–3695.
43 J. W. Ward, R. Li, A. Obaid, M. M. Payne, D.-M. Smilgies, J. E. Anthony, A. Amassian and O. D. Jurchescu, *Adv. Funct. Mater.*, 2014, **24**, 5052–5058.
44 C. I. Castro and J. C. Briceno, *Artif. Organs*, 2010, **34**, 622–634.
45 J. M. Janjic and E. T. Ahrens, *Wiley Interdiscip. Rev.: Nanomed. Nanobiotechnol.*, 2009, **1**, 492–501.
46 E. T. Ahrens, R. Flores, H. Xu and P. A. Morel, *Nat. Biotechnol.*, 2005, **23**, 983–987.
47 H. Bronstein, J. M. Frost, A. Hadipour, Y. Kim, C. B. Nielsen, R. S. Ashraf, B. P. Rand, S. Watkins and I. McCulloch, *Chem. Mater.*, 2013, **25**, 277–285.
48 J. W. Jo, S. Bae, F. Liu, T. P. Russell and W. H. Jo, *Adv. Funct. Mater.*, 2015, **25**, 120–125.

49 H. Sun, A. Putta, J. P. Kloster and U. K. Tottempudi, *Chem. Commun.*, 2012, **48**, 12085–12087.
50 E. M. Sletten and T. M. Swager, *J. Am. Chem. Soc.*, 2014, **136**, 13574–13577.
51 S. Shin, S. H. Gihm, C. R. Park, S. Kim and S. Y. Park, *Chem. Mater.*, 2013, **25**, 3288–3295.
52 M. S. T. Goncalves, *Chem. Rev.*, 2009, **109**, 190–212.
53 D. Magde, G. E. Rojas and P. G. Seybold, *Photochem. Photobiol.*, 1999, **70**, 737–744.
54 K. A. Colby, J. J. Burdett, R. F. Frisbee, L. Zhu, R. J. Dillon and C. J. Bardeen, *J. Phys. Chem. A*, 2010, **114**, 3471–3482.
55 E. K. L. Yeow, K. P. Ghiggino, J. N. H. Reek, M. J. Crossley, A. W. Bosnian, A. P. H. J. Scheming and E. W. Meijer, *J. Phys. Chem. B*, 2000, **104**, 2596–2606.
56 M. N. Berberan-Santos, P. Choppinet, A. Fedorov, L. Jullien and B. Valeur, *J. Am. Chem. Soc.*, 1999, **121**, 2526–2533.
57 K. Koynov and H. J. Butt, *Curr. Opin. Colloid Interface Sci.*, 2012, **17**, 377–387.
58 A. S. Klymchenko, E. Roger, N. Anton, H. Anton, I. Shulov, J. Vermot, Y. Mely and T. F. Vandamme, *RSC Adv.*, 2012, **2**, 11876–11886.
59 H.-Q. Peng, J.-F. Xu, Y.-Z. Chen, L.-Z. Wu, C.-H. Tung and Q.-Z. Yang, *Chem. Commun.*, 2014, **50**, 1334–1337.
60 H.-Q. Peng, Y.-Z. Chen, Y. Zhao, Q.-Z. Yang, L.-Z. Wu, C.-H. Tung, L.-P. Zhang and Q.-X. Tong, *Angew. Chem., Int. Ed.*, 2012, **51**, 2088–2092.
61 K. V. Rao, K. K. R. Datta, M. Eswaramoorthy and S. J. George, *Chem. – Eur. J.*, 2012, **18**, 2184–2194.
62 A. Adronov and J. M. J. Frechet, *Chem. Commun.*, 2000, 1701–1710.
63 J. G. Woller, J. K. Hannestad and B. Albinsson, *J. Am. Chem. Soc.*, 2013, **135**, 2759–2768.
64 B. O. Dabbousi, J. Rodriguez-Viejo, F. V. Mikulec, J. R. Heine, H. Mattoussi, R. Ober, K. F. Jensen and M. G. Bawendi, *J. Phys. Chem. B*, 1997, **101**, 9463–9475.
65 A. P. Alivisatos, *Science*, 1996, **271**, 933–937.
66 X. Michalet, F. F. Pinaud, L. A. Bentolila, J. M. Tsay, S. Doose, J. J. Li, G. Sundaresan, A. M. Wu, S. S. Gambhir and S. Weiss, *Science*, 2005, **307**, 538–544.
67 J. Hofkens, M. Maus, T. Gensch, T. Vosch, M. Cotlet, F. Kohn, A. Herrmann, K. Mullen and F. De Schryver, *J. Am. Chem. Soc.*, 2000, **122**, 9278–9288.
68 D. A. Vanden Bout, W. T. Yip, D. Hu, D. K. Fu, T. M. Swager and P. F. Barbara, *Science*, 1997, **277**, 1074–1077.
69 H. Lin, R. Camacho, Y. Tian, T. E. Kaiser, F. Würthner and I. G. Scheblykin, *Nano Lett.*, 2010, **10**, 620–626.
70 E. Rampazzo, S. Bonacchi, R. Juris, M. Montalti, D. Genovese, N. Zaccheroni, L. Prodi, D. C. Rambaldi, A. Zattoni and P. Reschiglian, *J. Phys. Chem. B*, 2010, **114**, 14605–14613.
71 D. Genovese, E. Rampazzo, S. Bonacchi, M. Montalti, N. Zaccheroni and L. Prodi, *Nanoscale*, 2014, **6**, 3022–3036.
72 H. Özhalıcı-Ünal and B. A. Armitage, *ACS Nano*, 2009, **3**, 425–433.
73 A. N. Jordan, N. Siraj, S. Das and I. M. Warner, *RSC Adv.*, 2014, **4**, 28471–28480.
74 H. Yao and K. Ashiba, *ChemPhysChem*, 2012, **13**, 2703–2710.
75 D. L. Farkas, M. Wei, P. Febbroriello, J. H. Carson and L. M. Loew, *Biophys. J.*, 1989, **56**, 1053–1069.
76 L. F. Mottram, S. Forbes, B. D. Ackley and B. R. Peterson, *Beilstein J. Org. Chem.*, 2012, **8**, 2156–2165.
77 P. K. S. Magut, S. Das, V. E. Fernand, J. Losso, K. McDonough, B. M. Naylor, S. Aggarwal and I. M. Warner, *J. Am. Chem. Soc.*, 2013, **135**, 15873–15879.
78 R. P. Haugland, *Handbook of fluorescent probes and research chemicals*, Molecular Probes Inc., Eugene, OR, 9th edn, 1996.
79 N. L. Thompson, in *Topics in Fluorescence Spectroscopy Techniques*, ed. J. R. Lakowicz, Plenum Press, New York, 1991, vol. 1, p. 337.

2.3 Non-coordinating anions assemble cyanine amphiphiles into ultra-small fluorescent nanoparticles

The aim of this project was to develop fluorescent organic NPs, assembled from organic molecules, featuring relatively small size ca 5-10 nm and bearing a large quantity of organic dyes (~100 units). The large number of fluorophore units would ensure high fluorescence brightness comparable or better than quantum dots, while their organic content would make them biodegradable, so that they could be applied for clinical diagnostics with minimum harm for the patient. The area of ultra-small organic nanoparticles for bioimaging is still unexplored, as only a few reports are available in the field.[1]

Development of fluorescent organic NPs remains a challenging task because when the dyes are confined in the nanoscopic space at very high concentrations, they tend to form poorly fluorescent aggregates. Recent reports showed remarkable exceptions,[1b, 2] suggesting that the key to highly fluorescent organic nanostructures is the control of self-assembly of organic dyes with engineered inter-fluorophore distance and orientation.This high level of control is achieved in micellar nanoparticles, very small structures (5-10 nm), self-assembled from fluorescent amphiphiles. Though micellar assembly is very well-established, only few examples in literature utilized this strategy to obtain fluorescent organic NPs[1a, 3] and their fluorescent quantum yield is limited (see one example in Fig. 1). In all these examples, dyes displayed very strong chromophore interactions, which led either to self-quenching (ACQ) or to significant distortion of the original emission spectra resulting in a poor red shifted fluorescence. In this work we tried to overcome these problems by using specially designed cyanine based amphiphiles together with bulky hydrophobic counterions, also known as non-coordinating anions. We hypothesized that these counterions, similarly to our previous work, would function as a glue and spacer, thus assembling dyes together and keeping sufficient distance between them. However, in contrast to our earlier work, we wanted the dye to have strong amphiphilic property in order to obtain smallest possible particles of micellar organization. To this end, we synthesized new fluorescent amphiphiles based on cyanine dyes (Cy3 and Cy5), consisting of two hydrophobic (dodecyl) and two dendronized hydrophilic (PEG) moieties (Fig. 2.3.1).

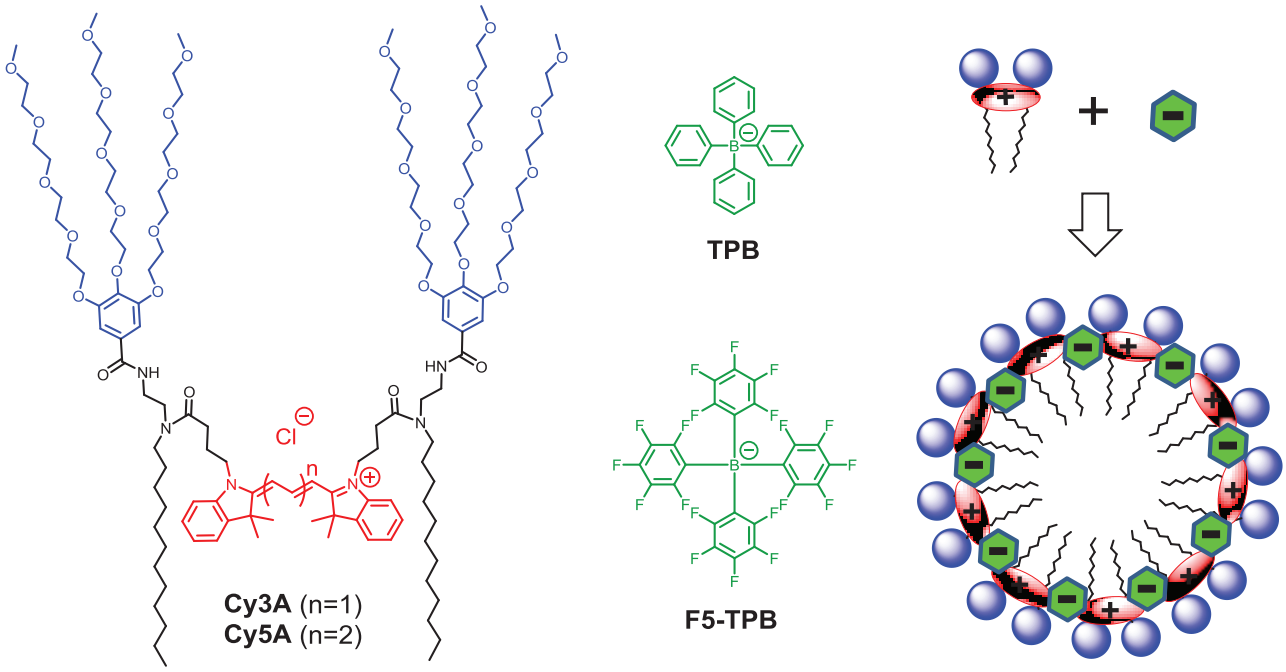

Figure 2.3.1. Amphiphilic dyes synthesized in this study and their assembly in the presence of non-coordinating anions into micellar NPs

Absorption spectroscopy showed that non-coordinating ions induce self-assembly of new amphiphiles Cy3A and Cy5A in the whole studied concentration range (0.1 – 5 μM). The obtained nano-structures are ~7-8 nm in size according to dynamic light scattering, fluorescence correlation spectroscopy (FCS), and atomic force microscopy, which suggests that they have micellar organization. Importantly, the obtained counterion-induced assemblies are characterized by high fluorescence quantum yield (up to 20%) comparable to that in organic solvents as well as very low fluorescence anisotropy due to fast energy hopping within the dye assembly. In contrast, non-fluorinated tetraphenylborate produces strongly self-quenched NPs, which shows the unique role of counterion fluorination to prevent dye self-quenching. FCS measurements confirmed very small size of Cy3A micelles with fluorinated counterion and revealed that they are >40-fold brighter than single cyanine 3 dye with an aggregation number in the range 25-41. Moreover, we created two-color fluorescent NPs by counterion assisted co-assembly of Cy3A and Cy5A amphiphiles, which allowed fluorescence resonance energy transfer (FRET). Remarkably, a single Cy5A acceptor was sufficient to achieve highly efficient FRET with the light-harvesting antenna effect of ~30. This high antenna effect to a single acceptor is probably because of small size of the obtained micelles combined with efficient energy hoping within donor dyes. Moreover, FRET studies suggested a remarkable stability of the counterion-assembled micelles even at 1 nM of the amphiphile, indicating that non-coordinating ion interacts very strongly with neighboring cyanines and thus brings them together

into stable nano-structure. Only fluorinated counterion produced dye micelles of excellent colloidal stability, while with other counterions (chloride and tetraphenyl borate), the Cy3A and Cy5A solutions showed significant adsorption and/or sedimentation over 24h. Our results suggest the new route to functional nanomaterials by combining electrostatic and hydrophobic interactions of non-coordinating anions with cationic dyes. In the present case, it enables preparation of ultra-small nanoparticles of 7-8 nm characterized by very high brightness, equivalent of 40 cyanine dyes. Thus, these counterions not only function as glue for dye nano-assemblies, but they also prevent their self-quenching, which may lead to new generation to highly emissive nanomaterials for light-harvesting and bioimaging applications.

The full description of this work can be found in the manuscript enclosed below.

References

(1) (a) Zhang, X.; Chen, Z.; Würthner, F. *J. Am. Chem. Soc.* **2007**, *129*, 4886. (b) Klymchenko, A. S. *J. Nanosci. Lett.* **2013**, *3*, 21.

(2) Kaeser, A.; Schenning, A. P. H. J. *Adv. Mater.* **2010**, *22*, 2985.

(3) Olivier, J.-H.; Widmaier, J.; Ziessel, R. *Chem. Eur. J.* **2011**, *17*, 11709.

MANUSCRIPT №1

Non-coordinating anions assemble cyanine amphiphiles into ultra-small fluorescent nanoparticles

Non-coordinating anions assemble cyanine amphiphiles into ultra-small fluorescent nanoparticles

Ievgen Shulov,[1,2] Youri Arntz,[1] Yves Mély,[1] Vasyl G. Pivovarenko[2] and Andrey S. Klymchenko[1,*]

[1]*Laboratoire de Biophotonique et Pharmacologie, UMR 7213 CNRS, Université de Strasbourg, Faculté de Pharmacie, 74, Route du Rhin, 67401 ILLKIRCH Cedex, France. E-mail: andrey.klymchenko@unistra.fr; Tel: +33 368 85 42 55*

[2]*Organic Chemistry Department, Chemistry Faculty, Taras Shevchenko National University of Kyiv, 01601 Kyiv, Ukraine.*

Abstract

Molecular self-assembly is a powerful bottom up approach, which exploits a limited number of non-covalent interactions (hydrophobic, H-bonding, ion-coordination, electrostatic, etc) to generate a large variety of nanostructures and functional materials. Here, by using non-coordinating anions (perfluorinated tetraphenylborate), we exploited a unique combination of hydrophobic and electrostatic interactions to assemble fluorescent amphiphilic molecules into well-organized fluorescent micellar nanoparticles (NPs) of 5-10 nm size. To this end, we synthesized new fluorescent amphiphiles based on cyanine dyes (Cy3 and Cy5), consisting of two hydrophobic (dodecyl) and two dendronized hydrophilic (PEG) moieties. Absorption spectroscopy suggested that non-coordinating ions induce self-assembly of new amphiphiles Cy3A and Cy5A, while dynamic light scattering, fluorescence correlation spectroscopy (FCS), and atomic force microscopy showed that obtained micellar nano-structures are ~7-8 nm in size. Remarkably, only perfluorinated tetraphenylborate induced assemblies characterized by high fluorescence quantum yield (up to 20%) and fast energy hopping (nearly zero anisotropy), indicating the unique role of counterion fluorination to prevent dye self-quenching. FCS measurements revealed that the Cy3A based micelles are >40-fold brighter than single cyanine dye and their aggregation number is in the range 25-41. Moreover, we created two-color fluorescent nanoparticles by counterion-assisted co-assembly of Cy3 and Cy5-based amphiphiles which allowed fluorescence resonance energy transfer (FRET). Remarkably, a single Cy5A acceptor was sufficient to achieve highly efficient FRET with the light-harvesting antenna effect of ~30. FRET data also confirmed remarkable stability of the counterion-assembled micelles even at 1 nM of the amphiphile. Our results suggest the new route to functional nanomaterials by combining electrostatic and hydrophobic interactions of non-coordinating anions with cyanine dyes. These counterions not only function as glue for dye nano-assemblies, but they also prevent their self-quenching, which may lead to new generation of highly emissive nanomaterials.

Introduction

Molecular self-assembly is a powerful bottom up approach that enables generation of large variety of nanostructures and functional materials.[1] Thus, macrocyclic compounds can produce host-guest complexes and functional supramolecules like catenanes. Coordination of metal ions with organic molecules can results in metal-organic frameworks, which are highly porous materials attractive for encapsulation of functional guest molecules.[2-5] Lipids and other amphiphilic molecules can generate vesicles, fibers, tubes and micelles, which are used for drug delivery, imaging and as templates for preparation of nanomaterials of higher level of complexity.[6-8] All these examples of self-assembly exploit quite limited number of non-covalent interactions:[9] (1) H-bonding and (2) metal-coordination, featuring high directionality, (3) hydrophobic, (4) pi-stacking interactions, which are especially strong in aqueous media, (5) electrostatic interactions oppositely charged groups, as well as (6) Van Der Waals interactions, the last being the weakest. The successful bottom up assembly requires combination of several types of these interactions together. The most common are combinations of H-bonding with hydrophobic and pi-stacking interaction, which is for instance realized in nature in nucleic acids and case of nucleic acids and proteins as well as in numerous examples with synthetic organic molecules forming for instance fibers and tubes.[6-8] Combination of electrostatic with hydrophobic interactions is another very important approach, but it was not explored well to date. In fact, electrostatic interactions are very efficient in apolar media, while in aqueous solutions especially in the presence of salts these interactions are strongly hindered. Therefore, to generate sufficiently strong forces one should use hydrophobic ions, which are poorly hydrated and weakly coordinated by inorganic counterions in solution. The best examples are so-called non-coordinating anions.[10] The key representatives are tetraphenylborates (TPB), negatively charged ions surrounded by hydrophobic aromatic groups. Fluorinated analogues are particularly efficient in this respect, and were successfully used in phase transfer catalysis and as charge carriers inside electrodes.[10] Our recent works showed that tetraphenyl borates can help encapsulation of organic dyes inside polymer[11] and lipid[12] matrixes of nanocarriers. Importantly, in the presence of non-coordinating anions, cationic dyes can form nanoparticles, called as ion-associated NPs[13,14] or GUMBOS.[15-17] Fluorination of these counterions is crucial to achieve high fluorescence quantum yield of NPs and sufficient stability in biological media.[18] In this case, relatively hydrophobic cationic dyes and non-coordinating anions give highly hydrophobic salts that rapidly precipitate in aqueous media, so that the whole process is kinetically controlled. However, so far these non-coordinating hydrophobic counterions have never been used to tune a thermodynamically controlled process, such as micelle formation from an amphiphile. The latter constitute one of the most basic and fundamental self-assembly process that give ultra-small nanoparticles.[19] Assembly of organic dyes into micelles is particularly interesting because it could enable preparation of ultra-small fluorescent nanoparticles,[20-23] which gain significant attention due to their enormous potential for bioimaging applications. However, it is well known that concentrating dyes at the nanoscale leads to aggregation caused quenching (ACQ),[24,25] so that the reported examples of ultra-small micelles from organic dye amphiphiles display relatively low fluorescence quantum yields. In this respect, fluorinated counterions that can prevent cationic dyes from ACQ, is of particular importance to generate bright fluorescent micellar NPs.

In the present work we show that non-coordinating counterions can trigger assembly of amphiphilic dyes into ultra-small fluorescent nanoparticles. To this end we synthesized cyanine-3 (Cy3) and cyanine-5 (Cy5) amphiphilic derivatives bearing hydrophobic alkyl chains and polar PEG groups. Without non-coordinating anions they showed poor capacity to form micelles due to relative large critical micelle concentration (cmc). However, in the presence of TPB anions they spontaneously formed micelles and did not show any sign of disassembly even at very high dilutions. Remarkably, micelles formed with fluorinated counterion displayed relatively high fluorescence quantum yields, similar to the solutions in organic solvents. Finally, combination of Cy3 and Cy5 dyes in the same micelles enable preparation of light-harvesting complex, with an antenna effect reaching 40, so that practically all donor dyes inside the micelles (Cy3) transferred the energy to a single acceptor dye (Cy5). This work suggests that non-coordinating anions are powerful building blocks in self-assembly of amphiphilic molecules. They exploit unique combination of electrostatic and hydrophobic forces that is orthogonal to other self-assembly forces, which opens new dimension in the preparation of highly organized supramolecular materials.

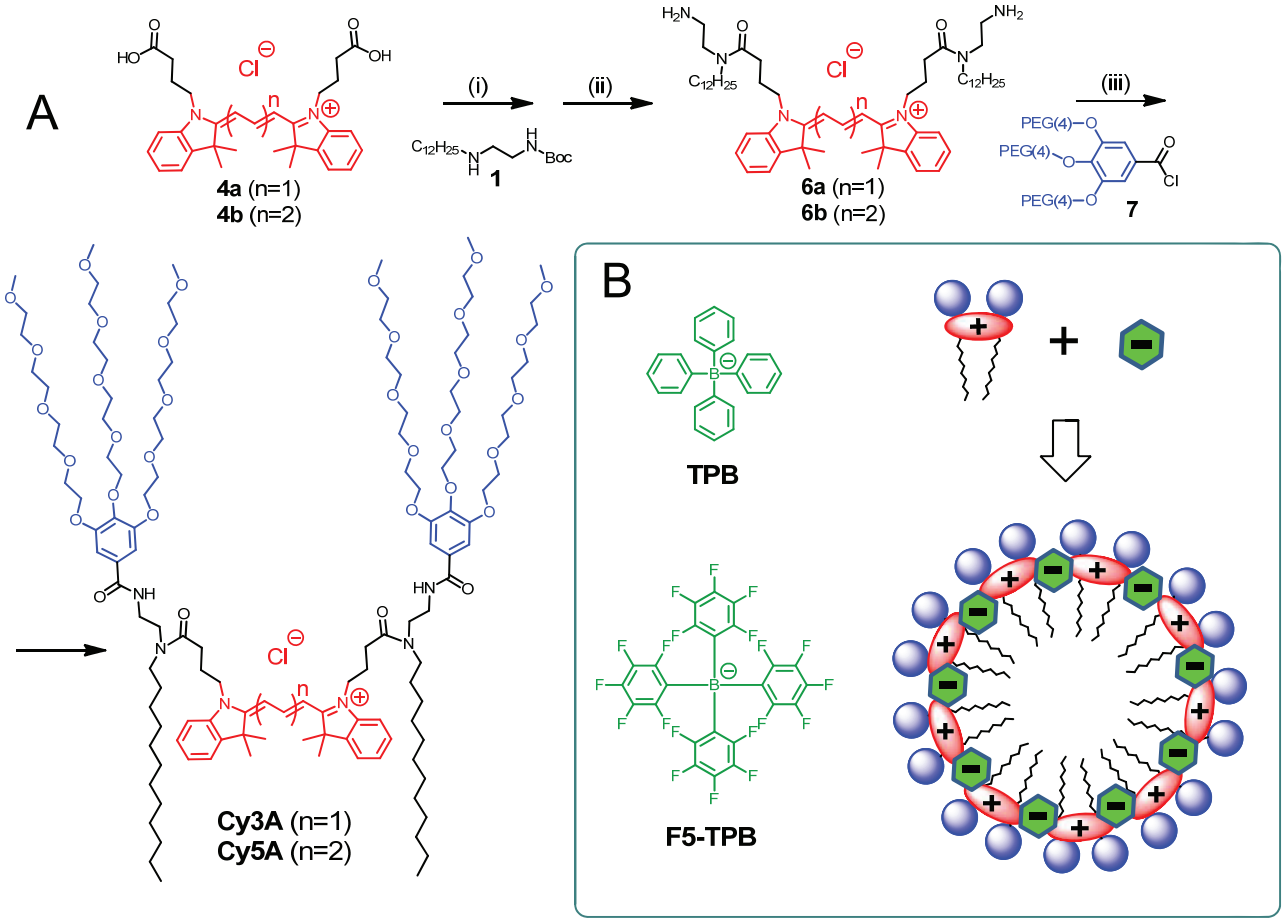

Figure 1. Design and synthesis of dyes as well as their assembly into micelles in the presence of non-coordinating anions. (A) Synthesis and chemical structure of new amphiphilic molecules based on Cy3 and Cy5 dyes. (B) Chemical structures of non-coordinating anions and schematic presentation of anion-driven assembly of fluorescent micelles.

Results and discussion

Synthesis of cyanine amphiphiles

To achieve assembly of dyes into smallest possible nanostructures, we considered preparation of fluorescent amphiphiles. As building block for their construction we selected cyanines. Firstly, these are cationic dyes with a positive charge delocalized within large hydrophobic aromatic structure. This allows us to combine hydrophobic and electrostatic interactions for assembly with the help of non-coordinating anions. Secondly, they possess very high molar absorption coefficients and good fluorescence quantum yields, which enable preparation of bright fluorescent nanoparticles. Finally, cyanines are classical example of dyes that aggregate in aqueous media giving non-fluorescent H-aggregates, so that we would be able to verify whether the non-coordinating anions can prevent self-quenching in the obtained nano-assemblies. To build amphiphiles, we decided to prepare symmetric gemini-like amphiphile containing two hydrophilic PEG groups and two apolar hydrocarbon chains. This design could also enable preparation of micelles where cyanine dyes would be oriented parallel to the micelle surface with freedom to form either J- or H-aggregates. Moreover, this design is more synthetically available because cyanines are symmetric structures that can be readily substituted at their heteroatoms with two functional groups. To obtain final Cy3A and Cy5A amphiphiles, firstly, we prepared Cy3 and Cy5 derivatives bearing two carboxylic groups, **4a** and **4b**, respectively (Figure 1). They were coupled with hydrophobic mono-boc-protected diamine **1** (prepared from 1-iododododecane and N-boc-ethylenediamine) to give compounds **5a** and **5b**, respectively, which after boc removal gave corresponding dye diamines **6a** and **6b**. The latter were then reacted with PEGylated gallic acid chloride **7** to afford final amphiphiles **Cy3A** and **Cy5A**, respectively.

Assembly of cyanine amphiphiles in solution

First, we studied the capacity of Cy-amphiphiles to assemble in aqueous media using absorption spectroscopy. At higher concentration of Cy3A in water, the contribution of the short-wavelength shoulder increased (intensity ratio shoulder to the pick maximum, A_{sh}/A_{max}), whereas in methanol no changes were observed (Figure 2A, C). In the case of Cy5A, the increase was much stronger and overall, in comparison to Cy3A, the contribution of the shoulder for Cy5A in water was much larger than in methanol (Figure 2B, D). These observations suggest that both dyes at higher concentration tend to form H-aggregates, probably of micellar origin. However, Cy5A exhibits much stronger capacity to self-assemble. The A_{sh}/A_{max} value increased faster and the curve changed the slope above 1 ı M, suggesting that critical micellar concentration for Cy5A is on the order of 1 ı M. In contrast, for Cy3A, the cmc value should be much larger and cannot be estimated from this data. We could speculate that Cy3A is more polar than Cy5A and thus unable to aggregate efficiently into micelles in this concentration range. In the presence of 150 mM sodium chloride, the contribution of the short-wavelength shoulder increased for both dyes, indicating that the presence of salt decreased the electrostatic repulsion between the cationic dyes and thus favor their assembly at lower concentrations. We also studied fluorescence properties of obtained assemblies in water (Table 1). Only for Cy3A in water the fluorescence quantum yield was as high as in methanol, which was expected as at these

conditions Cy3A is not yet aggregated. In contrast, for Cy5A in water the fluorescence quantum yield was about 10-fold lower, which is clearly related to the formation of dye aggregates. According to the absorption spectra these dyes tend to form H-aggregates, which are known to be poorly fluorescent, thus explaining the low fluorescence quantum yields. These results were expected, as micellar assembly of fluorescent amphiphiles favors formation of weakly fluorescent pi-stacked H-aggregates of dyes.[25]

Next, we added non-coordinating anions TPB and F5-TPB to our aqueous solutions of dye amphiphiles. Importantly, in the case of Cy3A and Cy5A both anions increased the short-wavelength shoulder in absorption spectra (Figure 2A, B) and the whole absorption band shifted slightly to the red. Moreover, in the presence of TPB and F5-TPB this shoulder did not vary significantly starting from 0.5 ı M (Figure 2C, D), which is in contrast to the data with chloride counterion. Thus, counterions induced self-assembly of Cy3A amphiphiles and this was observed in the concentration range 0.5 ¯ 5 ı M. In addition, the contribution of the shoulder was larger for TPB compared to F5-TPB, which indicates that the relative arrangement of cyanines inside the assemblies depended on the counterion. The most interesting effects were observed in fluorescence (Figure 2E, F). In the presence of TPB, the fluorescence quantum yield was significantly lower than in water, suggesting that TPB induced efficient self-assembly leading to ACQ effect. In sharp contrast, F5-TPB induced increase in the quantum yield for both amphiphiles, reaching values of 20 and 8% for Cy3A and Cy5A, respectively (Table 1). To confirm that this efficient fluorescence is observed from self-assembled nanostructures, we measured fluorescence anisotropy of our samples. Anisotropy is generally a measure of molecular rotation of a dye during an excited state. Smaller molecules in less viscous solvents demonstrate lower levels of anisotropy. However, in dye assemblies, despite their larger size, the migration of energy (exciton diffusion) can produce even stronger decrease of fluorescence anisotropy as the energy hops within dyes of different orientation.[26-28] In water without non-coordinating anion, our fluorescent amphiphiles showed anisotropy value close to that in methanol, thus reflecting rotation of free dye molecules (Table 1). Remarkably, in the presence of F5-TPB the anisotropy decreased 5-8 fold for both dyes. This result confirms that counterion induces self-assembly of fluorophores into emissive multi-fluorophore nanostructures.

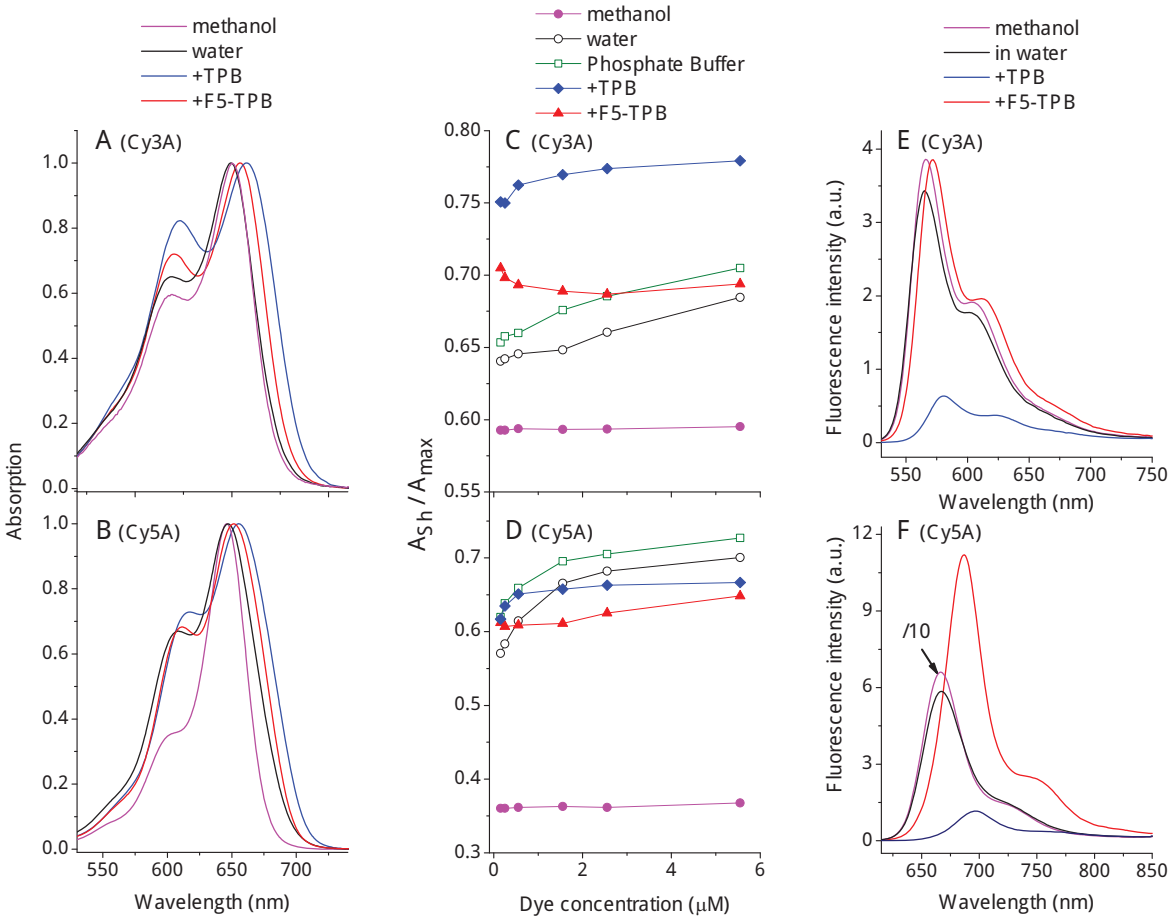

Figure 2. Absorption spectra of Cy3A (A) and Cy5A (B) dye amphiphiles, their dependence on dye concentration (C, D); and the emission spectra (E, F) in methanol and aqueous media in the presence of different counterions.

Table 1. Spectroscopic properties of Cy3A and Cy5A in molecular and micellar forms.

Sample	Solvent	λabs (nm)	λem (nm)	FWHM (nm)	Stokes shift (nm)	Φ (%)	Anisotropy
Cy3A	MeOH	550	566	40	16	15	0.153
Cy3A	Water	550	565	57	15	15	0.171
Cy3A/F5-TPB	Water	555	572	59	17	20	<0.020
Cy3A/TPB	Water	557	581	66	24	6	0.034
Cy5A (0.1ı M)	MeOH	646	666	40	20	39	0.115
Cy5A	Water	647	667	44	20	4	0.140
Cy5A/F5-TPB	Water	651	687	39	36	8	<0.020
Cy5A/TPB	Water	655	697	46	42	1	0.017

Table 2. Hydrodynamic diameter and zeta potential by DLS and diameter by AFM of NPs assembled from cyanine amphiphiles with different hydrophobic tetraphenylborate counterions.

Sample name	Diameter DLS nm	PDI	Diameter (AFM)[b] (nm)
Cy3A/TPB	7ě1	0.18	8 ě1
Cy3A/F5-TPB[a]	12ě3	0.22	7 ě1
Cy5A/TPB	ND	ND	7 ě1
Cy5A/F5-TPB	ND	ND	8 ě1

[a] The value obtained for these NPs by DLS are probably affected by their efficient fluorescence. [b] Diameter was obtained from height values in AFM measurements. ND ” Not determined. For the Cy5A samples (Cy5A/F5-TPB and Cy5A/TPB) the DLS measurements were not possible due to sample excitation (fluorescence) on the laser wavelength (standard 633 nm laser on Zetasizer Nano ZS). PDI ¯ polydispersity index.

Dynamic light scattering (DLS) suggested that Cy3A in the presence of TPB and F5-TPB formed particles of 7 and 12 nm hydrodynamic diameter, respectively (Table 2). Remarkably, zeta potential of Cy3A/F5-TPB nanoparticles was strongly negative (-81ě14 mV). We expect that the excess of the hydrophobic F5-TPB counterion is adsorbed at the surface of micelles which generates this strong negative potential. Unfortunately, it was not possible to measure size and zeta potential of Cy5A assemblies because the DLS laser source could directly excite the dye, which disturbed the measurements.

Therefore, we complemented DLS measurements with Atomic Force Microscopy (AFM). To this end, the dye amphiphiles in the presence of TPB or F5-TPB counterion were deposited on mica in aqueous solution of calcium chloride. The latter was used as a `bridge_ between negatively charged glass

surface and our negatively charged NPs. The best images were obtained for Cy3A with F5-TPB counterion, where relatively homogeneous NPs of 7 nm height were observed (Figure 3A, Table 2). This result is in line with the DLS data suggesting formation of ultra-small NPs. Taking into account that the length of Cy3A amphiphile (from the end of alkyl chain till the end of PEG chain) is about ~ 3 nm, this small size suggests the micellar organization of NPs. In these micelles, the alkyl chains, the dye and the counterions form the core, while the PEG groups play a role of polar shell exposed to water (Figure 1). In the presence of TPB counterion, we could detect NPs of 8 nm in height. However, these images were much more difficult to obtain (Figure S1), which was probably because NPs were not sufficiently stable on the mica surface. In the case of Cy5A with TPB and F5-TPB, we could obtain NPs of 7-8 nm height, though they appeared more heterogeneous and larger in the XY directions (Figure 3B and S1). We expect that these larger NPs of the same height could be micelles NPs of 8 nm in diameter, which aggregated at the mica surface.

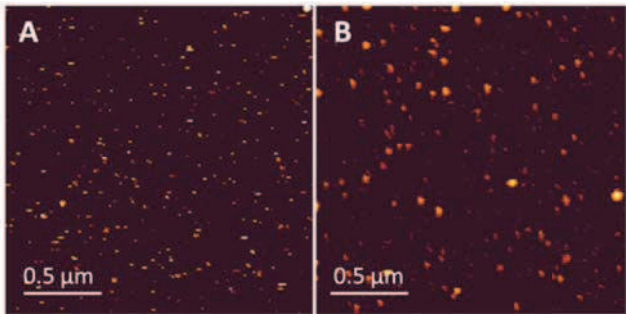

Figure 3. Atomic force micrsocpy of nanostrucutres formed by Cy3A (A) and Cy5A (B) in the presence of F5-TPB.

Single particle properties

Then, to evaluate their single particle properties, we performed fluorescence correlation spectroscopy (FCS). This unique technique, which measures diffusion of emissive species through a focal volume, provides direct access to the size, concentration and brightness of NPs.[29,30] As we used two-photon excitation source, we were able to study only Cy3A samples, which present appreciable two-photon absorption cross-section at 760 nm.[31] Surprisingly, solution of Cy3A with chloride and TPB counterions could not give any signal, which was most probably due to fast adsorption of the dye to the glass and/or plastic surface of the well. In contrast, solutions of Cy3A with F5-TPB displayed stable signal, which could be measured and analyzed. FCS data suggested that the size of NPs was 6.5 nm (Table 3), which is perfectly in line with the AFM data, but smaller than that obtained from DLS (Table 2). The latter is probably because DLS technique could overestimate the size due to the fluorescence of NPs. Taken together, all used techniques suggest the ultra-small size of Cy3A/F5-TPB NPs, which confirm our hypothesis on the micellar organization of these nanostructures. Secondly, the brightness of these particles is close to 6 molecules of tetramethyl-rhodamine (TMR). Taking into account the two-photon absorption cross-section (σ_2) of rhodamine at 760 nm (85 GM) and its quantum yields in water (0.4) and those for Cy3A dye (25 GM and 0.2, respectively),[31] we calculated that 6 rhodamines is

equivalent of 41 Cy3A dyes. This calculation suggests that the micelle contains around 41 dyes. This value is on the same order of magnitude as typical aggregation number of amphiphiles (25-100). Finally, from the concentration of emissive species, measured by FCS, and total Cy3A concentration, we could find that the number of dyes per micelle is 25, which is in agreement with the one obtained from the single particle brightness.

Table 3. Two-photon fluorescence correlation spectroscopy (FCS) data of Cy3A/F5-TPB NPs in comparison to tetramethyl-rhodamine dye (TMR).[a]

	TMR	Cy3A/F5-TPB
τ_{corr}, ms	0.033±0.002	0.19±0.02
N	13±2	18±2
Bri, kHz	0.25±0.07	1.9±0.4
size, nm	1	6.5±0.7
Bri/TMR	1	5.9±0.3
Bri/Cy3	6.8	41±5
Conc. nM	50	80±2
dye/NP	1	25±1

[a] τ_{corr} – correlation time, N – number of emissive species per excitation volume, Bri – brightness per particle, Conc. – concentration of species.

Energy transfer and stability measurements

All together the described data suggest that in the presence of F5-TPB anions, Cy3A is able to form micelles containing 25-60 dyes with highly efficient fluorescence accompanied by fast exciton migration. Therefore, we hypothesized that the presence of few FRET energy acceptors, such as Cy5A that should co-assemble with Cy3A within the micelle, may be sufficient to obtain efficient energy transfer. To this end, we prepared NPs from the mixtures of Cy3A and Cy5A in the presence of F5-TPB and studied their fluorescence spectra. Remarkably, FRET could be observed in all studied donor/acceptor ratio between 1000/1 up to 2/1 (Figure 4A). The increase in the acceptor concentration (i.e. decrease in the donor/acceptor ratio), the acceptor emission increased, while the donor emission decreased. The relative FRET efficiency ($I_{acceptor}/(I_{donor}+I_{acceptor})$) increased with decrease in the donor/acceptor ratios up to ratios 20/1 (Figure 4B). Below this ratio, FRET efficiency remained stable around 80%. This saturation behavior is probably connected with the number of donor Cy3A per micelle (aggregation number). We expect, when the donor/acceptor ratio is above the aggregation number, not all micelles contain the acceptor molecule, so that the FRET efficiency will depend on the acceptor concentration. However, when donor/acceptor ratio is below the aggregation number, each micelle will contain at least one acceptor, and the FRET efficiency may reach its maximum. As the saturation is achieved the donor/acceptor ratio between 50/1 and 20/1, we could expect that the aggregation number of Cy3A micelles should be between 50 and 20, which is perfectly in line with our

estimations based on FCS measurement. Moreover, we can also conclude that a single acceptor molecule is sufficient to achieve strong FRET efficiency, which can be explained by two factors. First, it is the small size of the micelles, which is on the same order as the Forster distance between Cy3 and Cy5 dyes (5.6 nm). Second, the exciton diffusion within the donor dyes should additionally improve FRET efficiency, as it was shown for fluorescent nanoparticles and light-harvesting systems.[18,32,33] Our micelles also behave in this case as light-harvesting system, that efficiently absorbs the energy and transfer it to a single acceptor. The antenna effect (AE) of our system, which is calculated as the ratio of intensities of donor and acceptor dyes in the excitation spectra, reaches values of 30 (Figure 4C). The theoretical value of antenna effect could be calculated as $AE = (n_D \cdot \varepsilon_D \cdot E)/(n_A \cdot \varepsilon_A)$, where n_D and n_A are numbers of donors and acceptors, respectively, per particle, ε_D and ε_A are extinction coefficients of donor and acceptor, respectively, and E is the FRET efficiency. Assuming that the n_A value is 1 for high donor/acceptor ratios, we could estimate n_D value as 63. The latter value is in a very good agreement with the aggregation number that was earlier estimated by different methods.

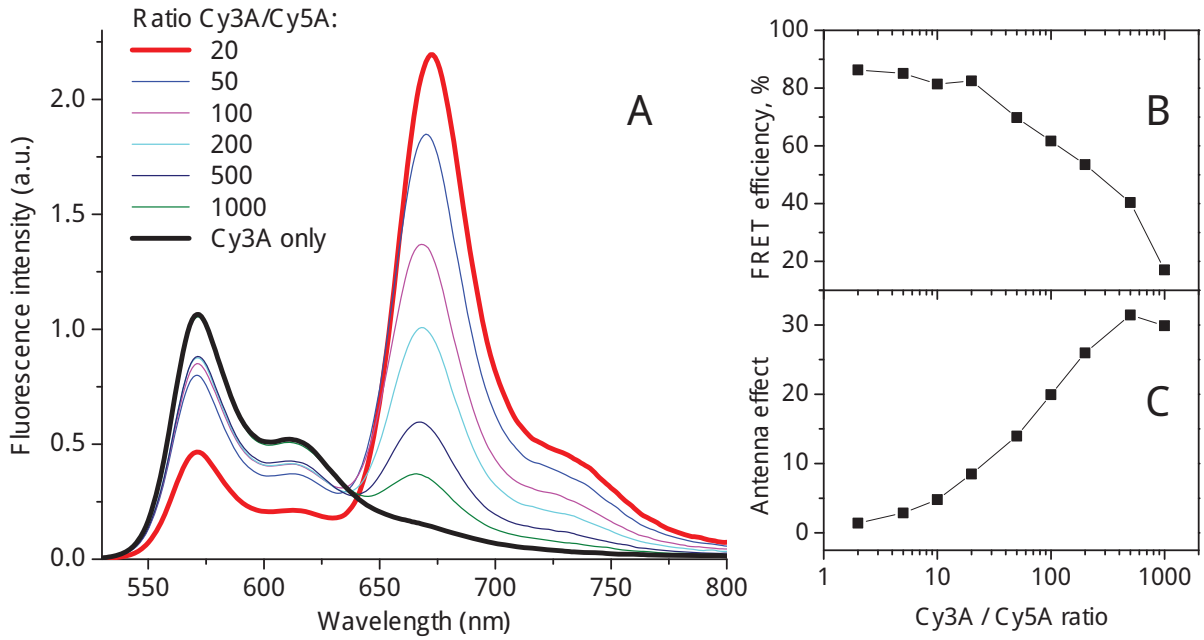

Figure 4. FRET from multiple donors of Cy3A micelles to co-assembled Cy5A amphiphiles at different donor/acceptor ratios (A). The changes in the relative FRET efficiency (B) and antenna effect value (C) as a function of donor/acceptor ratio.

As FRET is sensitive to the donor-acceptor distance, it is a powerful technique to study the integrity of nanostructures.[30,34] Indeed, in the case our FRET micelles dissociate, the donor and acceptor molecules should get separated, which would result in the loss of FRET signal. To address stability of our NPs, we recorded their emission spectra at different dilutions (Figure 5). Remarkably, dilution of our NPs prepared at 1 ı M concentration up to 1000-fold produced only minor modifications in the dual emission spectrum of our FRET NPs. After 1000-fold dilution (1 nM Cy3A concentration), the FRET

efficiency decreased only by 13%, indicating that the particles remained nearly intact, so that the cmc of Cy3A micelles in the presence of F5-TPB anion is much lower than 1 nM. This is an outstanding observation taking into account that cmc of Cy3A is >5 ı M. It shows that amphiphilic molecules that originally have poor capacity to self-assemble could be brought together into stable nanostructures by non-coordinating anions that exploit a combination of electrostatic and hydrophobic forces fully functional in aqueous media.

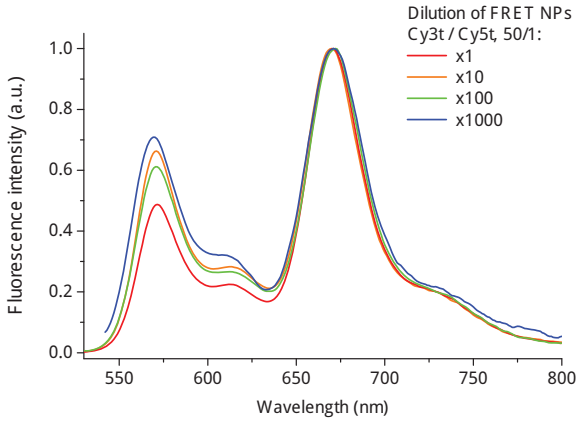

Figures 5. Normalized fluorescence spectra of FRET NPs at different dilutions. Initial concentration of Cy3A, Cy5A and F5-TPB in non-diluted (x1) solution were 1, 0.02 and 10 ı M, respectively. After preparation of NPs, they were diluted to different extent in miliQ water.

Finally, we then verified whether the counterion-assembled cyanine micelles with different borate counterions are stable over time. To this end, we studied the absorbance values of these solutions in plastic cuvettes as a function of time (Figure 6). The decrease in the absorbance value depended clearly on the counterion for both Cy3A and Cy5A. Indeed, in the presence of chloride and TPB, the absorbance clearly decreased over time (Figure 6). As the shape of the absorption spectra for these counterions remained unchanged with time (data not shown), we could conclude that the decrease in the absorption, observed mainly for chloride and TPB counterions, was related to sedimentation of the particles and their adsorption on the walls of the cuvette. Cy5A chloride showed much faster decrease in the absorption compared to Cy3A chloride, which is probably because the former is more hydrophobic due to presence of two additional methine groups. In sharp contrast, both Cy3A and Cy5A in the presence of highly fluorinated F5-TPB counterion displayed almost negligible decrease in the absorbance, indicating much higher stability of the obtained micelles. This result is well in line with our FCS measurements, where the samples with chloride and TPB counterions did not give any signal, probably due to the dye adsorption/sedimentation, while that with F5-TPB worked well. Moreover, the high stability of these micelles is supported by strongly negative surface potential of Cy3A/F5-TPB micelles as well as their resistance to dilution revealed by FRET measurements. Overall, we could conclude that fluorinated counterion F5-TPB plays unique role to stabilize micellar NPs against sedimentation and adsorption on surfaces. Our previous data with hydrophobic rhodamine B derivatives showed that highly fluorinated counterions indeed can increase colloidal stability of the ionic NPs and can even ensure their stability in living cells. Thus, non-coordinating counterions may

not only assemble the amphiphilic dye molecules into ultra-small fluorescent NPs, but can also ensure their stability in solutions.

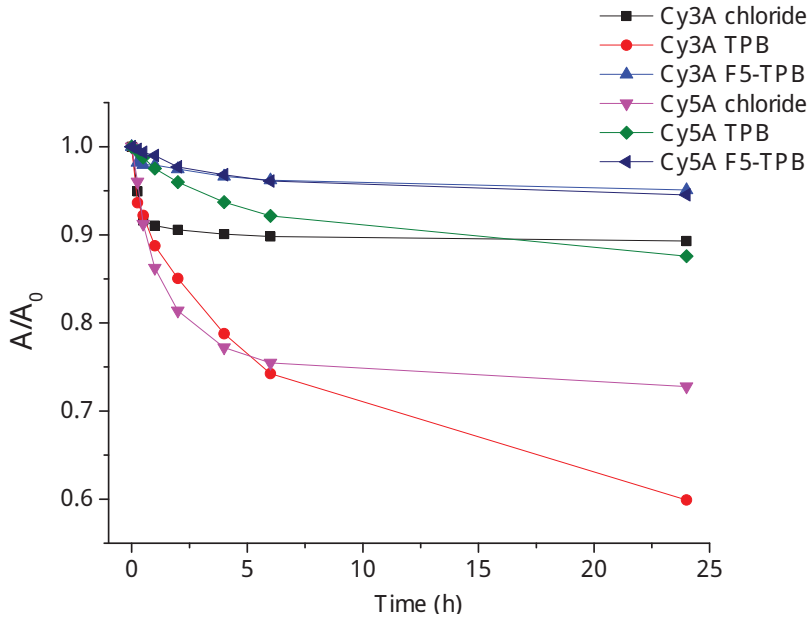

Figure 6. Maturation and stability of solutions of Cy3A and Cy5A dye amphiphiles with different borate counterions in plastic cuvettes measured from their absorbance at the maximum. Concentration of Cy3A and Cy5A dyes were 1 ı M, while concentration of the borate counterions was 10 ı M.

Conclusions

In this work, using non-coordinating perfluorinated tetraphenylborate anion we propose to combine hydrophobic and electrostatic interactions to assemble fluorescent amphiphilic molecules into well-organized fluorescent micellar nanoparticles (NPs) of 5-10 nm in size. We synthesized new fluorescent amphiphiles based on cationic cyanine dyes, Cy3A and Cy5A, consisting of two hydrophobic (dodecyl) and two dendronized hydrophilic (PEG) moieties. Absorption spectroscopy suggested that non-coordinating anions induce self-assembly of new amphiphiles Cy3A and Cy5A in the whole studied concentration range (0.1 ¯ 5 ı M). The obtained nano-structures are ~7-8 nm in size according dynamic light scattering, fluorescence correlation spectroscopy (FCS), and atomic force microscopy, which suggests that they have micellar organization. Importantly, the obtained counterion-induced assemblies are characterized by high fluorescence quantum yield (up to 20%) comparable to that in organic solvents as well as very low fluorescence anisotropy due to fast energy hopping within the dye assembly. In contrast, non-fluorinated tetraphenylborate produce strongly self-quenching NPs, which shows the unique role of counterion fluorination to prevent dye self-quenching. FCS measurements confirmed very small size of Cy3A micelles with fluorinated counterion and revealed that they are >40-fold brighter than single cyanine 3 dye with an aggregation number in the range 25-41. Moreover, we created two-color fluorescent NPs by counterion assisted co-assembly of Cy3A and Cy5A amphiphiles which allowed fluorescence resonance energy transfer (FRET). Remarkably, a single Cy5A acceptor

was sufficient to achieve highly efficient FRET with the light-harvesting antenna effect of ~30. This high antenna effect to a single acceptor is probably because of small size of the obtained micelles combined with efficient energy hoping within donor dyes. Moreover, FRET studies suggested a remarkable stability of the counterion-assembled micelles even at 1 nM of the amphiphile, indicating that non-coordinating ion interacts very strongly with neighboring cyanines and thus brings them together into stable nano-structure. Only fluorinated counterion produced dye micelles of excellent colloidal stability, while with other counterions (chloride and tetraphenyl borate), the Cy3A and Cy5A solutions showed significant adsorption and/or sedimentation over 24h. Our results suggest the new route to functional nanomaterials by combining electrostatic and hydrophobic interactions of non-coordinating anions with cationic dyes. In the present case, it enables preparation of ultra-small nanoparticles of 7-8 nm characterized by very high brightness, equivalent to 40 cyanines dyes. Thus, these counterions not only function as glue for dye nano-assemblies, but they also prevent their self-quenching, which may lead to new generation of highly emissive nanomaterials for light-harvesting and bioimaging applications.

Materials and methods

Synthesis of dye amphiphiles

***tert*-Butyl N-[2-(dodecylamino)ethyl]carbamate (1).** 1-iododododecane (1 eq., 3.08 g, 2.57 mL, 10.4 mmol) and N-boc-ethylenediamine (3 eq., 5 g, 31.2 mmol) were placed in a reaction flask. Anhydrous acetonitrile (40 mL) was added via syringe. The reaction mixture was stirred under reflux for 6h. Solvent was removed under reduced pressure. The crude product was purified by column chromatography (SiO_2, DCM/MeOH, 95:5). An additional purification step was done using recrystallization from acetonitrile, which furnished 2.53 g (yield 74%) of the title compound **1** as white solid. **^{1}H NMR (400 MHz, Chloroform-*d*) δ** 7.59 (br. s, 2H), 5.61 (t, J = 5.6 Hz, 1H), 3.59 (q, J = 5.3 Hz, 2H), 3.22 (t, J = 5.0 Hz, 2H), 3.08 ‾ 2.97 (m, 2H), 1.85 (p, J = 7.8 Hz, 2H), 1.44 (s, 9H), 1.40 ‾ 1.33 (m, 2H), 1.33 ‾ 1.17 (m, 16H), 0.86 (t, J = 6.7 Hz, 3H). **^{13}C NMR (101 MHz, Chloroform-*d*) δ** 157.78, 81.18, 49.05, 48.39, 37.72, 32.01, 29.72, 29.71, 29.61, 29.50, 29.43, 29.10, 28.49, 26.73, 26.17, 22.78, 14.21. **HRMS (*m/z*):** $[M+H]^+$ calcd. for $C_{19}H_{41}N_2O_2$, 329.3163; found, 329.3162.

1-(4-Ethoxy-4-oxobutyl)-2,3,3-trimethyl-3H-indol-1-ium bromide (2). 2,3,3-trimethylindolenine (1 eq., 2.97 g, 3 mL, 18.7 mmol) and ethyl 4-bromobutyrate (3 eq., 10.9 g, 8.03 mL, 56 mmol) were placed in a reaction flask. Anhydrous acetonitrile (40 mL) was added via syringe. The reaction mixture was stirred under reflux for 48 hours. After cooling to room temperature, diethyl ether (40 ml) was added and formed slightly red precipitate was removed by filtration, and washed several times with diethyl ether. The product was purified by recrystallization from acetonitrile, which furnished 4.3 g (yield 65%) of the title compound **2** as pink crystals. **^{1}H NMR (400 MHz, Chloroform-*d*) δ** 8.06 ‾ 7.96 (m, 1H), 7.61 ‾ 7.48 (m, 3H), 4.92 ‾ 4.83 (m, 2H), 4.05 (q, J = 7.1 Hz, 2H), 3.17 (s, 3H), 2.70 (t, J = 6.2 Hz, 2H), 2.29 ‾ 2.17 (m, 2H), 1.61 (s, 6H), 1.19 (t, J = 7.1 Hz, 3H). **^{13}C NMR (101 MHz, Chloroform-*d*) δ** 196.52, 172.78, 141.63, 141.27, 130.00, 129.65, 123.13, 115.93, 60.97, 54.67, 48.59,

30.56, 23.12, 22.94, 16.32, 14.16. **HRMS (*m/z*):** $[M]^+$ calcd. for $C_{17}H_{24}NO_2$, 274.1802; found, 274.1810.

Compound 3a (for structure ¯ see SI file). Compound **2** (1 eq., 3 g, 8.47 mmol) was placed in a reaction flask. Anhydrous pyridine (40 mL) was added via syringe. Obtained mixture was preheated to 110 éC until complete dissolving of indoleninium salt, then triethyl orthoformate (1.5 eq., 1.88 g, 2.12 mL, 12.7 mmol) was quickly added dropwise to the boiling solution of indoleninium salt using syringe. The reaction mixture was stirred under reflux for 4 hours. Then, solvent was removed under reduced pressure. The residue was redissolved in DCM (100 mL), washed with 1M aq. solution of hydrochloric acid (3 B 100 mL), once with brine, and dried over sodium sulphate. After solvent evaporation, the product was purified by gradient column chromatography (SiO_2, DCM/MeOH, 98:2 to 90:10), which furnished 3.83 g (yield 71%) of title compound **3a** as a red solid. **^{1}H NMR (400 MHz, Methanol-d_4) δ** 8.60 (t, *J* = 13.4 Hz, 1H), 7.59 (d, *J* = 7.4 Hz, 2H), 7.53 ¯ 7.45 (m, 4H), 7.39 ¯ 7.31 (m, 2H), 6.64 (d, *J* = 13.6 Hz, 2H), 4.27 (t, *J* = 7.7 Hz, 4H), 4.15 (q, *J* = 7.1 Hz, 4H), 2.63 (t, *J* = 6.7 Hz, 4H), 2.16 (p, *J* = 7.0 Hz, 4H), 1.81 (s, 12H), 1.27 (t, *J* = 7.1 Hz, 6H). **^{13}C NMR (101 MHz, Methanol-d_4) δ** 176.10, 174.36, 152.32, 143.30, 142.19, 129.98, 126.78, 123.55, 112.45, 103.96, 61.78, 50.66, 44.53, 31.63, 28.31, 23.33, 14.54. **HRMS (*m/z*):** $[M]^+$ calcd. for $C_{35}H_{45}N_2O_4$, 557.3374; found, 557.3360.

Compound 3b (for structure ¯ see SI file)**.** 1-(4-ethoxy-4-oxobutyl)-2,3,3-trimethyl-3H-indol-1-ium bromide (1 eq., 2.09 g, 5.9 mmol) were placed in a reaction flask. Anhydrous pyridine (40 mL) was added via syringe. The mixture was preheated to 110 éC until complete dissolving of the indoleninium salt, then 1,1,3,3-tetramethoxypropane (1.5 eq., 1.45 g, 1.47 mL, 8.85 mmol) was quickly added dropwise to the boiling solution of indoleninium salt. Reaction mixture was stirred under reflux for 4 hours. Then, solvent was removed under reduced pressure. The residue was redissolved in DCM (100 mL), washed three times with 1M aq. solution of hydrochloric acid (3 B 100 mL), once with brine, and dried over sodium sulphate. After solvent evaporation, crude product was purified by gradient column chromatography (SiO_2, DCM/MeOH, 95:5 to 9:1), which furnished 2.55 g (yield 65 %) of the title compound **3b** as a blue solid with metallic luster. **^{1}H NMR (400 MHz, Methanol-d_4) δ** 8.30 (t, *J* = 13.1 Hz, 2H), 7.49 (dd, *J* = 7.5, 1.1 Hz, 2H), 7.41 (ddd, *J* = 8.4, 7.3, 1.2 Hz, 2H), 7.35 (d, *J* = 7.9 Hz, 2H), 7.26 (td, *J* = 7.4, 1.1 Hz, 2H), 6.64 (t, *J* = 12.4 Hz, 1H), 6.38 (d, *J* = 13.7 Hz, 2H), 4.23 ¯ 4.08 (m, 8H), 2.56 (t, *J* = 6.6 Hz, 4H), 2.13 ¯ 2.02 (m, 4H), 1.72 (s, 12H), 1.26 (t, *J* = 7.1 Hz, 6H). **^{13}C NMR (101 MHz, Methanol-d_4) δ** 174.74, 174.44, 155.65, 143.45, 142.55, 129.72, 126.87, 126.26, 123.43, 111.96, 104.43, 61.79, 50.57, 44.25, 31.44, 27.94, 23.21, 14.56. **HRMS (*m/z*):** $[M]^+$ calcd. for $C_{37}H_{47}N_2O_4$, 583.3530; found, 583.3536.

Compound 4a. Compound **3a** (1 eq., 3 g, 4.7 mmol) was hydrolyzed using 30% aq. solution of hydrobromic acid (25 mL) while stirring at 110 éC for about 4 h (control by TLC). Then, solvent was removed under reduced pressure. The residue was redissolved in DCM (100 mL), and washed with 10% aq. solution of sodium carbonate (3 B 100 mL), once with brine, dried over sodium sulphate, filtered, and the filtrate evaporated to dryness in vacuum. The crude product **4a** had a purity of >90% and was used directly for the next step without further purification. Yield 1.59 g (58%) as a red solid. **^{1}H NMR (400 MHz, DMSO-d_6) δ** 12.50 (br s, 2H), 8.36 (t, *J* = 13.4 Hz, 1H), 7.64 (d, *J* = 7.4 Hz, 2H),

7.50 (d, J = 8.0 Hz, 2H), 7.45 (td, J = 8.0, 1.2 Hz, 2H), 7.30 (t, J = 7.4 Hz, 2H), 6.57 (d, J = 13.4 Hz, 2H), 4.15 (t, J = 7.7 Hz, 4H), 2.42 (t, J = 7.1 Hz, 4H), 1.96 (p, J = 7.3 Hz, 4H), 1.70 (s, 12H). **^{13}C NMR (101 MHz, DMSO-d_6) δ** 173.95, 173.75, 149.93, 141.86, 140.61, 128.59, 125.17, 122.49, 111.36, 102.68, 48.89, 43.18, 30.78, 27.41, 22.41. **HRMS (*m/z*):** $[M]^+$ calcd. for $C_{31}H_{37}N_2O_4$, 501.2748; found, 501.2756.

Compound 4b. The compound **3b** was hydrolyzed using 30% aq. solution of hydrobromic acid (50 mL) while stirring at 110 éC for about 4 h (control by TLC). Then, solvent was removed under reduced pressure. The residue was redissolved in DCM (100 mL), and washed with 10% aq. solution of sodium carbonate (3 B 100mL), once with brine, dried over sodium sulphate, filtered and the filtrate evaporated to dryness in vacuum. The crude product **4b** had a purity of >90% and was used directly for the next step without further purification. Yield 1.51 g (55%) as a dark blue solid. **^{1}H NMR (400 MHz, DMSO-d_6) δ** 8.35 (t, J = 13.1 Hz, 2H), 7.61 (d, J = 7.5 Hz, 2H), 7.46 ¯ 7.33 (m, 4H), 7.24 (td, J = 7.1, 1.7 Hz, 2H), 6.54 (t, J = 12.3 Hz, 1H), 6.37 (d, J = 13.8 Hz, 2H), 4.11 (t, J = 7.7 Hz, 4H), 2.42 (t, J = 7.0 Hz, 4H), 1.95 ¯ 1.83 (m, 4H), 1.68 (s, 12H). **^{13}C NMR (101 MHz, DMSO-d_6) δ** 173.87, 172.70, 154.14, 141.93, 141.07, 128.36, 125.50, 124.64, 122.40, 110.89, 103.14, 48.89, 42.76, 30.49, 27.10, 22.19. **HRMS (*m/z*):** $[M]^+$ calcd. for $C_{33}H_{39}N_2O_4$, 527.2904; found, 527.2915.

Compound 5a. Compound **4a** (1 eq., 500 mg, 0.86 mmol), HBTU (2.2 eq., 717 mg, 1.89 mmol), and HOBt (3 eq., 348 mg, 2.58 mmol) were placed in a reaction flask. DMF (5mL) and DIPEA (10 eq., 1.42 mL, 8.6 mmol) were added via syringe. After stirring the reaction mixture for 30 min, tert-butyl N-[2-(dodecylamino)ethyl]carbamate (2 eq., 564 mg, 1.72 mmol) dissolved in anhydrous DCM (2 mL) was added dropwise. The reaction mixture was stirred at ambient temperature for 24 h. Solvent was removed under reduced pressure. The residue was redissolved in DCM (50 mL), washed with saturated brine solution (3 B100 mL), dried over sodium sulphate, filtered, and the filtrate evaporated to dryness in vacuum. The crude product was purified by flash column chromatography (SiO_2, DCM/MeOH, 98:2), which furnished 796 mg (yield 77%) of the title compound **5a** as a red solid. **^{1}H NMR (400 MHz, Methanol-d_4) δ** 8.60 (t, J = 13.4 Hz, 1H), 7.59 (d, J = 7.5 Hz, 2H), 7.55 ¯ 7.45 (m, 4H), 7.35 (t, J = 7.3 Hz, 2H), 6.68 ¯ 6.53 (m, 2H), 4.29 ¯ 4.18 (m, 4H), 3.52 ¯ 3.44 (m, 4H), 3.45 ¯ 3.37 (m, 4H), 3.32 ¯ 3.22 (m, 4H), 2.77 ¯ 2.69 (m, 2H), 2.69 ¯ 2.60 (m, 2H), 2.20 ¯ 2.11 (m, 4H), 1.82 (s, 12H), 1.63 ¯ 1.55 (m, 4H), 1.46 (s, 9H), 1.45 (s, 9H), 1.41 ¯ 1.29 (m, 36H), 0.98 ¯ 0.89 (m, 6H). **^{13}C NMR (101 MHz, Methanol-d_4) δ** 176.09, 176.01, 174.13, 174.07, 173.85, 173.82, 158.37, 158.31, 152.32, 152.29, 143.37, 143.33, 142.21, 142.18, 130.01, 126.75, 123.48, 112.71, 112.53, 103.98, 103.93, 103.84, 103.82, 80.29, 80.05, 61.76, 50.65, 50.63, 50.16, 47.61, 47.23, 44.81, 44.68, 39.75, 39.53, 38.88, 33.06, 33.05, 30.76, 30.73, 30.54, 30.50, 30.46, 30.28, 29.82, 28.83, 28.82, 28.61, 28.41, 28.39, 28.37, 28.35, 28.09, 27.93, 27.92, 23.72, 23.71, 14.47, 14.45. **HRMS (*m/z*):** $[M]^+$ calcd. for $C_{69}H_{113}N_6O_6$, 1121.8716; found, 1121.8698.

Compound 5b. The compound **5b** prepared using the same procedure as described above for **5a**. Yield 748 mg (74%) as blue solid. **^{1}H NMR (400 MHz, Methanol-d_4) δ** 8.28 (td, J = 13.2, 4.7 Hz, 2H), 7.50 (d, J = 7.4 Hz, 2H), 7.45 ¯ 7.36 (m, 4H), 7.27 (t, J = 7.0 Hz, 2H), 6.73 (t, J = 12.4 Hz, 1H), 6.46 ¯ 6.35 (m, 2H), 4.25 ¯ 4.12 (m, 4H), 3.53 ¯ 3.45 (m, 4H), 3.45 ¯ 3.40 (m, 2H), 3.39 ¯ 3.32 (m, 2H), 3.31 ¯

3.23 (m, 4H), 2.69 (t, J = 7.0 Hz, 2H), 2.61 (t, J = 7.1 Hz, 2H), 2.19 ¯ 2.07 (m, 4H), 1.74 (s, 12H), 1.65 ¯ 1.54 (m, 4H), 1.46 (s, 9H), 1.45 (s, 9H), 1.38 ¯ 1.27 (m, 36H), 0.92 (t, J = 6.3 Hz, 6H). **^{13}C NMR (101 MHz, Methanol-d_4) δ** 174.54, 174.50, 173.94, 173.91, 173.70, 173.68, 167.33, 158.25, 155.42, 143.50, 142.54, 129.71, 127.27, 126.18, 123.34, 112.14, 112.02, 104.62, 104.57, 104.49, 104.43, 80.20, 79.95, 50.53, 50.50, 50.06, 48.18, 47.44, 47.11, 44.62, 44.39, 39.70, 39.58, 38.88, 33.02, 30.77, 30.75, 30.73, 30.71, 30.58, 30.56, 30.45, 30.42, 30.25, 29.78, 28.86, 28.84, 28.70, 28.63, 28.07, 28.05, 27.99, 27.88, 23.69, 23.64, 14.52, 14.49. **HRMS (*m/z*):** $[M]^+$ calcd. for $C_{71}H_{115}N_6O_6$, 1147.8873; found, 1147.8870.

Compound 6a. Compound **6a** (1 eq., 500 mg, 0.416 mmol) was dissolved in DCM (3 mL). TFA (100 eq., 3.18 mL, 41.6 mmol) was added dropwise and the reaction mixture was stirred at ambient temperature for 4 h. Solvent was removed under reduced pressure. To remove the remained traces of TFA, the residue was co-evaporated with methanol (3 B 50 mL). After removal of the Boc protecting group the crude product was used directly for the next step without further purification. Yield 426 mg (81%) as red viscous oil. **^{1}H NMR (400 MHz, Methanol-d_4) δ** 8.42 (t, J = 13.3 Hz, 1H), 7.43 ¯ 7.37 (m, 2H), 7.35 ¯ 7.27 (m, 4H), 7.21 ¯ 7.12 (m, 2H), 6.49 ¯ 6.32 (m, 2H), 4.15 ¯ 4.03 (m, 4H), 3.58 ¯ 3.47 (m, 4H), 3.20 ¯ 3.13 (m, 4H), 3.00 (t, J = 6.0 Hz, 4H), 2.54 ¯ 2.44 (m, 4H), 2.06 ¯ 1.96 (m, 4H), 1.64 (s, 12H), 1.43 ¯ 1.32 (m, 4H), 1.19 ¯ 1.08 (m, 36H), 0.74 (t, J = 6.6 Hz, 6H). **^{13}C NMR** spectrum was difficult to measure due to the sample aggregation. **HRMS (*m/z*):** $[M]^{3+}/3$ calcd. for $C_{59}H_{99}N_6O_2$, 307.9271; found, 307.9260.

Compound 6b. The compound prepared using the same procedure as described above for **6a**. After removal of the Boc protecting group the crude product **6b** was used directly in the next step without further purification. Yield 415 mg (79%) as blue viscous oil. **^{1}H NMR (400 MHz, Methanol-d_4) δ** 8.07 (t, J = 13.1 Hz, 2H), 7.29 (d, J = 7.6 Hz, 2H), 7.22 ¯ 7.16 (m, 4H), 7.09 ¯ 7.03 (m, 2H), 6.45 (t, J = 12.4 Hz, 1H), 6.19 (d, J = 13.7 Hz, 2H), 4.00 (t, J = 7.6 Hz, 4H), 3.45 (t, J = 6.0 Hz, 4H), 3.13 ¯ 3.08 (m, 4H), 2.94 (t, J = 6.0 Hz, 4H), 2.40 (t, J = 6.7 Hz, 4H), 1.98 ¯ 1.88 (m, 4H), 1.54 (s, 12H), 1.35 ¯ 1.24 (m, 4H), 1.10 ¯ 1.05 (m, 36H), 0.69 (t, J = 6.9 Hz, 6H). **^{13}C NMR** spectrum was difficult to measure due to the sample aggregation. **HRMS (*m/z*):** $[M]^{3+}/3$ calcd. for $C_{61}H_{101}N_6O_2$, 316.5990; found, 316.5998.

Compound Cy3A. Aliphatic amine derivative of cyanine **6a** and triethyl amine (10 eq.) were dissolved in anhydrous DMF (1 mL), and 3,4,5-tris(tetraethyleneoxy)benzoyl chloride **7** (4 eq.) (prepared in situ from corresponding acid and oxalyl chloride)[35] was added dropwise as a solution in anhydrous DMF at 0 éC using ice bath. After stirring at 0 éC for 2h, the reaction mixture was heated to 60 éC for another 2h until completion. After solvent evaporation in vacuum, the residue was redissolved in DCM (50 mL), washed with saturated brine solution (3 B100 mL), dried over sodium sulphate, filtered, and the filtrate evaporated to dryness in vacuum. The crude product was purified by flash column chromatography (SiO_2, DCM/MeOH, 95:5 to 90:10), which furnished 10 mg (yield 20%) of **Cy3A** as a red oil. **^{1}H NMR (400 MHz, Methanol-d_4) δ** 8.70 ¯ 8.44 (m, 1H), 7.63 (d, J = 7.4 Hz, 2H), 7.56 ¯ 7.44 (m, 4H), 7.40 (t, J = 7.3 Hz, 2H), 7.31 (s, 1H), 7.25 (s, 1H), 6.80 (s, 1H), 6.79 (s, 1H), 6.71 ¯ 6.42 (m, 2H), 4.31 ¯ 4.18 (m, 12H), 4.17 ¯ 4.05 (m, 4H), 3.99 ¯ 3.85 (m, 6H), 3.85 ¯ 3.79 (m, 6H), 3.79 ¯ 3.72

(m, 12H), 3.71 ¯ 3.62 (m, 52H), 3.62 ¯ 3.57 (m, 12H), 3.56 ¯ 3.45 (m, 4H), 3.41 (s, 18H), 3.39 ¯ 3.31 (m, 4H), 2.75 ¯ 2.63 (m, 2H), 2.62 ¯ 2.41 (m, 2H), 2.22 ¯ 2.09 (m, 4H), 1.85 (s, 12H), 1.73 ¯ 1.54 (m, 4H), 1.44 ¯ 1.18 (m, 36H), 0.97 (t, J = 7.4 Hz, 6H). **^{13}C NMR** spectrum was difficult to measure due to the sample aggregation. **HRMS ESI (*m/z*):** $[M]^+$ calcd. for $C_{127}H_{213}N_6O_{34}$, 2367.5151, found 2367.5054.

Compound Cy5A. The compound prepared using the same procedure as described above for **Cy3A**. The crude product was purified by flash column chromatography (SiO_2, DCM/MeOH, 95:5 to 90:10). Yield 15 mg (18%) as blue oil. **^{1}H NMR (400 MHz, Methanol-d_4) δ** 8.37 ¯ 8.20 (m, 2H), 7.54 (d, J = 7.5 Hz, 2H), 7.45 (t, J = 7.7 Hz, 2H), 7.38 (d, J = 7.9 Hz, 2H), 7.34 ¯ 7.30 (m, 2H), 7.29 (s, 1H), 7.28 (s, 1H), 7.23 (s, 1H), 7.22 (s, 1H), 6.72 ¯ 6.52 (m, 1H), 6.38 (d, J = 13.5 Hz, 2H), 4.29 ¯ 4.12 (m, 12H), 4.11 ¯ 3.97 (m, 4H), 3.88 (t, J = 4.6 Hz, 4H), 3.83 (t, J = 4.7 Hz, 4H), 3.81 ¯ 3.75 (m, 4H), 3.74 ¯ 3.69 (m, 12H), 3.69 ¯ 3.60 (m, 48H), 3.59 ¯ 3.52 (m, 12H), 3.41 (t, J = 8.0 Hz, 4H), 3.37 (s, 18H), 3.36 ¯ 3.33 (m, 8H), 2.79 ¯ 2.67 (m, 2H), 2.66 ¯ 2.56 (m, 2H), 2.18 ¯ 2.02 (m, 4H), 1.77 (s, 12H), 1.69 ¯ 1.55 (m, 4H), 1.45 ¯ 1.24 (m, 36H), 0.98 ¯ 0.88 (m, 6H). **^{13}C NMR** spectrum was difficult to measure due to an aggregation of the sample. **HRMS ESI (*m/z*):** $[M]^+$ calcd. for $C_{129}H_{215}N_6O_{34}$, 2393.5307; found, 2393.5314.

Other materials

Sodium tetraphenylborate (ħ99.5 %), lithium tetrakis(pentafluorophenyl)borate ethyl etherate, acetonitrile were purchased from Sigma-Aldrich and used as received. Sodium phosphate monobasic (>99.0 %, Sigma-Aldrich) and sodium phosphate dibasic dihydrate (>99.0 %, Sigma-Aldrich) were used to prepare 20 mM phosphate buffer solutions at pH 7.4. MilliQ-water (Millipore) was used in all experiments. All starting materials for synthesis were purchased from Alfa Aesar and Sigma Aldrich or TCI Europe and used as received unless stated otherwise. NMR spectra were recorded on a Bruker Avance III 400 MHz spectrometer. Mass spectra were obtained using an Agilent Q-TOF 6520 mass spectrometer. Synthesis of alkyl-rhodamine B dyes is described in supporting information.

Preparation of fluorescent NPs

The cyanine (Cy3A, either Cy5A) derivative was dissolved at 1 mM in DMSO. The concentration was measured by photometry using the extinction coefficient for Cy3 and Cy5 derivatives 150000 and 250000 M^{-1} cm^{-1} in methanol, respectively. To prepare 1 ı M of nanoparticle solution, 2 ı L of 1 mM cyanine (Cy3A, either Cy5A) derivative stock solution was added quickly under stirring (shaking) using a micropipette to 1.98 mL of Milli-Q÷ water (Millipore). Then, to the obtained solution a 10-fold excess of the corresponding borate solution (20 ı L of 1 mM stock solution) was added quickly under stirring, using a micropipette.

For the DLS measurements of nanoparticle suspension 2 ı M dye concentration was used to obtain sufficient signal. To this end, 4 ı L of 1 mM cyanine (Cy3A, either Cy5A) derivative stock solution was added quickly under stirring using a micropipette to a 1.96 mL of Milli-Q÷ water (Millipore).

Then to the obtained solution 10-fold excess of the corresponding borate solution (40 ı L of 1 mM stock solution) was added quickly under stirring using a micropipette. Zeta potential measurements were performed using 5 ı M dye concentration.

For the DLS and AFM measurements, to remove possible aggregates the obtained solution of prepared nanoparticles was additionally filtered through a 0.1 ı m PVDF NS `Ultrafree÷-CL_ centrifugal filter unit (Merck Millipore).

Optical spectroscopy

Absorption and emission spectra were recorded on a Cary 400 Scan UV-visible spectrophotometer (Varian) and a FluoroMax-4 spectrofluorometer (Horiba Jobin Yvon) equipped with a thermostated cell compartment, respectively. For standard recording of fluorescence spectra, the excitation wavelength was set to 520 nm. The fluorescence spectra were corrected for detector response and lamp fluctuations. Fluorescence quantum yields were calculated using rhodamine B in water (QY = 31%)[36] with an absorbance of 0.1 at 520 nm as a reference. Hydrodynamic diameter and zeta-potential measurements were performed on a Zetasizer Nano series DTS 1060 (Malvern Instruments S.A.) with a laser source at 633 nm.

AFM measurements

AFM measurements were performed using a Solver-Pro-M (NT-MDT) instrument. The measurements were in liquid phase. Cantilevers were NSG03 (NT-MDT) with a tip curvature radius of 10 nm. The NPs were prepared as described before. To deposit NPs on the mica surface, 100 μL of 10-100 mM calcium chloride solution (depends on the counterion) was first incubated for 30 min. Then, the solution was removed with a filter paper and 100 μL of an undiluted suspension of NPs was deposited on the mica surface. After 30 min, the solution was removed using a filter paper and then replaced with 100 μL of a 10-100 mM solution of calcium chloride. The obtained sample was imaged in liquid phase, using the tapping mode (~37 kHz).

Fluorescence correlation spectroscopy (FCS) and data analysis

FCS measurements were performed on a two-photon platform including an Olympus IX70 inverted microscope, as described previously.[58] Two-photon excitation at 760 nm (1¯5 mW laser output power) was provided using an InSight DeepSee laser (Spectra Physics). The measurements were carried out in a 96-well plate, using a 200 ı L volume per well. The focal spot was set about 20 ı m above the cover-slip. The normalized autocorrelation function, $G(\tau)$ was calculated online by using an ALV-5000E correlator (ALV, Germany) from the fluorescence fluctuations, $F(t)$, by $G(\tau) = \langle F(t)\, F(t+\tau)\rangle / \langle F(t)\rangle^2$, where $\langle F(t)\rangle$ is the mean fluorescence signal, and τ is the lag time. Assuming that fluorescent NPs diffuse freely in a Gaussian excitation volume, the correlation function, $G(\tau)$, calculated from the fluorescence fluctuations was fitted according to Thompson:[79]

$$G(\tau) = \frac{1}{N}\left(1+\frac{\tau}{\tau_{\mathrm{d}}}\right)^{-1}\left(1+\frac{1}{S^2}\frac{\tau}{\tau_{\mathrm{d}}}\right)^{-1/2}$$

where τ_{d} is the diffusion time, N is the mean number of fluorescent species within the two-photon excitation volume, and S is the ratio between the axial and lateral radii of the excitation volume. The excitation volume is about 0.34 fL and S is about 3 to 4. Typical data recording time was 5 min, using freshly prepared NPs without further dilution. The measurements were done with respect to a reference 5(6)-carboxytetramethylrhodamine (TMR, from Sigma-Aldrich) in water. The hydrodynamic diameter, d, of NPs was calculated as: $d_{\mathrm{NPs}} = \tau_{\mathrm{d(NPs)}} / \tau_{\mathrm{d(TMR}}) \mathrm{B}\, d_{\mathrm{TMR}}$, where d_{TMR} is a hydrodynamic diameter of TMR (1.0 nm). The concentration of NPs was calculated from the number of species by: $C_{\mathrm{NPs}} = N_{\mathrm{NPs}}/N_{\mathrm{TMR}}\, \mathrm{B}\, C_{\mathrm{TMR}}$, using a TMR concentration of 50 nM.

Acknowledgements

I.S. acknowledges support from French Embassy. This work was supported by ERC Consolidator grant BrightSens 648528.

References

1. Ariga, K.; Hill, J. P.; Lee, M. V.; Vinu, A.; Charvet, R.; Acharya, S. Challenges and breakthroughs in recent research on self-assembly. *Sci. Technol. Adv. Mater.* **2008**, *9*.
2. Horcajada, P.; Chalati, T.; Serre, C.; Gillet, B.; Sebrie, C.; Baati, T.; Eubank, J. F.; Heurtaux, D.; Clayette, P.; Kreuz, C.; Chang, J.-S.; Hwang, Y. K.; Marsaud, V.; Bories, P.-N.; Cynober, L.; Gil, S.; Ferey, G.; Couvreur, P.; Gref, R. Porous metal-organic-framework nanoscale carriers as a potential platform for drug delivery and imaging. *Nature Materials* **2010**, *9*, 172.
3. Eddaoudi, M.; Moler, D. B.; Li, H. L.; Chen, B. L.; Reineke, T. M.; O'Keeffe, M.; Yaghi, O. M. Modular chemistry: Secondary building units as a basis for the design of highly porous and robust metal-organic carboxylate frameworks. *Accounts of Chemical Research* **2001**, *34*, 319.
4. Cui, Y. J.; Yue, Y. F.; Qian, G. D.; Chen, B. L. Luminescent Functional Metal-Organic Frameworks. *Chemical Reviews* **2012**, *112*, 1126.
5. Furukawa, S.; Reboul, J.; Diring, S.; Sumida, K.; Kitagawa, S. Structuring of metal-organic frameworks at the mesoscopic/macroscopic scale. *Chemical Society Reviews* **2014**, *43*, 5700.
6. Shimizu, T.; Masuda, M.; Minamikawa, H. Supramolecular nanotube architectures based on amphiphilic molecules. *Chemical Reviews* **2005**, *105*, 1401.
7. Aida, T.; Meijer, E. W.; Stupp, S. I. Functional Supramolecular Polymers. *Science* **2012**, *335*, 813.
8. Hartgerink, J. D.; Beniash, E.; Stupp, S. I. Self-assembly and mineralization of peptide-amphiphile nanofibers. *Science* **2001**, *294*, 1684.
9. Lehn, J. M. Toward self-organization and complex matter. *Science* **2002**, *295*, 2400.
10. Krossing, I.; Raabe, I. Noncoordinating anions - Fact or fiction? A survey of likely candidates. *Angewandte Chemie-International Edition* **2004**, *43*, 2066.
11. Reisch, A.; Didier, P.; Richert, L.; Oncul, S.; Arntz, Y.; Mely, Y.; Klymchenko, A. S. Collective fluorescence switching of counterion-assembled dyes in polymer nanoparticles. *Nature Communications* **2014**, *5*.

12. Kilin, V. N.; Anton, H.; Anton, N.; Steed, E.; Vermot, J.; Vandamme, T. E.; Mely, Y.; Klymchenko, A. S. Counterion-enhanced cyanine dye loading into lipid nano-droplets for single-particle tracking in zebrafish. *Biomaterials* **2014**, *35*, 4950.
13. Yao, H.; Ashiba, K. Highly fluorescent organic nanoparticles of thiacyanine dye: a synergetic effect of intermolecular H-aggregation and restricted intramolecular rotation. *RSC Adv.* **2011**, *1*, 834.
14. Yao, H.; Yamashita, M.; Kimura, K. Organic styryl dye nanoparticles: Synthesis and unique spectroscopic properties. *Langmuir* **2009**, *25*, 1131.
15. Bwambok, D. K.; El-Zahab, B.; Challa, S. K.; Li, M.; Chandler, L.; Baker, G. A.; Warner, I. M. Near-Infrared Fluorescent NanoGUMBOS for Biomedical Imaging. *ACS Nano* **2009**, *3*, 3854.
16. de Rooy, S. L.; Das, S.; Li, M.; El-Zahab, B.; Jordan, A.; Lodes, R.; Weber, A.; Chandler, L.; Baker, G. A.; Warner, I. M. Ionically Self-Assembled, Multi-Luminophore One-Dimensional Micro- and Nanoscale Aggregates of Thiacarbocyanine GUMBOS. *J. Phys. Chem. C* **2012**, *116*, 8251.
17. Jordan, A. N.; Das, S.; Siraj, N.; de Rooy, S. L.; Li, M.; El-Zahab, B.; Chandler, L.; Baker, G. A.; Warner, I. M. Anion-controlled morphologies and spectral features of cyanine-based nanoGUMBOS - an improved photosensitizer. *Nanoscale* **2012**, *4*, 5031.
18. Shulov, I.; Oncul, S.; Reisch, A.; Arntz, Y.; Collot, M.; Mely, Y.; Klymchenko, A. S. Fluorinated counterion-enhanced emission of rhodamine aggregates: ultrabright nanoparticles for bioimaging and light-harvesting. *Nanoscale* **2015**, *7*, 18198.
19. Israelachvili, J. N.; Mitchell, D. J.; Ninham, B. W. THEORY OF SELF-ASSEMBLY OF HYDROCARBON AMPHIPHILES INTO MICELLES AND BILAYERS. *Journal of the Chemical Society-Faraday Transactions Ii* **1976**, *72*, 1525.
20. Zhang, X.; Chen, Z.; Würthner, F. Morphology control of fluorescent nanoaggregates by co-self-assembly of wedge- and dumbbell-shaped amphophilic perylene bisimides. *Journal of the American Chemical Society* **2007**, *129*, 4886.
21. Petkau, K.; Kaeser, A.; Fischer, I.; Brunsveld, L.; Schenning, A. P. H. J. Pre- and Postfunctionalized Self-Assembled pi-Conjugated Fluorescent Organic Nanoparticles for Dual Targeting. *Journal of the American Chemical Society* **2011**, *133*, 17063.
22. Olivier, J. H.; Widmaier, J.; Ziessel, R. Near-infrared fluorescent nanoparticles formed by self-assembly of lipidic (bodipy) dyes. *Chemistry - A European Journal* **2011**, *17*, 11709.
23. Kaeser, A.; Schenning, A. P. H. J. Fluorescent Nanoparticles Based on Self-Assembled pi-Conjugated Systems. *Advanced Materials* **2010**, *22*, 2985.
24. Hong, Y.; Lam, J. W. Y.; Tang, B. Z. Aggregation-induced emission. *Chem. Soc. Rev.* **2011**, *40*, 5361.
25. Niko, Y.; Arntz, Y.; Mely, Y.; Konishi, G.-i.; Klymchenko, A. S. Disassembly-Driven Fluorescence Turn-on of Polymerized Micelles by Reductive Stimuli in Living Cells. *Chemistry-a European Journal* **2014**, *20*, 16473.
26. Berberan-Santos, M. N.; Choppinet, P.; Fedorov, A.; Jullien, L.; Valeur, B. Multichromophoric cyclodextrins. 6. Investigation of excitation energy hopping by Monte-Carlo simulations and time-resolved fluorescence anisotropy. *J. Am. Chem. Soc.* **1999**, *121*, 2526.
27. Colby, K. A.; Burdett, J. J.; Frisbee, R. F.; Zhu, L.; Dillon, R. J.; Bardeen, C. J. Electronic energy migration on different time scales: Concentration dependence of the time-resolved anisotropy and fluorescence quenching of lumogen red in poly(methyl methacrylate). *J. Phys. Chem. A* **2010**, *114*, 3471.
28. Yeow, E. K. L.; Ghiggino, K. P.; Reek, J. N. H.; Crossley, M. J.; Bosnian, A. W.; Scheming, A. P. H. J.; Meijer, E. W. The dynamics of electronic energy transfer in novel multiporphyrin functionalized dendrimers: A time-resolved fluorescence anisotropy study. *J. Phys. Chem. B* **2000**, *104*, 2596.
29. Koynov, K.; Butt, H. J. Fluorescence correlation spectroscopy in colloid and interface science. *Curr. Opin. Colloid Interface Sci.* **2012**, *17*, 377.
30. Klymchenko, A. S.; Roger, E.; Anton, N.; Anton, H.; Shulov, I.; Vermot, J.; Mely, Y.; Vandamme, T. F. Highly lipophilic fluorescent dyes in nano-emulsions: Towards bright non-leaking nano-droplets. *RSC Adv.* **2012**, *2*, 11876.
31. Xu, C.; Webb, W. W. Measurement of two-photon excitation cross sections of molecular fluorophores with data from 690 to 1050 nm. *Journal of the Optical Society of America B-Optical Physics* **1996**, *13*, 481.

32. Trofymchuk, K.; Prodi, L.; Reisch, A.; Mely, Y.; Altenhoener, K.; Mattay, J.; Klymchenko, A. S. Exploiting Fast Exciton Diffusion in Dye-Doped Polymer Nanoparticles to Engineer Efficient Photoswitching. *Journal of Physical Chemistry Letters* **2015**, *6*, 2259.
33. Stevens, A. L.; Kaeser, A.; Schenning, A. P. H. J.; Herz, L. M. Morphology-Dependent Energy Transfer Dynamics in Fluorene-Based Amphiphile Nanoparticles. *ACS Nano* **2012**, *6*, 4777.
34. Morton, S. W.; Zhao, X.; Quadir, M. A.; Hammond, P. T. FRET-enabled biological characterization of polymeric micelles. *Biomaterials* **2014**, *35*, 3489.
35. Brunsveld, L.; Zhang, H.; Glasbeek, M.; Vekemans, J. A. J. M.; Meijer, E. W. Hierarchical Growth of Chiral Self-Assembled Structures in Protic Media†. *Journal of the American Chemical Society* **2000**, *122*, 6175.
36. Magde, D.; Rojas, G. E.; Seybold, P. G. Solvent dependence of the fluorescence lifetimes of xanthene dyes. *Photochem. Photobiol.* **1999**, *70*, 737.

Supporting information

AFM size statistics

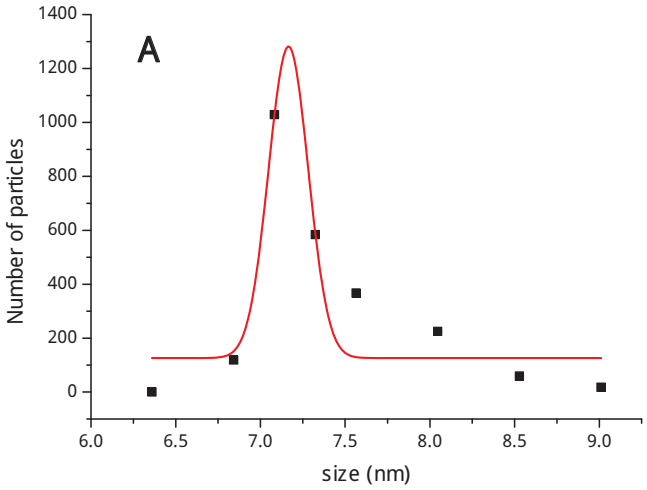

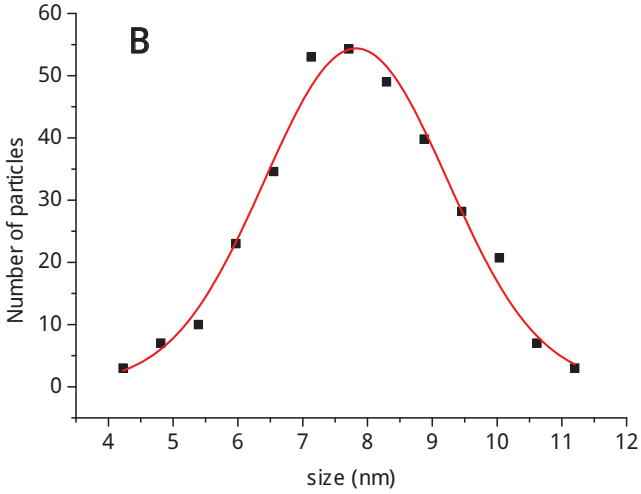

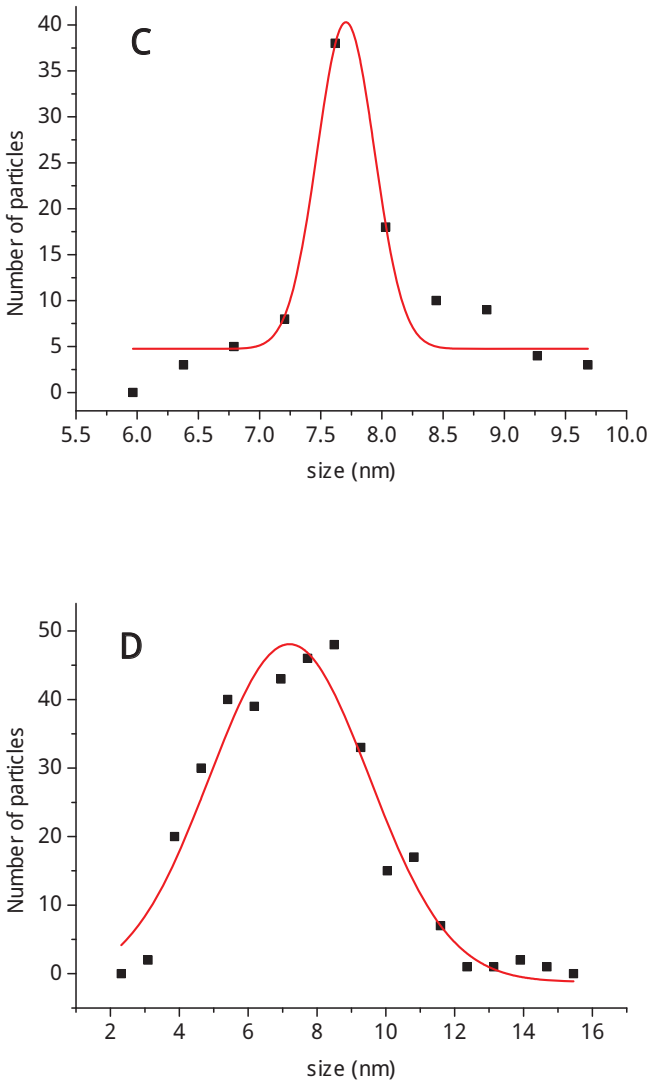

Figure S1. AFM size statistics of micellar NPs prepared by self-assembly of Cy3A and Cy5A amphiphiles with tetraphenylborate counterions: (A) **Cy3A — F5-TPB**, average size **7 nm**; (B) **Cy3A — TPB**, average size **8 nm**; (C) **Cy5A — F5-TPB**, average size **8 nm**; (D) **Cy5A — TPB**, average size **7 nm**. Particle diameter was estimated from the height measurements. Gaussian model was applied for the function fitting of the size distribution.

2.4 Shell-cross-linked calixarene micelles with cyanine corona: protein-sized ultrabright fluorogenic nanoparticles

Preparation of small monodispersed fluorescent nanoparticles bearing large number of donor chromophores remains an important issue. An attractive approach is to use micelles as platform for preparation of these NPs, because micellar assembly is robust allowing preparation of NPs of 5-10 nm size. This is already close to the size of proteins, which makes them attractive for broad range of applications in bioimaging. However, two problems should be resolved. First is aggregation caused quenching, which normaly takes place once the dyes are assembled within the micelle in form of non-fluorescent H-aggregates.[1] Second, because micelles are dynamic structures that can readily decompose in biological media, they have to be polymerized or even cross-linked. In 2012, Yang et al. have reported a synthesis of multifunctional surface-cross-linked micelles (SCMs) functionalized with several dyes for light harvesting application.[2] They designed a surfactant bearing three acetylene groups at its polar head and after formation of micelles cross-liked them with polar diazide cross-linker via Cu(I) catalyzed 1,3-dipolar cycloaddition, known as "click" reaction (Fig. 2.4.1). Moreover, the remaining non-reacted acetylene groups were further used to graft up to 50 molecules of 9,10-bis(4-methylphenyl)anthracene (DPA). Surprisingly, the spectroscopic data showed neither self-quenching nor excimer formation of such highly dye-crowded micelles. The authors assumed that these observations were an outcome of nonplanarity of the used DPA chromophores, as well as relatively rigid connection between chromophores and micelle surface. Moreover, electrostatic repulsion among the cationic micelles helped to preserve colloidal stability of SCMs.

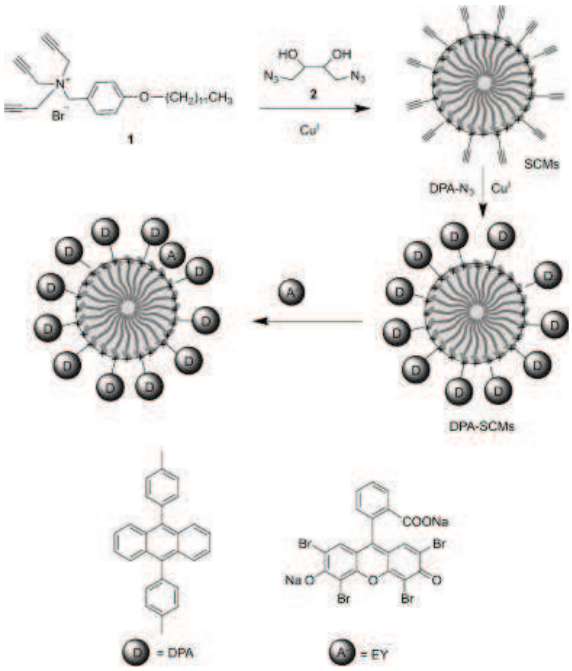

Figure 2.4.1. Preparation of donor-functionalized surface-cross-linked micelles and construction of a light-harvesting system by introducing of Eosin Y disodium salt through electrostatic interactions as an energy acceptor. D and A represent donor and acceptor, respectively. Adapted with permission from ref.[2] Copyright 2012 Wiley-VCH Verlag GmbH & Co. KGaA, Weinheim.

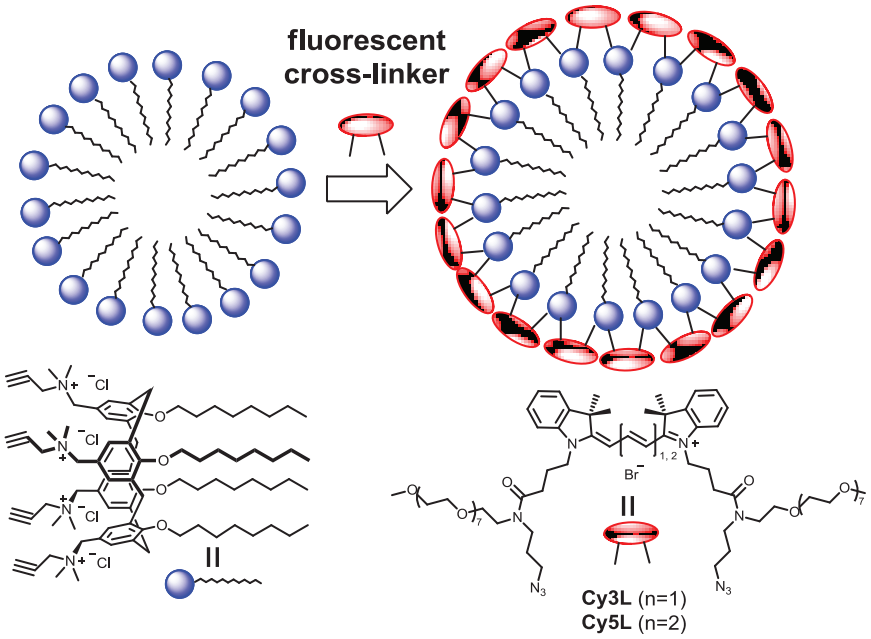

Figure 2.4.2. The concept of calixarene micelles shell-cross-linked with fluorescent amphiphiles based on cyanine dye.

Inspired the work of Yang et al. described above, we developed a concept of ultra-small fluorescent micellar NPs assembled from calixarene surfactant that are shell-cross-linked via click reaction by bi-functional fluorescent dye. The use of bi-functional fluorescent cross-linker enables the cross-linking together with the introduction of the fluorescent unit. To this end, we have chosen cyanine 3 and 5 dyes, because they display excellent optical properties and, due to symmetric structure, they are excellent candidates to prepare bi-functional cross-linkers. In our fluorescent cross-linkers the nitrogen heteroatoms of cyanines were substituted with two reactive azide groups and two polar PEG(8) chains (Fig. 2.4.2). In this design, we expected that the reactive groups would cross-link the calixarene molecules within the surface of the micelle, while the PEG(8) groups would create the hydrophilic shell to ensure its stability and biocompatibility. We call this design as “cyanine corona” because, similarly to well-known protein corona that modifies surfaces of variety of NPs,[3] these dyes are expected to create a stable biocompatible molecular layer on the surface of micellar NPs. As reactive surfactant, we designed amphiphilic calixarene. Calixarenes, due to persistent conical shape of their macrocycle, are powerful building blocks for nano-cages, supramolecular polymers and nanoparticles, etc.[4] Previously, we showed that calixarenes bearing charged groups at the upper rim and long alky chains at the lower rim can assemble into highly monodispersed micelles of 6 nm.[5] Here, we designed calixarene amphiphile that bears four alkyne groups at its polar heads for further “click” reaction with cyanine cross-linkers (Fig. 2.4.2). The obtained nanoparticles after crosslinking and purification by dialysis were 7 nm size according to atomic force microscopy and dynamic light

scattering techniques. In water solutions they showed relatively good fluorescence quantum yield (2%), indicating that cyanine dyes self-quenching is partially prevented based on our design concept. Even more importantly, in viscous glycerol they increased their quantum yield up to 10%. Remarkably, in the polyvinyl alcohol gels they showed >20-fold higher brightness than quantum dots (QD-585 at 532 nm excitation), which is an exceptional brightness for such small particles. They present excellent stability in aqueous and organic media according to Cy3-Cy5 energy transfer and they enter readily the living cells showing excellent signal to noise ratio without dye leakage. Thus, we developed a new platform for fabrication of ultrabright and protein-sized responsive nanoparticles for bioimaging.

The full description of this work can be found in the manuscript enclosed below.

References

(1) Niko, Y.; Arntz, Y.; Mely, Y.; Konishi, G.-i.; Klymchenko, A. S. *Chemistry-a European Journal* **2014**, *20*, 16473.
(2) Peng, H.-Q.; Chen, Y.-Z.; Zhao, Y.; Yang, Q.-Z.; Wu, L.-Z.; Tung, C.-H.; Zhang, L.-P.; Tong, Q.-X. *Angewandte Chemie-International Edition* **2012**, *51*, 2088.
(3) Lundqvist, M.; Stigler, J.; Elia, G.; Lynch, I.; Cedervall, T.; Dawson, K. A. *Proceedings of the National Academy of Sciences of the United States of America* **2008**, *105*, 14265.
(4) (a) Guo, D. S.; Liu, Y. *Chem. Soc. Rev.* **2012**, *41*, 5907. (b) Liu, M.; Liao, W. P.; Hu, C. H.; Du, S. C.; Zhang, H. J. *Angewandte Chemie-International Edition* **2012**, *51*, 1585.
(5) Rodik, R. V.; Klymchenko, A. S.; Jain, N.; Miroshnichenko, S. I.; Richert, L.; Kalchenko, V. I.; Mely, Y. *Chemistry-a European Journal* **2011**, *17*, 5526.

MANUSCRIPT №2

Shell-cross-linked calixarene micelles with cyanine corona: protein-sized ultrabright fluorogenic nanoparticles

Shell-Cross-Linked Calixarene Micelles with Cyanine Corona: Protein-Sized Bright Fluorogenic Nanoparticles

Ievgen Shulov, Roman V. Rodik, Youri Arntz, Andreas Reisch, Vitaly I. Kalchenko, and Andrey S. Klymchenko*

Abstract: The key challenge in the field of fluorescent nanoparticles (NPs) for biological applications is to achieve superior brightness for sizes equivalent to single proteins (3-7 nm). We propose a concept of shell-cross-linked fluorescent micelles, where PEGylated cyanine 3 and 5 bis-azides form a covalently attached `corona_ on micelles of amphiphilic calixarene bearing four alkyne groups. The obtained monodisperse NPs of 7 nm size increase their fluorescence quantum yield from 2% in water up to 10% in glycerol. Microscopy shows that they are ~2-fold brighter than quantum dots (QD-585 at 532 nm excitation), being ~3-fold smaller by hydrodynamic size. FRET between cyanine 3 and 5 cross-linkers at the surface of NPs suggests their integrity in physiological media, organic solvents and living cells, where they rapidly internalize showing excellent imaging contrast. Calixarene micelles with cyanine corona constitute a new platform for development of protein-sized ultrabright fluorescent NPs.

The research on fluorescent nanoparticles (NPs) is growing exponentially, as they are platforms for the fabrication of ultrabright multifunctional devices for imaging, diagnostics and therapy.[1] The most established examples of fluorescent NPs are quantum dots (QDs)[2] and dye-doped silica NPs,[3] which are of inorganic nature. Despite their unique photophysical properties, they lack biodegradability and flexibility for molecule encapsulation. Moreover, the typical hydrodynamic size of these NPs is ~20 nm, while for cellular imaging ideal NPs should be close to the size of proteins (3-7 nm). The solution is to develop fluorescent NPs assembled from organic molecules, featuring relatively small size (5-10 nm) and bearing a large quantity of dyes (~100 units). The large number of fluorophore units would ensure high fluorescence brightness comparable to or better than QDs, while their organic content would make them biocompatible, non-toxic and eco-friendly. The area of organic NPs for bioimaging develops very rapidly. Here, one should mention conjugated polymer NPs,[4] dye-loaded polymer NPs,[5] DNA nanostructures,[6] and dye-based NPs,[7] including those exploiting aggregation induced emission (AIE).[5b, 8] However, obtaining bright and stable fluorescent NPs of 5-10 nm hydrodynamic diameter remains a challenge. Moreover, when the dyes are confined in the nanoscopic space at very high concentrations, they tend to lose fluorescence due to aggregation-caused quenching (ACQ). The key to both small size and minimized ACQ is the superior control of self-assembly of organic dyes with engineered inter-fluorophore distance and orientation. This high level of control can in principle be achieved in micellar NPs, very small structures of 5-10 nm self-assembled from fluorescent amphiphiles. Though micellar assembly is very well-established,[9] only few examples in literature utilized this strategy to obtain fluorescent micellar NPs, notably using perylene diimides,[10] BODIPY[11] and AIE[12] dyes. However, several key problems remain to be addressed so far in this field. First, aggregation into micelles usually produces broad emission of dye aggregates with relatively low efficiency due to ACQ. Second, applications in cellular imaging requires polymerization of these micelles, otherwise, they will readily disintegrate and interact with lipid structures of the cells.[13]

Presently, we propose a concept of protein-sized fluorescent NPs based on calixarene micelles that are shell-cross-linked by fluorescent bi-functional dyes *via* Cu-catalysed `click_ chemistry. In one recent report, a surfactant bearing three acetylene groups was polymerized using non-fluorescent cross-linker, while the non-reacted alkynes were further modified with fluorescent mono-functional dyes.[14] In our strategy, we designed fluorescent cross-linkers to enable both micelle cross-linking and introduction of the fluorescent units. To this end, we selected cyanine 3 and 5 dyes, because of their excellent optical properties[15] and symmetric structure (Figure 1). They were modified at their nitrogen heteroatoms with two azide groups for crosslinking of the micelle and two hydrophilic PEG(8) chains to create its biocompatible shell. We call this design `cyanine corona_, similarly to well-known protein corona that modifies the surfaces of a variety of NPs.[16]

As a reactive surfactant, we designed amphiphilic calixarene. Calixarenes, due to the persistent conical shape, are powerful building blocks for nano-cages, supramolecular polymers and nanoparticles, etc.[17] They already found a variety of applications as antiviral, bactericidal and anticancer agents[18] as well as sensors[19] and vehicles for gene delivery.[20] Previously, we showed that amphiphilic calixarenes can assemble into highly monodispersed micelles of 6 nm.[21] Here, we synthesized a calixarene amphiphile that bears four alkyne groups at its polar heads for further `click_ reaction with cyanine cross-linkers (Figure 1). The obtained shell-cross-linked micelles are characterized by very small size and strong fluorescence according to single particle measurements. They also remain stable in biological media and show excellent fluorescence contrast after entering into living cells.

[*] Dr. I. Shulov, Dr Y. Arntz, Dr. A. Reisch, Dr. A.S. Klymchenko
Laboratoire de Biophotonique et Pharmacologie, UMR 7213 CNRS,
Universit¶ de Strasbourg, Facult¶ de Pharmacie,
67401 Route du Rhin, 74, ILLKIRCH Cedex (France)
E-mail: andrey.klymchenko@unistra.fr

Dr. R. V. Rodik, Prof. V. I. Kalchenko
Institute of Organic Chemistry, National Academy of Science of Ukraine, 02660 Kyiv (Ukraine)

Dr. I. Shulov
Organic Chemistry Department, Chemistry Faculty,
Taras Shevchenko National University of Kyiv,
01033 Kyiv (Ukraine)

Supporting information for this article is available on the WWW under http://

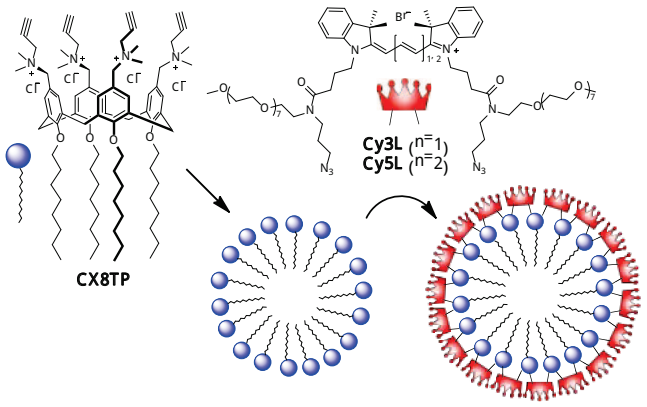

Figure 1. Chemical structure and synthesis of cyanine cross-linkers and their application to the preparation of fluorescent shell-cross-linked calixarene micelles.

The calixarene amphiphile CX8TP at 150 ı M concentration in aqueous solution (75 mM sodium sulfate) forms micelles of 5 nm according to dynamic light scattering (DLS) (Figure S1). This result is close to that for parent analogue CX8, bearing hydroxyethyl group instead of propargyl.[21] Then, we mixed these micelles (150 ı M of CX8TP) with 2 eq of the cross-linkers Cy3L or Cy5L in the presence of copper catalyst for 24h at 30 éC, to ensure that all the alkyne groups of CX8TP react with azide groups of the dyes. Then these reaction mixtures were dialyzed and their pick absorbance was compared to that before the dialysis. We found that after the reaction only a fraction (≤50%) of the cross-linkers was removed, whereas the control samples without added Cu-catalyst lost nearly all cross-linkers after dialysis (Figure S2). These results provide a clear evidence for the successful cross-linking `click_ reaction, resulting in stable micellar NPs with Cy3L and Cy5L dyes that cannot cross the dialysis membrane. From the absorption data, we could evaluate that the yields of the cross-linking were 59 and 49% for Cy3L and Cy5L dyes, respectively. Moreover the IR spectrum of the cross-linked micelles (CX8/Cy3L 1:2) showed strong decrease of the alkyne peak originally observed in CX8TP, which confirmed successful cross-linking (Figures S3). The absorption spectra of cross-linked micelles showed significant increase in the short-wavelength shoulder compared to free Cy3L and Cy5L dyes in water (Figure 2A). Appearance of this shoulder is an indication of the inter-fluorophore interaction, resulted from confinement of cyanine dyes grafted to calixarene micelles.

The dialyzed calixarene micelles shell-cross-linked with Cy3L displayed a hydrodynamic diameter of 7 nm according to DLS (Figure S1). Moreover, atomic force microscopy of these micelles showed a remarkably homogeneous population of NPs with the average height of 7±1 nm (Figures 3A and S6). Micelles based on Cy5L showed the same size according to AFM (Figures S5 and S6), though DLS measurements were not possible because the used 633 nm laser generated fluorescence of the sample. Thus, our structural data suggested that after-cross-linking micellar NPs preserved their small size and did not undergo undesired aggregation. The 2-nm increase in the diameter is clearly related to the additional corona-like shell of cyanine (Figure 1), which should be ~1 nm in thickness according to the height of Cy3L and Cy5L molecules.

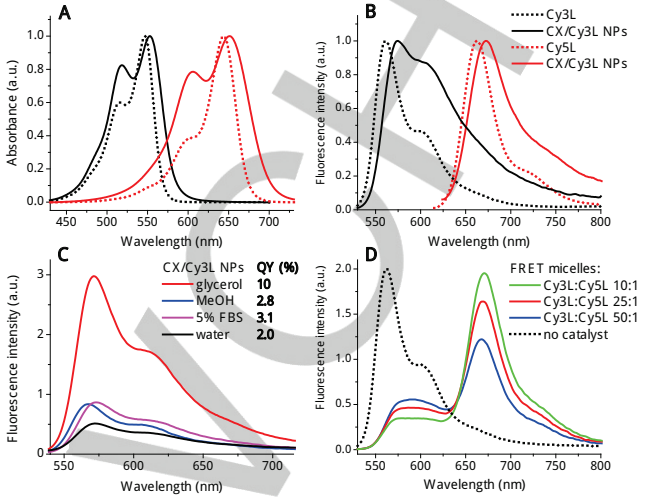

Figure 2. Absorption and fluorescent properties of cross-linked micelles (A) absorption and (B) fluorescence spectra of free cross-linker dyes and the corresponding cross-linked micelles after dialysis. (C) Fluorescence spectra of Cy3L cross-linked micelles in different media. Excitation wavelengths for Cy3L and Cy5L were 520 and 605 nm, respectively. (D) Fluorescence spectra of FRET micelles. Shell-cross-linked micelles prepared at different Cy3L (donor) to Cy5L (acceptor) ratio in water.

Importantly, the obtained micelles remained fluorescent, though their emission bands were red shifted and broadened compared to the free dyes Cy3L and Cy5L (Figure 2B). Moreover, the fluorescence quantum yield of the cross-linked micelles was lower compared to the free dye, namely ~2 vs 13% for Cy3L. This decrease is clearly linked to the aggregation caused quenching, commonly observed for dye assemblies at high local concentration.[8, 22] Remarkably, in methanol the fluorescence intensity for Cy3L increased by ~1.5-fold (Figure 2C), but its QY (2.8%) remained lower than for the free dye. This indicates that the micelles remained intact in methanol, though solvation of dyes within the micelles improved slightly QY. Strikingly, the fluorescence intensity of Cy3L micelles jumped many-fold in glycerol with respect to water with quantum yield reaching 10%, suggesting that viscosity plays a crucial role in the efficient fluorescence of our micelles (Figure 2C). The absorption and excitation spectra in glycerol were similar to those in methanol showing a characteristic short-wavelength shoulder of emissive aggregates (Figure S4). The first reason for the fluorescence enhancement is that viscosity could directly affect the internal rotation in the grafted cyanine dyes and thus increased their QY.[23] Second, glycerol should decrease the mobility of the cyanines at the surface and thus decrease their collisional quenching. Interestingly, ~2-fold increase in the fluorescence intensity was also observed for CX/Cy3L micelles in water with 5 vol% of serum (Figure 2C). The latter contains proteins and lipoproteins that could produce effects similar to those of glycerol, but at lower extent. To the best of our knowledge this is the first demonstration of fluorogenic

nanoparticles that light up in viscous environment. The existing examples are limited to the turn-on response of aggregates produced by their disassembly in organic solvents or biological media.[13] Here, it is an intrinsic property of our micelles to respond to the environment, which could be interesting for development of fluorogenic probes for bioimaging.[24]

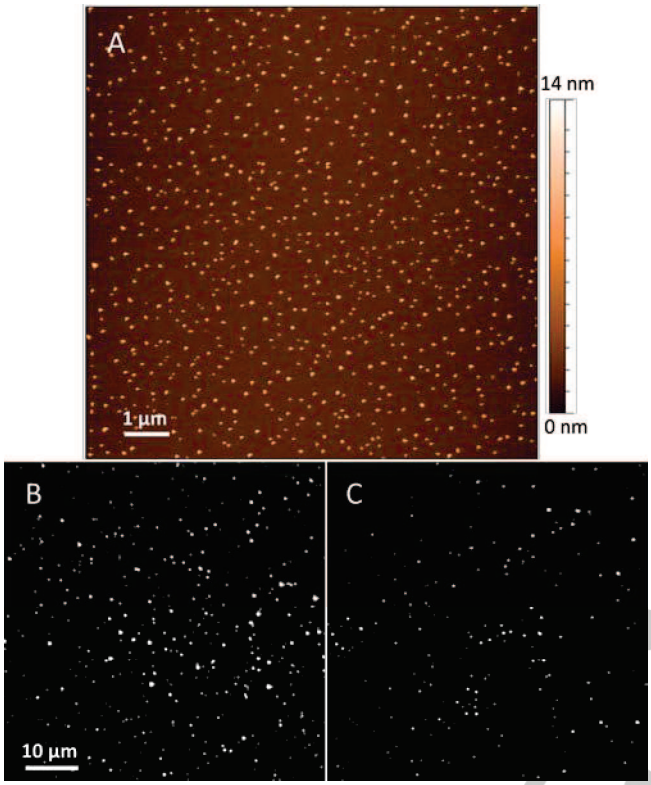

Figure 3. Single particle properties of fluorescent micelles. (A) AFM image of shell-cross-linked micelles build from CX8TP and Cy3L at 1:2 molar ratio. (B-D) Wide-field fluorescence images of the same shell-cross-linked micelles deposited on glass in glycerol (B) and QD585 deposited on PEI/glass surface (C). The laser power density was 10 W cm^{-2} at 532 nm.

To further evaluate single particle brightness, our NPs and quantum dots (QD-585) immobilized on the glass surface were compared by wide-field fluorescence microscopy. Strikingly, the brightness of our 7-nm NPs was ~2-fold higher than that of QD-585 (~22 nm diameter)[25] (Figures 3B,C, S7). The estimated brightness of these QDs when excited at 532 nm is ε × QY = 310 000 M^{-1} cm^{-1} B 0.67 = 2.1 B 10^5 M^{-1} cm^{-1}.[25] This means that our Cy3L-based calixarene micelles displayed a brightness ~4 B 10^5 M^{-1} cm^{-1}. Taking into account that the aggregation number 40 of a parent calixarene amphiphile CX8,[21] the expected number of Cy3L molecules grafted at the micellar surface is 80. We could estimate that the theoretical brightness of our NPs in glycerol at 532 nm excitation is 80 B 100 000 M^{-1} cm^{-1} B 0.1 = 8B10^5 M^{-1} cm^{-1}. This value is close to the experimental value obtained by microscopy. It is slightly higher than the experimental one probably because the number of grafted Cy3L molecules per is probably <80, because the grafting yield is <100%. It should be noted that micelles deposited on glass in water showed lower brightness than those in glycerol, in line with their lower QYs, though significant fraction of these NPs was as bright as QDs (Figure S8).

We also explored a possibility to prepare multi-component shell-cross-linked micelles using both Cy3L and Cy5L cross-linkers, which would serve as FRET donor and acceptor, respectively. It was found that strong FRET signal was observed already at donor/acceptor ratios of 50/1, and further increased for 25/1 and 10/1 ratio, which can be seen from the gradual increase in the relative intensity of the acceptor (Figure 2D). These results provide evidence for successful grafting of both cross-linkers within the same micelle and the possibility to control the grafting ratio. The high FRET efficiency at 50/1 ratio shows that a single acceptor is surrounded by a large number of donors within a 7-nm space of the micelle. As FRET is sensitive to the donor-acceptor distance, it can be used to probe integrity of NPs.[26] Indeed, in case our FRET micelles dissociate in organic solvent or biological media, the donor and acceptor molecules would separate, resulting in the loss of the FRET signal. However, in methanol or in water with 5% serum the acceptor fluorescence intensity remained higher than that of the donor (Figure S9), indicating that the FRET was preserved. Thus, shell-cross-linking of calixarene micelles ensured their stability in organic solvent and biological medium.

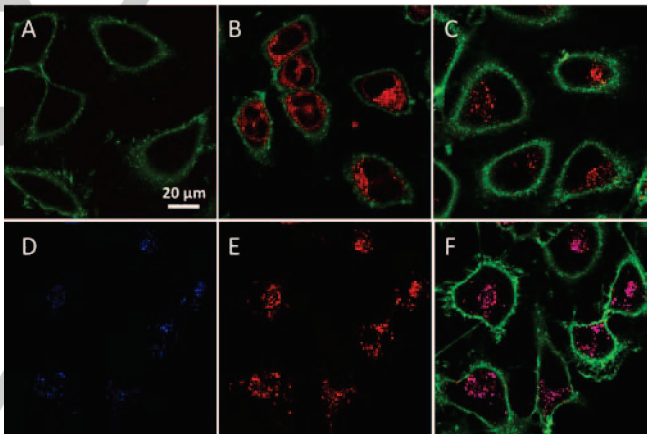

Figure 4. Fluorescence confocal imaging of HeLa cells incubated with fluorescent micelles for 3h at 37°C. Control cells without micelles (A); cells incubated with non-cross-linked micelles (B) or cross-linked micelles (C) (CX/Cy3L). Green corresponds to plasma membrane staining with WGA-Alexa Fluor488 (50nM), while red corresponds the micelles. Concentration of Cy3L in free form and in cross-linked micelles was 0.5 ı M. (D-F) Images of HeLa cells incubated with FRET micelles (Cy3L/Cy5L ratio 10/1). (D) Signal from the FRET donor recorded at 576-640 nm (Cy3 channel). (E) Signal from the FRET acceptor recorded at 650-750 nm (Cy5 channel). (F) Merged images of donor, FRET and membrane marker channels. Excitation wavelength for the FRET micelles and WGA-Alexa Fluor488 was 561 and 488 nm, respectively.

Finally, to check their applicability to bioimaging, Cy3L-based calixarene micelles were incubated in HeLa cells for 3h. Confocal fluorescence microscopy revealed that the particles appeared inside the cells as bright dots, showing a distribution typical for endosomes and lysosomes (Fig. 4C). In contrast, control experiments without NPs showed no signs of fluorescence, while addition of non-cross-linked micelles (Cy3L with CX8TP without catalyst) gave diffuse intracellular fluorescence (Fig. 4A,B). Thus, without cross-linking the free dye

internalized and distributed over the cytoplasm, whereas cross-linked micelles probably remained intact inside the cells. Remarkably, our FRET NPs incubated for 3h with HeLa cells and excited at 561 nm showed co-localized dotted emission in Cy3 and FRET acceptor (Cy5) channels (Fig. 4D-F). By contrast, very poor emission in the Cy5 channel was observed for non-cross-linked micelles, where Cy3L and Cy5L cannot undergo FRET (Fig. S10). Thus, our FRET experiments provided direct proof of the integrity of the cross-linked NPs inside the cells.

In summary, we propose a concept of fluorescent shell-cross-linked micelles presenting very small size, fluorogenic behavior in viscous media and high brightness. It is based on PEGylated cyanine bis-azides, which form covalently attached `corona_ on micelles of calixarene amphiphiles bearing four alkyne groups at the polar heads. Our results show that these nanoparticles are 7 nm size and they increase their fluorescence efficiency from 2% in water up to 10% in glycerol. Microscopy shows that they are ~2-fold brighter than quantum dots (QD-585 at 532 nm excitation). Remarkably, superior brightness vs QDs is achieved for >3-fold smaller hydrodynamic diameter, which is a crucial advantage. They present excellent stability in aqueous and organic media according to FRET between cyanine 3 and 5 cross-linkers, and enter readily the cells showing high signal to noise ratio without dye leakage. Thus, we provide a new platform for development of ultrabright and protein-sized responsive nanoparticles for bioimaging.

Acknowledgements

This work was supported by ERC Consolidator grant BrightSens 648528. Pascal Didier and Yves Mely are acknowledged for providing access to single molecule microscopy.

Keywords: fluorescence ðcyanines ðcalixarenes ðclick chemistry ðnanoparticles

[1] a) P. D. Howes, R. Chandrawati, M. M. Stevens, *Science* **2014**, *346*, 1247390; b) O. S. Wolfbeis, *Chem. Soc. Rev.* **2015**, *44*, 4743-4768.

[2] a) A. P. Alivisatos, *Science* **1996**, *271*, 933-937; b) X. Michalet, F. F. Pinaud, L. A. Bentolila, J. M. Tsay, S. Doose, J. J. Li, G. Sundaresan, A. M. Wu, S. S. Gambhir, S. Weiss, *Science* **2005**, *307*, 538-544.

[3] S. Bonacchi, D. Genovese, R. Juris, M. Montalti, L. Prodi, E. Rampazzo, N. Zaccheroni, *Angew. Chem. Int. Ed.* **2011**, *50*, 4056-4066.

[4] a) C. Wu, B. Bull, C. Szymanski, K. Christensen, J. McNeill, *ACS Nano* **2008**, *2*, 2415-2423; b) C. Wu, D. T. Chiu, *Angew. Chem. Int. Ed.* **2013**, *52*, 3086-3109.

[5] a) A. Reisch, P. Didier, L. Richert, S. Oncul, Y. Arntz, Y. Mely, A. S. Klymchenko, *Nat. Commun.* **2014**, *5*; b) K. Li, B. Liu, *Chem. Soc. Rev.* **2014**, *43*, 6570-6597; c) A. Reisch, A. S. Klymchenko, *Small* **2016**, *DOI: 10.1002/smll.201503396*.

[6] A. L. Benvin, Y. Creeger, G. W. Fisher, B. Ballou, A. S. Waggoner, B. A. Armitage, *J. Am. Chem. Soc.* **2007**, *129*, 2025-2034.

[7] a) A. Kaeser, A. P. H. J. Schenning, *Adv. Mater.* **2010**, *22*, 2985-2997; b) J. Schill, A. P. H. J. Schenning, L. Brunsveld, *Macromol. Rapid Commun.* **2015**, *36*, 1306-1321; c) E. Genin, Z. Gao, J. A. Varela, J. Daniel, T. Bsaibess, I. Gosse, L. Groc, L. Cognet, M. Blanchard-Desce, *Adv. Mater.* **2014**, *26*, 2258-2261; d) S. Fery-Forgues, *Nanoscale* **2013**, *5*, 8428-8442.

[8] Y. N. Hong, J. W. Y. Lam, B. Z. Tang, *Chem. Soc. Rev.* **2011**, *40*, 5361-5388.

[9] J. N. Israelachvili, D. J. Mitchell, B. W. Ninham, *J. Chem. Soc. Faraday Trans.* **1976**, *72*, 1525-1568.

[10] X. Zhang, Z. Chen, F. Wærthner, *J. Am. Chem. Soc.* **2007**, *129*, 4886-4887.

[11] J.-H. Olivier, J. Widmaier, R. Ziessel, *Chem. Eur. J.* **2011**, *17*, 11709.

[12] W. Guan, W. Zhou, C. Lu, B. Z. Tang, *Angew. Chem. Int. Ed.* **2015**, *54*, 15160¯15164.

[13] a) O. A. Kucherak, S. Oncul, Z. Darwich, D. A. Yushchenko, Y. Arntz, P. Didier, Y. Mely, A. S. Klymchenko, *J. Am. Chem. Soc.* **2010**, *132*, 4907; b) Y. Niko, Y. Arntz, Y. Mely, G.-i. Konishi, A. S. Klymchenko, *Chem. Eur. J.* **2014**, *20*, 16473-16477; c) G. Fan, Y.-X. Lin, L. Yang, F.-P. Gao, Y.-X. Zhao, Z.-Y. Qiao, Q. Zhao, Y.-S. Fan, Z. Chen, H. Wang, *Chem. Commun.* **2015**, *51*, 12447-12450.

[14] H.-Q. Peng, Y.-Z. Chen, Y. Zhao, Q.-Z. Yang, L.-Z. Wu, C.-H. Tung, L.-P. Zhang, Q.-X. Tong, *Angew. Chem. Int. Ed.* **2012**, *51*, 2088-2092.

[15] A. Mishra, R. K. Behera, P. K. Behera, B. K. Mishra, G. B. Behera, *Chem. Rev.* **2000**, *100*, 1973-2011.

[16] a) M. P. Monopoli, D. Walczyk, A. Campbell, G. Elia, I. Lynch, F. B. Bombelli, K. A. Dawson, *J. Am. Chem. Soc.* **2011**, *133*, 2525-2534; b) S. Tenzer, D. Docter, J. Kuharev, A. Musyanovych, V. Fetz, R. Hecht, F. Schlenk, D. Fischer, K. Kiouptsi, C. Reinhardt, K. Landfester, H. Schild, M. Maskos, S. K. Knauer, R. H. Stauber, *Nat. Nanotechnol.* **2013**, *8*, 772-781.

[17] a) D. S. Guo, Y. Liu, *Chem. Soc. Rev.* **2012**, *41*, 5907-5921; b) M. Liu, W. P. Liao, C. H. Hu, S. C. Du, H. J. Zhang, *Angew. Chem. Int. Ed.* **2012**, *51*, 1585-1588.

[18] R. V. Rodik, V. I. Boyko, V. I. Kalchenko, *Curr. Med. Chem.* **2009**, *16*, 1630-1655.

[19] H. J. Kim, M. H. Lee, L. Mutihac, J. Vicens, J. S. Kim, *Chem. Soc. Rev.* **2012**, *41*, 1173-1190.

[20] a) R. Rodik, A. Klymchenko, Y. Mely, V. Kalchenko, *J. Incl. Phenom. Macrocycl. Chem.* **2014**, *80*, 189-200; b) V. Bagnacani, V. Franceschi, M. Bassi, M. Lomazzi, G. Donofrio, F. Sansone, A. Casnati, R. Ungaro, *Nat. Commun.* **2013**, *4*.

[21] R. V. Rodik, A. S. Klymchenko, N. Jain, S. I. Miroshnichenko, L. Richert, V. I. Kalchenko, Y. Mely, *Chem. Eur. J.* **2011**, *17*, 5526-5538.

[22] D. Genovese, E. Rampazzo, S. Bonacchi, M. Montalti, N. Zaccheroni, L. Prodi, *Nanoscale* **2014**, *6*, 3022-3036.

[23] R. B. Mujumdar, L. A. Ernst, S. R. Mujumdar, C. J. Lewis, A. S. Waggoner, *Bioconjugate Chem.* **1993**, *4*, 105-111.

[24] A. Nadler, C. Schultz, *Angew. Chem. Int. Ed.* **2013**, *52*, 2408-2410.

[25] I. Shulov, S. Oncul, A. Reisch, Y. Arntz, M. Collot, Y. Mely, A. S. Klymchenko, *Nanoscale* **2015**, *7*, 18198-18210.

[26] a) S. W. Morton, X. Zhao, M. A. Quadir, P. T. Hammond, *Biomaterials* **2014**, *35*, 3489-3496; b) A. S. Klymchenko, E. Roger, N. Anton, H. Anton, I. Shulov, J. Vermot, Y. Mely, T. F. Vandamme, *RSC Adv.* **2012**, *2*, 11876-11886.

Entry for the Table of Contents

COMMUNICATION

Protein -sized fluorescent nanoparticles are developed, where PEGylated cyanine bis-azides form a covalently attached `corona_ on micelles of amphiphilic calixarene bearing alkyne groups. The obtained 7 nm nanoparticles are ~2-fold brighter than quantum dots-585. FRET studies suggest their high stability in aqueous and organic media as well as in living cells, where they show excellent imaging contrast.

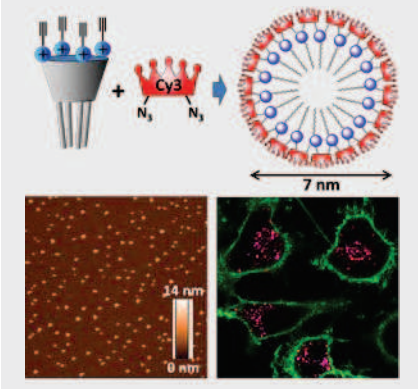

*Ievgen Shulov, Roman V. Rodik, Youri Arntz, Andreas Reisch, Vitaly I. Kalchenko, and Andrey S. Klymchenko**

Page No. – Page No.

Shell-Cross -Linked Calixarene Micelles with Cyanine Corona: Protein -Sized Bright Fluorogenic Nanoparticles

General conclusions & perspectives

The aim of the current project was to develop fluorescent organic nanoparticles characterized by small size and high brightness. We explored the field of fluorescent organic nanoparticles by following four strategies : (1) dye-loading of nano-droplets, (2) counterion-induced dye nanoprecipitation, (3) counterion-induced micellization of fluorescent amphiphiles, and (4) polymerization of calixarene-based micelles with functional groups on the surface by fluorescent cross-linkers.

The first approach is dye-loaded lipid nano-droplets, where we synthesized highly lipophilic dyes to achieve their efficient encapsulation. We found that it is imperative to modify fluorescent dyes with long hydrophobic chains in order to prevent their leakage from lipid droplets into biological media. Moreover, this study showed the possibility to prepare very bright nano-objects that can be then used for instance to visualize blood circulation in zebrafish. However, we should stress that the prepared nano-droplets are of dynamic liquid nature, so that they may undergo slow disassembly in biological systems. In particular, the droplet surface is composed of surfactant. This renders surface modification of nano-droplets rather challenging. Moreover, generally these droplets are relatively large (25-100 nm) in size. Therefore, we consider that fluorescent nano-droplets will be mainly used for in vivo imaging. In this respect encapsulation of near-infrared dyes inside these droplets with further application for imaging of small animals (mice) is a particularly promising direction.

By nanoprecipitation of rhodamine B dye esters bearing alkyl chains using hydrophobic counterions we have obtained ultra-bright fluorescent NPs with a narrow band emission in the red spectral region. For rhodamines with longest alkyl chains in combination with the most fluorinated counterion, we obtained small nanoparticles of the highest fluorescence brightness. According to FCS they were ~20 nm size showing the brightness ~300-times superior to a single rhodamine dye. Moreover, we observed 50% FRET efficiency from the particles containing >300 dyes to a single encapsulated acceptor. Finally, we found that the particles internalize rapidly inside the cells showing excellent signal to noise ratio on the fluorescence images. Here, for the first time we demonstrated the unique role of the counterion fluorination to improve a number of nanoparticle properties: brightness, emission bandwidth, photostability, colloidal stability as well as stability inside the cells. However, our cellular studies showed that even the most stable NPs with the most fluorinated counterion start decomposing at the time scale >6h. Moreover, bioconjugation of these NPs is challenging, as they do not present any potential groups for chemical modification at their surface. Therefore, it is important to think about coating of NPs with polymer surfactants, like it has been already done for the CdSe quantum dots, which provide both biocompatible shell and the means for

their further bioconjugation. Therefore, the future development of counterion-assembled rhodamine NPs will rely on coating of their surface by surfactants, polysaccharides or polymers of amphiphilic type. Afterwards, the grafting of short peptides specific for cancer cells can open the way to nanomaterials for the early diagnosis of cancer in live organisms. Our preliminary results, which are not described in this thesis, showed that it is possible to coat these NPs with Pluronic® F-127 and TWEEN®80 surfactants with minimal increase in their size, according to the FCS measurements. Furthermore, cytotoxicity of these NPs should be tested by standard MTT cell assay. Finally, many other types of highly emissive organic-ion pairs remain to be investigated.

With a help of modern supramolecular chemistry, which provides methodology for designing organic molecules capable to form organic nanostructures of precise dimensions, we have developed two cyanine amphiphiles Cy3A and Cy5A. According to the absorption spectroscopy it was found that the CMC of our fluorescent amphiphiles is relatively high and not suitable for the preparation of the stable NPs. Therefore, micellization process was promoted by the introduction of the highly hydrophobic bulky counterion, perfluorinated tetraphenylborate. We obtained micellar NPs of 7 nm in size with a remarkably high brightness, which is equivalent of 40 cyanine dye units. Moreover, we created two-color fluorescent nanoparticles by counterion assisted co-assembly of Cy3 and Cy5-based amphiphiles which allows efficient fluorescence resonance energy transfer (FRET). This is one of the first examples of micellar NPs, where the encapsulated fluorophores are not self-quenched, showing efficient emission. However, we expect that this system will not be sufficiently stable in biological media, because its building blocks are not covalently connected. Therefore, introduction of the polymerizable groups into these amphiphiles may provide a possibility to prepare highly stable NPs of very small size. Moreover, reactive groups should be added to these amphiphiles for their further bioconjugation and biological applications as for other NPs described above.

In this counterion-promoted micellization approach, the use of specially designed rhodamine amphiphiles could improve the total quantum efficiency of the system, as it was already shown in our publication about fluorescence enhancement and emission band sharpening of nanoprecipitated alkyl rhodamine B derivatives. Although not discussed, it should be noted that in most cases the number of synthetic steps to prepare the amphiphilic fluorescent building blocks is rather high. From an application point of view it would be desirable to obtain final amphiphiles with minimal number of steps, which would significantly decrease the cost of the obtained NPs.

Finally, we introduced a new concept based on non-fluorescent micelles that can be shell-cross-linked with fluorescent cross-linkers. This is probably the most promising approach because the obtained NPs feature small size (7 nm), high brightness (brighter than QDs-585) together with high stability due to cross-linked nature of the obtained micelles. They showed promising for cellular

imaging applications as we could see from our confocal imaging data, where intact particles could be observed without diffuse fluorescence of possible dye monomers. Moreover, of particular interest is the fluorogenic “turn-on” behavior in biological media, which could in the future help to construct fluorogenic nanoparticles for biological targets. The cross-linked fluorescent nanoparticles can be further modified with the biological ligands/biomolecules, such as folic acid, RGD, etc bearing azide group, using “click” reaction directly on the remaining alkyne groups of the calixarenes. This will make them specific to biological targets, such as cell receptors. Nanoparticles modified with viral peptides can be used for single molecule measurements of protein-DNA and protein-protein interactions. The nanoparticles modified with Annexin V can be tested on cells and tissues using fluorescence microscopy techniques with the aim to detect cell apoptosis.

In addition, some improvements in these shell-cross-linked micellar systems could be envisaged. Thus, the use of the water soluble copper ligand, that makes a stable complex with a Cu(I), can potentially increase the rate and yield of micelle crosslinking. Another way for the improvement of this micellar NPs can be modulation of the total charge of the system. Currently, we have created the cross-linked NPs, which are positively charged. However, in the literature it is noted the fact that positively charged NPs may present some toxicity and non-specific binding to the cells. Thus, introduction of negatively charged groups (*e.g.,* phosphate and sulfonate) into a structure of calixarene and cross-linker will open the way to the pegylated NPs possessing neutral (zwitterionic) or negative charge. The other type of system optimization can be a color of the NPs. For this purpose different homo-bifunctional dye cross-linkers can be synthesized and applied. As examples an oxacarbocyanine-based cross-linker can be synthesized in order to prepare the NPs with the emission in green region, while cross-linker based on arylidene–squaraine dye could enable preparation of the NPs that emit in the far-red region. A new crosslinkers based on the derivatives of cyanine Cy5.5, Cy7, Cy7.5 can be applied in order to create NPs with the emission in NIR region, which is important for the *in vivo* studies such as disease diagnostics and early detection and image guided surgery. The next generations of fluorescent cross-linkers of the well-selected fluorophores should minimize H-aggregation and electron transfer phenomena, which can significantly improve the brightness and the turn-on behavior of these systems. On the other hand, the synthesis of new calixarene amphiphile derivatives bearing longer alkyl chains, such as dodecyl, hexadecyl or octadecyl, which can self-assemble into micelles larger size than 6 nm, will open the way for the NPs that can bear more fluorophores on the surface, and therefore present higher brightness. Finally, the incorporation of multiple reactive groups in a cross-linker structure for Staudinger ligation, maleimide-thiol coupling etc will open a way for the fabrication dual-targeting NPs suitable for multiplexing assays (multiple analyte detection).

Each of the four developed approaches bears its advantages and limitations. From the synthetic point of view, the preparation and purification of the new highly water-soluble fluorescent cross-linkers by HPLC seem to be easier than fluorescent amphiphiles, which have been used in our third approach. However, the cost of scale-up of such state-of-art fluorescent derivatives is still rather high, compared to fluorescent NPs based on lipid nanodroplets (first approach) or dye NPs precipitated by the counterions (second approach). Regarding the size, the nano-droplets approach provides the largest size NPs, while the micellar concepts (last two) allows preparation of the smallest possible NPs (5-10 nm size). Therefore, we expect that the first approach will be probably more suitable for *in vivo* imaging applications, while the last two will be more suitable for cellular imaging, where the small NPs are preferred. It is also clear that the shell-cross-linked micelle approach provides the most stable NPs, due to their polymerized nature, and they already can be readily functionalized using “click” reaction.

In any case, further work on all four strategies is definitely needed to develop fluorescent organic NPs that can compete with the state of the art quantum dots and other inorganic NPs in the bioimaging applications.

3. MATERIALS AND METHODS

3.1 Synthetic procedures of fluorescent organic building blocks

All starting materials for synthesis were purchased from Alfa Aesar and Sigma Aldrich or TCI Europe and used as received unless stated otherwise. NMR spectra were recorded on a Bruker Avance III 400 MHz and 500 MHz spectrometers. Mass spectra were obtained using an Agilent Q-TOF 6520 mass spectrometer. MilliQ-water (Millipore) was used in all experiments.

3.1.1 Synthesis of lipophilic dyes for the encapsulation into lipid or polymer matrix

Flavone derivatives

4'-Dioctylamino-3-octyloxyflavone (F888) (1)

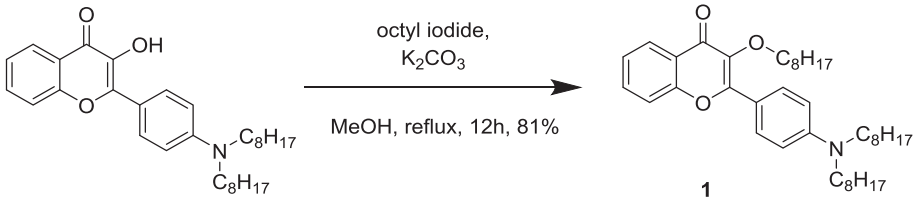

1

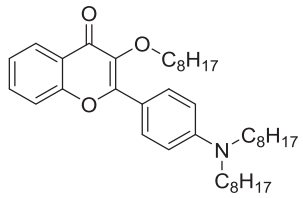

100 mg (0.21 mmol) of 4'-(N,N-dioctylamino)-3-hydroxyflavone, which was prepared as described elsewhere,[1] was dissolved in 10 ml of dry methanol. Then, 191 ml (1.05 mmol) of 1-iodooctane and 60 mg (0.42 mmol) of potassium carbonate were added. The resulting mixture was refluxed overnight under an inert atmosphere. Solvent was removed under reduced pressure. The obtained residue was purified by TLC plate chromatography on silica gel (EtOAc : heptane, 1 : 9 as the eluent) to give the product (100 mg, 81%) as a yellow oil.

^{1}H NMR (400 MHz, Chloroform-*d*) δ 8.24 (dd, *J* = 8.0, 1.7 Hz, 1H), 8.09 (d, *J* = 9.0 Hz, 2H), 7.60 (ddd, *J* = 8.8, 7.0, 1.7 Hz, 1H), 7.47 (dd, *J* = 8.8, 1.1 Hz, 1H), 7.34 (ddd, *J* = 8.0, 7.0, 1.1 Hz, 1H), 6.69 (d, *J* = 8.9 Hz, 2H), 4.05 (t, *J* = 6.7 Hz, 2H), 3.34 (t, *J* = 7.7 Hz, 4H), 1.79 (p, *J* = 7.4 Hz, 2H), 1.63 (p, *J* = 6.8 Hz, 4H), 1.48 – 1.38 (m, 2H), 1.36 – 1.23 (m, 28H), 0.91 – 0.83 (m, 9H).
^{13}C NMR (101 MHz, Chloroform-*d*) δ 174.74, 156.83, 155.16, 149.82, 139.28, 132.73, 130.32, 125.77, 124.46, 124.22, 117.73, 117.13, 110.83, 72.45, 51.10, 31.94, 30.32, 29.59, 29.54, 29.43, 29.41, 27.41, 27.26, 26.15, 22.78, 22.76, 14.21, 14.20.
HRMS (ESI) m/z: $[M+H]^+$ calcd for $C_{39}H_{60}NO_3$, 590.4568; found, 590.4604.

Nile Red derivatives

9-Dihexylamino-2-hydroxy-benzo[a]phenoxazin-5-one (NR66) (2)

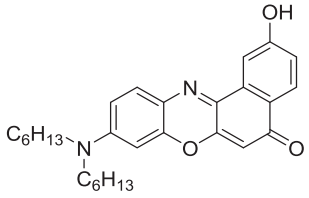

NR66 was synthesized using the same protocol as for 9-diethylamino-2-hydroxy-benzo[a]phenoxazin-5-one[2] starting from 3-dihexylaminophenol. Dark green solid, yield 50%.

^{1}H NMR (400 MHz, DMSO-d6, δ): 10.36 (s, 1H), 7.93 (d, *J* = 8.7 Hz, 1H), 7.84 (d, *J* = 2.4 Hz, 1H), 7.47 (d, *J* = 9.0 Hz, 1H), 7.05 (dd, *J* = 8.6, 2.5 Hz, 1H), 6.64 (dd, *J* = 9.1, 2.5 Hz, 1H), 6.44 (d, *J* = 2.5 Hz, 1H), 6.08 (s, 1H), 3.30 (t, *J* = 7.7 Hz, 4H), 1.57 – 1.43 (m, 4H), 1.31 – 1.21 (m, 12H), 0.88 – 0.81 (m, 6H).
^{13}C NMR (101 MHz, DMSO-d6, δ): 181.43, 160.52, 151.40, 150.86, 146.13, 138.66, 133.65, 130.56, 127.31, 123.79, 123.75, 118.19, 109.76, 108.09, 104.04, 95.93, 50.43, 40.15, 39.94, 39.73, 39.52, 39.31, 39.10, 38.89, 31.05, 26.76, 25.93, 22.10, 13.83.
LCMS (MM-ES+APCI) m/z: $[M+H]^+$ calcd for $C_{28}H_{35}N_2O_3^+$, 447.2; found, 447.2.

9-Dihexylamino-2-(2-ethylhexyloxy)-benzo[a]phenoxazin-5-one (NR668) (3)

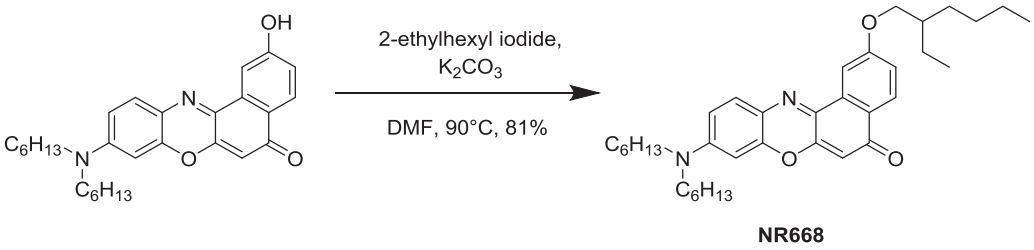

NR668

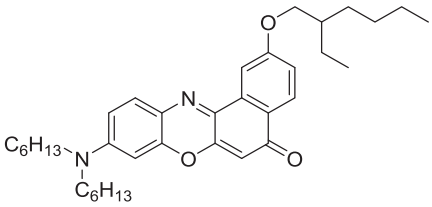

NR66 (1 eq., 100 mg, 0.224 mmol), 2-ethylhexyl iodide (1.5 eq., 80.7 mg, 60.3 µL, 0.336 mmol) and potassium carbonate (1.5 eq., 46.4 mg, 0.336 mmol) were placed in round-bottom flask equipped with magnetic stirring bar, 2mL of DMF was added via syringe. The mixture was stirred upon heating at 90°C for 24 h. Solvent was removed under vacuum, obtained residue was redissolved in 50mL of DCM, washed three times with brine, dried over sodium sulphate, then evaporated. Crude product was purified using flash column chromatography (SiO_2, EtOAc/heptane, 2 : 8 as the eluent). Dark red oil, 102 mg, yield 81%.

^{1}H NMR (400 MHz, Chloroform-d, δ): 8.14 (d, *J* = 8.8 Hz, 1H), 7.97 (d, *J* = 2.5 Hz, 1H), 7.52 (d, *J* = 9.0 Hz, 1H), 7.09 (dd, *J* = 8.8 Hz, *J2* = 2.5 Hz, 1H), 6.55 (dd, *J* = 9.0 Hz, *J2* = 2.5 Hz, 1H), 6.33 (d, *J* = 2.5 Hz, 1H), 6.25 (s, 1H), 3.98 (dd, *J* = 5.6 Hz, *J2* = 1.4 Hz, 2H), 3.29 (m, 4H), 1.70–1.75 (m, 1H), 1.35–1.53 (m, 6H), 1.28 (m, 18H), 0.81–0.95 (m, 12H).
^{13}C NMR (100 MHz, Chloroform-d, δ): 183.43, 162.24, 152.19, 151.22, 146.90, 140.15, 134.17, 131.05, 127.82, 125.59, 124.78, 118.32, 109.72, 106.81, 105.39, 96.52, 70.90, 51.61, 39.59, 31.77, 30.73, 29.29, 27.43, 26.88, 24.07, 23.19, 22.79, 14.24, 14.16, 11.34.
HRMS (ESI) m/z: $[M+H]^+$ calcd for $C_{36}H_{51}N_2O_3$, 559.3894; found, 559.3903.

Perylene derivatives

N,N'-Bis(1-heptyloctyl)-3,4,9,10-perylenebis-(dicarboximide) (PDI-1) (4)

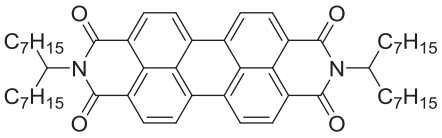

Compound was synthesized from 1-heptyloctylamine and perylene-3,4,9,10-tetracarboxylic dianhydride as was described previously.[3, 4]

Squaraine derivatives

Synthetic scheme for squaraine derivative of arene-type (aSQ)

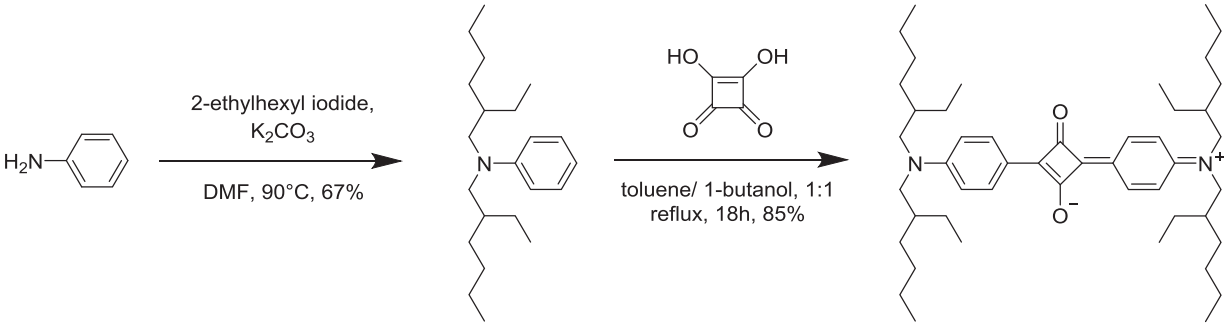

5 6

N,N-bis(2-ethylhexyl)aniline (5)

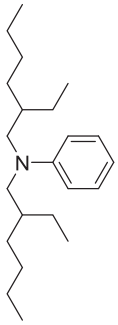

A mixture of aniline (1 equiv., 21.9 mmol, 2 mL), 2-ethylhexyl iodide (2.5 equiv., 54.9 mmol, 9.85 mL) and potassium carbonate (3 equiv., 65.8 mmol, 9.1 g) in dry DMF (50 mL) was stirred upon heating at 90°C for 4 hours. After cooling to room temperature the excess of potassium carbonate was filtered off and the volatiles were removed under vacuum. DCM (100 mL) was added to the residue and the obtained solution was washed three times with brine (3 × 100 mL). The organic layer was dried over sodium sulfate, filtered and the filtrate concentrated under vacuum. The residue was purified by column chromatography on silica gel (eluted with heptane) to give 7 as a colorless liquid (4.68 g, 67%).

^{1}H NMR (400 MHz, Chloroform-d, δ): 7.24 – 7.13 (m, 2H), 6.66 (d, J = 8.0 Hz, 2H), 6.61 (m, 1H), 3.29 – 3.09 (m, 4H), 1.85 – 1.71 (m, 2H), 1.45 – 1.15 (m, 16H), 0.96 – 0.82 (m, 12H).
^{13}C NMR (100 MHz, Chloroform-d, δ): 148.58, 129.04, 115.31, 113.02, 56.58, 36.87, 30.88, 28.88, 24.12, 23.38, 14.22, 10.82.
HRMS (ESI) m/z: $[M+H]^+$ calcd for $C_{22}H_{40}N^+$, 318.3161; found, 318.3159.

2-(4-(bis(2-ethylhexyl)amino)phenyl)-4-(4-(bis(2-ethylhexyl)iminio)cyclohexa-2,5-dien-1-ylidene)-3-oxocyclobut-1-en-1-olate (aSQ) (6)

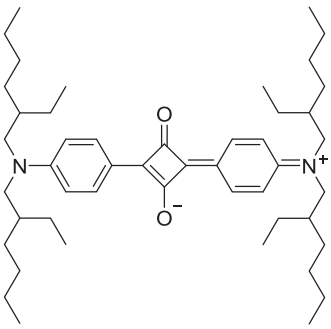

A solution of 7 (2 equiv., 3.16 mmol, 1002 mg) and squaric acid (1 equiv., 1.58 mmol, 180 mg) in a mixture of 1-butanol (20 mL) and toluene (20 mL) was refluxed overnight. After cooling to a room temperature the solvents were removed under vacuum. The residue was purified by flash column chromatography on silica gel (eluted with EtOAc/heptane 2/8) to give desired compound as a dark green oil (957 mg, 85%).

^{1}H NMR (400 MHz, Chloroform-d, δ): 8.35 (d, J = 9.3 Hz, 4H), 6.75 (d, J = 9.3 Hz, 4H), 3.53 – 3.11 (m, 8H), 1.92 – 1.77 (m, 4H), 1.43 – 1.11 (m, 32H), 1.08 – 0.62 (m, 24H).
^{13}C NMR (100 MHz, Chloroform-d, δ): 187.49, 183.63, 153.74, 133.02, 119.61, 113.23, 56.66, 37.72, 30.69, 28.72, 24.04, 23.16, 14.12, 10.77.
HRMS (ESI) *m/z*: $[M+H]^+$ calcd for $C_{48}H_{77}N_2O_2^+$, 713.5985; found, 713.5957.

Synthetic scheme for squaraine derivative of arylidene-type (C12SQ)

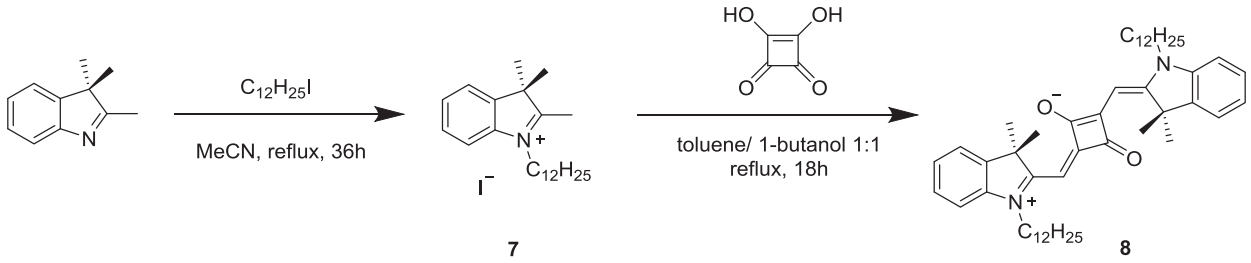

1-dodecyl-2,3,3-trimethyl-3H-indol-1-ium iodide (7)

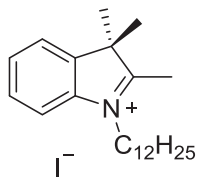

2,3,3-trimethylindolenine (1 eq., 3.69 g, 3.73 mL, 23.2 mmol) and 1-iodododecane (3.5 eq., 20 mL, 81.1 mmol) were placed in a reaction flask. Anhydrous acetonitrile (25 mL) was added via syringe. The reaction mixture was stirred under reflux under Ar atmosphere for 36 h. Excess of the solvent was removed under reduced pressure. Upon addition of diethyl ether (50 mL), the crude product has been precipitated and afterwards, filtered off and washed once with diethyl ether. Purification was done by reprecipitation. The residue was redissolved in minimal amount of acetone and precipitated by its addition into a large amount of diethyl ether (400 mL). Obtained crystals were filtered off, washed once with diethyl ether (40 mL) and dried at r.t. Yield 7.7 g (73%) as slightly reddish crystals.

^{1}H NMR (400 MHz, Chloroform-*d*) δ 7.62 – 7.50 (m, 4H), 4.47 (t, *J* = 7.8 Hz, 2H), 2.82 (s, 3H), 1.89 (p, *J* = 7.8 Hz, 2H), 1.57 (s, 6H), 1.46 – 1.37 (m, 2H), 1.36 – 1.29 (m, 2H), 1.28 – 1.15 (m, 14H), 0.86 (t, *J* = 6.8 Hz, 3H).
^{13}C NMR (101 MHz, Chloroform-*d*) δ 195.91, 141.83, 141.04, 130.18, 129.52, 123.39, 115.22, 54.78, 48.77, 31.97, 29.66, 29.55, 29.42, 29.39, 29.16, 27.99, 26.84, 22.91, 22.76, 14.43, 14.20.
HRMS (ESI) *m/z*: $[M]^+$ calcd for $C_{23}H_{38}N$, 328.2999, found 328.3009.

2-(1-Dodecyl-3,3-dimethyl-2,3-dihydro-1*H*-2-indolylidenmethyl)-4-[(*E*)-1-(1-dodecyl-3,3-dimethyl-3*H*-2-indoliumyl)methylidene]-3-oxo-1-cyclobuten-1-olate (C12SQ) (8)

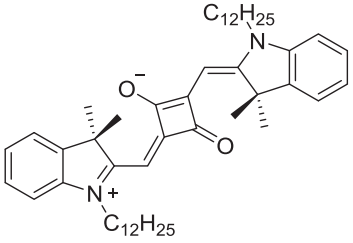

1-Dodecyl-2,3,3-trimethyl-3H-indol-1-ium iodide (2 eq., 2000 mg, 4.39 mmol) and 3,4-dihydroxy-3-cyclobutene-1,2-dione (1 eq., 250 mg, 2.2 mmol) were placed in a reaction flask. Toluene (25 mL) and 1-

butanol (25 mL) were added via syringe, and the reaction mixture was refluxed with Dean-Stark apparatus for 18 h. Solvent was removed under reduced pressure. The residue was purified by column chromatography (SiO_2, EtOAc/Hept, 40:60), which furnished 1.08 g (yield 67%) of the title compound **C12SQ** as a blue solid.

^{1}H NMR (400 MHz, Chloroform-*d*) δ 7.34 (d, *J* = 7.3 Hz, 2H), 7.29 (td, *J* = 7.7, 1.2 Hz, 2H), 7.13 (t, *J* = 7.4 Hz, 2H), 6.97 (d, *J* = 7.9 Hz, 2H), 5.95 (s, 2H), 4.06 – 3.86 (m, 4H), 1.88 – 1.66 (m, 4H), 1.78 (s, 12H), 1.47 – 1.37 (m, 4H), 1.36 – 1.20 (m, 32H), 0.86 (t, *J* = 6.7 Hz, 6H).
^{13}C NMR (101 MHz, Chloroform-*d*) δ 182.44, 179.74, 170.09, 142.62, 142.36, 127.82, 123.71, 122.38, 109.43, 86.67, 49.39, 43.85, 32.02, 29.70, 29.64, 29.60, 29.49, 29.43, 27.21, 27.19, 27.16, 22.79, 14.23.
HRMS (ESI) *m/z*: $[M+H]^+$ calcd for $C_{50}H_{73}N_2O_2$, 733.5667, found 733.5669.

Cyanine derivatives

Synthetic scheme for 1,1'-Dioctadecyl-3,3,3'3'-tetramethyl-benzo[e]indocarbocyanine (C18Cy5.5)

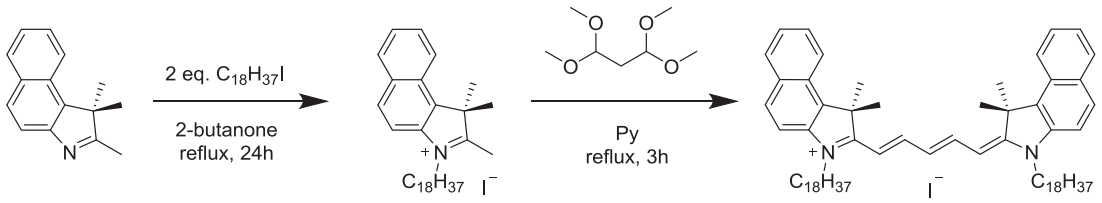

9 **10**

1,1,2-Trimethyl-3-octadecyl-1H-benzo[e]indol-3-ium iodide (9)

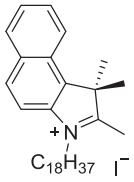

250 mL round-bottom flask equiped with magnetic stirring bar was charged with 1,1,2-trimethylbenz[e]indole (1 eq., 6.88 g, 32.9 mmol) and 1-iodooctadecane (2 eq., 25 g, 65.7 mmol), 100 mL of 2-butanone was added subsequently. Reaction mixture was refluxed for 24h. Reaction mixture was cooled down to r.t., diethyl ether was added and formed solid part was filtered off and washed with a 100 mL of diethyl ether. Obtained crystals of crude product was redissolved in DCM and precipitated back while adding diethyl ether, filtered and washed with diethyl ether. Compound (**9**) was obtained as a slightly green crystals in 76% yield (14.73g).

^{1}H NMR (400 MHz, Chloroform-*d*) δ 8.10 (d, *J* = 8.7 Hz, 1H), 8.08 (dd, *J* = 8.0, 1.1 Hz, 1H), 8.04 (dd, *J* = 8.2, 1.3 Hz, 1H), 7.76 (d, *J* = 8.9 Hz, 1H), 7.72 (ddd, *J* = 8.3, 6.9, 1.4 Hz, 1H), 7.65 (ddd, *J* = 8.1, 6.9, 1.2 Hz, 1H), 4.78 (t, *J* = 7.7 Hz, 2H), 3.19 (s, 3H), 1.97 (p, *J* = 7.8 Hz, 2H), 1.87 (s, 6H), 1.52 – 1.41 (m, 2H), 1.40 – 1.30 (m, 2H), 1.28 – 1.19 (m, 26H), 0.85 (t, *J* = 7.0 Hz, 3H).
^{13}C NMR (101 MHz, Chloroform-*d*) δ 195.25, 138.34, 137.29, 133.82, 131.56, 130.17, 128.77, 127.97, 127.74, 122.96, 112.59, 56.04, 50.56, 32.00, 29.77, 29.76, 29.73, 29.70, 29.65, 29.55, 29.43, 29.41, 29.24, 28.26, 26.92, 22.85, 22.76, 17.03, 14.18.
HRMS (ESI, TOF, *m/z*): $[M]^+$ calcd for $C_{33}H_{52}N$ 462.4094; found, 462.4085.

1,1'-Dioctadecyl-3,3,3'3'-tetramethyl-benzo[e]indocarbocyanine (C18Cy5.5) (10)

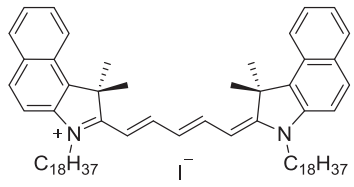

1,1,2-trimethyl-3-octadecyl-1H-benzo[e]indol-3-ium iodide (1 eq., 2 g, 3.39 mmol) was placed in 50mL round-bottom flask. 10mL of dry pyridine was added via syringe. Then, 1,1,3,3-tetramethoxypropane (1.5 eq., 0.835 g, 0.838 mL, 5.09 mmol)) was quickly added dropwise to the boiling solution of indoleninium salt using syringe. Reaction mixture was stirred under reflux for 3 hours. After cooling down to room temperature solvent was removed under reduced pressure. To the obtained residue 50mL of dichloromethane were added. Obtained solution was washed three times with 1M aq. solution of hydrochloric acid. The crude product was purified by flash column chromatography on silica gel using ethyl acetate/dichloromethane (9:1) mixture as eluent. Compound **C18Cy5.5** was obtained as dark green solid in 76% yield (2.8 g).

^{1}H NMR (400 MHz, Chloroform-*d*) δ 8.55 (t, *J* = 13.0 Hz, 2H), 8.20 (d, *J* = 8.5 Hz, 2H), 7.90 (d, *J* = 8.6 Hz, 4H), 7.64 – 7.54 (m, 2H), 7.44 (t, *J* = 7.5 Hz, 2H), 7.32 (d, *J* = 8.8 Hz, 2H), 6.74 (t, *J* = 12.4 Hz, 1H), 6.24 (d, *J* = 13.7 Hz, 2H), 4.14 (t, *J* = 7.5 Hz, 4H), 2.12 (s, 12H), 1.83 (p, *J* = 7.6 Hz, 4H), 1.46 (p, *J* = 7.6, 7.0 Hz, 4H), 1.40 – 1.33 (m, 4H), 1.30 – 1.18 (m, 52H), 0.85 (t, *J* = 6.7 Hz, 6H).
^{13}C NMR (101 MHz, Chloroform-*d*) δ 174.61, 153.24, 139.35, 134.46, 131.79, 130.40, 129.88, 128.27, 127.75, 126.05, 125.05, 122.61, 110.44, 103.02, 51.52, 44.62, 31.94, 29.73, 29.71, 29.69, 29.68, 29.64, 29.60, 29.49, 29.43, 29.38, 27.90, 27.75, 27.02, 22.70, 14.14.
HRMS (ESI, TOF, *m/z*): $[M]^+$ calcd for $C_{69}H_{103}N_2$ 959.81158; found, 959.8098.

3.1.2 Synthesis of alkyl rhodamines for the NPs by nanoprecipitation approach

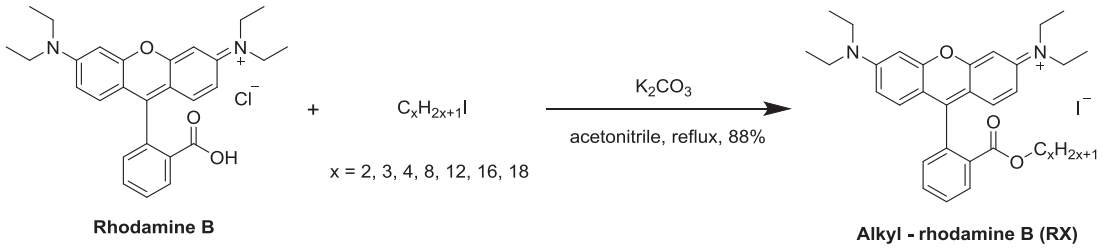

General protocol for the synthesis of alkyl-rhodamine B dyes.

Rhodamine B (300 mg, 1 eq.) and potassium carbonate (173 mg, 2 eq.) were placed in a reaction flask, 30 ml of acetonitrile were then added *via* syringe. The vessel was closed with a rubber septum and purged with argon for 5 min. After pre-heating to 60 °C for 30 min the corresponding alkyl iodide (2 eq.) was added dropwise via syringe. The contents of the flask were briefly mixed and stirred under reflux overnight. After cooling to room temperature, 30 mL of acetonitrile were added and the excess of potassium carbonate was filtered off, followed by concentrating the filtrate under vacuum. The crude product was purified by gradient flash column chromatography (SiO_2, DCM/MeOH, from 99:1 to 95:5), which afforded desired product in form of red solid (yield in range of 75-91%) of corresponding Rhodamine B alkyl ester iodide salt**.**

Rhodamine B ethyl ester iodide (R2, N-(6-(Diethylamino)-9-(2-(ethoxycarbonyl)phenyl)-3H-xanthen-3-ylidene)-N-ethylethan-aminium iodide)

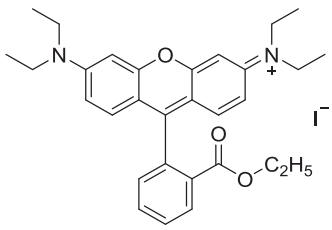

Compound **R2** was synthesized as described in the general protocol above. Yield 88%, red solid.

^{1}H NMR (400 MHz, Chloroform-d, δ): 8.18 (dd, J = 7.9, 1.3 Hz, 1H), 7.72 (td, J = 7.6, 1.4 Hz, 1H), 7.64 (td, J = 7.7, 1.4 Hz, 1H), 7.20 (dd, J = 7.6, 1.2 Hz, 1H), 6.97 (d, J = 9.5 Hz, 2H), 6.81 (dd, J = 9.5, 2.5 Hz, 2H), 6.69 (d, J = 2.4 Hz, 2H), 3.96 (q, J = 7.1 Hz, 2H), 3.55 (q, J = 7.2 Hz, 8H), 1.22 (t, J = 7.1 Hz, 12H), 0.96 (t, J = 7.1 Hz, 3H).
^{13}C NMR (100 MHz, Chloroform-*d*, δ): 164.78, 158.66, 157.45, 155.26, 133.14, 132.80, 131.04, 130.16, 129.88, 114.10, 113.26, 96.01, 61.26, 46.03, 13.59, 12.51.
HRMS (ESI) *m/z*: $[M]^+$ calcd for $C_{30}H_{35}N_2O_3$, 471.2642; found, 471.2643.

Rhodamine B n-propyl ester iodide (R3, N-(6-(diethylamino)-9-(2-(propoxycarbonyl)phenyl)-3H-xanthen-3-ylidene)-N-ethylethan-aminium iodide)

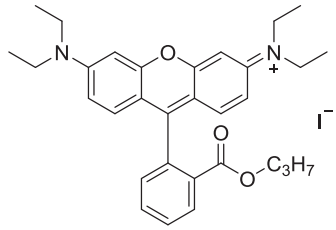

Compound **R3** was synthesized as described in the general protocol above. Yield 89%, red solid.

^{1}H NMR (400 MHz, Chloroform-*d*, δ): 8.26 (dd, *J* = 7.7, 1.3 Hz, 1H), 7.79 (td, *J* = 7.6, 1.4 Hz, 1H), 7.71 (td, *J* = 7.7, 1.4 Hz, 1H), 7.28 (dd, *J* = 7.6, 1.3 Hz, 1H), 7.05 (d, *J* = 9.4 Hz, 2H), 6.87 (dd, *J* = 9.5, 2.5 Hz, 2H), 6.77 (d, *J* = 2.5 Hz, 2H), 3.95 (t, *J* = 6.7 Hz, 2H), 3.62 (q, *J* = 7.1 Hz, 8H), 1.44 (h, *J* = 7.1 Hz, 2H), 1.30 (t, *J* = 7.1 Hz, 12H), 0.75 (t, *J* = 7.4 Hz, 3H).
^{13}C NMR (100 MHz, Chloroform-*d*, δ): 165.18, 158.99, 157.77, 155.55, 133.46, 133.09, 131.35, 131.33, 130.43, 130.24, 130.21, 114.34, 113.58, 96.36, 67.26, 46.31, 21.73, 12.77, 10.32.
HRMS (ESI) *m/z*: $[M]^+$ calcd for $C_{31}H_{37}N_2O_3$, 485.2799; found, 485.2795.

Rhodamine B *n*-butyl ester iodide (R4, N-(9-(2-(butoxycarbonyl)phenyl)-6-(diethylamino)-3H-xanthen-3-ylidene)-N-ethylethan-aminium iodide)

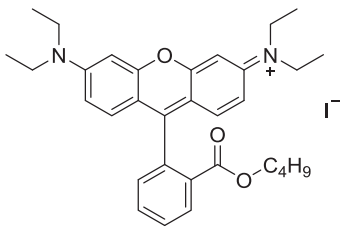

Compound **R4** was synthesized as described in the general protocol above. Yield 77%, red solid.

^{1}H NMR (400 MHz, Chloroform-*d*, δ): 8.23 (dd, *J* = 7.9, 1.3 Hz, 1H), 7.77 (td, *J* = 7.5, 1.4 Hz, 1H), 7.69 (td, *J* = 7.7, 1.4 Hz, 1H), 7.25 (dd, *J* = 7.9, 1.2 Hz, 1H), 7.02 (d, *J* = 9.5 Hz, 2H), 6.86 (dd, *J* = 9.5, 2.5 Hz, 2H), 6.74 (d, *J* = 2.4 Hz, 2H), 3.95 (t, *J* = 6.5 Hz, 2H), 3.60 (q, *J* = 7.2 Hz, 8H), 1.34 (p, *J* = 14.7, 6.8 Hz, 2H), 1.27 (t, *J* = 7.1 Hz, 12H), 1.09 (h, *J* = 7.4 Hz, 2H), 0.74 (t, *J* = 7.4 Hz, 3H).
^{13}C NMR (100 MHz, Chloroform-*d*, δ): 165.16, 158.84, 157.69, 155.49, 133.26, 132.99, 131.28, 130.36, 130.19, 130.13, 114.29, 113.49, 96.25, 65.48, 46.24, 30.30, 19.00, 13.61, 12.70.
HRMS (ESI) *m/z*: $[M]^+$ calcd for $C_{32}H_{39}N_2O_3$, 499.2955; found, 499.2953.

Rhodamine B isooctyl ester iodide (R8i, N-(6-(diethylamino)-9-(2-(((2-ethylhexyl)oxy)carbonyl)phenyl)-3H-xanthen-3-ylidene)-N-ethylethanaminium iodide

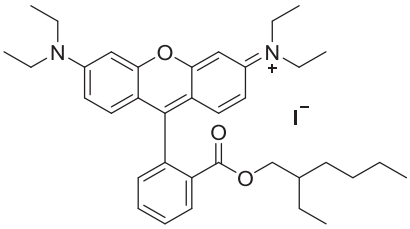

Compound **R8i** was synthesized as described in the general protocol above. Yield 78%, red solid.

^{1}H NMR (400 MHz, Chloroform-*d*, δ): 8.19 (dd, *J* = 8.0, 1.3 Hz, 1H), 7.74 (td, *J* = 7.5, 1.4 Hz, 1H), 7.67 (td, *J* = 7.7, 1.3 Hz, 1H), 7.22 (dd, *J* = 7.6, 1.3 Hz, 1H), 7.00 (d, *J* = 9.5 Hz, 2H), 6.83 (dd, *J* = 9.5, 2.4 Hz, 2H), 6.72 (d, *J* = 2.4 Hz, 2H), 3.91 – 3.78 (m, 2H), 3.58 (q, *J* = 7.2 Hz, 8H), 2.02 (s, 1H), 1.24 (t, *J* = 7.1 Hz, 12H), 1.12 – 0.90 (m, 8H), 0.72 (t, *J* = 6.8 Hz, 3H), 0.64 (t, *J* = 7.4 Hz, 3H).
^{13}C NMR (100 MHz, Chloroform-*d*, δ): 165.28, 158.65, 157.61, 155.40, 133.04, 132.93, 131.17, 130.30, 130.14, 114.21, 113.37, 96.16, 67.95, 46.14, 38.46, 30.01, 28.63, 23.46, 22.66, 13.87, 12.59, 10.77.
HRMS (ESI) *m/z*: $[M]^+$ calcd for $C_{36}H_{47}N_2O_3$, 555.3581; found, 555.3567.

Rhodamine B *n*-octyl ester iodide (R8, N-(6-(diethylamino)-9-(2-((octyloxy)carbonyl)phenyl)-3H-xanthen-3-ylidene)-N-ethylethanaminium iodide)

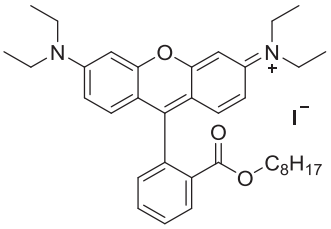

Compound **R8** was synthesized as described in the general protocol above. Yield 79%, red solid.

^{1}H NMR (400 MHz, Chloroform-*d*, δ): 8.20 (dd, *J* = 7.9, 1.3 Hz, 1H), 7.74 (td, *J* = 7.5, 1.4 Hz, 1H), 7.66 (td, *J* = 7.7, 1.3 Hz, 1H), 7.22 (dd, *J* = 7.5, 1.2 Hz, 1H), 6.99 (d, *J* = 9.5 Hz, 2H), 6.83 (dd, *J* = 9.5, 2.5 Hz, 2H), 6.71 (d, *J* = 2.4 Hz, 2H), 3.91 (t, *J* = 6.6 Hz, 2H), 3.58 (q, *J* = 7.2 Hz, 8H), 1.32 (p, *J* = 6.8 Hz, 2H), 1.24 (t, *J* = 7.1 Hz, 12H), 1.20 – 0.97 (m, 10H), 0.76 (t, *J* = 6.9 Hz, 3H).
^{13}C NMR (100 MHz, Chloroform-*d*, δ): 165.03, 158.76, 157.56, 155.36, 133.17, 132.92, 131.17, 131.16, 130.26, 130.04, 130.02, 114.18, 113.36, 96.11, 65.61, 46.12, 31.57, 28.94, 28.89, 28.13, 25.61, 22.42, 13.93, 12.60.
HRMS (ESI) *m/z*: $[M]^+$ calcd for $C_{36}H_{47}N_2O_3$, 555.3581; found, 555.3583.

Rhodamine B dodecyl ester iodide (R12, N-(6-(diethylamino)-9-(2-((dodecyloxy)carbonyl)phenyl)-3H-xanthen-3-ylidene)-N-ethylethanaminium iodide)

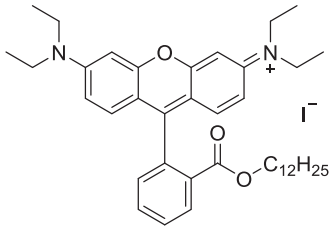

Compound **R12** was synthesized as described in the general protocol above. Yield 82%, red solid.

^{1}H NMR (400 MHz, Chloroform-*d*, δ): 8.20 (dd, *J* = 7.9, 1.3 Hz, 1H), 7.75 (td, *J* = 7.6, 1.4 Hz, 1H), 7.67 (td, *J* = 7.7, 1.3 Hz, 1H), 7.23 (dd, *J* = 7.5, 1.2 Hz, 1H), 7.00 (d, *J* = 9.5 Hz, 2H), 6.84 (dd, *J* = 9.5, 2.5 Hz, 2H), 6.72 (d, *J* = 2.4 Hz, 2H), 3.92 (t, *J* = 6.6 Hz, 2H), 3.58 (q, *J* = 7.2 Hz, 8H), 1.33 (p, *J* = 6.7 Hz, 2H), 1.25 (t, *J* = 7.1 Hz, 12H), 1.21 – 0.99 (m, 18H), 0.78 (t, *J* = 6.7 Hz, 3H).
^{13}C NMR (100 MHz, Chloroform-*d*, δ): 165.04, 158.80, 157.59, 155.39, 133.21, 132.94, 131.20, 131.18, 130.28, 130.07, 130.04, 114.20, 113.40, 96.14, 65.65, 46.14, 31.74, 29.47, 29.41, 29.28, 29.17, 29.03, 28.17, 25.66, 22.52, 13.98, 12.62.
HRMS (ESI) *m/z*: $[M]^+$ calcd for $C_{40}H_{55}N_2O_3$, 611.4207; found, 611.4208.

Rhodamine B hexadecyl ester iodide (R16, N-(6-(diethylamino)-9-(2-((hexadecyloxy)carbonyl)phenyl)-3H-xanthen-3-ylidene)-N-ethylethanaminium iodide)

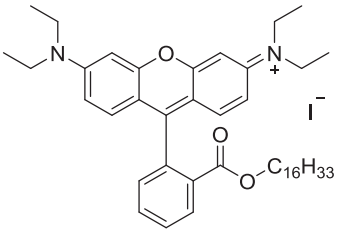

Compound **R16** was synthesized as described in the general protocol above. Yield 72%, red solid.

^{1}H NMR (400 MHz, Chloroform-*d*, δ): 8.25 (dd, *J* = 7.8, 1.2 Hz, 1H), 7.79 (td, *J* = 7.6, 1.3 Hz, 1H), 7.71 (td, *J* = 7.8, 1.3 Hz, 1H), 7.28 (dd, *J* = 7.6, 1.2 Hz, 1H), 7.04 (d, *J* = 9.5 Hz, 2H), 6.87 (dd, *J* = 9.5, 2.5 Hz, 2H), 6.77 (d, *J* = 2.4 Hz, 2H), 3.97 (t, *J* = 6.6 Hz, 2H), 3.62 (q, *J* = 7.2 Hz, 8H), 1.38 (p, *J* = 6.7 Hz, 2H), 1.30 (t, *J* = 7.1 Hz, 12H), 1.26 – 0.99 (m, 26H), 0.83 (t, *J* = 6.7 Hz, 3H).
^{13}C NMR (100 MHz, Chloroform-*d*, δ): 165.19, 158.99, 157.77, 155.57, 133.39, 133.07, 131.36, 131.31, 130.41, 130.25, 114.36, 113.59, 96.35, 77.48, 77.16, 76.84, 65.81, 46.29, 31.91, 29.69, 29.64, 29.64, 29.58, 29.45, 29.34, 29.20, 28.34, 25.82, 22.68, 14.11, 12.76.
HRMS (ESI) *m/z*: $[M]^+$ calcd for $C_{44}H_{63}N_2O_3$, 667.4833; found, 667.4839.

Octadecyl Rhodamine B iodide (R18, N-(6-(diethylamino)-9-(2-((octadecyloxy)carbonyl)phenyl)-3H-xanthen-3-ylidene)-N-ethylethanaminium iodide)

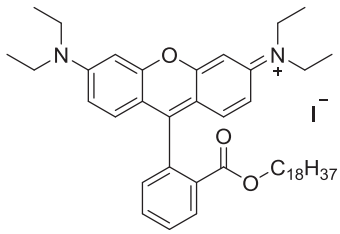

The general protocol above was modified by using DMF as a solvent. Then, after removal the excess of potassium carbonate by filtration, mature solution was concentrated under vacuum, redissolved in 50mL of DCM and washed three times with brine, then organic layer was

separated, dried over sodium sulphate and evaporated. Purification was done by flash column chromatography as described above. Yield 80%, red solid.

^{1}H NMR (400 MHz, Chloroform-*d*, δ): 8.24 (dd, *J* = 7.9, 1.3 Hz, 1H), 7.79 (td, *J* = 7.5, 1.4 Hz, 1H), 7.70 (td, *J* = 7.7, 1.4 Hz, 1H), 7.28 (dd, *J* = 7.5, 1.3 Hz, 1H), 7.04 (d, *J* = 9.5 Hz, 2H), 6.87 (dd, *J* = 9.5, 2.5 Hz, 2H), 6.76 (d, *J* = 2.4 Hz, 2H), 3.96 (t, *J* = 6.6 Hz, 2H), 3.62 (q, *J* = 7.2 Hz, 8H), 1.37 (p, *J* = 6.8 Hz, 2H), 1.29 (t, *J* = 7.1 Hz, 12H), 1.25 – 0.96 (m, 30H), 0.83 (t, *J* = 6.7 Hz, 3H).
^{13}C NMR (100 MHz, Chloroform-*d*, δ): 165.16, 158.96, 157.74, 155.54, 133.36, 133.05, 131.33, 131.29, 130.39, 130.22, 114.34, 113.57, 96.32, 65.79, 46.27, 31.90, 29.67, 29.62, 29.57, 29.43, 29.33, 29.18, 28.32, 25.80, 22.66, 14.09, 12.74.
HRMS (ESI) *m/z*: $[M]^+$ calcd for $C_{46}H_{67}N_2O_3$, 695.5146; found, 695.5157.

Synthetic scheme for Rhodamine 101 dodecyl ester iodide (C12Rh101):

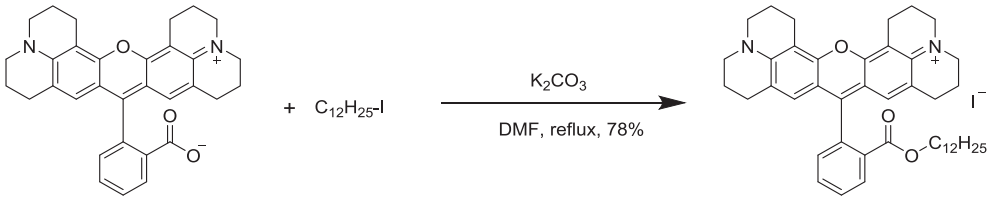

Rhodamine 101 inner salt

C12Rh101

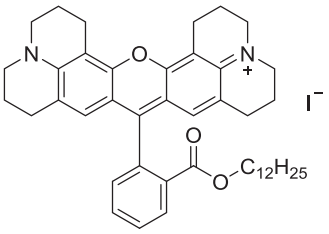

Rhodamine 101 inner salt (1 eq., 100 mg, 0.204 mmol) , potassium carbonate (3 eq., 84.5 mg, 0.612 mmol) were placed in a reaction flask. Anhydrous DMF (10 mL) was added via syringe. Obtained mixture was preheated to 80 °C for 30 min, then 1-iododododecane (3 eq., 181 mg, 150 µL, 0.612 mmol) was added via syringe. The reaction mixture was stirred at 110 °C overnight. After cooling to room temperature, solvent was removed under reduced pressure. The residue was redissolved by addition of water (25 mL) and dichloromethane (25 mL). The organic layer was separated and washed three times with brine, dried over sodium sulphate, filtered and evaporated to dryness. The crude product was purified by gradient flash column chromatography (SiO_2, DCM/MeOH, 98:2 to 95:5), which furnished 103 mg (yield 64%) of a title compound as dark red solid.

^{1}H NMR (500 MHz, Chloroform-*d*, δ): 8.25 (dd, *J* = 8.0, 1.3 Hz, 1H), 7.78 (td, *J* = 7.5, 1.4 Hz, 1H), 7.70 (td, *J* = 7.7, 1.3 Hz, 1H), 7.24 (dd, *J* = 7.6, 1.3 Hz, 1H), 6.51 (s, 2H), 3.98 (t, *J* = 6.6 Hz, 2H), 3.64 – 3.43 (m, 8H), 3.10 – 2.94 (m, 4H), 2.74 – 2.58 (m, 4H), 2.14 – 2.03 (m, 4H), 2.00 – 1.91 (m, 4H), 1.38 (p, *J* = 6.7 Hz, 2H), 1.29 – 1.04 (m, 18H), 0.85 (t, *J* = 7.0 Hz, 3H).
^{13}C NMR (126 MHz, Chloroform-*d*, δ): 165.47, 155.88, 152.11, 151.22, 134.34, 132.96, 131.19, 130.62, 130.29, 130.00, 125.95, 123.78, 113.00, 105.39, 65.75, 51.12, 50.68, 31.96, 29.73, 29.70, 29.68, 29.55, 29.41, 29.32, 28.43, 27.74, 25.91, 22.74, 20.73, 20.04, 19.82, 14.19.
HRMS (ESI) *m/z*: $[M]^+$ calcd for $C_{44}H_{55}N_2O_3$, 659.4207; found, 659.4218.

1,1'-diethyl-3,3,3'3'-tetramethylindocarbocyanine perchlorate (C2-Cy5, 1-ethyl-2-((1E,3E)-5-((Z)-1-ethyl-3,3-dimethylindolin-2-ylidene)penta-1,3-dien-1-yl)-3,3-dimethyl-3H-indol-1-ium bromide)

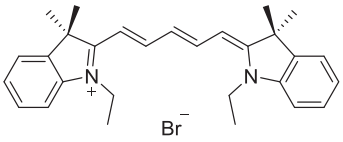

Synthesis of C2-Cy5 was done as described elsewhere.[5]

3.1.3 Synthesis of building blocks for counterion-assembled micelles.

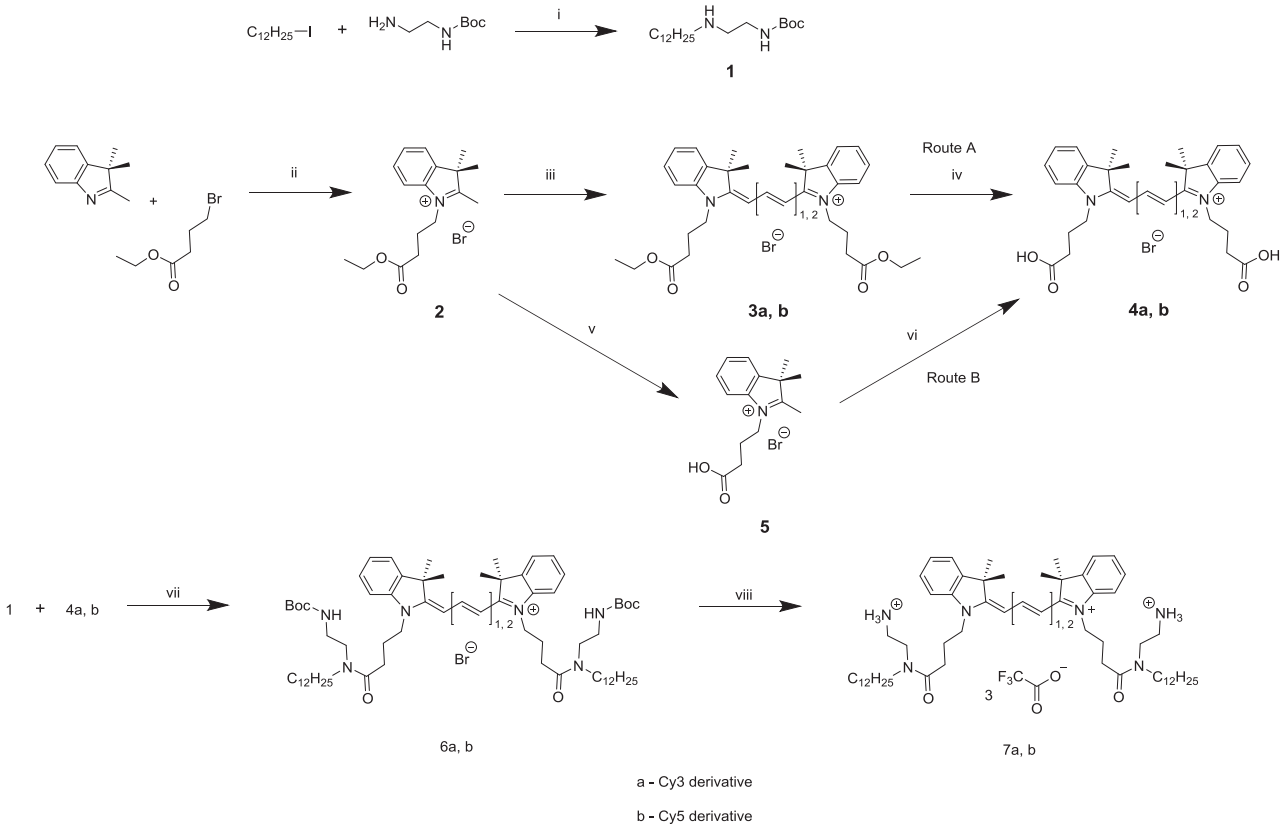

i) MeCN, reflux, 6h (74%); ii) MeCN, reflux, 12h (65%); iii) $HC(OEt)_3$ or $(MeO)_2CHCH_2CH(OMe)_2$, Py, 110°C, 4h (71%); iv) HBr (30% aq.), 110°C (58%); v) HBr (30% aq.), 110°C (79%); vi) $HC(OEt)_3$ or $(MeO)_2CHCH_2CH(OMe)_2$, Py, 110°C, 4h (69%); vii) HBTU, HOBt, DIPEA, DMF, r.t., 12h (77%); viii) TFA conc., r.t., 4h (81%).

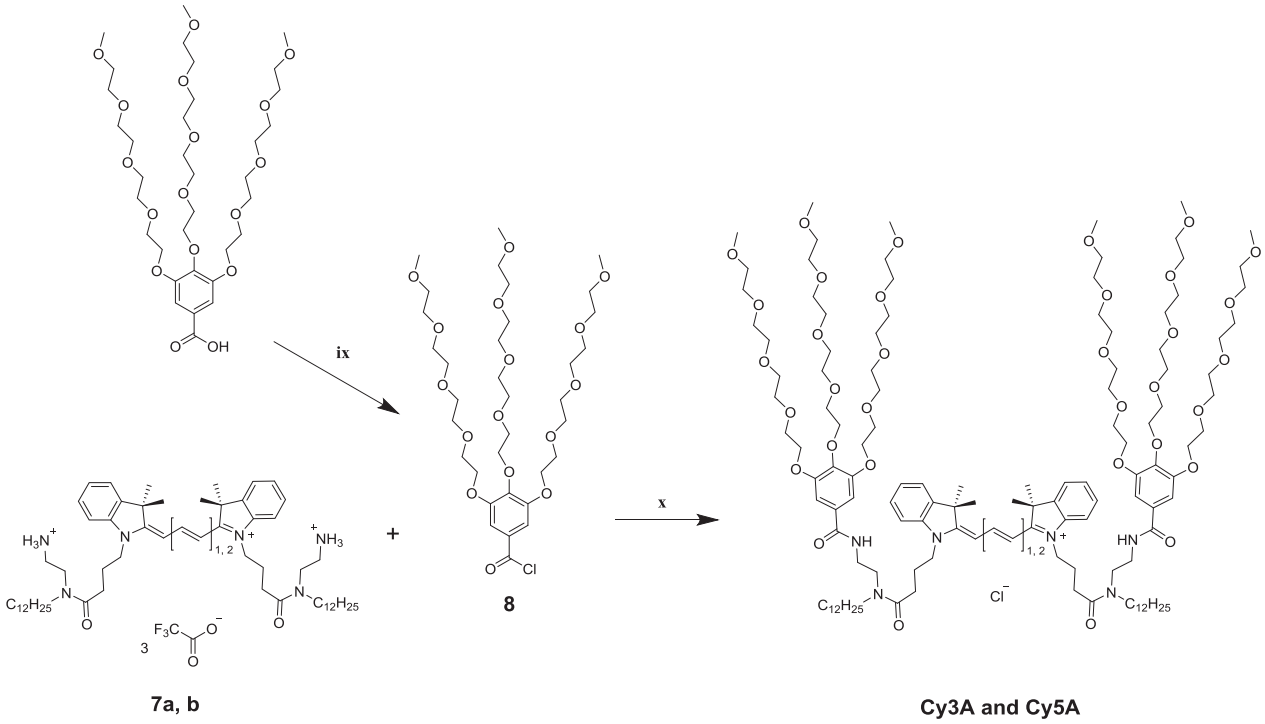

ix) $(COCl)_2$, r.t., 24h, quantative yield; x) TEA, DMF, 0-60°C, 2h (20%).

Tert-butyl N-[2-(dodecylamino)ethyl]carbamate (1)

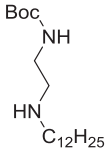

1-Iodododecane (1 eq., 3.08 g, 2.57 mL, 10.4 mmol) and N-boc-ethylenediamine (3 eq., 5 g, 31.2 mmol) were placed in a reaction flask. Anhydrous acetonitrile (40 mL) was added via syringe. The reaction mixture was stirred under reflux for 6h. Solvent was removed under reduced pressure. The crude product was purified by column chromatography (SiO_2, DCM/MeOH, 95:5). An additional purification step was done using recrystallization from acetonitrile, which furnished 2.53 g (yield 74%) of the title compound **1** as a white solid.

^{1}H NMR (400 MHz, Chloroform-*d*) δ 7.59 (br. s, 2H), 5.61 (t, *J* = 5.6 Hz, 1H), 3.59 (q, *J* = 5.3 Hz, 2H), 3.22 (t, *J* = 5.0 Hz, 2H), 3.08 – 2.97 (m, 2H), 1.85 (p, *J* = 7.8 Hz, 2H), 1.44 (s, 9H), 1.40 – 1.33 (m, 2H), 1.33 – 1.17 (m, 16H), 0.86 (t, *J* = 6.7 Hz, 3H).
^{13}C NMR (101 MHz, Chloroform-*d*) δ 157.78, 81.18, 49.05, 48.39, 37.72, 32.01, 29.72, 29.71, 29.61, 29.50, 29.43, 29.10, 28.49, 26.73, 26.17, 22.78, 14.21.
HRMS (*m/z*): $[M+H]^+$ calcd. for $C_{19}H_{41}N_2O_2$, 329.3163; found, 329.3162.

1-(4-Ethoxy-4-oxobutyl)-2,3,3-trimethyl-3H-indol-1-ium bromide (2)

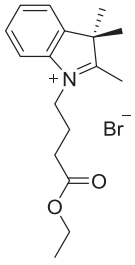

2,3,3-trimethylindolenine (1 eq., 2.97 g, 3 mL, 18.7 mmol) and ethyl 4-bromobutyrate (3 eq., 10.9 g, 8.03 mL, 56 mmol) were placed in a reaction flask. Anhydrous acetonitrile (40 mL) was added via syringe. The reaction mixture was stirred under reflux for 48 hours. After cooling to room temperature, diethyl ether (40 ml) was added and formed slightly red precipitate was removed by filtration, and washed several times with diethyl

ether. The product was purified by recrystallization from acetonitrile, which furnished 4.3 g (yield 65%) of the title compound **2** as pink crystals.

^{1}H NMR (400 MHz, Chloroform-*d*) δ 8.06 – 7.96 (m, 1H), 7.61 – 7.48 (m, 3H), 4.92 – 4.83 (m, 2H), 4.05 (q, *J* = 7.1 Hz, 2H), 3.17 (s, 3H), 2.70 (t, *J* = 6.2 Hz, 2H), 2.29 – 2.17 (m, 2H), 1.61 (s, 6H), 1.19 (t, *J* = 7.1 Hz, 3H).
^{13}C NMR (101 MHz, Chloroform-*d*) δ 196.52, 172.78, 141.63, 141.27, 130.00, 129.65, 123.13, 115.93, 60.97, 54.67, 48.59, 30.56, 23.12, 22.94, 16.32, 14.16.
HRMS (*m/z*): $[M]^+$ calcd. for $C_{17}H_{24}NO_2$, 274.1802; found, 274.1810.

1-(3-Ethyloxycarbonylpropyl)-2-(*E*)-3-[1-(3-ethyloxycarbonylpropyl)-3,3-dimethyl-2,3-dihydro-1*H*-2-indolyliden]-1-propenyl-3,3-dimethyl-3*H*-indolium (3a)

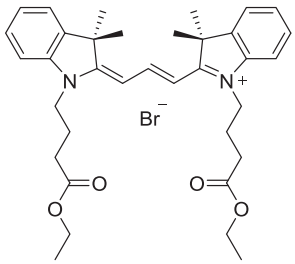

Compound **2** (1 eq., 3 g, 8.47 mmol) was placed in a reaction flask. Anhydrous pyridine (40 mL) was added via syringe. Obtained mixture was preheated to 110 °C until complete dissolving of indoleninium salt, then triethyl orthoformate (1.5 eq., 1.88 g, 2.12 mL, 12.7 mmol) was quickly added dropwise to the boiling solution of indoleninium salt using syringe. The reaction mixture was stirred under reflux for 4 hours. Then, solvent was removed under reduced pressure. The residue was redissolved in DCM (100 mL), washed with 1M aq. solution of hydrochloric acid (3 × 100 mL), once with brine, and dried over sodium sulphate. After solvent evaporation, the product was purified by gradient column chromatography (SiO_2, DCM/MeOH, 98:2 to 90:10), which furnished 3.83 g (yield 71%) of title compound **3a** as a red solid.

^{1}H NMR (400 MHz, Methanol-d_4) δ 8.60 (t, *J* = 13.4 Hz, 1H), 7.59 (d, *J* = 7.4 Hz, 2H), 7.53 – 7.45 (m, 4H), 7.39 – 7.31 (m, 2H), 6.64 (d, *J* = 13.6 Hz, 2H), 4.27 (t, *J* = 7.7 Hz, 4H), 4.15 (q, *J* = 7.1 Hz, 4H), 2.63 (t, *J* = 6.7 Hz, 4H), 2.16 (p, *J* = 7.0 Hz, 4H), 1.81 (s, 12H), 1.27 (t, *J* = 7.1 Hz, 6H).
^{13}C NMR (101 MHz, Methanol-d_4) δ 176.10, 174.36, 152.32, 143.30, 142.19, 129.98, 126.78, 123.55, 112.45, 103.96, 61.78, 50.66, 44.53, 31.63, 28.31, 23.33, 14.54.
HRMS (*m/z*): $[M]^+$ calcd. for $C_{35}H_{45}N_2O_4$, 557.3374; found, 557.3360.

1-(3-Ethyloxycarbonylpropyl)-2-(1*E*,3*E*)-5-[1-(3-ethyloxycarbonylpropyl)-3,3-dimethyl-2,3-dihydro-1*H*-2-indolyliden]-1,3-pentadienyl-3,3-dimethyl-3*H*-indolium (3b)

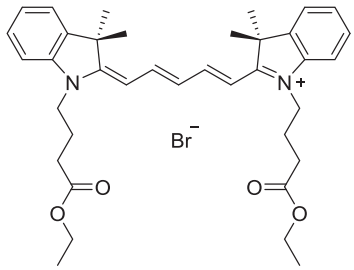

Compound **3b** was prepared by the same protocol reported above for **3a** using 1,1,3,3-tetramethoxypropane as condensing agent. Blue solid with metallic luster. Yield 2.55 g (65 %).

^{1}H NMR (400 MHz, Methanol-d_4) δ 8.30 (t, *J* = 13.1 Hz, 2H), 7.49 (dd, *J* = 7.5, 1.1 Hz, 2H), 7.41 (ddd, *J* = 8.4, 7.3, 1.2 Hz, 2H), 7.35 (d, *J* = 7.9 Hz, 2H), 7.26 (td, *J* = 7.4, 1.1 Hz, 2H), 6.64 (t, *J* = 12.4 Hz, 1H),

6.38 (d, *J* = 13.7 Hz, 2H), 4.23 – 4.08 (m, 8H), 2.56 (t, *J* = 6.6 Hz, 4H), 2.13 – 2.02 (m, 4H), 1.72 (s, 12H), 1.26 (t, *J* = 7.1 Hz, 6H).
^{13}C NMR (101 MHz, Methanol-d_4) δ 174.74, 174.44, 155.65, 143.45, 142.55, 129.72, 126.87, 126.26, 123.43, 111.96, 104.43, 61.79, 50.57, 44.25, 31.44, 27.94, 23.21, 14.56.
HRMS (*m/z*): $[M]^+$ calcd. for $C_{37}H_{47}N_2O_4$, 583.3530; found, 583.3536.

1-(3-Carboxypropyl)-2-(*E*)-3-[1-(3-carboxypropyl)-3,3-dimethyl-2,3-dihydro-1*H*-2-indolyliden]-1-propenyl-3,3-dimethyl-3*H*-indolium (4a)

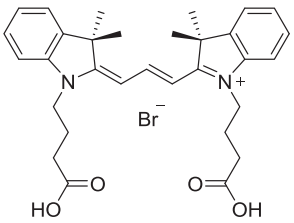

Route A. Compound **3a** (1 eq., 3 g, 4.7 mmol) was hydrolyzed using 30% aq. solution of hydrobromic acid (25 mL) while stirring at 110 °C for about 4 h (control by TLC). Then, solvent was removed under reduced pressure. The residue was redissolved in DCM (100 mL), and washed with 10% aq. solution of sodium carbonate (3 × 100 mL), once with brine, dried over sodium sulphate, filtered, and the filtrate evaporated to dryness in vacuum. The crude product **4a** had a purity of >90% and was used directly for the next step without further purification. Yield 1.59 g (58%) as a red solid.

Route B. Compound **5** (1 eq., 2 g, 6.13 mmol) was placed in a reaction flask. Anhydrous pyridine (40 mL) was added via syringe. Obtained mixture was preheated to 110 °C until complete dissolving of indoleninium salt, then triethyl orthoformate (1.5 eq., 1.53 mL, 9.2 mmol) was quickly added dropwise to the boiling solution of indoleninium salt using syringe. The reaction mixture was stirred under reflux for 4 h. Solvent was removed under reduced pressure. The residue was dissolved in DCM (100 mL), washed with 1M aq. solution of hydrochloric acid (3 × 100 mL), and once with brine, dried over sodium sulphate. After solvent evaporation, the product was purified by gradient column chromatography (SiO_2, DCM/MeOH/HCOOH, 9:1:0 to 9:1:0.1), which furnished 2.46 g (yield 69%) of the title compound **4a** as a red solid.

^{1}H NMR (400 MHz, DMSO-d_6) δ 12.50 (br s, 2H), 8.36 (t, *J* = 13.4 Hz, 1H), 7.64 (d, *J* = 7.4 Hz, 2H), 7.50 (d, *J* = 8.0 Hz, 2H), 7.45 (td, *J* = 8.0, 1.2 Hz, 2H), 7.30 (t, *J* = 7.4 Hz, 2H), 6.57 (d, *J* = 13.4 Hz, 2H), 4.15 (t, *J* = 7.7 Hz, 4H), 2.42 (t, *J* = 7.1 Hz, 4H), 1.96 (p, *J* = 7.3 Hz, 4H), 1.70 (s, 12H).
^{13}C NMR (101 MHz, DMSO-d_6) δ 173.95, 173.75, 149.93, 141.86, 140.61, 128.59, 125.17, 122.49, 111.36, 102.68, 48.89, 43.18, 30.78, 27.41, 22.41.
HRMS (*m/z*): $[M]^+$ calcd. for $C_{31}H_{37}N_2O_4$, 501.2748; found, 501.2756.

1-(3-Carboxypropyl)-2-(1*E*,3*E*)-5-[1-(3-carboxypropyl)-3,3-dimethyl-2,3-dihydro-1*H*-2-indolyliden]-1,3-pentadienyl-3,3-dimethyl-3*H*-indolium (4b)

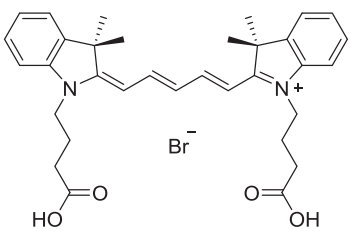

Route A. Compound **4b** was hydrolyzed by the same protocol reported above for the compound **4a**. The crude product **4b** had a purity of >90% and was used directly for the next step without further purification.Yield 1.51 g (55%) as a dark blue solid.

Route B. Compound **5** (1 eq., 2 g, 6.13 mmol) was placed in a reaction flask. Anhydrous pyridine (40 mL) was added via syringe. Obtained mixture was preheated to 110 °C until complete dissolving of indoleninium salt, then 1,1,3,3-tetramethoxypropane (1.5 eq., 1.53 mL, 9.2 mmol) was quickly added dropwise to the boiling solution of indoleninium salt using syringe. The reaction mixture was stirred under reflux for 4 hours. Solvent was removed under reduced pressure. The residue was redissolved in DCM (100 mL), washed with 1M aq. solution of hydrochloric acid (3 × 100 mL), and once with brine, dried over sodium sulphate. After solvent evaporation, the product was purified by gradient column chromatography (SiO_2, DCM/MeOH/HCOOH, 9:1:0 to 9:1:0.1), which furnished 2.64 g (yield 71%) of the title compound **4b** as a dark blue solid.

^{1}H NMR (400 MHz, DMSO-d_6) δ 8.35 (t, *J* = 13.1 Hz, 2H), 7.61 (d, *J* = 7.5 Hz, 2H), 7.46 – 7.33 (m, 4H), 7.24 (td, *J* = 7.1, 1.7 Hz, 2H), 6.54 (t, *J* = 12.3 Hz, 1H), 6.37 (d, *J* = 13.8 Hz, 2H), 4.11 (t, *J* = 7.7 Hz, 4H), 2.42 (t, *J* = 7.0 Hz, 4H), 1.95 – 1.83 (m, 4H), 1.68 (s, 12H).
^{13}C NMR (101 MHz, DMSO-d_6) δ 173.87, 172.70, 154.14, 141.93, 141.07, 128.36, 125.50, 124.64, 122.40, 110.89, 103.14, 48.89, 42.76, 30.49, 27.10, 22.19.
HRMS (*m/z*): $[M]^+$ calcd. for $C_{33}H_{39}N_2O_4$, 527.2904; found, 527.2915.

1-(3-Carboxypropyl)-2,3,3-trimethyl-3H-indol-1-ium bromide (5)

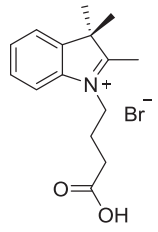

1-(4-Ethoxy-4-oxobutyl)-2,3,3-trimethyl-3*H*-indol-1-ium bromide (1 eq., 4 g, 11.3 mmol) was placed in a reaction flask. 20 mL of 30% aq. solution of hydrobromic acid were added. Obtained mixture was stirred at 110 °C for 4 hours. After cooling to room temperature, solvent was removed under reduced pressure. To the residue 50 mL of acetonitrile were added and a white precipitate was removed by filtration, washed several times with acetonitrile, then once with diethyl ether. This furnished 2.91 g (yield 79%) of the title compound **5** as a white solid.

^{1}H NMR (400 MHz, DMSO-d_6) δ 12.21 (s, 1H), 8.08 – 7.98 (m, 1H), 7.90 – 7.80 (m, 1H), 7.68 – 7.57 (m, 2H), 4.54 – 4.45 (m, 2H), 2.86 (s, 3H), 2.54 (t, *J* = 7.0 Hz, 2H), 2.07 (p, *J* = 7.3 Hz, 2H), 1.55 (s, 6H).
^{13}C NMR (101 MHz, DMSO-d_6) δ 196.80, 173.64, 141.85, 141.15, 129.32, 128.86, 123.48, 115.27, 54.17, 46.97, 30.32, 22.47, 21.98, 14.05.
HRMS (*m/z*): $[M]^+$ calcd. for $C_{15}H_{20}NO_2$, 246.1489; found, 246.1496.

2-((*E*)-3-3,3-dimethyl-1-[3-(2-*t*-butoxycarboxamidoethylcarbamoyl)propyl]-2,3-dihydro-1*H*-2-indolyliden-1-propenyl)-3,3-dimethyl-1-[3-(2-*t*-butoxycarboxamidoethylcarbamoyl)propyl]-3*H*-indolium (6a)

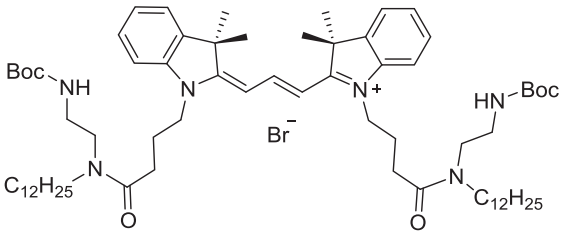

Compound **4a** (1 eq., 500 mg, 0.86 mmol), HBTU (2.2 eq., 717 mg, 1.89 mmol), and HOBt (3 eq., 348 mg, 2.58 mmol) were placed in a reaction flask. DMF (5mL) and DIPEA (10 eq., 1.42 mL, 8.6 mmol) were added via syringe. After stirring the reaction

mixture for 30 min, tert-butyl N-[2-(dodecylamino)ethyl]carbamate (2 eq., 564 mg, 1.72 mmol) dissolved in anhydrous DCM (2 mL) was added dropwise. The reaction mixture was stirred at ambient temperature for 24 h. Solvent was removed under reduced pressure. The residue was redissolved in DCM (50 mL), washed with saturated brine solution (3 ×100 mL), dried over sodium sulphate, filtered, and and the filtrate evaporated to dryness in vacuum. The crude product was purified by flash column chromatography (SiO_2, DCM/MeOH, 98:2), which furnished 796 mg (yield 77%) of the title compound **6a** as a red solid.

^{1}H NMR (400 MHz, Methanol-d_4) δ 8.60 (t, *J* = 13.4 Hz, 1H), 7.59 (d, *J* = 7.5 Hz, 2H), 7.55 – 7.45 (m, 4H), 7.35 (t, *J* = 7.3 Hz, 2H), 6.68 – 6.53 (m, 2H), 4.29 – 4.18 (m, 4H), 3.52 – 3.44 (m, 4H), 3.45 – 3.37 (m, 4H), 3.32 – 3.22 (m, 4H), 2.77 – 2.69 (m, 2H), 2.69 – 2.60 (m, 2H), 2.20 – 2.11 (m, 4H), 1.82 (s, 12H), 1.63 – 1.55 (m, 4H), 1.46 (s, 9H), 1.45 (s, 9H), 1.41 – 1.29 (m, 36H), 0.98 – 0.89 (m, 6H).
^{13}C NMR (101 MHz, Methanol-d_4) δ 176.09, 176.01, 174.13, 174.07, 173.85, 173.82, 158.37, 158.31, 152.32, 152.29, 143.37, 143.33, 142.21, 142.18, 130.01, 126.75, 123.48, 112.71, 112.53, 103.98, 103.93, 103.84, 103.82, 80.29, 80.05, 61.76, 50.65, 50.63, 50.16, 47.61, 47.23, 44.81, 44.68, 39.75, 39.53, 38.88, 33.06, 33.05, 30.76, 30.73, 30.54, 30.50, 30.46, 30.28, 29.82, 28.83, 28.82, 28.61, 28.41, 28.39, 28.37, 28.35, 28.09, 27.93, 27.92, 23.72, 23.71, 14.47, 14.45.
HRMS (*m/z*): $[M]^+$ calcd. for $C_{69}H_{113}N_6O_6$, 1121.8716; found, 1121.8698.

2-((1*E*,3*E*)-3-3,3-dimethyl-1-[3-(2-*t*-butoxycarboxamidoethylcarbamoyl)propyl]-2,3-dihydro-1*H*-2-indolyliden-1,3-pentadienyl)-3,3-dimethyl-1-[3-(2-*t*-butoxycarboxamidoethylcarbamoyl)propyl]-3*H*-indolium (6b)

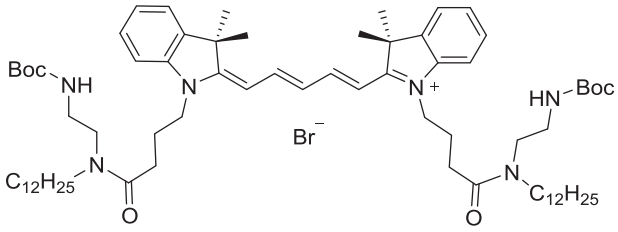

The compound **6b** prepared using the same procedure as described above for **6a**. Yield 748 mg (74%) as blue solid.

^{1}H NMR (400 MHz, Methanol-d_4) δ 8.28 (td, *J* = 13.2, 4.7 Hz, 2H), 7.50 (d, *J* = 7.4 Hz, 2H), 7.45 – 7.36 (m, 4H), 7.27 (t, *J* = 7.0 Hz, 2H), 6.73 (t, *J* = 12.4 Hz, 1H), 6.46 – 6.35 (m, 2H), 4.25 – 4.12 (m, 4H), 3.53 – 3.45 (m, 4H), 3.45 – 3.40 (m, 2H), 3.39 – 3.32 (m, 2H), 3.31 – 3.23 (m, 4H), 2.69 (t, *J* = 7.0 Hz, 2H), 2.61 (t, *J* = 7.1 Hz, 2H), 2.19 – 2.07 (m, 4H), 1.74 (s, 12H), 1.65 – 1.54 (m, 4H), 1.46 (s, 9H), 1.45 (s, 9H), 1.38 – 1.27 (m, 36H), 0.92 (t, *J* = 6.3 Hz, 6H).
^{13}C NMR (101 MHz, Methanol-d_4) δ 174.54, 174.50, 173.94, 173.91, 173.70, 173.68, 167.33, 158.25, 155.42, 143.50, 142.54, 129.71, 127.27, 126.18, 123.34, 112.14, 112.02, 104.62, 104.57, 104.49, 104.43, 80.20, 79.95, 50.53, 50.50, 50.06, 48.18, 47.44, 47.11, 44.62, 44.39, 39.70, 39.58, 38.88, 33.02, 30.77, 30.75, 30.73, 30.71, 30.58, 30.56, 30.45, 30.42, 30.25, 29.78, 28.86, 28.84, 28.70, 28.63, 28.07, 28.05, 27.99, 27.88, 23.69, 23.64, 14.52, 14.49.
HRMS (*m/z*): $[M]^+$ calcd. for $C_{71}H_{115}N_6O_6$, 1147.8873; found, 1147.8870.

2-((*E*)-3-3,3-dimethyl-1-[3-(2-aminoethylcarbamoyl)propyl]-2,3-dihydro-1*H*-2-indolyliden-1-propenyl)-3,3-dimethyl-1-[3-(2-aminoethylcarbamoyl)propyl]-3*H*-indolium, triple trifluoroacetic acid salt (7a)

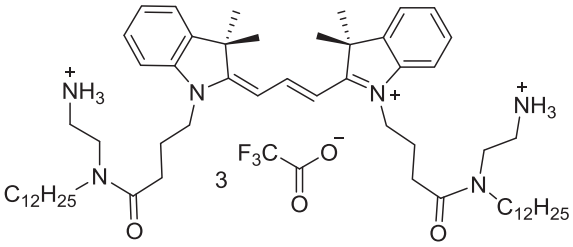

Compound **6a** (1 eq., 500 mg, 0.416 mmol) was dissolved in DCM (3 mL). TFA (100 eq., 3.18 mL, 41.6 mmol) was added dropwise and the reaction mixture was stirred at ambient temperature for 4 h. Solvent was removed under reduced pressure. To remove the remained traces of TFA, the residue was co-evaporated with methanol (3 × 50 mL). After removal of the Boc protecting group the crude product was used directly for the next step without further purification. Yield 426 mg (81%) as red viscous oil.

^{1}H NMR (400 MHz, Methanol-d_4) δ 8.42 (t, *J* = 13.3 Hz, 1H), 7.43 – 7.37 (m, 2H), 7.35 – 7.27 (m, 4H), 7.21 – 7.12 (m, 2H), 6.49 – 6.32 (m, 2H), 4.15 – 4.03 (m, 4H), 3.58 – 3.47 (m, 4H), 3.20 – 3.13 (m, 4H), 3.00 (t, *J* = 6.0 Hz, 4H), 2.54 – 2.44 (m, 4H), 2.06 – 1.96 (m, 4H), 1.64 (s, 12H), 1.43 – 1.32 (m, 4H), 1.19 – 1.08 (m, 36H), 0.74 (t, *J* = 6.6 Hz, 6H).
^{13}C NMR spectrum was difficult to measure due to the sample aggregation.
HRMS (*m/z*): $[M]^{3+}/3$ calcd. for $C_{59}H_{99}N_6O_2$, 307.9271; found, 307.9260.

2-((1*E*,3*E*)-3-3,3-dimethyl-1-[3-(2- aminoethylcarbamoyl)propyl]-2,3-dihydro-1*H*-2-indolyliden-1,3-pentadienyl)-3,3-dimethyl-1-[3-(2- aminoethylcarbamoyl)propyl]-3*H*-indolium, triple trifluoroacetic acid salt (7b)

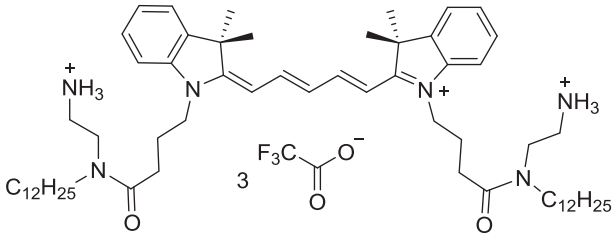

Compound **7b** was prepared using the same procedure as described above for **7a**. After removal of the Boc protecting group the crude product **7b** was used directly in the next step without further purification. Yield 415 mg (79%) as blue viscous oil.

^{1}H NMR (400 MHz, Methanol-d_4) δ 8.07 (t, *J* = 13.1 Hz, 2H), 7.29 (d, *J* = 7.6 Hz, 2H), 7.22 – 7.16 (m, 4H), 7.09 – 7.03 (m, 2H), 6.45 (t, *J* = 12.4 Hz, 1H), 6.19 (d, *J* = 13.7 Hz, 2H), 4.00 (t, *J* = 7.6 Hz, 4H), 3.45 (t, *J* = 6.0 Hz, 4H), 3.13 – 3.08 (m, 4H), 2.94 (t, *J* = 6.0 Hz, 4H), 2.40 (t, *J* = 6.7 Hz, 4H), 1.98 – 1.88 (m, 4H), 1.54 (s, 12H), 1.35 – 1.24 (m, 4H), 1.10 – 1.05 (m, 36H), 0.69 (t, *J* = 6.9 Hz, 6H).
^{13}C NMR spectrum was difficult to measure due to the sample aggregation.
HRMS (*m/z*): $[M]^{3+}/3$ calcd. for $C_{61}H_{101}N_6O_2$, 316.5990; found, 316.5998.

3,4,5-Tris(tetraethyleneoxy)benzoyl chloride (8)

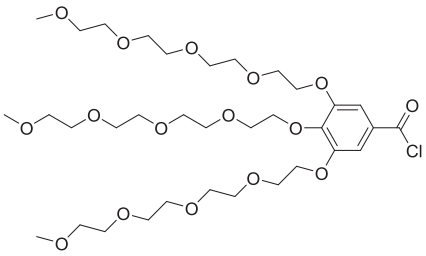

Acid chloride derivative **8** was prepared *in situ* according to a literature procedure from its corresponding acid and oxalyl chloride.[6]

Cy3A

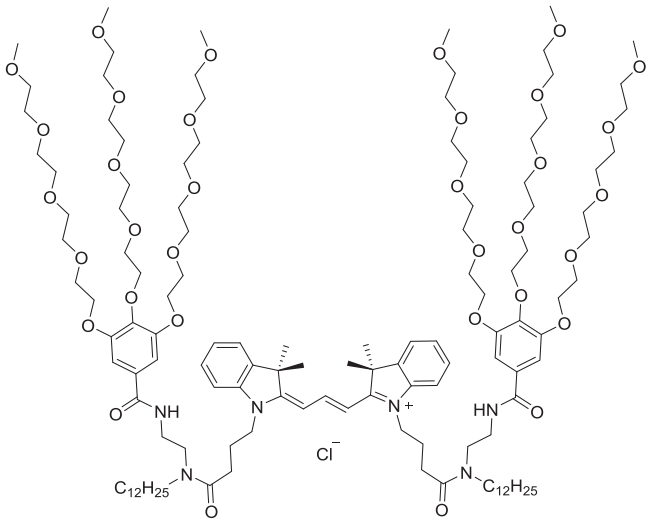

Aliphatic amine derivative of cyanine **7a** and triethyl amine (10 eq.) were dissolved in anhydrous DMF (1 mL), and the acid chloride (4 eq.) was added dropwise as a solution in anhydrous DMF at 0 °C using ice bath. After stirring at 0 °C for 2h, the reaction mixture was heated to 60 °C for another 2h until completion. After solvent evaporation in vacuum, the residue was redissolved in DCM (50 mL), washed with saturated brine solution (3 ×100 mL), dried over sodium sulphate, filtered, and the filtrate evaporated to dryness in vacuum. The crude product was purified by flash column chromatography (SiO_2, DCM/MeOH, 95:5 to 90:10), which furnished 10 mg (yield 20%) of **Cy3A** as a red oil.

^{1}H NMR (400 MHz, Methanol-d_4) δ 8.70 – 8.44 (m, 1H), 7.63 (d, *J* = 7.4 Hz, 2H), 7.56 – 7.44 (m, 4H), 7.40 (t, *J* = 7.3 Hz, 2H), 7.31 (s, 1H), 7.25 (s, 1H), 6.80 (s, 1H), 6.79 (s, 1H), 6.71 – 6.42 (m, 2H), 4.31 – 4.18 (m, 12H), 4.17 – 4.05 (m, 4H), 3.99 – 3.85 (m, 6H), 3.85 – 3.79 (m, 6H), 3.79 – 3.72 (m, 12H), 3.71 – 3.62 (m, 52H), 3.62 – 3.57 (m, 12H), 3.56 – 3.45 (m, 4H), 3.41 (s, 18H), 3.39 – 3.31 (m, 4H), 2.75 – 2.63 (m, 2H), 2.62 – 2.41 (m, 2H), 2.22 – 2.09 (m, 4H), 1.85 (s, 12H), 1.73 – 1.54 (m, 4H), 1.44 – 1.18 (m, 36H), 0.97 (t, *J* = 7.4 Hz, 6H).
^{13}C NMR spectrum was difficult to measure due to the sample aggregation.
HRMS ESI (*m/z*): $[M]^+$ calcd. for $C_{127}H_{213}N_6O_{34}$, 2367.5151, found 2367.5054.

Cy5A

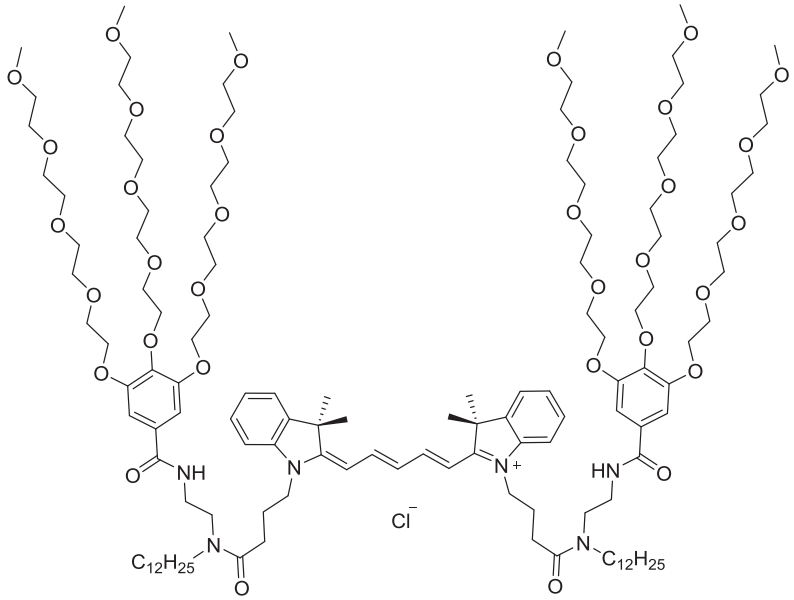

The compound prepared using the same procedure as described above for **Cy3A**. The crude product was purified by flash column chromatography (SiO_2, DCM/MeOH, 95:5 to 90:10). Yield 15 mg (18%) as blue oil.

^{1}H NMR (400 MHz, Methanol-d_4) δ 8.37 – 8.20 (m, 2H), 7.54 (d, *J* = 7.5 Hz, 2H), 7.45 (t, *J* = 7.7 Hz, 2H), 7.38 (d, *J* = 7.9 Hz, 2H), 7.34 – 7.30 (m, 2H), 7.29 (s, 1H), 7.28 (s, 1H), 7.23 (s, 1H), 7.22 (s, 1H), 6.72 – 6.52 (m, 1H), 6.38 (d, *J* = 13.5 Hz, 2H), 4.29 – 4.12 (m, 12H), 4.11 – 3.97 (m, 4H), 3.88 (t, *J* = 4.6 Hz, 4H), 3.83 (t, *J* = 4.7 Hz, 4H), 3.81 – 3.75 (m, 4H), 3.74 – 3.69 (m, 12H), 3.69 – 3.60 (m, 48H), 3.59 – 3.52 (m, 12H), 3.41 (t, *J* = 8.0 Hz, 4H), 3.37 (s, 18H), 3.36 – 3.33 (m, 8H), 2.79 – 2.67 (m, 2H), 2.66 – 2.56 (m, 2H), 2.18 – 2.02 (m, 4H), 1.77 (s, 12H), 1.69 – 1.55 (m, 4H), 1.45 – 1.24 (m, 36H), 0.98 – 0.88 (m, 6H).
^{13}C NMR spectrum was difficult to measure due to an aggregation of the sample.
HRMS ESI (*m/z*): $[M]^+$ calcd. for $C_{129}H_{215}N_6O_{34}$, 2393.5307; found, 2393.5314.

3.1.4 Synthesis of building blocks for polymerized micelles.

Synthesis of amphiphilic calixarene derivative (CX8TP)

5,11,17,23-Tetra(N,N-dimethyl-N-(propargyl)ammonium)methylene-25,26,27,28-tetraoctyloxycalix[4]arene tetrachloride.

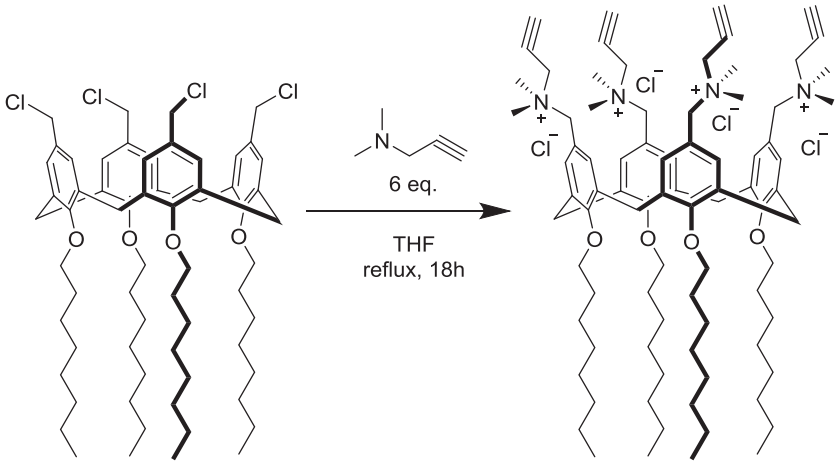

1 **CX8TP**

A solution of 3-dimethylamino-1-propyne (6 eq., 112 mg, 145 µL, 1.35 mmol) in THF (5 mL) was added dropwise to a solution of 5,11,17,23-tetrachloromethyl-25,26,27,28-tetraoctyloxycalix[4]arene[7] (1 eq., 240 mg, 0.225 mmol) in dry THF (10 mL) at r.t. Then the reaction mixture was refluxed for 18h. After cooling, the formed precipitate (calixarene **CX8TP**) was filtered off and washed with dry THF (10 mL) and dry diethyl ether (10 mL). The precipitate was dried under vacuum (0.05 mm Hg, 20 °C, 4 h) to give a desired product as a pale-yellow crystalline compound. Yield 239mg, 76%.

^{1}H NMR (400 MHz, Methanol-d_4) δ 7.07 (s, 8H), 4.58 (d, *J* = 13.3 Hz, 4H), 4.57 (s, 8H), 4.23 (s, 8H), 4.05 (t, *J* = 7.3 Hz, 8H), 3.68 (t, *J* = 2.3 Hz, 4H), 3.46 (d, *J* = 13.4 Hz, 4H), 3.11 (s, 24H), 2.05 (p, *J* = 7.3 Hz, 8H), 1.55 – 1.38 (m, 40H), 0.98 (t, *J* = 6.7 Hz, 12H).
^{13}C NMR (101 MHz, MeOD) δ 159.98, 137.12, 134.61, 122.50, 83.46, 76.95, 72.76, 68.35, 54.51, 50.26, 33.23, 31.71, 31.45, 31.19, 30.86, 27.66, 23.83, 14.49.
HRMS (ESI) *m/z*: $[M]^{4+}$/4 calcd for $C_{84}H_{128}N_4O_4^{4+}$, 314.2478; found, 314.2487; **HRMS ESI (*m/z*):** $[M+Cl]^{3+}$/3 calcd for $C_{84}H_{128}ClN_4O_4^{3+}$, 430.6536; found, 430.6538.

Synthesis of homobifunctional cyanine fluorescent crosslinkers(Cy3L and Cy5L)

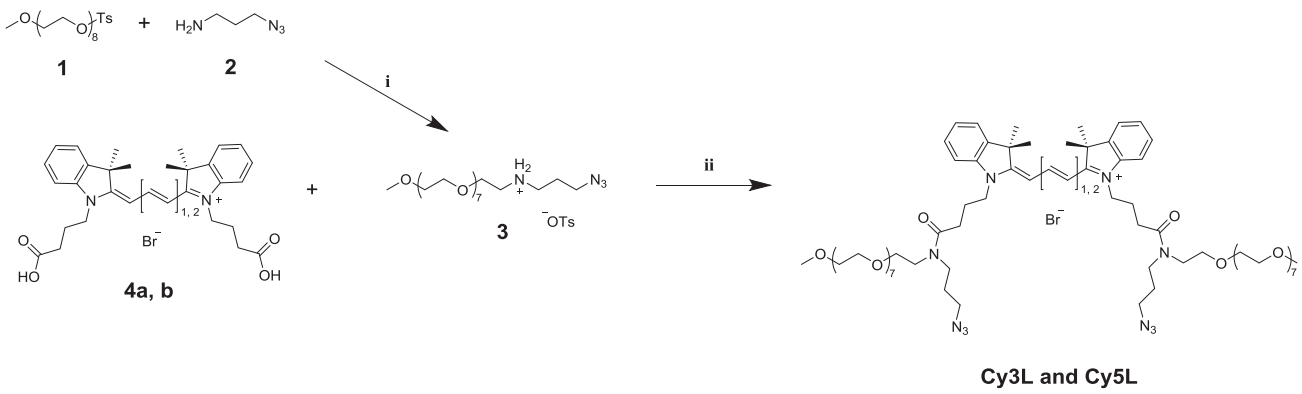

i) EtOH, reflux, 24h (75%); ii) HBTU, HOBt, DIPEA, DMF, r.t., 24h (74%).

Synthetic procedures for **1** (octaethylene glycol monomethyl ether tosylate)[8] and dicarboxyl derivatives (bisacids) of cyanines **4a, b** is described elsewhere.[9]

N-(3-azidopropyl)-2,5,8,11,14,17,20,23-octaoxapentacosan-25-aminium 4-methylbenzenesulfonate (3)

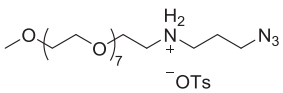

Octaethylene glycol monomethyl ether tosylate[8] (1 eq., 1.79 g, 3.33 mmol) and 3-azidopropyl-1-amine (3 eq., 1 g, 9.99 mmol) were dissolved in anhydrous ethanol (20 mL). Reaction mixture was stirred under reflux for 24 h. After cooling down to room temperature solvent was removed under reduced pressure. The product was purified by gradient column chromatography (SiO_2, DCM/MeOH, 95:5 to 90:10), which furnished 1.595 g (yield 75%) of a title compound **3**.

^{1}H NMR (400 MHz, Methanol-d_4) δ 7.76 (d, *J* = 8.0 Hz, 2H), 7.29 (d, *J* = 7.9 Hz, 2H), 3.79 (t, *J* = 5.1 Hz, 2H), 3.72 – 3.67 (m, 26H), 3.62 – 3.57 (m, 2H), 3.52 (t, *J* = 6.5 Hz, 2H), 3.41 (s, 3H), 3.24 (t, *J* = 5.1 Hz, 2H), 3.18 – 3.09 (m, 2H), 2.42 (s, 3H), 1.98 (p, *J* = 6.8 Hz, 2H).
^{13}C NMR (101 MHz, Methanol-d_4) δ 143.65, 141.63, 129.81, 126.95, 72.92, 71.59, 71.56, 71.54, 71.53, 71.52, 71.49, 71.42, 71.31, 71.25, 71.24, 71.08, 67.28, 59.09, 49.72, 48.73, 46.59, 27.08, 21.32.
HRMS ESI (m/z): $[M]^+$ calcd. for $C_{20}H_{43}N_4O_8$, 467.3075; found, 467.3083.

"Clickable" cyanine 3 cross-linker (Cy3L)

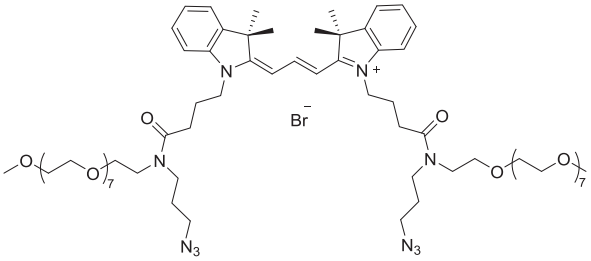

Cy3 bisacid **4a**[9] (1 eq., 100 mg, 0.2 mmol), HBTU (2.2 eq., 166 mg, 0.439 mmol), and HOBt (3 eq., 81 mg, 0.599 mmol) were placed in a reaction flask. Anhydrous DMF (3 mL) and DIPEA (10 eq., 330 µL, 2 mmol) were added via syringe. After stirring for 30 min, N-(3-azidopropyl)-2,5,8,11,14,17,20,23-octaoxapentacosan-25-aminium 4-methylbenzenesulfonate (1.9 eq., 242 mg, 0.38 mmol) was added dropwise. The reaction mixture was set to stir at r.t. for 24 h under argon atmosphere. Solvent was removed under reduced pressure. The residue was redissolved in 50 mL of DCM and washed with brine (3 × 100 mL) to remove traces of DMF, dried over sodium sulphate, filtered and the filtrate evaporated to dryness in vacuum. The product was purified by gradient column chromatography (SiO_2, DCM/MeOH, 98:2 to 95:5), which furnished 207 mg (yield 74%) of a title compound as a red viscous oil.

^{1}H NMR (400 MHz, Chloroform-*d*) δ 8.38 (t, *J* = 13.4 Hz, 1H), 7.62 – 7.51 (m, 2H), 7.42 (t, *J* = 7.5 Hz, 2H), 7.32 (d, *J* = 7.2 Hz, 2H), 7.22 (t, *J* = 7.5 Hz, 2H), 6.59 (dd, *J* = 13.5, 2.5 Hz, 2H), 4.14 – 4.03 (m, 4H), 3.67 – 3.55 (m, 60H), 3.54 – 3.46 (m, 8H), 3.44 – 3.38 (m, 2H), 3.35 (s, 6H), 3.32 (t, *J* = 6.7 Hz, 2H), 2.78 – 2.69 (m, 4H), 2.12 – 2.01 (m, 4H), 1.96 – 1.80 (m, 4H), 1.70 (s, 12H).
HRMS ESI (*m/z*): $[M+Na]^{2+}/2$ calcd. for 710.4217; found 710.4237. **HRMS ESI (*m/z*):** $[M+2Na]^{3+}/3$ calcd. for 481.2775; found 481.2780.

"Clickable" cyanine 5 cross-linker (Cy5L)

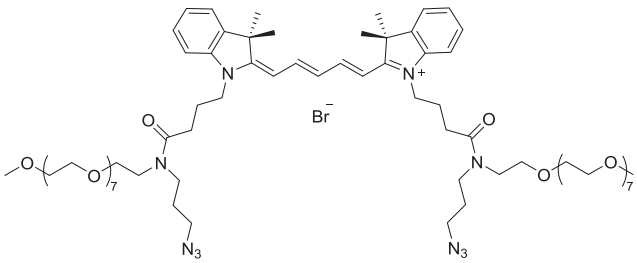

The compound **Cy5P** was synthesized by the same protocol as descibed above for the compound **Cy3P** starting from Cy5 bisacid **4b**[9]. The product was purified by gradient column chromatography (SiO_2, DCM/MeOH, 98:2 to 95:5), which yielded 229 mg (65%) of a title compound as blue viscous oil.

^{1}H NMR (400 MHz, Chloroform-*d*) δ 7.82 (t, *J* = 13.0 Hz, 2H), 7.40 – 7.33 (m, 4H), 7.31 (d, *J* = 7.4 Hz, 2H), 7.22 – 7.15 (m, 2H), 6.90 – 6.74 (m, 1H), 6.29 (d, *J* = 13.5 Hz, 2H), 4.09 – 4.00 (m, 4H), 3.66 – 3.57 (m, 60H), 3.55 – 3.50 (m, 8H), 3.40 – 3.36 (m, 2H), 3.35 (s, 6H), 3.33 – 3.29 (m, 2H), 2.69 – 2.58 (m, 4H), 2.11 – 2.01 (m, 4H), 1.89 – 1.80 (m, 4H), 1.66 (s, 12H).
HRMS ESI (*m/z*): $[M]^+$ calcd. for $C_{73}H_{119}N_{10}O_{18}$, 1423.8698; found, 1423.8705.

3.2 Preparation of fluorescent nanoparticles

3.2.1 Preparation of lipid nanodroplets

Nano-emulsions were prepared by spontaneous nano-emulsification. Briefly, the fluorescent dyes were solubilised in Labrafac® CC. Then, Solutol® HS 15 was added and the mixture was homogenized under magnetic stirring at 90 °C. Nano-emulsions were formed by adding ultrapure water. Two sizes of nanodroplets were prepared by varying the proportions between the different components.

3.2.2 Preparation of ion-associated NPs from rhodamine B alkyl esters

The rhodamine B derivative was dissolved at 1 mM in DMSO. The concentration was measured by photometry using the extinction coefficient for all rhodamine B derivatives 125000 M^{-1} cm^{-1} in methanol.[10] To prepare 1 µM of nanoparticle solution, 2 µL of 1 mM rhodamine B derivative stock solution was added quickly under stirring (shaking) using a micropipette to 2 mL of Milli-Q® water (Millipore). Then to the obtained solution a 10-fold excess of the corresponding borate solution (20 µL of 1 mM stock solution) was added quickly under stirring using a micropipette.

For the DLS measurements of nanoparticle suspension 5 µM dye concentration was used to obtain sufficient signal. To this end, 10 µL of 1 mM rhodamine B derivative stock solution was added quickly under stirring using a micropipette to a 1.9 mL of Milli-Q® water (Millipore). Then to the obtained solution 10-fold excess of the corresponding borate solution (100 µL of 1 mM stock solution) was added quickly under stirring using a micropipette. Zeta potential measurements were performed using 20 µM dye concentration.

For the DLS and AFM measurements, to remove possible aggregates the obtained solution of prepared nanoparticles was additionally filtered through a 0.1 µm PVDF NS "Ultrafree®-CL" centrifugal filter unit (Merck Millipore).

3.2.3 Counterion-promoted micellization as a synthesis of micellar NPs

The cyanine (Cy3t, either Cy5t) derivative was dissolved at 1 mM in DMSO. The concentration was measured by photometry using the extinction coefficient for Cy3 and Cy5 derivatives 150000 and 250000 M^{-1} cm^{-1} in methanol, respectively.[10] To prepare 1 µM of nanoparticle (nanomicelle) solution, 2 µL of 1 mM cyanine (Cy3t, either Cy5t) derivative stock solution was added quickly under stirring (shaking) using a micropipette to 1.98 mL of Milli-Q® water (Millipore). Then, to the obtained solution a 10-fold excess of the corresponding borate solution (20 µL of 1 mM stock solution) was added quickly under stirring using a micropipette.

For the DLS measurements of nanoparticle (nanomicelle) suspension 2 µM dye concentration was used to obtain sufficient signal. To this end, 4 µL of 1 mM cyanine (Cy3t, either Cy5t) derivative stock solution was added quickly under stirring using a micropipette to a 1.96 mL of Milli-Q® water (Millipore). Then to the obtained solution 10-fold excess of the corresponding borate solution (40 µL of 1 mM stock solution) was added quickly under stirring using a micropipette. Zeta potential measurements were performed using 5 µM dye concentration.

For the DLS and AFM measurements, to remove possible aggregates the obtained solution of prepared nanoparticles was additionally filtered through a 0.1 µm PVDF NS "Ultrafree®-CL" centrifugal filter unit (Merck Millipore).

3.2.4 Preparation of shell-cross-linked micelles

The cyanine (Cy3L, either Cy5L) derivative was dissolved at 10 mM in Milli-Q® water. The concentration was measured by photometry using the extinction coefficient for Cy3 and Cy5 derivatives 150 000 and 250 000 M −1 cm −1 in methanol, respectively. Calixarene derivative was dissolved at 10 mM in Milli-Q® water. Copper sulfate and sodium ascorbate were dissolved in water at 100mM.

The CX8TP derivative (15 µL of 10 mM, 150 µM final) was injected quickly to a solution of sodium sulfate (919µL, 75mM final) in 1.5mL eppendorf tube under stirring (shaking) using a micropipette, than the solution was vortexed for 30 s. To the obtained suspension of micellar NPs copper sulfate solution (12 µL of 100mM, 1.2 mM final) and sodium ascorbate (24 µL of 100 mM, 2.4mM final). After vortexing for another 30 s, the formation of Cu(I) precipitate (stable colloid of microparticles) was observed. The solution of fluorescent homobifunctional crosslinker (Cy3L, either Cy5L) was added last one via quick injection using a micropipette (30 µL of 10 mM, 300 µM final) and the obtained mixture was vortexed for another 30 s. The reaction mixture was stirred under gentle shaking (Thermomixer comfort, Eppendorf, 900 rpm) at 30 °C for 24 h. After completion, when precipitate of Cu(I) microparticles disappeared and the solution became clear, the reaction mixture was diluted two times using 75mM solution of sodium sulfate and dialyzed against 1000x volume excess of Milli-Q® water (2000mL) using dialysis tubing cellulose membrane (D9652 Sigma, typical molecular weight cut-off = 14,000 Da). All dialysis systems were covered by aluminum foil to protect fluorescent micellar NPs against sunlight. For the DLS and AFM measurements of cross-linked particles, to remove possible aggregates the obtained solution of prepared nanoparticles was filtered through a 0.1 µm PVDF NS "Ultrafree®-CL" centrifugal filter unit (Merck Millipore). In the case of FRET NPs, the same synthetic protocol was followed, but in this case Cy3L and Cy5L were taken in

different ratios, 10/1, 25/1 and 50/1, while keeping the total concentration of cross-linker 300 µM. Then the samples were dialyzed as described above.

3.3 Physical measurements

3.3.1 Optical spectroscopy

Absorption spectra were recorded on a double-beam spectrophotometer Cary 4000 (Varian). The absorbance is characterized by:

$$A = \frac{I_0}{I}$$

where I_0 and I are the incident and transmitted intensities, respectively.

A correction for the cuvettes was also done, as the two cuvettes are never perfectly identical. To this end, the baseline of the instrument is first recordered (with both cuvettes filled with the same solvent). Then, the aliquot of the dye stock solution was added into the solvent of the sample cuvette and the true absorption spectrum is recorded. The solvents for the optical measuments were of spectroscopic grade.

Fluorescence measurements were performed on a spectrofluorometer FluoroMax 4.0 or Fluorolog (Jobin Yvon, Horiba) equipped with a thermostated cuvette holder. Both spectrofluorometers are a photon counting devices with a linear response in the range of measurements (< 3 Mcps). The source of light is a xenon lamp of 450 and 150 W for the Fluorolog and FluoroMax, respectively. While fluorescence emission and excitation spectra recording the correction of the signal on the lamp intensity was done. Fluorescence emission spectra were systematically recorded at 20°C using the following excitation wavelengths: 520nm for Rhodamine B and Cyanine3 (Cy3) derivatives; 605 nm for the Cyanine5 (Cy5) derivatives. The wavelength-dependent correction function for the photomultiplier response and for the excitation-emission monochromators is defined by the device manufacturer and already included into the corresponding software of Fluorolog and FluoroMax 4.0.

Fluorescence quantum yields for the Rhodamine B and Cyanine3 (Cy3) derivatives were calculated using rhodamine B in water (Φ= 31%)[11] with an absorbance of 0.1 at 520 nm as a reference; and for the Cyanine5 (Cy5) derivatives using DID (1,1'-Dioctadecyl-3,3,3',3'-Tetramethylindodicarbocyanine Perchlorate) in methanol (Φ= 33%)[12] with an absorbance of 0.1 at 605 nm as a reference. For the flavone (F888) and Nile Red (NR668) derivatives encapsulated into the core of the lipid nanodroplet we have used 4'-dimethylamino-3-hydroxyflavone in ethanol (Φ= 29%),[13] and Nile Red in ethanol

(Φ= 52%),[14] as reference, respectively. The following equation was used for calculation of fluorescence quantum yield (Φ):

$$\Phi_x = \Phi_r \frac{I_x}{I_r}\frac{A_r}{A_x}\frac{n_x^2}{n_r^2}$$

where Φ_x is the quantum yield of the dye; Φ_r is the known quantum yield of the dye used as a reference; A_x and A_r are respectively the absorbance of the dye and the reference at an appropriate excitation wavelength; I_x and I_r are their respective fluorescence intensities as measured by integration of the surface under the emission spectrum corrected for the photomultiplier response; n_x and n_r are the refractive indexes of solvents used for the dye and reference dye, respectively.

Hydrodynamic diameter and zeta-potential measurements were performed on a Zetasizer® Nano ZSP (Malvern Instruments S.A.) with a laser source at 633 nm. The detector was set to measure scattered light at 173°.

3.3.2 Atomic force microscopy (AFM) measurements

AFM measurements were performed using a Solver-Pro-M (NT-MDT) instrument. The measurements were performed in the liquid phase. Cantilevers were NSG03 (NT-MDT) with a tip curvature radius of 10 nm. To deposit NPs on the mica surface, 100 µL of 10–100 mM calcium chloride solution was first incubated for 30 min. Then, the solution was removed with a filter paper and 100 µL of an undiluted suspension of NPs was deposited on the mica surface. After 30 min, the solution was removed using a filter paper and then replaced with 100 µL of 10–100 mM solution of calcium chloride. The obtained sample was imaged in the liquid phase, using the tapping mode (~37 kHz).

3.3.3 Fluorescence correlation spectroscopy (FCS) and data analysis

FCS measurements were performed on a two-photon platform including an Olympus IX70 inverted microscope, as described previously.[15] Two-photon excitation, which was provided using an InSight DeepSee laser (Spectra Physics), was set at 830 nm and 760 nm (1–5 mW laser output power) for the Rhodamine B and Cyanine3 (Cy3) derivatives, respectively. The measurements were carried out in a 96-well plate, using a 200 µL volume per well. The focal spot was set about 20 µm above the cover-slip. The normalized autocorrelation function, $G(\tau)$ was calculated online by using an ALV-5000E correlator (ALV, Germany) from the fluorescence fluctuations, $\delta F(t)$, by $G(\tau) = \langle \delta F(t)\delta F(t+\tau)\rangle / \langle F(t)\rangle^2$ where $\langle F(t)\rangle$ is the mean fluorescence signal, and τ is the lag time. Assuming that fluorescent NPs diffuse freely in a Gaussian excitation volume, the correlation function, $G(\tau)$, calculated from the fluorescence fluctuations was fitted according to Thompson:[16]

$$G(\tau) = \frac{1}{N}\left(1 + \frac{\tau}{\tau_d}\right)^{-1}\left(1 + \frac{1}{S^2}\frac{\tau}{\tau_d}\right)^{-1/2}$$

where τ_d is the diffusion time, N is the mean number of fluorescent species within the two-photon excitation volume, and S is the ratio between the axial and lateral radii of the excitation volume. The excitation volume is about 0.34 fL and S is about 3 to 4. Typical data recording time was 5 min, using freshly prepared NPs without further dilution. The measurements were done with respect to a reference 5(6)-carboxytetramethylrhodamine (TMR, from Sigma-Aldrich) in water. The hydrodynamic diameter, *d*, of NPs was calculated as: $d_{NPs} = \tau_{d(NPs)} / \tau_{d(TMR)}) \times d_{TMR}$, where d_{TMR} is a hydrodynamic diameter of TMR (1.0 nm). The concentration of NPs was calculated from the number of species by: $C_{NPs} = N_{NPs}/N_{TMR} \times C_{TMR}$, using a TMR concentration of 50 nM.

3.3.4 Single-particle imaging

3 g of poly(vinyl alcohol) (M_w 89 000–98 000, 99+%) in 10 mL of degassed Milli-Q® water (Millipore) was stirred at 90–100 °C for two hours to obtain a homogeneous 30 wt% PVA gel. Then 300 µL of the PVA gel were added into a cell of the Lab-Tek® plate and immediately after 50 µL of particle solution were injected into the PVA gel and mixed using the tip of the micropipette. Then the Lab-Tek® plate was kept for 5 h in a desiccator under vacuum. Quantum dots (QDot-585 streptavidin conjugate, Life Technologies) and FluoroSpheres® 535/575 (diameter 0.028 µm, carboxylate modified, Invitrogen) at ~6 pM concentration were immobilized and imaged in the same way. Single particle measurements were performed in the TIRF (Total Internal Reflection Fluorescence) mode on a home-made wide-field setup based on an Olympus IX-71 microscope with an oil immersion objective (NA = 1.49, 100×). A DPPS (Cobolt) continuous wave (CW) laser emitting at 532 nm was used for excitation. The laser intensity was set to 1 W cm^{-2} using a polarizer and a half-wave plate
(532 nm). The fluorescence signal was recorded with an EMCCD (ImagEM Hamamatsu). The presented images were an average of the first 30 frames recorded with an acquisition time of 30.67 ms per frame.

3.3.5 Cellular studies

HeLa cells (ATCC® CCL-2) were grown in Dulbecco's modified Eagle's medium (DMEM, Gibco-Invitrogen), supplemented with 10% fetal bovine serum (FBS, Lonza) and 1% antibiotic solution (penicillin–streptomycin, Gibco-Invitrogen) at 37 °C under a humidified atmosphere containing 5% CO_2. Cells were seeded onto a chambered coverglass (IBiDi) at a density of 5×10^4 cells per well 24 h before the microscopy measurement. For imaging, the culture medium was removed and the attached cells were washed with Opti-MEM (Gibco-Invitrogen).

Then, a freshly prepared solution of NPs (corresponding to ~50 nM dye) in Opti-MEM was added to the cells and incubated for different time periods. Cell membrane staining with wheat germ agglutinin-Alexa488 was done for 10 min at rt before the measurements. Fluorescence images were taken on a Leica TSC SPE confocal microscope. The microscope settings were: a 561 nm laser source with a 567–700 nm detection range for imaging counterion-assembled rhodamine NPs and 488 nm excitation with a 503–550 nm emission range for imaging the plasma membrane marker WGA-AlexaFluor®488 (green) or MitoTracker® Green (Life Technologies).

3.3.6 Other software

The calculations were performed using Hyperchem 8.0. The starting geometry of borate ions was subsequently optimized using a Polak–Ribière algorithm (conjugate gradient) under vacuum with a RMS gradient of 0.1 kcal (A mol)$^{-1}$. The resulting structures of counter-ions were relatively similar to each other and showed common features such as a symmetric arrangement.

The names of chemical compounds according to the IUPAC guidelines were generated using ACD Labs software package or ChemOffice suite 15.0 (2015).

References

(1) Ozturk, T.; Klymchenko, A. S.; Capan, A.; Oncul, S.; Cikrikci, S.; Taskiran, S.; Tasan, B.; Kaynak, F. B.; Ozbey, S.; Demchenko, A. P. *Tetrahedron* **2007**, *63*, 10290.

(2) Kucherak, O. A.; Oncul, S.; Darwich, Z.; Yushchenko, D. A.; Arntz, Y.; Didier, P.; Mely, Y.; Klymchenko, A. S. *Journal of the American Chemical Society* **2010**, *132*, 4907.

(3) Demmig, S.; Langhals, H. *Chemische Berichte-Recueil* **1988**, *121*, 225.

(4) Langhals, H.; Demmig, S.; Potrawa, T. *Journal Fur Praktische Chemie* **1991**, *333*, 733.

(5) Pisoni, D. S.; Todeschini, L.; Borges, A. C. A.; Petzhold, C. L.; Rodembusch, F. S.; Campo, L. F. *Journal of Organic Chemistry* **2014**, *79*, 5511.

(6) Brunsveld, L.; Zhang, H.; Glasbeek, M.; Vekemans, J.; Meijer, E. W. *Journal of the American Chemical Society* **2000**, *122*, 6175.

(7) Rodik, R. V.; Klymchenko, A. S.; Jain, N.; Miroshnichenko, S. I.; Richert, L.; Kalchenko, V. I.; Mely, Y. *Chemistry-a European Journal* **2011**, *17*, 5526.

(8) Senler, S.; Cui, L.; Broomes, A. M.; Smith, E. L.; Wilson, J. N.; Kaifer, A. E. *Journal of Physical Organic Chemistry* **2012**, *25*, 592.

(9) Shulov, I. *Chemical Science* **2016**.

(10) Haugland, R. P., Spence, M. T. Z., Johnson, I. D., and Basey, A. *The Handbook: A Guide to Fluorescent Probes and Labeling Technologies,10th ed.*; Molecular Probes: Eugene, OR, 2005.

(11) Magde, D.; Rojas, G. E.; Seybold, P. G. *Photochemistry and Photobiology* **1999**, *70*, 737.

(12) Texier, I.; Goutayer, M.; Da Silva, A.; Guyon, L.; Djaker, N.; Josserand, V.; Neumann, E.; Bibette, J.; Vinet, F. *Journal of Biomedical Optics* **2009**, *14*, 054005.

(13) Ormson, S. M.; Brown, R. G.; Vollmer, F.; Rettig, W. *Journal of Photochemistry and Photobiology a-Chemistry* **1994**, *81*, 65.

(14) La Deda, M.; Ghedini, M.; Aiello, I.; Pugliese, T.; Barigelletti, F.; Accorsi, G. *Journal of Organometallic Chemistry* **2005**, *690*, 857.

(15) Klymchenko, A. S.; Roger, E.; Anton, N.; Anton, H.; Shulov, I.; Vermot, J.; Mely, Y.; Vandamme, T. F. *RSC Adv.* **2012**, *2*, 11876.

(16) Thompson, N. L.; Plenum Press: New York, 1991; Vol. 1.

(17) Reisch, A.; Didier, P.; Richert, L.; Oncul, S.; Arntz, Y.; Mely, Y.; Klymchenko, A. S. *Nature Communications* **2014**, *5*.

Publication list of I. Shulov

Articles in peer-reviewed journals:

1. Highly lipophilic fluorescent dyes in nano-emulsions: towards bright non-leaking nano-droplets
Andrey S. Klymchenko, Emilie Roger, Nicolas Anton, Halina Anton, Ievgen Shulov, Julien Vermot, Yves Mely and Thierry F. Vandamme, *RSC Advances*, 2012, 2, 11876-11886.

2. Tuning the color and photostability of perylene diimides inside polymer nanoparticles: towards biodegradable substitutes of quantum dots
Kateryna Trofymchuk, Andreas Reisch, Ievgen Shulov, Yves Mély, Andrey S. Klymchenko, *Nanoscale*, 2014, 6, 12934-12942

3. Squaraine as a bright, stable and environment-sensitive far-red label for receptor-specific cellular imaging
I. A. Karpenko, A. S. Klymchenko, S. Gioria, R. Kreder, I. Shulov, P. Villa, Y. Mély, M. Hibert and D. Bonnet, *Chemical Communications*, 2015, 51, 2960-2963

4. Fluorinated counterion-enhanced emission of rhodamine aggregates: ultrabright nanoparticles for bioimaging and light-harvesting
Shulov I., Oncul S., Reisch A., Arntz Y., Collot M., Mely Y., Klymchenko A.S., *Nanoscale*, 2015, 7, 18198-18210.

5. Non-coordinating anions assemble cyanine amphiphiles into ultra-small fluorescent nanoparticles
Ievgen Shulov, Youri Arntz, Yves Mély, Vasyl G. Pivovarenko and Andrey S. Klymchenko (in preparation).

6. Shell-cross-linked calixarene micelles with cyanine corona: protein-sized ultrabright fluorogenic nanoparticles
Ievgen, Shulov, Roman V. Rodik, Youri Arntz, Andreas Reisch, Vitaly I. Kalchenko and Andrey S. Klymchenko (in preparation).

Conference presentations:

1. Ievgen Shulov, Youri Arntz, Vasyl G. Pivovarenko, Yves Mély, Andrey S. Klymchenko,
Highly fluorescent micellar nanoparticles assembled from new Cy3- and Cy5-based amphiphiles (poster)
EMBO-EMBL Symposium : Seeing is Believing - Imaging the Processes of Life – 3 - 6th October 2013, Heidelberg, Germany

2. Ievgen Shulov, Youri Arntz, Vasyl G. Pivovarenko, Yves Mély, Andrey S. Klymchenko,
Highly fluorescent micellar nanoparticles assembled from new Cy3- and Cy5-based amphiphiles (poster)
13th Conference on Methods and Applications of Fluorescence Spectroscopy, Imaging and Probes – 8 – 11th September 2013, Genoa, Italy

3. Ievgen Shulov, Youri Arntz, Vasyl G. Pivovarenko, Yves Mély, Andrey S. Klymchenko,
Highly fluorescent micellar nanoparticles assembled from new Cy3- and Cy5-based amphiphiles (oral presentation)
50ème Semaine d'Etudes de Chimie Organique – 26 – 2nd Juin 2013, Saint-Trojan-les-Bains, France

4. ERC Grantees Conference 2012, Frontier Research in Chemistry – 22 – 24th November 2012, Strasbourg, France (Participation)

5. 12th Conference on Methods and Applications of Fluorescence Spectroscopy, Imaging and Probes – 11 - 14th September 2011, Strasbourg, France (Participation)

Résumé de la thèse en Français

Introduction

Les techniques basées sur les phénomènes de fluorescence sont très puissantes pour l'étude des processus biologiques. Les nouveaux développements et applications de ces techniques nécessitent le développement d'*un nouveau type* de sondes fluorescentes en regard à celles déjà existantes. Il s'agit d'obtenir une luminosité, une photostabilité et une biocompatibilité supérieures. En effet, les fluorophores actuellement utilisés en microscopie de fluorescence présentent des limitations pour les propriétés citées précédemment.

Les nano-cristaux semi-conducteurs (*quantum-dots*), en particulier, permettent de surmonter une partie de ces inconvénients en offrant une brillance importante et une stabilité dans le temps. Ces nano-cristaux sont des outils particulièrement prometteurs pour les domaines émergents de l'imagerie biologique et biomédicale. Cependant, leur application dans le cadre d'expériences *in vivo* se heurte à un inconvénient majeur : ils sont souvent composés d'éléments toxiques et ne sont pas biodégradables. De plus leur taille, incluant la couche externe (*shell*) organique est relativement grande (de l'ordre de plusieurs dizaines de nm) et leur émission présente un phénomène de clignotement. Ces inconvénients, qui contrebalancent les qualités de ces sondes, limitent leurs applications en biologie et en médecine.

Dans le cadre de ma thèse, j'ai travaillé sur le développement de nouveaux types de nanoparticules organiques fluorescentes (NOFs), caractérisés par une luminosité élevée (comparable ou meilleure que les *quantum-dots)* ainsi qu'une taille très petite (comparable ou inférieure aux *quantum-dots)*, apparaissant ainsi comme une bonne alternative aux *quantum-dots*. Ces nanoparticules sont entièrement biodégradables, car elles sont constituées de matériaux organiques non toxiques et peuvent remédier les problèmes de biocompatibilité et de biodégradabilité décrits ci-dessus. Ce sujet de recherche est très attrayant, car ce nouveau type de nanoparticules, comme outils moléculaires pour la bio-imagerie, apparaît très prometteur. Pour atteindre ces objectifs, plusieurs stratégies chimiques différentes ont été mises en œuvre.

Résultats et discussion

Le but de ce travail était de synthétiser, caractériser et appliquer ces nouveaux types de nanoparticules organiques fluorescentes (NOFs) dans le cadre d'études *in vitro* et *in vivo,* qui représentent le concept d'un système « intelligent » présentant une grande brillance avec une concentration élevée de fluorophores dans un espace confiné.

1. Les nano-gouttelettes lipidiques fluorescentes.

L'introduction de molécules fluorescentes dans des nano-gouttelettes composées de lipides biodégradables est relativement aisée. Néanmoins, pour des concentrations élevées nécessaires pour obtenir une grande brillance, les fluorophores s'auto-agrègent, ce qui induit une auto-inhibition qui diminue fortement la fluorescence (*quenching*).

Dans une première approche, nous avons réussi à encapsuler les colorants fluorescents dans le cœur de particules lipidiques tout en préservant une brillance importante. En effet, nous sommes parvenu à concevoir des dérivés fluorescents hautement lipophiles dérivés de 3-alkoxyflavones et de colorants de type Rouge Nil modifiés (Fig. 1) qui ont été encapsulés dans le noyau d'huile d'une nano-émulsion extrêmement stable, avec des concentrations de colorant exceptionnellement élevées sans auto-extinction ni phénomène de relargage dans les milieux biologiques. En dépit de cette importante concentration en colorants, les nano-gouttelettes gardent une fluorescence avec un bon rendement quantique et donc une forte luminosité. Ces molécules de fluorophores lipophiles possèdent des chaînes alkyles hydrophobes, contribuant à l'efficacité d'encapsulation supérieure et dont l'encombrement stérique, permet de prévenir l'auto-extinction de fluorescence par π-π *stacking.*

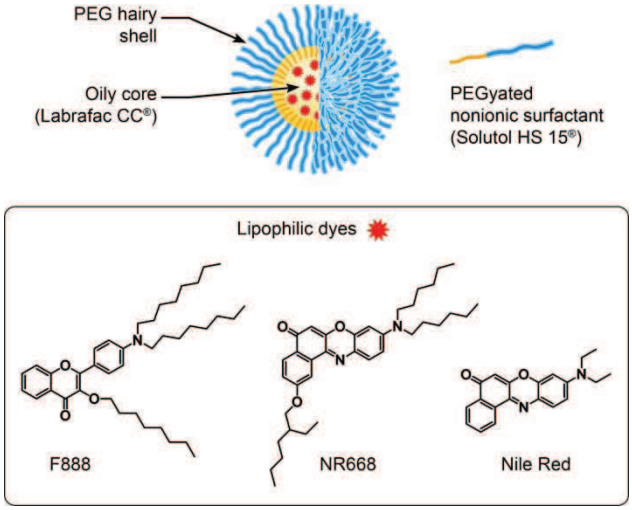

Fig. 1 Structures des colorants préparés NR668, F888 et Rouge Nil non modifié.

En outre, l'encapsulation simultanée de deux colorants à des concentrations élevées dans une même nano-gouttelette nous a permis d'étudier les propriétés de relargage de ces molécules. Des études par spectroscopie de corrélation de fluorescence (FCS) et FRET ont démontré que la fuite du nouveau dérivé du Rouge Nil (NR668) dans un milieu contenant du sérum est très lente, alors que le Rouge Nil non modifié, utilisé comme référence dans nos expériences, fuit immédiatement (Fig. 2). Cette forte différence de relargage entre les colorants Rouge Nil et Rouge Nil modifié a été confirmée par des études cellulaires *in vitro* ainsi qu'*in vivo* par imagerie d'angiographie, le modèle utilisé étant le

poisson zèbre (*zebrafish*). Dans ces expériences, les nano-gouttelettes chargées avec le Rouge Nil modifié sont restées stables et chargées dans la circulation sanguine, alors que le Rouge Nil non modifié fuit rapidement et se distribue dans le corps de l'animal. Cette étude montre que notre concept permet de satisfaire l'objectif recherché : l'obtention de nano-gouttelettes brillantes et sans relargage du colorant encapsulé, ce qui permet d'entrevoir une application prometteuse comme nouveaux agents de contraste optique, efficaces et stables *in vitro* et *in vivo*. Ce travail fait l'objet d'une publication dans la revue RSC Advances[1].

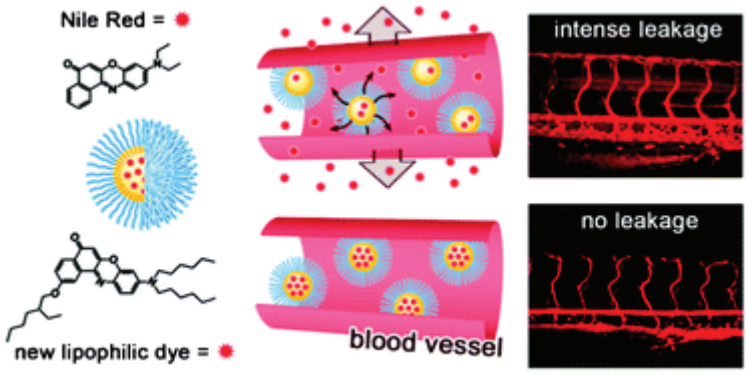

Fig. 2 Comportement de deux colorants à base de Rouge Nil dans le flux sanguin du poisson zèbre par imagerie *in vivo.*

2. Les nanoparticules fluorescentes de dérivés de la rhodamine B assemblés par contre-ion hydrophobe fluoré.

Nous avons commencé cette étude de nanoprécipitation de dérivé lipophile de la rhodamine B possédant un résidu alkyle d'octadecyl ester dans l'eau. Cependant, suite à l'agrégation des noyaux aromatiques du chromophore par *stacking* π- π, nous avons observé une perte totale de fluorescence. Pour résoudre ce problème, nous avons cette fois-ci utilisé un contre-ion hydrophobe fluoré fortement stérique, ce qui a permis d'éloigner les fluorophores et ainsi de diminuer fortement leur auto-agrégation et de ce fait lever l'auto-inhibition de fluorescence (*quenching*). A cet effet, nous avons préparé les NOFs par nanoprécipitation de ce dérivé lipophile de la rhodamine B par contre-ion hydrophobe fluoré de tétraphényleborate en milieu aqueux (Fig. 3)

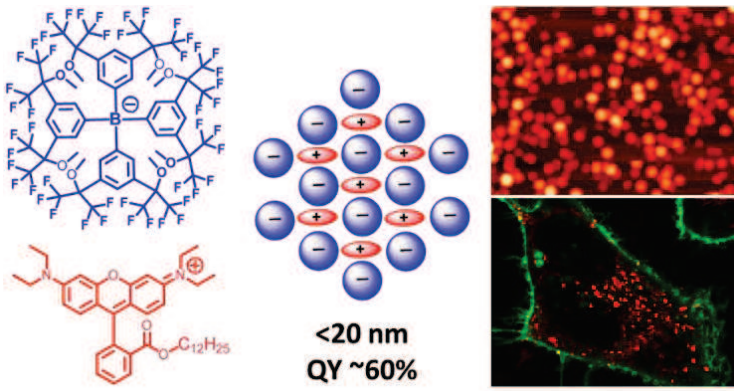

Fig. 3 Structure d'un sel composé d'un dérivé de la rhodamine B anionique lipophile et d'un contre-ion cationique hydrophobe fluoré à base de tétraphénylborate, situé à l'intérieur de la nanoparticule fluorescente. Etudes par AFM et imagerie confocale du processus d'internalisation des nanoparticules obtenues

Pour développer ce type de particules nous avons synthétisé des dérivés de rhodamine B portant des chaînes alkyle de longueur différente. Concernant les contre-ions hydrophobes, nous avons sélectionné une famille de contre-ions hydrophobes fluorés basée sur le tétraphénylborate avec des niveaux de fluoration variés. Nous émettons l'hypothèse que le niveau de fluoration pourrait influencer l'organisation des fluorophores dans les nanoparticules et ainsi améliorer leurs propriétés de fluorescence. Les nanoparticules ont été obtenues en mélangeant des solutions aqueuses des dérivés de rhodamine B avec les contre-ions, ce qui provoque l'association d'ions sous forme de NOFs. La formation des NOFs a été étudiée par diffusion dynamique de la lumière (DLS) et par microscopie à force atomique (AFM). Pour des dérivés de rhodamine B portant des chaînes alkylées plus longues, nous avons ainsi obtenu des nanoparticules relativement petites, entre 10-30 nm en diamètre selon le contre-ion utilisé, qui possèdent une luminosité de fluorescence supérieure. Les propriétés spectroscopiques de ces nanoparticules ont été caractérisées en utilisant diverses techniques de fluorescence (spectroscopie de fluorescence classique, microscopie de molécules uniques, et spectroscopie de corrélation de fluorescence (FCS). Ces études nous ont permis de conclure que les caractéristiques photophysiques sont dépendantes du nombre d'atomes de fluor dans la structure du contre-ion utilisé. En particulier, cette augmentation de la proportion d'atomes de fluor améliore considérablement les caractéristiques de fluorescence de ces particules: augmentation de luminosité et de photostabilité et rétrécissement de la bande d'émission. Il semble que les contre-ions hautement fluorés diminuent la formation d'agrégats de la rhodamine par stacking π-π à des concentrations élevées (*H-aggregates*).

Les particules ainsi obtenues peuvent contenir jusqu'à 400 fluorophores et sont 40 fois plus brillantes que des nanocristaux semi-conducteurs (quantum-dots), avec comme référence QD585. Les expériences menées par spectroscopie de corrélation de fluorescence (FCS) confirment la petite taille

de 20 nm et une luminosité >300 fois supérieure par rapport à la référence rhodamine (TMR). De manière remarquable, les nanoparticules formées avec le contre-ion tétra(perfluorophényl)-borate montrent un phénomène d'alternance photo-induite entre un état lumineux et un état noir. Cette alternance peut être utilisée en imagerie super-résolutive (STORM), permettant ainsi de distinguer des particules à des distances inférieures à 100 nm, démontrant ainsi une excellente résolution spatiale. Ce comportement en émission est dû à une migration ultra-rapide d'excitons entre tous les fluorophores à l'intérieur de la nanoparticule, qui induit la possibilité de *light-harvesting* (récolte de lumière), ce qui a été étudié par les spectres d'excitation en encapsulant un accepteur d'énergie FRET à base d'un colorant cyanine Cy5. Nous avons observé 50% d'efficacité de FRET pour les particules ayant 400 donneurs et un accepteur unique. Ce phénomène n'avait jamais été décrit auparavant. Enfin, les particules obtenues ont été incubées avec des cellules HeLa et étudiées par microscopie de fluorescence confocale. Nous avons constaté que ces particules s'internalisent rapidement dans ces cellules et présentent un excellent rapport signal/bruit en imagerie de fluorescence. De manière remarquable, la stabilité des particules en milieu intracellulaire est la plus élevée pour les contre-ions hautement fluorés. Ces résultats font l'objet d'un autre article soumis[2].

3. Les micelles fluorescentes assemblées par contre-ion hydrophobe.

Une troisième approche pour produire des NOFs consiste en l'auto-assemblage de molécules amphiphiles fluorescentes, constituées de fragments hydrophobes et hydrophiles, pour former des nanostructures monodisperses en taille et hautement organisées présentant différentes morphologies[3], telles que des micelles sphériques (généralement d'un diamètre de 5-10 nm). Jusqu'alors, les exemples de NOFs micellaires étaient rares en raison de la forte auto-extinction de la fluorescence des colorants du à leur état agrégé, résultant du *stacking* π-π des chromophores et des processus de transfert d'électrons. Nous avons spécialement conçu et synthétisé deux nouvelles molécules fluorescentes amphiphiles à base de sondes moléculaires de type cyanine (Cy3 et Cy5), possédant des groupements hydrophobes et hydrophiles (Fig. 4). Dans cette approche les dérivés de type cyanine ont été sélectionnés car ils possèdent de bonnes propriétés spectroscopiques, en particulier un bon rendement quantique, un coefficient d'extinction molaire élevé et une bonne résistance au photoblanchiment.

La capacité des molécules synthétisées à s'auto-assembler et à former des nanoparticules de structure micellaire a été étudiée par diffusion dynamique de la lumière (DLS). Nous avons constaté que leur concentration micellaire critique (CMC) était élevée (de l'ordre du µM). Pour réduire la CMC, nous avons utilisé deux des contre-ions hydrophobes fortement stériques précédemment utilisés dans la deuxième approche, favorisant ainsi le processus de micellisation par ses interactions

électrostatiques et hydrophobes avec les molécules amphiphiles. La brillance de fluorescence a été évaluée en mesurant le rendement quantique de fluorescence des molécules amphiphiles à l'état micellaire. Des mesures par spectroscopie à corrélation de fluorescence (FCS) ont également été effectuées. Nos résultats suggèrent que le contre-ion contribue à l'auto-assemblage de deux molécules amphiphiles pour produire de petites nanoparticules micellaires (environ 7 nm de diamètre) et que les NOFs obtenus présentent une luminosité de fluorescence remarquablement élevée par rapport à une molécule de fluorophore isolée. En outre, les colorants Cy3 et Cy5 sont bien connus comme étant un bon couple en transfert d'énergie de fluorescence par résonance (FRET). Nous avons donc créé des NOFs à deux couleurs via le co-assemblage de molécules Cy3t et Cy5t amphiphiles avec un contre-ion stérique permettant un FRET au sein des NOFs. Cette approche a mené à l'un des premiers exemples de NOFs micellaires où les fluorophores encapsulés ne sont pas sujet à une auto-extinction, montrant ainsi une luminosité supérieure. Les micelles obtenues sont d'un grand intérêt pour la fabrication de nanoparticules fluorescentes fonctionnelles comme outils de fluorescence en chimie et biologie. Ces résultats font l'objet d'un article en preparation[4].

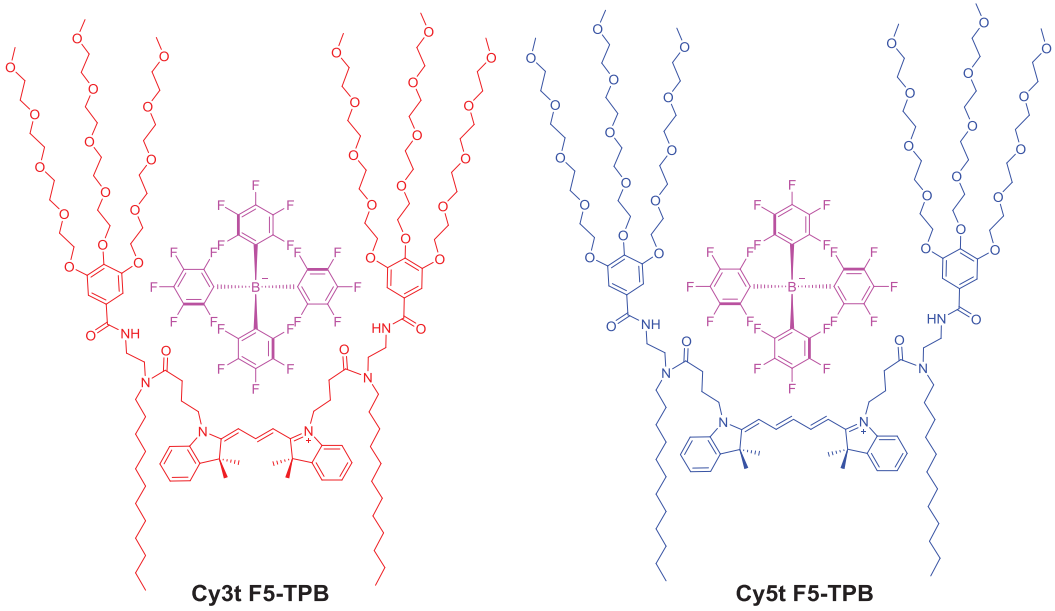

Fig. 4 Structures des molecules synthetisées à base de colorant de type cyanine, en particulier Cy3 et Cy5 assemblé par un contre-ion hydrophobe fluoré à base de tétraphényleborate.

4. Les micelles polymérisées par des agents de réticulation (*crosslinking*) fluorescents.

Zhang et al. ont présenté une nouvelle approche biomimétique de construction de nanoparticules fluorescentes organiques à partir de micelles multifonctionnelles par réticulation de leur surface par *click-chemistry*[5]. En quatrième approche, nous avons développé cette méthodologie en utilisant des agents de réticulation à base de colorants fluorescents de type cyanine, possédant une partie hydrophile PEG et des groupes fonctionels - azotures. Les molécules amphiphiles macrocycliques

basé sur des calix[4]arènes sont très attrayantes en vue d'un assemblage supramoléculaire contrôlé dans de petites nanostructures[6], car ils présentent une architecture conique et peuvent comporter plusieurs groupes chargés. Dans le présent travail, nous avons utilisé un nouveau dérivé de calix[4]arènes amphiphile portant des groupes cationiques réactifs (amine quaternaire avec le groupe alkyne) au bord supérieur et des chaînes alkyle au bord inférieur. Leur auto-assemblage en solution aqueuse a été caractérisé par des sondes fluorescentes (pyrène, bromure d'éthidium), par spectroscopie de corrélation de fluorescence, diffusion dynamique de la lumière (DLS) et microscopie à force atomique. Nous avons constaté que les calix[4]arènes portant de longues chaînes alkyles (octyle) s'auto-assemblent en micelles de diamètre 6 nm à faible CMC et présentent la capacité unique de pouvoir être fonctionnalisés après l'assemblage (Fig. 5). Nous avons utilisé des agents de réticulation à base de colorant de type cyanine, en particulier Cy3 et Cy5, pour capturer et ainsi stabiliser ces nano-objets sous forme sphérique de micelles. Ces agents de réticulation fournissent aux micelles la possibilité d'être lumineuses sous la forme de petites nanoparticules fluorescentes (NOFs) d'un diamètre d'environ 10 nm. Cette méthode de synthèse de NOFs par réticulation permet une bonne stabilité en milieu biologique pour les nanoparticules ainsi obtenues. Il est possible d'envisager ultérieurement la fonctionnalisation de telles nanoparticules par des ligands de cibles thérapeutiques en utilisant à nouveau la *click chemistry* à la suite de la réticulation (*post*-fonctionnalisation). Ce travail fait l'objet d'une publication en cours de préparation[7].

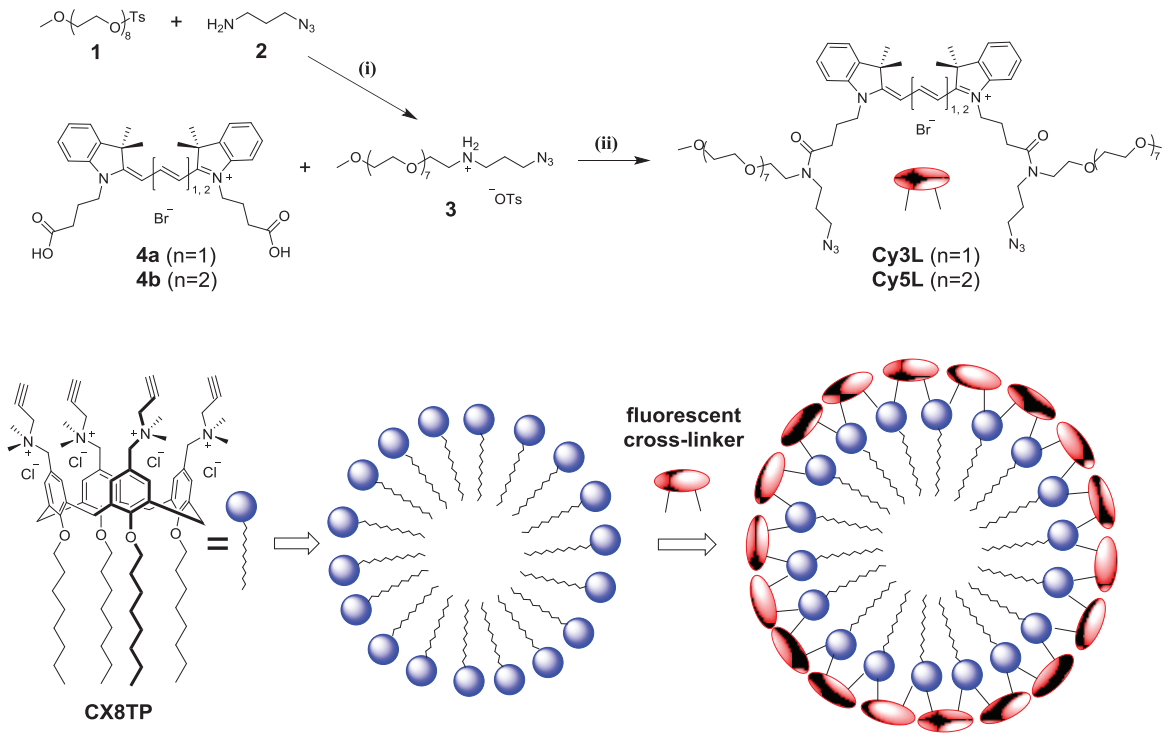

Fig. 5 Structure de molécule amphiphile fonctionnelle de calixarene, en présentant le schèma de la réticulation par des agents réactifs à base de colorants de type cyanine.

Conclusions

L'utilisation de nanoparticules fluorescentes en imagerie biomédicale présente un triple défi : obtenir des particules d'une très grande brillance, de plus petite taille possible, tout en utilisant des matériaux organiques biodégradables.

Le but de ce travail était de développer des stratégies différentes afin de préparer, de caractériser et d'appliquer de nouveaux modèles de nanoparticules organiques fluorescentes (NOFs) ultra-petites et très lumineuses pour l'études de bio-imagerie *in vitro* puis *in vivo*. A cet effet, plusieurs nouvelles familles de NOFs ont été développées et quatre approches existantes de construction de NOFs ont été prises en compte. La première approche est basée sur l'encapsulation des fluorophores 3-alkoxyflavones et un dérivé du Rouge Nil dans les nano-gouttelettes lipidiques. A cette occasion, nous avons mis au point une application de ces nano-gouttelettes pour la détection du flux sanguin chez le poisson zèbre.

Le second type de nanoparticules est basé sur la co-précipitation de dérivés de rhodamine B par la famille de contre-ions hydrophobes fluorés basée sur le tétraphénylborate. Leurs propriétés d'émission sont directement dépendantes du nombre d'atomes de fluor dans la structure du contre-ion utilisé. En troisième approche, nous avons utilisé des contre-ions hydrophobes de tétraphénylborate pour stimuler le processus de micellisation de molécules amphiphiles et ainsi obtenir des nanoparticules fluorescentes sous forme de micelles. La quatrième approche était de polymériser des micelles construites à partir de calixarènes cationiques en utilisant des agents de réticulation à base de colorants fluorescents cyanine.

En conclusion, ces nouveaux types de NOFs présentement décrites, au-delà de la compréhension fondamentale de leurs propriétés physiques, apparaissent par leurs performances photophysiques, comme d'excellents outils pour les études en biologie intracellulaire. Ces nanoparticules, qui peuvent être spontanément absorbées par des cellules vivantes, montrent un excellent rapport signal sur bruit en microscopie cellulaire, ainsi qu'une absence de toxicité. Les approches, fondées sur le contrôle de l'organisation spatiale des fluorophores par des contre-ions, ainsi que l'approche fondée sur la polymérisation (*crosslinking*) de micelles par des agents de réticulation fluorescents, ouvrent la voie vers une nouvelle classe améliorée de nanomatériaux organiques pour des applications en imagerie cellulaire et biomédicale. Ces particules peuvent par exemple permettre la détection et le suivi de biomolécules individuelles dans des cellules vivantes, notamment des marqueurs tumoraux, et ainsi contribuer à une future médecine personnalisée du cancer.

Références

1. Highly lipophilic fluorescent dyes in nano-emulsions: towards bright non-leaking nano-droplets
Andrey S. Klymchenko, Emilie Roger, Nicolas Anton, Halina Anton, Ievgen Shulov, Julien Vermot, Yves Mely and Thierry F. Vandamme, *RSC Advances*, 2012, 2, 11876-11886.

2. Shulov I., Oncul S., Reisch A., Arntz Y., Collot M., Mely Y., Klymchenko A.S. Fluorinated counterion-enhanced emission of rhodamine aggregates: ultrabright nanoparticles for bioimaging and light-harvesting. Nanoscale. 2015, 7, 18198-18210.

3. Morphology Control of Fluorescent Nanoaggregates by Co-Self-Assembly of Wedge- and Dumbbell-Shaped Amphiphilic Perylene Bisimides
Xin Zhang, Zhijian Chen, and Frank Würthner, *J. Am. Chem. Soc.*, 2007, 129 (16), 4886–4887.

4. Non-coordinating anions assemble cyanine amphiphiles into ultra-small fluorescent nanoparticles
Ievgen Shulov, Youri Arntz, Yves Mély, Vasyl G. Pivovarenko and Andrey S. Klymchenko, *Chemical science*, submitted.

5. Artificial Light-Harvesting System Based on Multifunctional Surface-Cross-Linked Micelles
Hui-Qing Peng, Yu-Zhe Chen, Yan Zhao, Qing-Zheng Yang, Li-Zhu Wu, Chen-Ho Tung, Li-Ping Zhang and Qing-Xiao Tong, *Angewandte Chemie*, 2012, 51 (9), 2088–2092.

6. Virus-Sized DNA Nanoparticles for Gene Delivery Based on Micelles of Cationic Calixarenes
Roman V. Rodik, Andrey S. Klymchenko, Namrata Jain, Stanislav I. Miroshnichenko, Ludovic Richert, Vitaly I. Kalchenko and Yves Mély, *Chemistry - A European Journal*, 2011, 17, 20, 5526–5538.

7. Shell-cross-linked calixarene micelles with cyanine corona: protein-sized ultrabright fluorogenic nanoparticles
Ievgen, Shulov, Roman V. Rodik, Youri Arntz, Andreas Reisch, Vitaly I. Kalchenko and Andrey S. Klymchenko (in preparation).

UNIVERSITÉ DE STRASBOURG

Ievgen SHULOV

Synthesis of fluorescent organic nanoparticles for biological applications

Les techniques basées sur la fluorescence sont très efficaces pour l'étude des processus biologiques. Les nanoparticules fluorescentes ont révolutionné le domaine de la bioimagerie tant par leur luminosité, leur photostabilité supérieures que par leur capacité à s'insérer dans différents modes d'imagerie. A ce jour, les mieux caractérisées sont les particules inorganiques comme les *quantum-dots* et les particules de silices dopées en colorants. Cependant, du à leur biodégradabilité limitée et à la présence d'éléments toxiques, le développement de nouvelles nanoparticules organiques fluorescentes (NOFs) présente un grand intérêt, étant donné leur luminosité souvent meilleure que les *quantum dots*, leur totale biodégradabilité et leur non-toxicité. Le but du présent travail fût de développer ce type de nanoparticules organiques, de petites tailles et de luminosité élevée. Nous avons d'abord mis au point l'encapsulation de colorants hautement lipophiles dérivés des 3-alkoxyflavones et du Rouge du Nil dans des nano-gouttelettes lipidiques (25-40 nm) et leur application in vivo chez le poisson zèbre. Ensuite, nous avons obtenu des NOFs par mélange de solutions aqueuses de dérivés de rhodamine avec des contre-ions hydrophobes volumineux et fluorés à base de tétraphénylborate, ce qui provoque une association ionique sous forme de NOFs de taille 11-20 nm et d'un rendement quantique de ~60%. Des études comparatives ont montré que l'augmentation du nombre d'atomes de fluor dans la structure du contre-ion améliore la luminosité, la photostabilité et la stabilité en milieu biologique. En outre, nous avons conçu des marqueurs fluorescents amphiphiles de type cyanine, capables de s'auto-organiser sous forme de NOFs. Le processus de micellisation a été induit par les contre-ions hydrophobes fluorés de tétraphénylborate, donnant des NOFs très lumineuses de taille 7 nm. Enfin, une synthèse de NOFs par réticulation de micelles formés à partir de molécules de calix[4]arène a été élaborée par *click-chemistry* avec des colorants cyanines bi-fonctionnels positionnés en surface. Une telle réticulation permet d'obtenir des NOFs (7 nm) résistants en milieu biologique, tout en possédant une luminosité élevée et un comportement fluorogène. Les NOFs ainsi décrites sont spontanément endocytosées par les cellules vivantes et montrent un excellent rapport signal sur bruit en microscopie cellulaire. Ces NOFs apparaissent donc comme des outils prometteurs pour les applications en imagerie cellulaire et biomédicale.

Mots clés : nanoparticules organiques, fluorescence, auto-assemblage, calix[4]arène, imagerie biologique, contre-ion, stabilité colloïdale, transfert d'énergie.

The fluorescence techniques are very effective for studying biological processes. Fluorescent nanoparticles have revolutionized the domain of bioimaging by their superior brightness and photostability as well as their possibility to be used in combination with other modalities in imaging. In particular, the best characterized to this date are inorganic nanoparticles such as quantum dots and dye-doped silica nanoparticles. However, because of their limited biodegradability and presence of toxic elements, the development of new types of fluorescent nanoparticles is of high interest. Fluorescent organic nanoparticles (NPs) can show comparable or better brightness to the quantum dots, and moreover can be fully biodegradable and non-toxic when constructed from corresponding organic materials. The aim of the PhD project is to develop fluorescent organic NPs characterized by small size and high brightness. At first, we have successfully encapsulated the highly lipophilic dyes derived from 3-alkoxyflavone and Nile Red into lipid nano-droplets (25-40 nm) for in vivo application in zebrafish. The second family of NPs was obtained by mixing aqueous solutions of rhodamine B derivatives with bulky hydrophobic fluorinated counterions based on tetraphenylborate, causing their association in form of NPs of 11-20 nm size and up to 60% quantum yield. Comparative studies have shown that increasing the number of fluorine atoms in the structure of counterion improves their brightness, photostability and stability in biological media. We also designed the new cyanine dyes of amphiphilic type, which are capable to self-organize in the form of NPs. The micellization process was promoted by introduction of the hydrophobic highly fluorinated tetraphenylborate counterions, giving highly emissive 7 nm-sized NPs. Finally, we have developed the synthesis of shell-cross-linked micelles formed from the amphiphilic calix[4]arene and bi-functional cyanine-based crosslinkers. The crosslinking allows obtaining 7 nm-sized NPs stable in biological media and showing high brightness and fluorogenic behavior. The NPs described here, being spontaneously endocytosed by living cells, feature an excellent signal-to-noise ratio in live-cell microscopy. Therefore they are promising building blocks for constructing new tools for cellular and biomedical imaging.

Keywords : organic nanoparticles, fluorescence, self-assembly, bioimaging, counterion, counterion, energy transfer.